Brittle-ductile transition in subduction zones : the role of quartz

Giulia Palazzin

To cite this version:

Giulia Palazzin. Brittle-ductile transition in subduction zones : the role of quartz. Earth Sciences. Université d'Orléans, 2016. English. NNT : 2016ORLE2001 . tel-01407260

HAL Id: tel-01407260
https://theses.hal.science/tel-01407260v1

Submitted on 1 Dec 2016

UNIVERSITÉ D'ORLÉANS

ÉCOLE DOCTORALE
ENERGIE, MATERIAUX, SCIENCES DE LA TERRE ET DE L'UNIVERS

Institut des Sciences de la Terre d'Orléans

THÈSE présentée par :

Giulia PALAZZIN

soutenue le : **18 mars 2016**

pour obtenir le grade de : **Docteur de l'université d'Orléans**

Discipline/ Spécialité : Sciences de la Terre

Transition fragile-ductile en zone de subduction: le rôle du quartz

THÈSE dirigée par :	
Laurent JOLIVET	Professeur, Université d'Orléans
CO-encadrant :	
Hugues RAIMBOURG	Maître de Conférences, Université d'Orléans
RAPPORTEURS :	
Alexandre DIMANOV	Chargé de recherche, MINES ParisTech
Frédéric GUEYDAN	Professeur, Université de Montpellier

JURY :	
Michel FAURE	Professeur, Université d'Orléans
Olivier LACOMBE	Professeur, Université Paris 6
Francesca MENEGHINI	Chargée de recherche, Institut des Géosciences et Ressources de Pise

Remerciements

Tout d’abord je remercie Laurent Jolivet et Hugues Raimbourg, mes directeurs de thèse pour m’avoir suivie, conseillée et soutenue pendant ces trois années (et un peu plus...). Je garderai toujours des très bons souvenirs de nos missions sur le terrain… les Alpes, le Japon, des lieux uniques d’apprentissage avec des maîtres d’exception.

Je remercie également les rapporteurs, Alexandre Dimanov et Frédéric Gueydan, ainsi que tous les membres du jury, Michel Faure, Olivier Lacombe et Francesca Meneghini, de bien avoir accepté de lire ce manuscrit de thèse.

Merci également à Holger Stünitz pour m’avoir introduite à la presse Griggs. Je le remercie également pour l'enseignement qu'il m'en a fait et pour tous les précieux conseils qu'il m’a donnés. Je remercie aussi Renée Heilbronner pour son aide dans le traitement des données mécaniques et le traitement d’image… sacré boulot !

Je remercie Jacques Malavieille pour m’avoir donné le bon conseil au bon moment…

Au sein du labo je remercie tout le personnel administratif, notamment Marie-Noelle, Virginie et Oliver pour leur précieux aide et leur présence. Je remercie aussi Marlène et Marielle ainsi que Catherine du coté OSUC.
Un très grand merci à Nathalie pour ses inestimables services de recherches bibliographique… !
Et aussi à Yohann, Tatiana et Laurent pour avoir résolus mes infinis problèmes avec l’ordinateur !
Et merci à mon ordinateur qui, enfin, est encore parmi nous même s’il a risqué d’être jeté par la fenêtre pas mal de fois.

Un grand remerciement à Sylvain et MR Badin, toujours disponibles, pour leur travail sur les lames minces et à Patricia pour les métallisations.
Merci Ida pour ton soutien pendant les longues séances à l’EBSD ! Ça a été très important.
A ce propos je remercie aussi Jacques qui a passé pas mal d’heure pour lancer mes cartographies pendant les horaires les plus bizarres…merci !
Un grand merci à Rémi Champallier qui a essayé de me former à la Paterson…même si le projet n’as pas abouti tu m’as toujours donné un coup de main et des bons conseils.
Je remercie aussi tous les membres de l'atelier mécanique, Petit Rémi, Estéban et Fred, pour leur disponibilité et bonne humeur.

J’ai bien peur d’oublier quelqu’un…

Je remercie toutes les personnes que j’ai connues pendant mes pérégrinations.

Pour commencer les copains de Bâle… Sina et Bettina (mes Charlie’s angels!), Rudiger et surtout Rosalie, Francesca, Sébastien (et son maté), Leif (ça déchire !) et Justin. J’ai adoré prendre les apéros avec vous sur les bords du Rhin !

La Réunion m’a fait cadeaux de super rencontres aussi : Gaëlle et Mickael, Pierre, Marie… les coraux, les courses (pas programmées) sous la pluie tropicale, les ravines sauvages. Je remercie bien Vincent Famin qui m’as accueillie dans son labo et introduite à la technique de l’infrarouge. Il a été aussi bon copain de sport pendant mon séjour sur l’île.

C’est grâce à Giacomo, Iseline et Joanna que j’ai survécu aux sombres hivers norvégiens ! J’ai eu en plus l’honneur de diner au restaurant le meilleur de Tromso, *Chez Holger* !

Tout ça fait un bon paquet de souvenirs !

En fin je remercie les membres/copains de l’Equipe Géodynamique et de l’Equipe Magma qui ont fait partie de mon quotidien pendant ces trois dernières années… je vais surement oublier quelqu’un mais j’essaye : Nicole, Max, Romain, Charles, Guillaume, Leslie, Lydie, Max, Armel, Adrien, Eloïse, Bashar, Mohammed, Gaëlle, Lionel, Michel, Giada, Dirandra, Aurélien, Seb, Malcolm, Colin, Luca, Julie, Isabelle, Arnaud, Claudie, Manuel, Caroline, Clarette, Teddy, Yann-Aurelien, Yves, Olivier…

Je vais être très mélancolique à mon départ… !

En particulier je remercie et embrasse Mickael (mon premier copain au labo! ta plante est encore en vie !), Pietro (quel bonheur se connaitre !), mon « copain » de bureau Clém, Saskia, Alexandra, Leila, Zineb, Manuela, Vince, Hugues, Val, Hugo, Alex, Adrien, Keke, Myriam, Nolwenn, Pierangelo, Abdel, Anne-Asiliz, Manon.

La thèse m’a même permis de rencontrer des bons copains en faisant le sport que j’adore…Homan, Sam, Fred, Thom, Cedric, Eric ! Sans oublier quand même Lahsen, et les copains de hand/ultimate.

Un grand remerciement enfin à mes potes italiens… Gio, Marzio, Luca, Pelix, Lallo, Alberto, Lu, Etta, Steo, Clint, Cri, Gianlu, Ba, Eli, Albi. Et Andrea Festa.

Et les colocs qui ont vu changer mes humeurs à la vitesse des nuages pendant les ouragans ! Merci Claudio, Luca, Amélie, Aurélien pour votre support. Et aussi Guilhem et Théo. Et Solange, Jacques, Louis, François, Emilie, Lucie … c’est bon tout ça !

En fin je remercie ma famille, en particulier ma maman Lucia, que j’adore.

Camille, cette aventure se termine à ton coté et nous allons bientôt en commencer une autre…merci pour tout !

Transition-fragile ductile en zone de subduction: le rôle du quartz

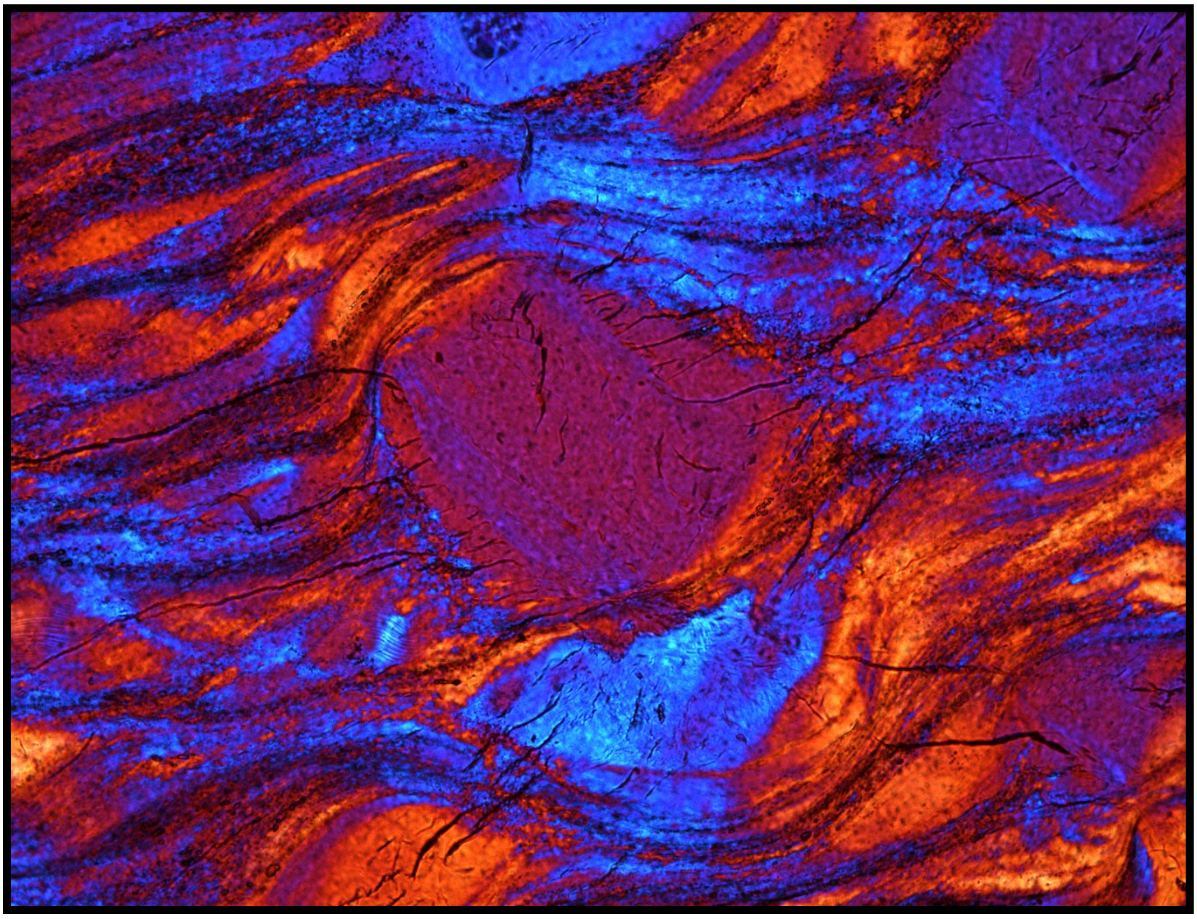

Giulia Palazzin

Directeur de thèse : Laurent JOLIVET
Co-encadrant : Hugues RAIMBOURG, Holger Stunitz

Table de matière

Chapitre I

Chapitre II

Deformation processes at the down-dip limit of the seismogenic zone: the example of Shimanto Belt

Chapitre III

Chapitre IV

Conclusion

Annexe I

Annexe II

Chapitre I

INTRODUTION

Ce chapitre a pour objectif de cerner le contexte et la problématique de ce travail de thèse, dont l'intérêt est de mettre en évidence les modalités de déformation du quartz dans le cas spécifique de la partie en aval de la zone sismogénique en zones de subduction. En ce conteste de déformation, très riche en circulation de fluides, une fonction très important est joué par l'eau: nous explorerons aussi son influence sur les modalités de déformation du quartz.

Après une introduction générale sur la structure d'une zone de subduction, nous présenterons les connaissances actuelles sur la distribution et la spécificité des manifestations sismiques en fonction de la profondeur. Par la suite, nous exposerons un résumé des lois de frottement et des mécanismes proposés dans la littérature pour expliquer la genèse des séismes. Ces mêmes expérimentations permettent d'associer le changement du comportement mécanique du quartz comme représentatif de changement frictionnel observées en aval des zones sismogéniques, la transition fragile-ductile. Nous présenterons donc une synthèse des connaissances actuelles vis-à-vis des processus de glissement récemment identifiés et qui caractérisent en particulier la portion inférieure de la zone sismogénique. Par le biais de quelques exemples, nous introduirons les mélanges tectoniques qui correspondent aux roches déformés à l'interface entre les deux plaques. Ces corps rocheux, déformés à la transition fragile-ductile, présentent évidences de l'activation de plusieurs mécanismes de déformation, notamment les mécanismes qui concernent le quartz : la pression-dissolution et la plasticité à basse température. Cela nous amènera à énoncer la problématique de ce travail de thèse qui concerne donc la déformation du quartz et l'influence de l'eau à la transition fragile-ductile.

CHAPTER I
INTRODUCTION

In this dissertation I study the role that quartz plays at the brittle-ductile transition in subduction zones. Superficial earthquakes hypocenters are mainly distributed in a certain depth range along plate interface, the seismogenic zone, while the shallower and deeper portions of this zone are characterized by a net decrease of the seismic behavior. This change in seismic properties is attributed for the up-dip portion to clay dehydration reactions while, at the down-dip limit, the transition has been ascribed to the activation of quartz plasticity, with increasing temperature. This last concept is based on results of frictional tests on granitic rocks which well represent of the upper crust behavior. However, subductions zones are very water-rich contexts, and the presence of water bears a strong influence on the mechanical properties of quartz. First, the presence of water strongly enhances the plastic deformation of quartz. This water-weakening behavior, demonstrated in the 60' by *Griggs et al.* [1965, 1967] is nevertheless not well quantitatively constrained, nor the microscopic processes underlying it is well understood. Second, deformation experiments on polyphase rocks and observations of naturally deformed samples provide evidences of the interplay of several deformation mechanisms in quartz, including pressure solution, at the transition from principally brittle to principally ductile deformation. This dissertation provides new insights about the rheology of quartz deformed in water-rich context such as subduction plate interface.

1 Subduction zones

Subduction is a major process of Earth dynamics that contributes to keep Earth surface at equilibrium and drives mantle convection [*Ricard and Vigny*, 1989]. From a kinematic point of view several authors [e.g. *Forsyth and Uyeda*, 1975; *Stern,* 2002] propose subduction as the principal source of plate tectonic. Slab traction is considered as one of the most important causes for plate force balance [*Lallemand*, 1999; *Conrad and Lithgow-Bertelloni*, 2002]. Subduction zones also contribute to geochemical cycles because the subducting lithosphere transfers oceanic crust and seawater-rich sediments into the mantle. In turn, the slab-derived fluids percolating into the mantle wedge result in its partial melting and to the formation of new continental crust [*Stern*, 2002]. Not recycled sinking slab portions can reach the core-mantle boundary where they are reheated until their upwelling as mantle plumes [*Hofmann*, 1997].

Furthermore, subduction is associated to earthquakes which reflect the important deformation processes acting at converging plates. Earthquakes related to the subducting plate are registered from surface till depth of 700 km. While the intermediate and deep earthquakes (~300 to 700 km) have been interpreted as the result of slab dehydration and minerals phase changes [*Hacker et al.,* 2003; *Green et al.,* 2010], the shallower ones (0 to ~40 km depth) are the result of decoupling and rapid slip along the plate interface and are responsible for the nucleation of “mega” earthquakes. This particular seismic behavior gradually decrease at depth of about 35-40 km, to totally no manifestations at higher depths.

1.1 General structure of a subduction zone

Subduction zones (**Figure 1**) are morphologically expressed by the presence of a narrow depression called trench which develops along the entire system, reaching lengths of several thousands of kilometers. Volcanic island arcs are located several hundred kilometers away from the trench. This configuration allows to define the arc-trench systems which are generally divided into three major constituents, the forearc, the magmatic arc, and the back-arc basin.

The forearc region is thus the portion composed by the trench, the accretionary prism and the forearc basin. The depth of the trench seems related to the age of the oceanic lithosphere: for example, the relatively young hot oceanic crust at Peru-Chile trench reaches depth of 2-4 km, contrarily to the Mariana trench in the western Pacific region which develops at depth of 10-11 km.

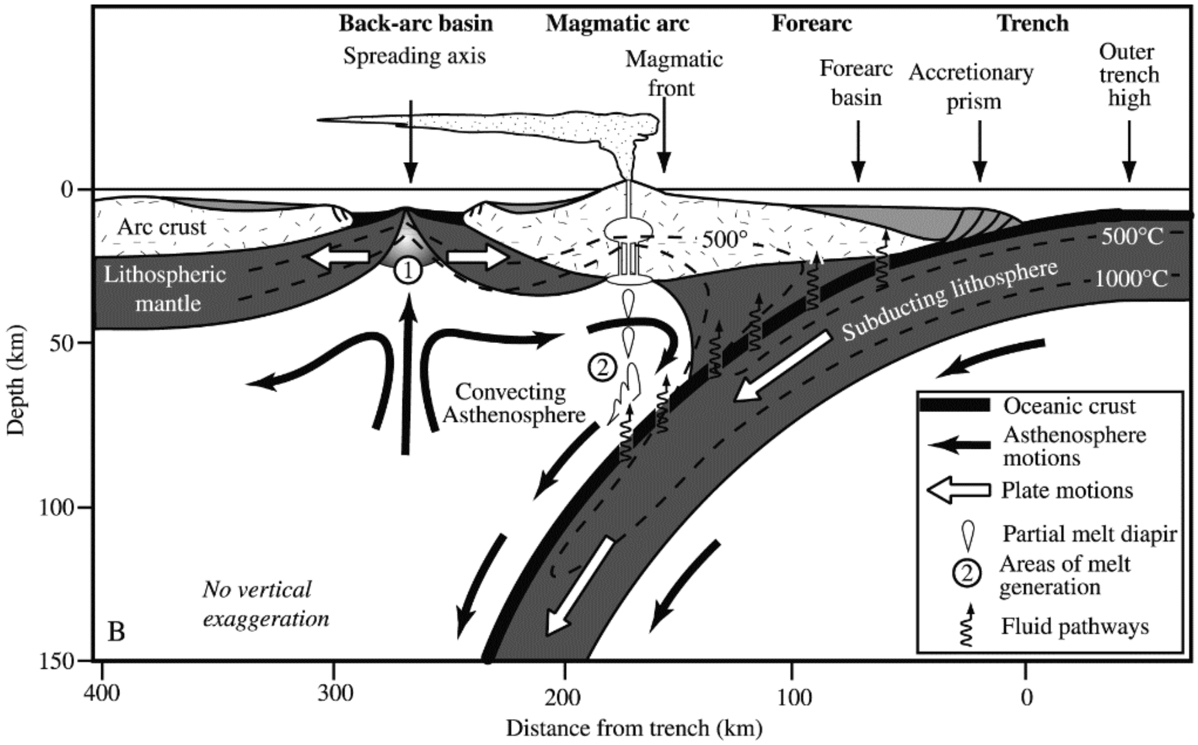

Figure 1. *Conceptual representation of a subduction zone [from Stern, 2002].*

Whereas the forearc basin is a region of relatively slow sedimentation, the accretionary prism is site of intense accumulation of sediments. Accretionary prisms are in fact the result of off-scraping and accretion of the sedimentary cover belonging to subducting lower plate. Two categories of prisms are described in literature (**Figure** 2), depending on the amount of sediments being subducted. When the thickness of the sediments is more than 400 m [*Dahlen*, 1990; *von Huene and Scholl*, 1991; *Le Pichon et al.,* 1993] a portion of the sedimentary cover enters in subduction while the remaining part accumulates at the trench to form an accretionary prisms. Contrarily, for lower sediment supply, the forearc region will be non-accretionary and all sediments are underthrusted at the trench.

A well-studied accretionary margin is the Nankai Trough where the prism presents a thick sedimentary section. Seismic reflection imaging allowed highlighting some major characteristics of the Nankai prism (**Figure 3**) which can be applied to most accretionary prisms. They grow by frontal accretion on a frontal thrust at which sediments are continuously accumulated. The zone of active deformation episodically jumps seaward as a new frontal thrust is generated and the former one becomes inactive.

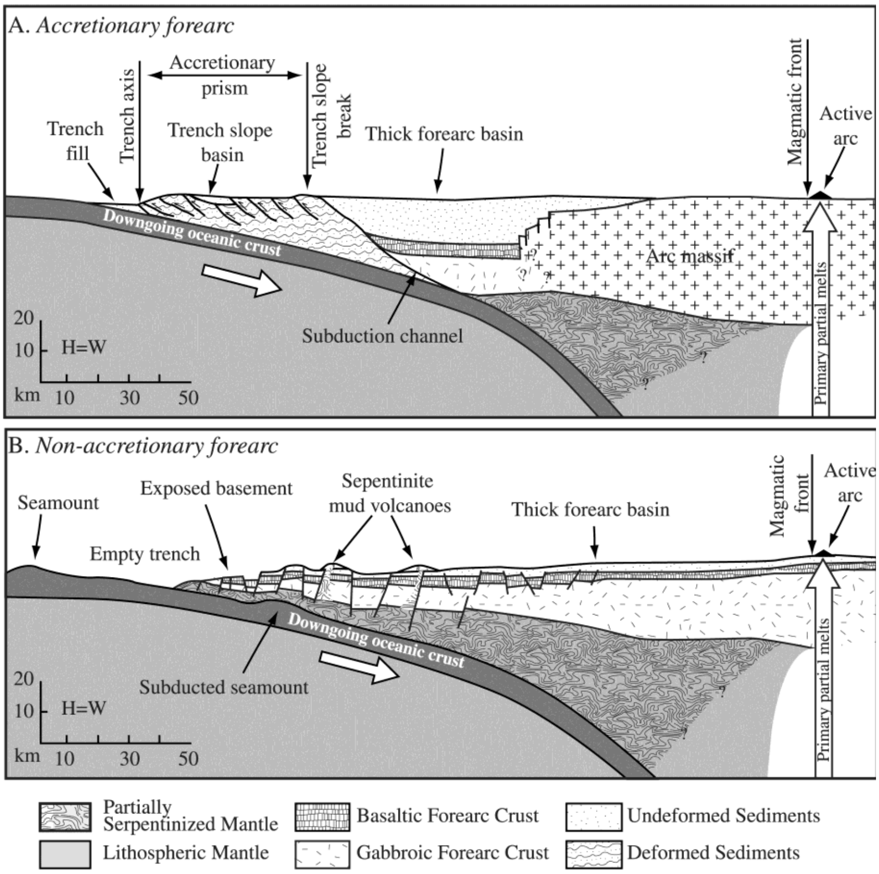

***Figure 2**. A) Accretionary forearc and B) non-accretionary forearc. Accretionary forearc are mostly adjacent to or near continents where large amounts of sediments can be eroded and incorporated in the accretionary prism. The accretionary prism is deformed by imbricate thrusts that build the wedge. In non-accretionary forearc the trench is empty and the exposed oceanic basement is eroded at its base and characterized by normal faulting. From Stern [2002].*

In parallel of this seaward propagation of deformation described as *in-sequence thrusting*, new thrust faults, called *out-of-sequence-thrust*s (OOST), possibly nucleate landward of the frontally deforming domain [*Moore et al.,* 2001]. These sequences of thrusts, which delimit folded and cleaved domains, are branched on a main gently-dipping décollement, which defines the plate boundary beneath the prism. Off-scraped sediments may be underthrusted beneath the prism along the plate boundary and subducted. They will be mainly accreted by imbricated thrusts faults and a portion of the sediments will be subducted in the "subduction channel" [*Cloos and Shreve,* 1988].

Magmatic island arcs develop several hundred kilometers away from the trench, behind the forearc basin (**Figure 1**). They are usually convex toward the underthrusting ocean lithosphere. This geometry is explained partly as a result of spherical geometry for very long trenches [*Frank*, 1986] and by slab retreat for short trenches such as the Mediterranean ones [*Faccenna et al.,* 2004].

Behind the magmatic volcanic arc, a back-arc basin may develop as a consequence of slab retreat [*Karig*, 1972; *Malinverno and Ryan*, 1986].

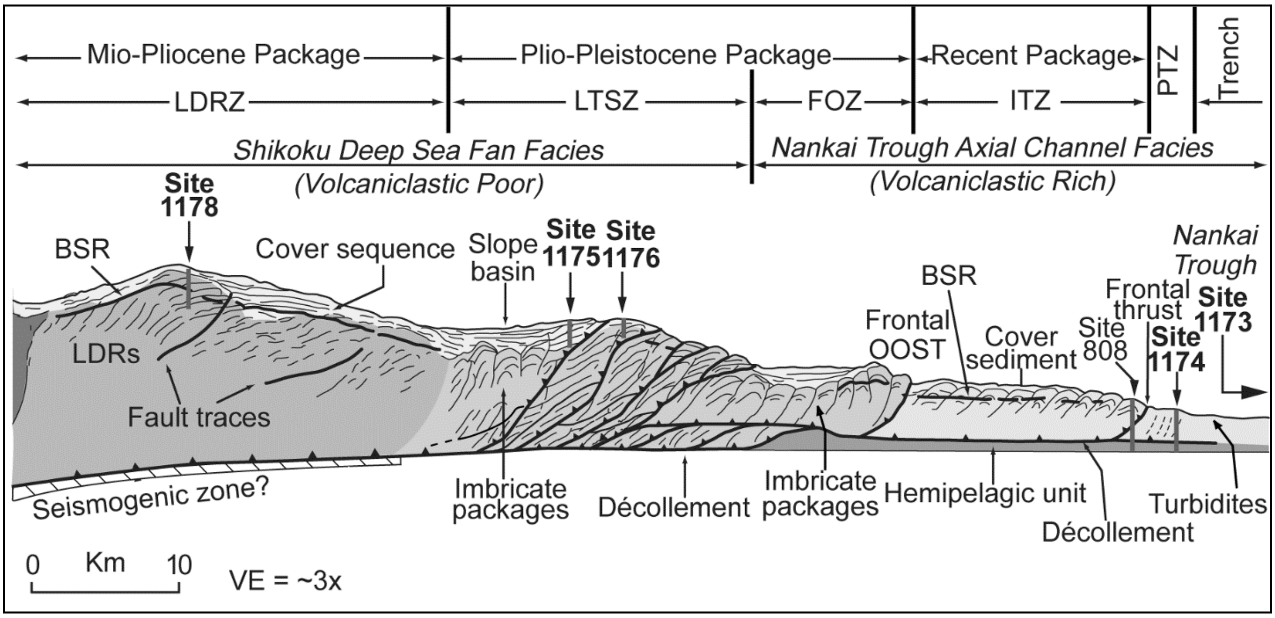

Figure 3. *Schematic tectonic interpretation of a seismic line in the Muroto Transect, in front of Shikoku Island (Japan) (see Moore et al. [2001] for exact location). Vertical Exaggeration is about ~3x. LDRs, landward-dipping reflections; BSR, bottom-simulating reflection; OOST, out-of-sequence thrust; PTZ, Proto-thrust zone; LDRZ, landward-dipping reflector zone; LTSZ, large thrust slice zone; FOZ, frontal out-of-sequence thrust zone; ITZ, imbricate thrust zone [from Moore et al., 2001].*

1.2 Distribution of earthquakes along the plate interface

Seismicity in the lower plate can be associated to lithospheric bending or to plate relative motion. A first distinction was provided by *Stauder* [1968] on the basis of the different focal mechanisms observed in the Aleutian arc with respect to their localization to the trench (**Figure 4**). Focal mechanisms for normal faulting are observed in the outer portion of the subduction system and associated with oceanic lithosphere bending. Contrarily, thrust focal mechanisms found in the inner part of the island arc are interpreted as thrust fault and thus associated to earthquakes nucleated at plate interface.

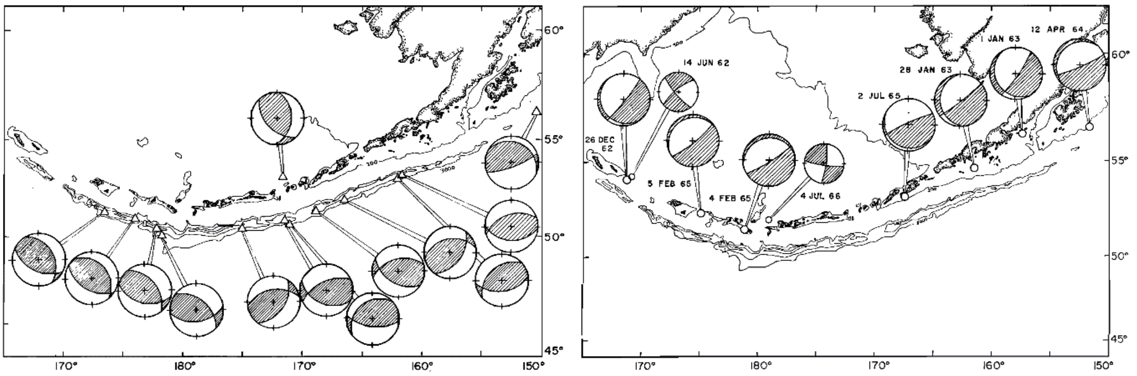

Figure 4. *Focal mechanisms solutions for earthquakes around the Aleutian Islands. Note that hatched areas are associated to extension and white areas to compression [from Stauder, 1968]. The portion closer to the trench shows normal faulting, associated to the flexural bending of the lithosphere; the deeper part, beneath the island arc, shows thrust focal mechanisms associated to the thrust fault.*

Successively, *Byrne* [1988] proposed a classification on the basis of the seismogenic behavior considering only compressional events related to plate interface. The record of hypocenter locations over a period of several years in the Nankai Trough, Aleutian arc, Lesser Antilles arc [*Byrne,* 1988] allowed to define three major zones, starting from the trench axis and located between 0 to ~50 km in depth.

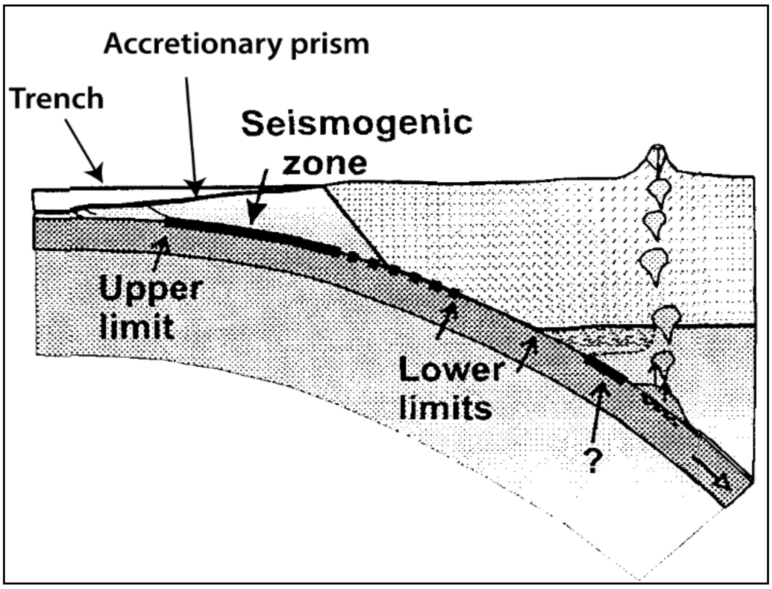

Figure 5. *Synoptic scheme of seismicity distribution with depth of a subduction zone from Hyndman et al., [1997]. The seismogenic zone is delimited by a net upper limit, the seismic front, while the down-dip part is represented by a transitional zone (dashed line).*

The shallower part is comprises between 0 to ~10 km from the trench axis and it is considered aseismic because no earthquakes nucleation is observed.

The seismogenic portion, between ~10 and 40-50 km in depth, shows the highest seismogenic behavior and it is separated by the upper aseismic portion by the seismic front. Then, a transition to the aseismic behavior is observed in the deeper portion (**Figure 5**) at about ~450-50 Km.

1.2.1 Seismic behavior of the plate interface

Earthquakes generated at the seismogenic zone along plate interface, are the result of frictional instabilities. This phenomenon is known as *stick-slip* behavior and it was described for the first time by *Brace and Byerlee* [1966]. These authors explored frictional coefficient variations of pre-fractured granite and observed that the *stick-slip* behavior is triggered when the ratio of shear stress and normal stress reaches a critical value, the static friction coefficient (μ_s), which depends on material properties. When slip occurs, friction coefficient falls again to a second critical value, the dynamic frictional coefficient (μ_d). This drop induces a dynamic instability that is responsible for the propagation of a fracture. *Brace and Byerlee* [1966] compared the *stick-slip* behavior to earthquake nucleation: elastic stress and strain accumulate during the interseismic period (stick) and are released during the earthquake (slip). The stress drop corresponds to sample failure and, after this first failure, a cyclic evolution of strength is observed: strength rises and drops again, all along the same fault plane.

1.2.1.1 Thermally controlled frictional behavior

Following these experiments, *Dieterich* [1978, 1979] and *Ruina* [1983] formulated frictional laws. The stability of a material, during sliding, depends on a critical distance (L) and on the friction parameter (*a* - *b*) [*Ruina*, 1983]. This difference represents the frictional coefficient dependence to slip velocity variations (V):

$$a - b = \frac{\partial \mu ss}{\partial [\ln(V)]} \qquad \textit{eq. 1}$$

When (a - b) < 0, materials behave in an unstable way: once a rupture initiates, the frictional coefficient decreases while the slip velocity increases, thus inducing slip acceleration. This behavior is known as *velocity-weakening* behavior. Contrarily, when (a - b) > 0, materials show *velocity-strengthening* behavior and frictional strength increases as slip velocity increases. Materials are thereby stable and behave in aseismic way. At plate interface, only portions with predominant instable regime may give rise to earthquakes.

The frictional properties of granite were explored by *Stesky* [1978], *Dieterich* [1978, 1981] with different frictional apparatus. They commonly found that samples with mature sliding surfaces display negative (a - b) values at room temperature. *Stesky* [1978] performed some higher-temperature experiments showing that (a - b) becomes positive above approximately at ~350°C. He concluded that the temperature has an effect on frictional granite rheology. Additional frictional tests were carried out on both wet and dry granite gouges by *Chester and Higgs* [1992], *Lockner et al.,* [1986] and *Blanpied et al.,* [1995] at different temperatures. These results confirm again the dependence of (a - b) on temperature changes and describe *velocity-strengthening* behavior between ~100 and ~350°C (**Figure 6**).

At the same time, these experiments have elucidated the microstructural change observed at the transition from the frictional to the stable regime. Initially*, Tullis and Yund* [1977, 1980] carried out deformation experiments on granite at constant pressure and strain rate with increasing temperature. The authors outline the differences in deformation style between quartz and feldspar: at temperatures of 300 - 400°C quartz displays evidences of low-grade plasticity while feldspar still deforms in a brittle way. Furthermore the onset of plastic deformation is not abrupt but it is accompanied by the coeval activation of several deformation mechanisms, as micro-cracks, cataclastic flow and pressure solution which interact to accommodate strain.

The authors outline also that, in presence of water, granite weakening is enhanced. Their conclusion is that pressure, temperature and water play a major role in controlling the activation of deformation mechanisms. These observations are complementary with the results reported by *Chester and Higgs* [1992], who described a change of microstructures in response to the frictional regime in frictional tests. They identify a low-temperature unstable and a high-temperature stable field are characterized respectively by (i) cataclastic deformation with significant slip and by (ii) solution-precipitation-aided cataclastic flow and insignificant slip history effects. The authors concluded that solution-precipitation may be activated during the interseismic period when slip rates are small.

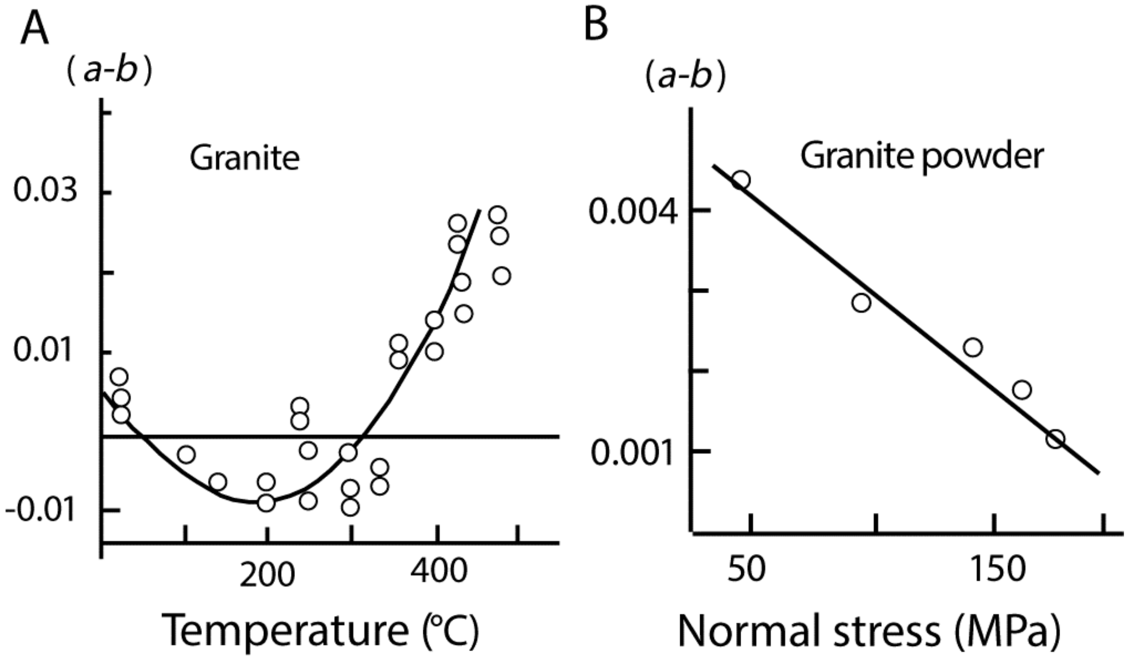

Figure 6. *Dependence of (a-b) to temperature (a) for granites and on pressure (b) for granulated granite. The dependence on pressure due to lithification (b), should be augmented with temperature. From Scholtz [1998]. Data from Stesky et al. [1974], Blanpied et al. [1991] and Marone et al. [1990].*

Tse and Rise [1986] compared these data with natural observations on faults and postulate that the cut-off of crustal earthquakes activity with depth may be explained in terms of the variation of the frictional response of rocks with increasing temperature. Successively, *Wang et al.* [1993] and *Hyndman et al.* [1993, 1997] proposed that the on-set of low-grade quartz ductility could be also responsible for the cut-off of the seismic activity at the down-dip limit of subduction zones (**Figure 6**).

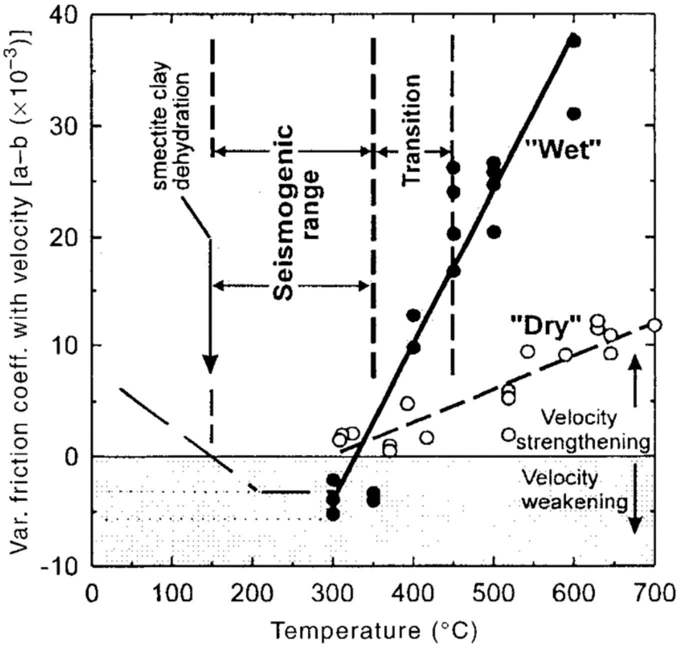

Figure 7. *The velocity weakening (a – b <0) or velocity strengthening (a - b >0) behavior is expressed by the friction coefficient variation with respect to temperature increase. From Hyndman et al. [1997].*

Earthquakes nucleation is thus not expected at temperatures higher than ~350°C and at depths larger than ~40 km, depending on the geothermal gradient characteristic for each subduction zone. **Figure 8** shows a synoptic model proposed by *Scholz* [1998] for the different stability regimes inferred for plate interface in subduction zones. The seismogenic zone (rose field) is delimited in the upper and lower parts by conditionally stable behavior transition zones till stable portions (yellow and blue field).

While the study of the physical properties of the sediments constituting the shallower stable portion of plate interface (the first 1000 meters, see **Figure 3** for borehole locations) are object of direct studies by the way of boreholes, this is not possible for the down-dip limit so that they can only be extrapolated by indirect measurements. The following dissertation is focuses on this deeper part of the seismogenic zone, known as the brittle-ductile transition.

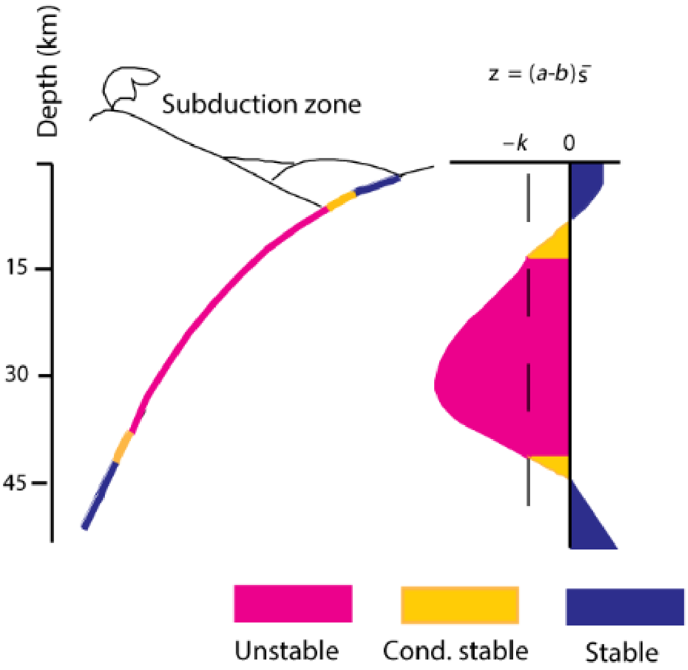

***Figure 8**. Synoptic model for stability (a - b) as a function of depth for plate interface in subduction zones. From Scholz [1998].*

1.3 Brittle-ductile transition at the down-dip limit of the seismogenic zone

1.3.1 Seismogenic behavior at the down-dip limit of the seismogenic zone

In the last decade, with the improvement of techniques for resolving the spatial distribution of slip, the characterization and interpretation of the seismic/aseismic properties of the upper and lower portion of the seismogenic region of subduction zones has seen a great evolution. A wide range of previously unknown fault slip behaviors have been recognized in addition to "normal" fast-slip earthquakes. Coseismic slip and silent earthquakes, slow-slip events (SSE), episodic tremor and slip (ETS), low frequency earthquakes (LFE), very low-frequency earthquakes (VLF) and non-volcanic tremors (NVT) (**Figure 9**) have been recognized at the up and down-dip limit of seismogenic zones worldwide (e.g., Nankai, Cascadia, Mexico) [e.g. *Obara*, 2002; *Rogers and Dragert*, 2003; *Schwartz and Rokosky*, 2007; *Shelly et al.,* 2007]. All these events are characterized by low rates with respect to earthquake manifestation, of the order of hours or years (**Figure 9**).

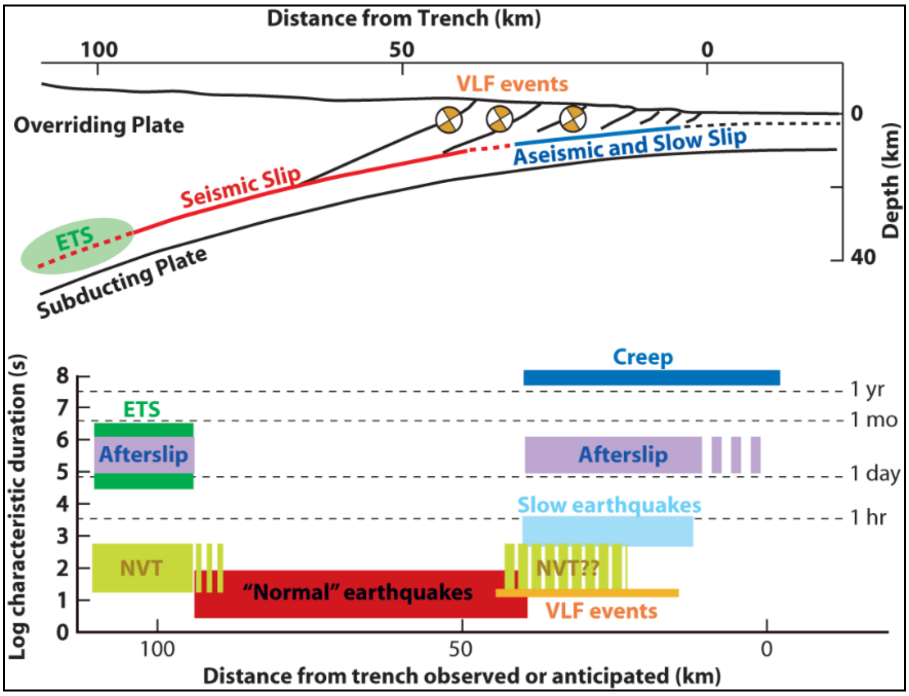

Figure 9*. The range of fault slip behaviors recognized in subduction zone setting. The down-dip limit of the seismogenic zone is characterized by seismic event with very variable duration, from months as the episodic tremor and slip (ETS) to several seconds, as the non-volcanic tremor (NVT); from Marone and Richardson, [2010].*

Obara [2010] recognized for example the presence of slow earthquakes in the shallower portion of the seismogenic zones along the subducting Philippine plate in SW Japan. The down-dip limit of the seismogenic zone in the Nankai Trough (depth in the range of 35 to 45 km) is instead characterized by intense slow-slip events accompanied by non–volcanic tremors activity (**Figure 10)** *Obara* [2002]. The epicenters of these events, with duration varying from several days to weeks, have been detected in western and eastern Shikoku area, in the Kii peninsula and in the Tokai region [*Obara,* 2002*; Katsumata and Kamaya,* 2003*; Hirose and Obara,* 2006*, Obara and Hirose*, 2006*; Shelly et al.*, 2007].

The relative slowness of these events has been attributed to unusual material properties along the fault interface [e.g., *Bilek et al.,* 2004] such that a large amount of energy is dissipated during deformation, making less energy available for seismic radiation.

Even though the causes of these slow slips are not thoroughly understood, it is common interpretation that the slow slip events and associated non-volcanic tremors at the down-dip limit of seismogenic zones are due to fluid overpressure at plate interface.

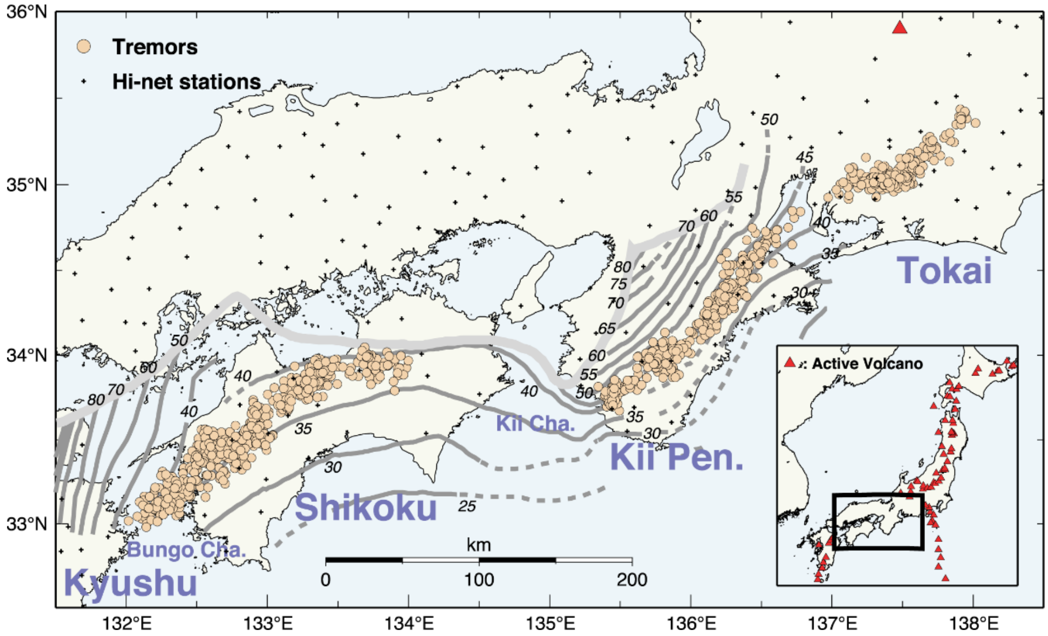

***Figure 10**. Distribution of non-volcanic tremors episodes hypocenters (yellow points) along Shikoku and Kii Islands. Crosses represent the high sensitivity seismograph network (Hi-net) stations. The depth contour line indicates the maximum depth-distribution of earthquakes inside the subducting Philippine Sea plate; the gray line represents the leading edge of the subducting Philippine Sea plate. From Obara [2002].*

The thermal models proposed by *Peacock and Wang* [1999] and *Wada et al.* [2008] predict a significant water release at ~35-40 km depth, due to metamorphic slab dehydration. Thus, the fluid produced by the breakdown of chlorite and glaucophane to form horneblende and epidote [*Fagereng et al.,* 2011 GRL], may migrate at plate interface and be responsible for the raise in pore fluid pressure [e.g., *Liu and Rice*, 2007] observed at these locations [e.g. *Saffer and Tobin*, 2011] (**Figure 11**).

This will then lower effective stresses triggering slow-slip events and tremors [*Brown et al.,* 2005; *Saffer and Tobin*, 2011]. *Obara* [2002] proposes that supercritical fluid due to aqueous fluid mixed with silicate melts may reduce the friction of the rock by increasing the pore pressure and/or the propagation of new small fractures. Independently of the origin of these fluids, these hypothesis converge to the common interpretation that high pore fluid pressure may be the trigger of the slow slip events opening new questions about the role played by water at the transition from the locked-seismic to the stable sliding zone. It is thus very important to provide accurate descriptions of the microstructural archive recorded by rocks deformed at such conditions.

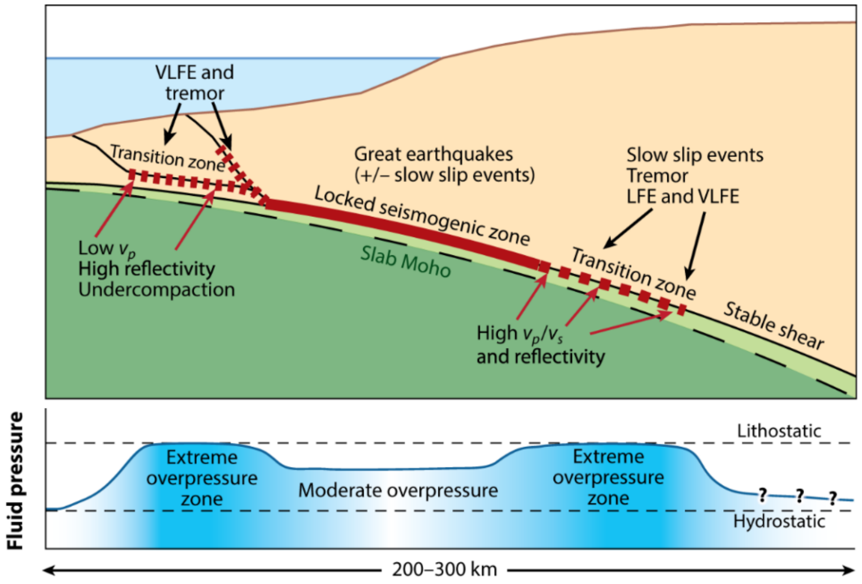

***Figure 11**. Distribution of high pore-fluid pressure along the plate interface expressed by low Vp / High Vp/Vs and high reflectivity the up-dip and down-dip limit of the seismogenic zone. From Saffer and Tobin [2011].*

One of the objective of this dissertation is to better define the role of water in triggering deformation mechanisms at the brittle-ductile transition and the consequence for macroscopic deformation. A detailed analysis about deformation mechanisms acting at such conditions will be provided in the next paragraphs by the meaning of the observation of rocks deformed at depth close to the brittle-ductile transition.

1.3.2 Tectonic mélanges and the brittle-ductile transition

The brittle-ductile transition in subduction zones is recorded by rocks bodies which are known as tectonic mélanges. Tectonic mélanges have been recognized as faults rocks associated to plate boundary motion [e.g. *Festa et al.,* 2010a; *Kitamura and Kimura,* 2012] and are exhumed in mountain chains, revealing the depths of subduction zones (**Figure 12**). Tectonic mélanges associated with deformation at plate interface are characterized by common structural features [e.g. *Festa et al.,* 2010a]: relatively competent blocks are disrupted from their original coherent sedimentary sequence (mostly turbidites) and mixed with blocks of different origins and ages (as basalts associated to cherts and varicolored clays or tuffites). Together, they are embedded within a cleaved, anisotropic clay matrix, resulting in a block-in-matrix structure (e.g. **Figure 13**). Tectonic mélanges fabrics show commonly strongly simple shear deformation (Figure 14) expressed by S-C shear zones, asymmetric boudinage, sheath folds, scaly fabric [*Pini,* 1999; *Vannucchi et al.,* 2003] and micro-scale duplex [e.g. *Kondo et al.,* 2005; *Kitamura and Kimura,* 2012].

Tectonic mélanges associated with deformation at plate interface are characterized by common structural features [e.g. *Festa et al.,* 2010a]: relatively competent blocks are disrupted from their original coherent sedimentary sequence (mostly turbidites) and mixed with blocks of different origins and ages (as basalts associated to cherts and varicolored clays or tuffites). Together, they are embedded within a cleaved, anisotropic clay matrix, resulting in a block-in-matrix structure (e.g. **Figure 13**).

Tectonic mélanges fabrics show commonly strongly simple shear deformation (**Figure 14**) expressed by S-C shear zones, asymmetric boudinage, sheath folds, scaly fabric [*Pini,* 1999; *Vannucchi et al.,* 2003] and micro-scale duplex [e.g. *Kondo et al.,* 2005; *Kitamura and Kimura* 2012].

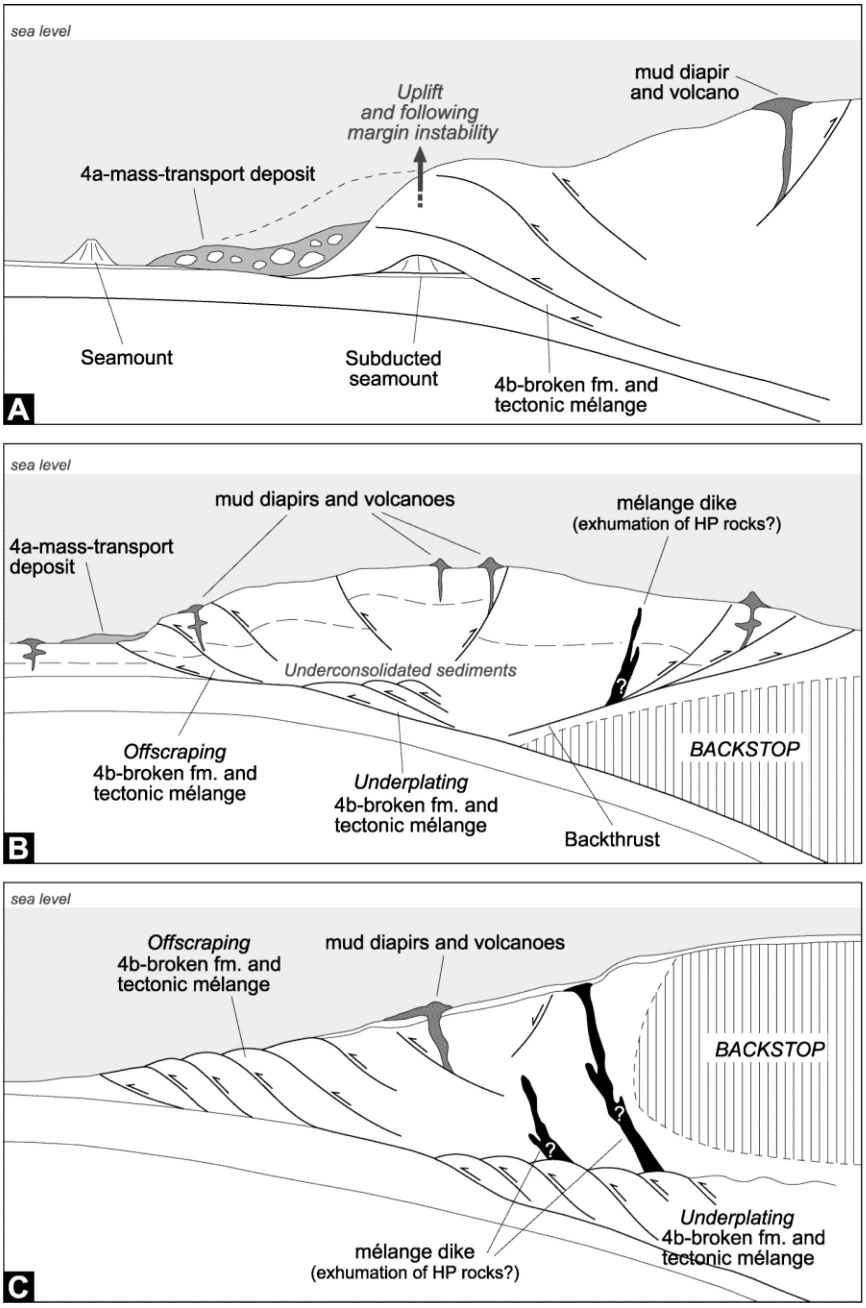

Figure 12. *Three possible scenarios describing the formation of tectonic mélanges during accretion. a) Mass-transport deposit are sedimentary mélanges generated from slope instabilities in the prism; at the same time broken formations and tectonic mélanges are due to accretion by underplating at deeper portions of the prism b) and c);The difference between tectonic mélanges and broken formations is the degree of disruption and the presence of exotic blocks in the former. From Festa et al.* [2010a].

Figure 13. *Example of tectonic mélange where fragments of greenstone, sandstone, and other rocks in disrupted argillite. Bell Pass Melange below the Shuksan Thrust Fault, south side of Suiattle Mountain. http://geomaps.wr.usgs.gov/parks/noca/t3bellpass.html*

A layer sub-parallel extension is also reported [*Hashimoto*, 2006; *Meneghini et al.,* 2009; *Fagereng*, 2011] with the formation of pinch-and-swell structures and boudins (**Figure 14**). This extension is generally considered to be in association with shear along the foliation [*Onishi and Kimura*, 1995]. Particularly well-studied examples of such plate boundary rocks are exposed, for example, in the Kodiak Accretionary Complex [*Fisher and Byrne,* 1990; *Meneghini et al.,* 2009**]**, in the Shimanto accretionary belt [*Taira,* 1988; *Shibata and Hashimoto,* 1995] or in the Franciscan Complex [*Meneghini et al.,* 2009; *Wassman and Stockert,* 2012].

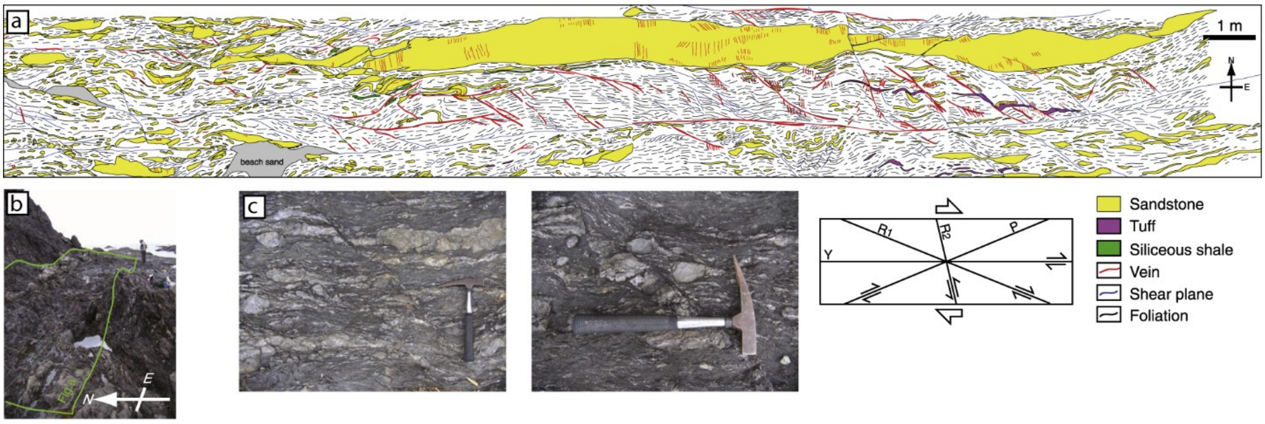

***Figure 14**. Structural interpretation of a portion of the Mugi mélange. From Kitamura and Kimura [2012].*

1.3.2.1 Examples of tectonic mélanges deformed at the brittle-ductile transition

Several examples of tectonic mélanges deformed at conditions close to that of the brittle-ductile transition are described in literature. One of these is the Late Eocene to Early Oligocene Hyuga Tectonic Mélange described by *Saito et al.* [1996]. The Hyuga Tectonic Mélange is a mixture of sandstone and shale, mainly constituted of illite and chlorite, deformed at temperatures of ~250-270°C [*Kondo et al.,* 2005; *Kameda et al.,* 2011]. The block-and-matrix structure is strongly deformed by numerous shear zones, faults and veins filled by quartz and carbonates [e.g. *Kondo et al.,* 2005]. The deformation is brittle accompanied by pressure solution as inferred from microstructural observations on quartz aggregates in sandstone blocks [*Kondo et al.*, 2005]. Another example is the Ghost Rocks Formation in Kodiak Island [e.g. *Meneghini et al.,* 2009]. *Vrolijk et al.* [1988] estimated metamorphic conditions to the prehnite-pumpellyite facies (at about 260°C) by microthermometry on fluid inclusions. This mélange, supposed to correspond to plate boundary interface [e.g. *Fisher and Byrne,* 1990], consists primarily of tightly folded to stratally-disrupted sandstones and shales with occurrences of pillow basalts [e.g. *Fisher and Byrne,* 1990]. *Meneghini et al.* [2009] provide a good microstructural description of the basal portion of the Ghost Rocks Formation where tectonic disruption is amplified and characterized by boudins, cataclastic flow, S-C structures, intense veining and scaly fabric. Coherent blocks are reduced in thickness, strike length and frequency; shear bands are concentrated in shale-rich portion of the rock while massive sandstone and volcanic blocks survive as mega- to micro-boudins with pinched tips and structural signs of internal extension consistent with overall shear indicators [*Meneghini et al.,* 2009]. Multiple cataclastic shear surfaces have been observed within the basal mélange, showing evidence of growth and reactivation during displacement and demonstrating continued re-localization of shear surfaces even at the depth of underplating [*Rowe et al.,* 2005].

1.4 Deformation mechanisms

Thus, microstructures in tectonic mélanges depends strongly on depth and strain rates experienced by the rock. The compilation proposed by [*Moore et al.,* 2007] and showed in **Figure 15**, summarizes the principal deformation features and the associated temperature ranges. Tectonic mélanges deformed at about ~350°C [e.g. *Helper,* 1986; *Norris and Bishop*, 1990; *Ring and*

Brandon, 1999; *Fisher and Brantley,* 2014], namely at the down-dip limit of seismogenic zones, are thus expected to by characterized by two major deformation mechanisms, pressure-solution (with consequent quartz veining and cementation), and the activation of mineral ductile deformation. Thus, unexpected quartz plasticity has been reported in veins of the Ghost Rocks Formation at temperature as low as ~260°C [e.g. *Meneghini et al.*, 2009; *Fisher and Brantley,* 1992].

In the next paragraphs we will get insight more detailed description about pressure solution and crystal plastic deformation, providing examples for tectonic mélanges described in literature.

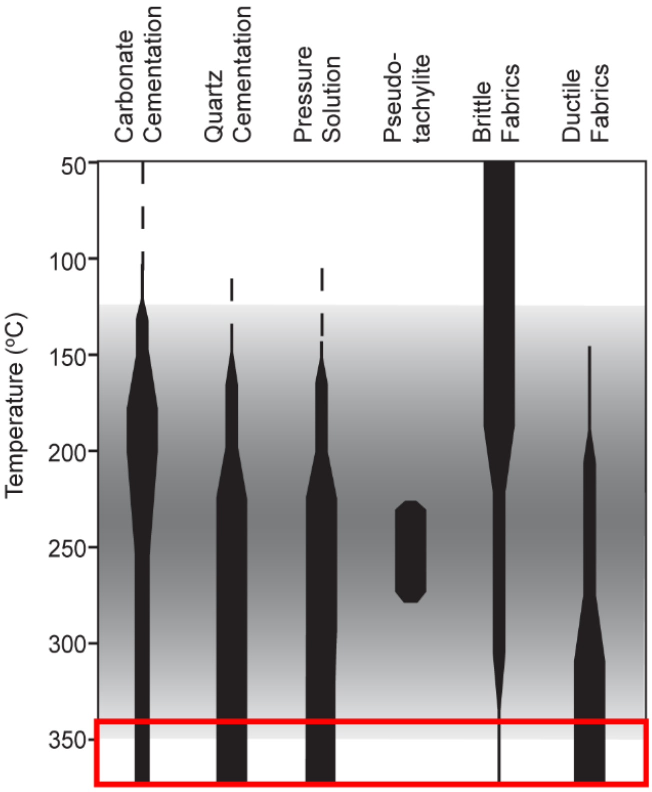

Figure 15. *Activation of deformation processes with temperatures in accretionary prisms. The red box highlight the temperatures at the brittle-ductile transition. From Moore et al. [2007], modified.*

1.4.1 Pressure solution

Pressure solution is considered as the dominant ductile deformation mechanism in sedimentary rocks acting from diagenesis to high metamorphic grade [e.g. *Rutter,* 1983]. Deformation in the clay matrix of most studied tectonic mélanges, as for example the Chrystalls Beach Complex

[*Fagereng et al.,* 2011], the Kodiak formation [*Meneghini et al.,* 2009; *Fisher and Brantley,* 2014], the Mugi and Makiminé mélange [*Mackenzie,* 1987, *Kitamura and Kimura,* 2012], are predominantly accommodated by dissolution–precipitation creep. *Kondo et al.* [2005] describe the shale-dominated zones of the matrix of the Kitagawa group as deformed by pressure solution at temperature of ~350°C.

The overall evidence of pressure solution deformation in the clay matrix is the development of a foliation [*Hashimoto,* 2006; *Wassman and Stoeckert*, 2012; *Hamahashi et al.,* 2015], characterized by black seams of insoluble material, interpreted as dissolution seams [*Mackenzie,* 1987; *Shibata and Hashimoto,* 1995; *Kitamura and Kimura, 2012*; *Rowe and Moore,* 2003] (**Figure 16**). The presence of strain caps and strain shadows around rigid mineral grains are also clear evidence of dissolution and precipitation of quartz [e.g. *Wassman and Stockert,* 2012].

The intense veining observed in many mélanges has been interpreted as the direct result of the precipitation of the quartz dissolved in the nearby matrix (**Figure 17**) [e.g., *Fisher and Brantley,* 2014]. Distributed veins can occur in extensional fractures in lithified boudinaged sandstone blocks necks [e.g. *Hashimoto, 2012, Wassman and Stockert,* 2012].

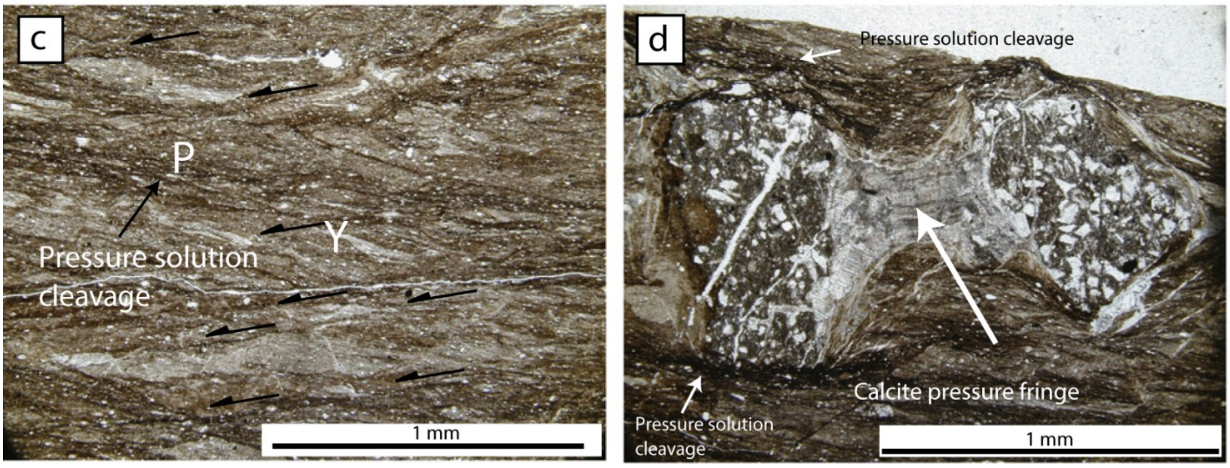

Figure 16. *Examples of shale matrix whit well developed pressure solution cleavages (c) and boudinaged sandstone clast and calcite fringe between the fragments (d). From Kitamura and Kimura [2012].*

Veins are also found on sub-horizontal localized shear zones [*Meneghini et al.,* 2009; *Fagereng*, 2010; *Hashimoto,* 2012] and interpreted as recording cycles of cracking and healing contemporaneous with simple shear. Veins thus express spatio-temporal relationship between different deformational processes which were active during mélange deformation [*Kameda et al.,* 2011]. Veining is considered by several authors as a candidate of strain hardening of plate interface, leading to a velocity-weakening behavior [e.g. *Rowe and Moore,* 2003].

Silica impoverishment along anastomosed pressure solution surfaces and in the regions near to veins [*Fisher and Brantley*, 2014] is detected by electron micro probe [e.g. *Fagereng et al.,* 2010], attesting that pressure solution contributes to lithification of the rock. In this sense pressure solution may contributes to lowering rock porosity already considerably reduced (< 3 %) at depth comparable to the brittle-ductile transition [e.g. *Hashimoto,* 2006].

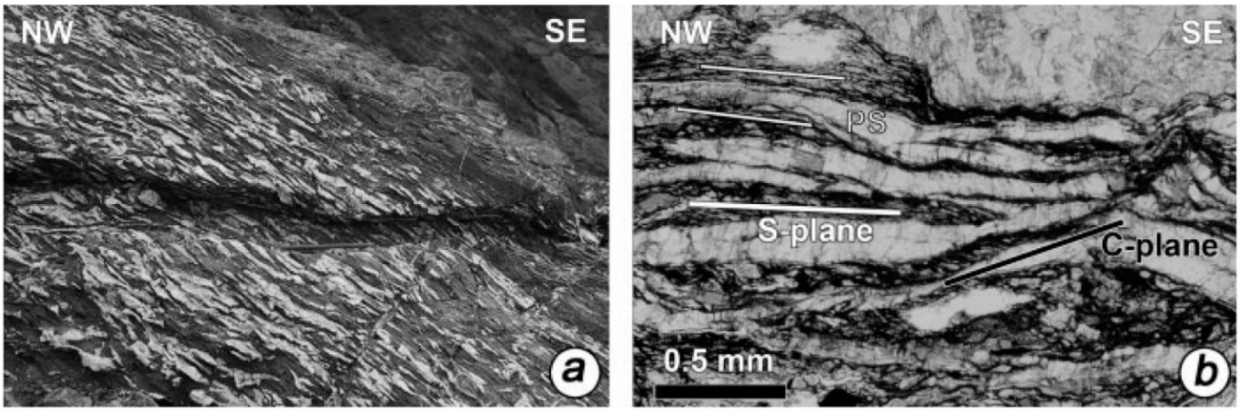

Figure 17. *Example of the penetrative veining characterizing the tectonic mélange of the Kodiak accretionary prism. From Meneghini et al., [2009].*

The rate of solution creep in quartz-rich rocks is a difficult parameter to constrain but it is fundamental to better understand the contribution of pressure solution creep in the seismic cycle.

Gratier et al. [1999] showed that strain rates of the order of 10^{-12} s^{-1} were accommodated by solution transfer in quartz indenter experiments at conditions of 350° and 20-120 MPa. *Renard et al.* [*1*997], *Anzalone et al.* [2006], *Hickman and Evans* 1995] outlined that the rate at which the process is effective can be strongly enhanced by the presence phyllosilicates.

1.4.2 Quartz low-grade plasticity

Despite to the fact that quartz rheology is thought to control the transition from seismic to aseismic behavior in subduction zones, the description of microstructures related to this mineral at the brittle-ductile conditions are not so common. Quartz plasticity is supposed to be active at about 350°C [e.g. *Tullis and Yund,* 1977, 1980]. The principal features associated to these low temperatures plasticity are generally undulose extinction and elongated subgrains [e.g. *Hirth and Tullis,* 1992]. More complex microstructures are bulging, sutured grain boundaries and new subgrains but they are usually observed at higher temperatures because associated to dislocation creep regime. These microstructures are anyway observed in tectonic mélanges: *Needham and Mackenize* [1988] and *Meneghini et al.* [2009] document the activation of plastic flow and dynamic recrystallization of quartz in sandstones layers and veins in the Makimine mélange (~ 330°C) and Kodiak Formation (~ 260°C). The temperatures associated to these microstructures are however quite low with respect to the minimum expected temperature need for the activation of quartz plasticity [e.g. *Hyndman et al.,* 1997]. This aspect is in accord with experimental observations [e.g. *Hirth and Tullis,* 1992] about the co-participation of many factors in triggering the onset of quartz plasticity. The fundamental theory of hydrolytic water effect in quartz was described for the first time by the experimental works of *Griggs and Blacic,* [1965, 1967] and successively many experiments were done to understand the influence of water on quartz rheology. In spite of the major results reported e.g. by *Kronenberg and Tullis* [1984], *Luan and Paterson* [1992], *Gleason and Tullis* [1995], *Hirth et al.* [2001], a universal model of water-weakening and resulting flow law is still lacking. So, despite to the enormous relevance that the activation of low-grade quartz plasticity may play at the lower limit of the seismogenic zones, a model able to explain the rheology of water-rich quartz does not exist. This also because the process of water uptake in quartz is poorly understood. Furthermore, quartz rheology has been explored by using synthetic or metamorphic materials which are not representative of quartz in subduction zones.

1.5 Conclusions and thesis organization

From the simple model proposed by *Hyndman et al.* [1997] the onset of quartz plasticity is supposed to control the change from seismic to aseismic behavior at the down-dip limit of seismogenic zones, at temperature of ~350°C.

In this water-rich context, the two end-member brittle-ductile behavior model is possibly not totally representative of the complex deformation processes acting at plate-boundary rocks. Pressure solution creep is the first candidate to play potentially a major role which could influence the rheology of plate-boundary interface. Furthermore, assuming that quartz plastic deformation controls the onset of the stable sliding behavior [*Hyndman et al.,* 1997], it is essential to investigate the weakening effect of water on this mineral in such water-rich environment.

In the present dissertation I address my research in understanding the microstructures characterizing tectonic mélange deformed at conditions close to the brittle-ductile transition and the role of water in quartz deformation.

Chapter II, entitled “Deformation processes at the down-dip limit of the seismogenic zone: the example of Shimanto Belt”, provides the description of quartz microstructures observed in plate-boundary metasediments from the exhumed accretionary prism of Shimanto (Japan). The investigation about quartz deformation mechanisms are used to draw conclusions about strength distribution at plate interface.

Chapter III deals about the rheological behavior of water-rich quartz from the Hyuga tectonic mélange deformed in laboratory. This material and classic dry Brazil quartz have been deformed at the same conditions to explore the potential effect of water on strength. The results are presented in the form of a scientific publication.

Chapter IV comprises a discussion and general conclusions on the implications of my work for the rheology of mélange deformed along plate interface at the down-dip limit of the seismogenic zone and the mechanical behavior of water rich quartz.

References

Anzalone, A., Boles, J., Greene, G., Young, K., Israelachvili, J., Alcantar, N., 2006. Confined fluids and their role in pressure solution. Chem. Geol. 230, 220–231. doi:10.1016/j.chemgeo.2006.02.027.

Blanpied, M.L., Lockner, D.A., Byerlee, J.D., 1991. Fault stability inferred from granite sliding experiments at hydrothermal conditions. Geophys. Res. Lett. 18, 609–612. doi:10.1029/91GL00469.

Blanpied, M.L., Lockner, D.A., Byerlee, J.D., 1995. Frictional slip of granite at hydrothermal conditions. J. Geophys. Res. 100, 13045. doi:10.1029/95JB00862.

Bilek, S.L., Lay, T., Ruff, L.J., 2004. Radiated seismic energy and earthquake source duration variations from teleseismic source time functions for shallow subduction zone thrust earthquakes. J. Geophys. Res. 109. doi:10.1029/2004JB003039.

Brace, W.F., Byerlee, J.D., 1966. Stick-Slip as a Mechanism for Earthquakes. Science 990.

Brown, K. M., Tryon, M. D., DeShon, H. R., Dorman, L. M., Schwartz, S. Y., 2005. Correlated transient fluid pulsing and seismic tremor in the Costa Rica subduction zone, Earth Planet. Sci. Lett., 238, 189–203.Conrad, C.P., Lithgow-Bertelloni, C., 2002. How Mantle Slabs Drive Plate Tectonics. Science 298, 207–209. doi:10.1126/science.1074161.

Byrne, D.E., Davis, D.M., Sykes, L.R., 1988. Loci and maximum size of thrust earthquakes and the mechanics of the shallow region of subduction zones. Tectonics 7, 833–857. doi:10.1029/TC007i004p00833.

Chester, F.M., Higgs, N.G., 1992. Multimechanism friction constitutive model for ultrafine quartz gouge at hypocentral conditions. J. Geophys. Res. Solid Earth 97, 1859–1870. doi:10.1029/91JB02349.

Cloos, M., Shreve, R.L., 1988. Subduction-channel model of prism accretion, melange formation, sediment subduction, and subduction erosion at convergent plate margins; Part 1, Background and description. Pure Appl. Geophys. 128, 455–500.

Conrad, C.P., Lithgow-Bertelloni, C., 2002. How Mantle Slabs Drive Plate Tectonics. Science 207.

Dahlen, F.A., 1990. Critical taper model of fold-and-thrust belts and accretionary wedges. Annu. Rev. Earth Planet. Sci. 18, 55–99.Faccenna, C., Piromallo, C., Crespo-Blanc, A., Jolivet, L., Rossetti, F., 2004. Lateral slab deformation and the origin of the western Mediterranean arcs. Tectonics 23. doi:10.1029/2002TC001488.

Dieterich, J.H., 1978. Time-dependent friction and the mechanics of stick-slip. Pure Appl. Geophys. 116, 790–806. doi:10.1007/BF00876539.

Dieterich, J., 1979. Modeling of rock friction 1. Experimental results and constitutive equations.

Dieterich, J.H., 1981. Constitutive properties of faults with simulated gouge. Geophys. Monogr. 103–120.

Faccenna, C., Piromallo, C., Crespo Blanc, A., Jolivet, L., Rosselli, F., 2004. Lateral slab deformation and the origin of the arcs of the western Mediterranean. Tectonics 23, doi:1O.1029!2002TCOO 1488:TC I 0 12.

Fagereng, Å., Remitti, F., Sibson, R.H., 2010. Shear veins observed within anisotropic fabric at high angles to the maximum compressive stress. Nat. Geosci. 3, 482–485. doi:10.1038/ngeo898.

Fagereng, Å., Diener, J.F.A., 2011. Non-volcanic tremor and discontinuous slab dehydration. Geophys. Res. Lett. 38, L15302. doi:10.1029/2011GL048214.

Fagereng, Å., Remitti, F., Sibson, R.H., 2011. Incrementally developed slickenfibers — Geological record of repeating low stress-drop seismic events? Tectonophysics 510, 381–386. doi:10.1016/j.tecto.2011.08.015.

Festa, A., Pini, G.A., Dilek, Y., Codegone, G., 2010. Melanges and melange-forming processes; a historical overview and new concepts. Int. Geol. Rev. 52, 1040–1105. doi:10.1080/00206810903557704.

Fisher, D., Byrne, T., 1990. The character and distribution of mineralized fractures in the Kodiak Formation, Alaska: Implications for fluid flow in an underthrust sequence. J. Geophys. Res. Solid Earth 1978–2012 95, 9069–9080. doi:10.1029/JB095iB06p09069.

Fisher, D.M., Brantley, S.L., 1992. Models of quartz overgrowth and vein formation: Deformation and episodic fluid flow in an ancient subduction zone. J. Geophys. Res. Solid Earth 97, 20043–20061. doi:10.1029/92JB01582.

Fisher, D.M., Brantley, S.L., 2014. The role of silica redistribution in the evolution of slip instabilities along subduction interfaces: Constraints from the Kodiak accretionary complex, Alaska. Fluids Struct. Fold Thrust Belts Recognit. Work David V Wiltschko 69, Part B, 395–414. doi:10.1016/j.jsg.2014.03.010.

Forsyth, D.W., Uyeda, S., 1975. On the relative importance of the driving forces of plate motion. Geophys. J. R. Astron. Soc. 43, 163–200.

Frank, F., C., 1968. Curvature of island arc. Nature 220: 363.

Gleason, G.C., Tullis, J., 1995. A flow law for dislocation creep of quartz aggregates determined with the molten salt cell. Tectonophysics 247, 1–23. doi:10.1016/0040-1951(95)00011-B.

Green, D.H., Hibberson, W.O., Kovacs, I., Rosenthal, A., 2010. Water and its influence on the lithosphere-asthenosphere boundary. Nat. Lond. 467, 448–451. doi:10.1038/nature09369.

Griggs, D. T., Blacic, J. D., 1965. Quartz: anomalous weakness of synthetic crystals, Science, 147(3655), 292–295.

Griggs, D., 1967. Hydrolytic Weakening of Quartz and Other Silicates*. Geophys. J. R. Astron. Soc. 14, 19–31. doi:10.1111/j.1365-246X.1967.tb06218.x.

Hacker, B.R., Peacock, S.M., Abers, G.A., Holloway, S.D., 2003. Subduction factory 2. Are intermediate-depth earthquakes in subducting slabs linked to metamorphic dehydration reactions? J. Geophys. Res. Solid Earth 108, 2030. doi:10.1029/2001JB001129.

Hashimoto, Y., Nakaya, T., Ito, M., Kimura, G., 2006. Tectonolithification of sandstone prior to the onset of seismogenic subduction zone; evidence from tectonic melange of the Shimanto Belt, Japan. Geochem. Geophys. Geosystems - G Super 3 7. doi:10.1029/2005GC001062.

Hashimoto, Y., Eida, M., Kirikawa, T., Iida, R., Takagi, M., Furuya, N., Nikaizo, A., Kikuchi, T., Yoshimitsu, T., 2012. Large amount of fluid migration around shallow seismogenic depth preserved in tectonic mélange: Yokonami mélange, the Cretaceous Shimanto Belt, Kochi, Southwest Japan. Isl. Arc 21, 53–64. doi:10.1111/j.1440-1738.2011.00806.x.

Helper, M., A., 1986. Deformation and high P/T metamorphism in the central part of the Condrey Mountain window, north-central Klamath Mountains, California and Oregon, in Blueschists and Eclogites, edited by B. W. Evans and E. H. Brown, Mem. Geol. Soc. Am. 164, 107 – 123.

Hirose, H., Obara, K., 2006. Short-term slow slip and correlated tremor episodes in the Tokai region, central Japan. Geophys. Res. Lett. 33.

Hickman, S.H., Evans, B., 1995. Kinetics of pressure solution at halite-silica interfaces and intergranular clay films. J. Geophys. Res. Solid Earth 100, 13113–13132. doi:10.1029/95JB00911.

Hirth, G., Teyssier, C., Dunlap, J.W., 2001. An evaluation of quartzite flow laws based on comparisons between experimentally and naturally deformed rocks. Int. J. Earth Sci. 90, 77–87. doi:10.1007/s005310000152.

Hirth, G., Tullis, J., 1992. Dislocation creep regimes in quartz aggregates. J. Struct. Geol. 14, 145–159. doi:10.1016/0191-8141(92)90053-Y.

Hyndman, R.D., Wang, K., Yuan, T., Spence, G.D., 1993. Tectonic sediment thickening, fluid expulsion, and the thermal regime of subduction zone accretionary prisms: The Cascadia Margin off Vancouver Island. J. Geophys. Res. Solid Earth 98, 21865–21876. doi:10.1029/93JB02391.

Hyndman, R.D., Yamano, M., Oleskevich, D.A., 1997. The seismogenic zone of subduction thrust faults. Isl. Arc 6, 244–260. doi:10.1111/j.1440-1738.1997.tb00175.x.

Hofmann, A.W., 1997. Mantle geochemistry: the message from oceanic volcanism. Nature 385, 219–229.

Ito, Y., Obara, K., 2006. Dynamic deformation of the accretionary prism excites very low frequency earthquakes. Geophys. Res. Lett. 33. doi:10.1029/2005GL025270.

Kameda, J., Raimbourg, H., Kogure, T., Kimura, G., 2011. Low-grade metamorphism around the down-dip limit of seismogenic subduction zones: Example from an ancient accretionary complex in the Shimanto Belt, Japan. Tectonophysics 502, 383–392. doi:10.1016/j.tecto.2011.02.010.

Karig, D.E., 1972. Remnant Arcs. Geol. Soc. Am. Bull. 83, 1057–1067. doi:10.1130/0016-7606(1972)83[1057:RA]2.0.CO;2.

Katsumata, A., Kamaya N., 2003. Low-frequency continuous tremor around the Moho discontinuity away from volcanoes in the southwest Japan, Geophys. Res. Lett., 30(1), 1020, doi:10.1029/2002GL015981.

Kitamura, Y., Kimura, G., 2012. Dynamic role of tectonic mélange during interseismic process of plate boundary mega earthquakes. Tectonophysics, Chaos and Geodynamics: Melanges, Melange Forming Processes and Their Significance in the Geological Record 568–569, 39–52. doi:10.1016/j.tecto.2011.07.008.

Kondo, H., Kimura, G., Masago, H., Ohmori-Ikehara, K., Kitamura, Y., Ikesawa, E., Sakaguchi, A., Yamaguchi, A., Okamoto, S. 'ya, 2005. Deformation and fluid flow of a major out-of-sequence thrust located at seismogenic depth in an accretionary complex: Nobeoka Thrust in the Shimanto Belt, Kyushu, Japan. Tectonics 24, TC6008. doi:10.1029/2004TC001655.

Kronenberg, A.K., Tullis, J., 1984. Flow strengths of quartz aggregates: Grain size and pressure effects due to hydrolytic weakening. J. Geophys. Res. Solid Earth 89, 4281–4297. doi:10.1029/JB089iB06p04281.

Lallemand, S., 1999. La subduction océanique ; Gordon and Breach Science Publishers, 208 pp.

Liu, Y., Rice, J.R., 2007. Spontaneous and triggered aseismic deformation transients in a subduction fault model. J. Geophys. Res. 112, B09404.

Le Pichon, X., Henry, P., Lallemant, S.J., 1993. Accretion and erosion in subduction zones; the role of fluids. Annu. Rev. Earth Planet. Sci. 21, 307–331.

Lockner, D.A., Summers, R., Byerlee, J.D., 1986. Effects of temperature and sliding rate on frictional strength of granite. Pure Appl. Geophys. 124, 445–469. doi:10.1007/BF00877211.

Luan, F.C., Paterson, M.S., 1992. Preparation and deformation of synthetic aggregates of quartz. J. Geophys. Res. Solid Earth 97, 301–320. doi:10.1029/91JB01748.

Mackenzie, J.S., Needham, D.T., Agar, S.M., 1987. Progressive deformation in an accretionary complex: An example from the Shimanto belt of eastern Kyushu, southwest Japan. Geology 15, 353–356. doi:10.1130/0091-7613(1987)15<353:PDIAAC>2.0.CO;2.

Malinverno, A., Ryan, W.B.F., 1986. Extension in the Tyrrhenian Sea and shortening in the Apennines as result of arc migration driven by sinking of the lithosphere. Tectonics 5, 227.

Marone, C., Raleigh, C.B., Scholz, C.H., 1990. Frictional behavior and constitutive modeling of simulated fault gouge. J. Geophys. Res. 95, 7007–7025. doi:10.1029/JB095iB05p07007.

Marone, C., Richardson, E., 2010. Learning to read fault-slip behavior from fault-zone structure. Geology 38, 767–768.

Meneghini, F., Marroni, M., Moore, J.C., Pandolfi, L., Rowe, C.D., 2009. The processes of underthrusting and underplating in the geologic record: structural diversity between the

Franciscan Complex (California), the Kodiak Complex (Alaska) and the Internal Ligurian Units (Italy). Geol. J. 44, 126–152. doi:10.1002/gj.1144.

Moore, G.F., Taira, A., Klaus, A., Becker, L., Boeckel, B., Cragg, B.A., Dean, A., Fergusson, C.L., Henry, P., Hirano, S., Hisamitsu, T., Hunze, S., Kastner, M., Maltman, A.J., Morgan, J.K., Murakami, Y., Saffer, D.M., Sánchez-Gómez, M., Screaton, E.J., Smith, D.C., Spivack, A.J., Steurer, J., Tobin, H.J., Ujiie, K., Underwood, M.B., Wilson, M., 2001. New insights into deformation and fluid flow processes in the Nankai Trough accretionary prism: Results of Ocean Drilling Pro.

Moore, J.C., Rowe, C., Meneghini, F., 2007. How accretionary prisms elucidate seismogenesis in subduction zones MARGINS theoretical and experimental earth science series. Columbia University Press, United States, United States, pp. 288–315.

Needham, D.T., Mackenzie, J.S., 1988. Structural evolution of the Shimanto Belt accretionary complex in the area of the Gokase River, Kyushu, SW Japan. J. Geol. Soc. Lond. 145, 85–94.

Norris, R. J., Bishop, D. G., 1990. Deformed conglomerates and textural zones in the Otago Schists, South island, New Zealand, Tectonophysics, 174, 331 – 349.

Obara, K., 2002. Nonvolcanic Deep Tremor Associated with Subduction in Southwest Japan. Science 1679.

Obara, K., Hirose, H., 2006. Non-volcanic deep low-frequency tremors accompanying slow slips in the southwest Japan subduction zone. Tectonophysics 417, 33–51.

Obara, K., Tanaka, S., Maeda, T., Matsuzawa, T., 2010. Depth-dependent activity of non-volcanic tremor in southwest Japan (English). Geophys Res Lett 37.

Onishi, C.T., Kimura, G., 1995. Change in fabric of melange in the Shimanto Belt, Japan: Change in relative convergence? Tectonics 14, 1273–1289. doi:10.1029/95TC01929.

Peacock, S.M., Wang, K., 1999. Seismic Consequences of Warm versus Cool Subduction Metamorphism: Examples from Southwest and Northeast Japan. Science 937.

Pini, G.A., 1999, Tectonosomes and olistostromes in the Argille Scagliose of the Northern Apennines, Italy: Geological Society of America Special Paper 335, 73 p.

Ricard, Y., Vigny, C., 1989. Mantle dynamics with induced plate tectonics. J. Geophys. Res. Solid Earth 94, 17543.

Renard, F., Ortoleva, P., Gratier, J.-P., 1997. Pressure solution in sandstones; influence of clays and dependence on temperature and stress. Tectonophysics 280, 257–266.

Ring, U., Brandon, M. T., 1999. Ductile deformation as mass loss in the Franciscan Subduction Complex: Implications for exhumation processes in accretionary wedges, in Ehumation Processes: Normal Faulting, Ductile Flow, and Erosion, edited by U. Ring et al., pp. 55 – 86, Geol. Soc., London.

Rogers, G., Dragert, H., 2003. Episodic Tremor and Slip on the Cascadia Subduction Zone: The Chatter of Silent Slip. Science 1942.

Rowe, C., Moore, J. C., Meneghini, F., McKiernan, A. W., 2005. Large-scale pseudotachylytes and fluidized cataclasites from an ancient subduction thrust fault, Geology, 33(12), 937 – 940.

Rowe, C. D., Moore J. C., 2003. The upper aseismic to seismic transition: A silica mobility threshold, Eos Trans. AGU, 84(46), Fall Meet. Suppl., Abstract T41E-02.

Rutter, E.H., 1983. Pressure solution in nature, theory and experiment. J. Geol. Soc. 140, 725–740. doi:10.1144/gsjgs.140.5.0725.

Ruina, A., 1983. Slip instability and state variable friction laws. J. Geophys. Res. Solid Earth 88, 10359.

Saffer, D.M., Tobin, H.J., 2011. Hydrogeology and Mechanics of Subduction Zone Forearcs: Fluid Flow and Pore Pressure. Annu. Rev. Earth Planet. Sci. 39, 157–186.

Saito, M., 1996. Geological Map of Japan, 1:50,000, Geol. Surv. Jpn., Shiibamura.

Scholz, C.H., 1998. Earthquakes and friction laws. Nature 391, 37–42. doi:10.1038/34097.

Schwartz, S.Y., Rokosky, J.M., 2007. Slow slip events and seismic tremor at circum-Pacific subduction zones. Rev. Geophys. 45, RG3004. doi:10.1029/2006RG000208.

Shelly, D.R., Beroza, G.C., Ide, S., 2007. Non-volcanic tremor and low-frequency earthquake swarms. Nat. Lond. 446, 305–307. doi:10.1038/nature05666.

Shibata, T., Hashimoto, Y., 2005. Deformation style of slickenlines on melange foliations and change in deformation mechanisms along subduction interface; example from the Cretaceous Shimanto Belt, Shikoku, Japan. Gondwana Res. 8, 433–442. doi:10.1016/S1342-937X(05)71145-X.

Stauder, W., 1968. Tensional character of earthquake foci beneath the Aleutian Trench with relation to sea-floor spreading. J. Geophys. Res. 73, 7693.

Stesky, R.M., Brace, W.F., Riley, D.K., Robin, P.-Y.F., 1974. Friction in faulted rock at high temperature and pressure. Tectonophysics 23, 177–203.

Stesky, R.M., 1978. Mechanisms of high temperature frictional sliding in Westerly granite. Can. J. Earth Sci. 15, 361–375. doi:10.1139/e78-042.

Stern, R.J., 2002. Subduction Zones. Rev Geophys 40, 1012. doi:10.1029/2001RG000108.

Tse, S.T., Rice, J.R., 1986. Crustal earthquake instability in relation to the depth variation of frictional slip properties. J. Geophys. Res. 91, 9452–9472. doi:10.1029/JB091iB09p09452.

Tullis, J., Yund, R.A., 1977. Experimental deformation of dry westerly granite. J. Geophys. Res. 82, 5705–5718. doi:10.1029/JB082i036p05705.

Tullis, J., Yund, R.A., 1980. Hydrolytic weakening of experimentally deformed Westerly granite and Hale albite rock. J. Struct. Geol. 2, 439–451. doi:10.1016/0191-8141(80)90005-X.

Vannucchi, P., Maltman, A., Bettelli, G., Clennell, B., 2003. On the nature of scaly fabric and scaly clay: Journal of Structural Geology. 25, 673–688.

von Huene, R., Scholl, D.W., 1991. Observations at convergent margins concerning sediment subduction, subduction erosion, and the growth of continental crust. Rev. Geophys. 29, 279. doi:10.1029/91RG00969.

Vrolijk, P., Myers, G. Moore, J.C., 1988. Warm fluid migration along the Kodiak accretionary complex, Alaska, J. Geophys. Res. 93, 10313-10324.

Wada, I., Wang, K., He, J., Hyndman, R.D., 2008. Weakening of the subduction interface and its effects on surface heat flow, slab dehydration, and mantle wedge serpentinization. J. Geophys. Res. 113, B04402.

Wang, K., Hyndman, R.D., Davis, E.E., 1993. Thermal effects of sediment thickening and fluid expulsion in accretionary prisms: model and parameter analysis. J. Geophys. Res. 98, 9975–9984.

Wassmann, S., Stöckhert, B., 2012. Matrix deformation mechanisms in HP-LT tectonic mélanges — Microstructural record of jadeite blueschist from the Franciscan Complex, California. Tectonophysics, Chaos and Geodynamics: Melanges, Melange Forming Processes and Their Significance in the Geological Record 568–569, 135–153. doi:10.1016/j.tecto.2012.01.009.

Chapitre II

Processus de deformation à la limite inférieure de la zone seismogenique: l'example du prisme d'accretion de Shimanto

Article accepté dans la revue « Tectonophysics»

Dans ce chapitre, présenté sous forme d'un article scientifique accepté de la revue «*Tectonophysics*», nous présentons les résultats d'une étude sur les mécanismes de déformations des roches soumises à conditions proches de la transitions fragile-ductile.

Les unités rocheuses étudiées, le mélange tectonique de Hyuga et l'unité de Morotsuka, sont originaires du prisme d'accrétion fossile de Shimanto, exposé sur l'ile de Kyushu (Japon). En premier résultat, les analyses de spectroscopie du matériel carbonaté (Raman) montrent que le mélange tectonique de Hyuga et l'unité de Morotsuka ont été déformées respectivement à des températures de 250°C et 350°C. Cela permet d'associer les conditions de déformation des deux unités comme proche des conditions prévues en aval de la zone seismogenic. L'analyse microstructurales en microscopie optique sur le quartz, a permis d'observer des microstructures propres aux deux unités : le mélange tectonique de Hyuga est caractérisé par de rubans de quartz très étirés distinct par une intense microfracturation et localement nous observons la présence de nouveaux grains recristallisés au sein de vieux cristaux; contrairement, au sein de l'unité de Morotsuka, le quartz est généralement très recristallisé.

Les orientations des axes cristallographiques «c» des quartzs, obtenus par microscopie à balayage électronique (EBSD), dévoilent deux tendances différentes: les axes de rubans sont orientés parallèlement à la direction d'étirement, cependant les axes du quartz recristallisé dans l'unité de Morotsuka sont concentrés dans la direction perpendiculaire à la foliation. Cette disposition est interprétable comme le résultat de différents mécanismes de déformations. At basse températures la plasticité du quartz n'est pas totalement activée mais le mécanisme de déformation principale est la pression dissolution accompagné par la microfracturation. Les deux sont responsables de la croissance des rubans de quartz. Pour de températures légèrement plus élevées, le quartz est recristallisé en suite à l'activation du fluage dislocation. La transition entre les deux régimes de déformation, i.e. la transition fragile-ductile, est donc localisée à T ~300-350°C. L'abondance d'eau mesuré par FTIR qui caractérise ces quartzs, est supposée d'être promotrice de l'activation de la recristallisation du quartz à si faibles températures. En fin nous proposons que le mécanisme de dissolution par pression observé dans le domaine de déformation fragile, est responsable des faibles contraintes de cisaillement mesurées le long des zones sismogéniques.

CHAPTER II

Deformation processes at the down-dip limit of the seismogenic zone:the example of Shimanto Belt

Deformation processes at the down-dip limit of the seismogenic zone: the example of Shimanto accretionary complex

Palazzin G. (1, 2, 3), Raimbourg H. (1, 2, 3), Famin V. (4), Jolivet L. (1, 2, 3), Kusaba Y. (5), Yamaguchi A(5).

(1) *Univ. d'Orléans, Institute de Science de la Terre d'Orléans, UMR 7327, 45071 Orléans, France*

(2) *CNRS/INSU, Institute de Science de la Terre d'Orléans, UMR 7327, 45071 Orléans, France*

(3) *BRGM, Institute de Science de la Terre d'Orléans, UMR 7327, BP 36009, 45060 Orléans, France*

(4) *Université de La Reunion, Laboratoire Géosciences Réunion, IPG, 97715 France*

(5) *Atmosphere and Ocean Research Institute, the University of Tokyo, 5-1-5-Kashiwanoha, Kashiwa, Chiba 277-8564, Japan*

ABSTRACT

In order to constrain deformation processes close to the brittle-ductile transition in seismogenic zone, we have carried out a microstructural study in the Shimanto accretionary complex (Japan), the fossil equivalent of modern Nankai accretionary prisms. The Hyuga Tectonic Mélange was sheared along the plate interface at mean temperatures of 245°C ± 30°C, as estimated by Raman spectroscopy of carbonaceous material (RSCM). It contains strongly elongated quartz ribbons, characterized by very high fluid inclusions density, as well as micro-veins of quartz. Both fluid inclusion planes and micro-veins are preferentially developed orthogonal to the stretching direction. Furthermore, crystallographic preferred orientation (CPO) of quartz c-axes in the ribbons have maxima parallel to the stretching direction. Recrystallization to a small grain size is restricted to rare deformation bands cutting across the ribbons. In such recrystallized quartz domains, CPO of quartz c-axes are orthogonal to foliation plane. The evolution of deformation micro-processes with increasing temperature can be further analyzed using the Foliated Morotsuka, a slightly higher-grade metamorphic unit (342 ± 30°C by RSCM) from the Shimanto accretionary complex. In this unit, in contrast to Hyuga Tectonic Mélange, recrystallization of quartz veins is penetrative. CPO of quartz c-axes are concentrated perpendicularly to foliation plane. These variations in microstructures and quartz crystallographic fabric reflect a change in the dominant deformation mechanism with increasing temperatures: above ~300°C, dislocation creep is dominant and results

in intense quartz dynamic recrystallization. In contrast, below ~300°C, quartz plasticity is not totally activated and pressure solution is the major deformation process responsible for quartz ribbons growth. In addition, the geometry of the quartz ribbons with respect to the phyllosilicate-rich shear zones shows that bulk rheology is controlled by quartz behavior. Consequently, below 300°C, the application of quartz pressure-solution laws, based on realistic geometry derived from Hyuga microstructures, results in strongly lowering the overall strength of the plate interface with respect to the classical brittle envelop.

INTRODUCTION

As illustrated by the rheological envelopes model [e.g. *Kohlstedt et al.,* 1995; *Stöckhert and Gerya,* 2005; *Burov,* 2011], crustal deformation is usually accounted for brittle/plastic deformation in its upper/lower part. The transition from dominant cataclastic flow to dislocation creep, often referred to as the brittle-ductile transition [*Rutter,* 1986; *Chester,* 1995] is promoted by increasing depth and temperature.

This transition is generally associated to the temperature of ~350°C corresponding to the limit for the onset of quartz plasticity [*Tse and Rice,* 1986; *Hyndman et al.,* 1997] in quartzo-feldspatic rocks [e.g. *Tullis and Yund,* 1977, 1980; *Blanpied et al.,* 1991]. As observed in deformed rocks of the upper crust [*Ramsay,* 1967; *Durney,* 1972; *Kerrich et al.,* 1977*; Gratier and Gamond*, 1990; *Becker,* 1995] above the brittle/ductile transition and in the presence of abundant intergranular fluid phase [e.g. *Gratier,* 1987] cataclastic flow is accompanied by the contribution of another process, pressure solution creep (PSC). PSC has been defined as a non-equilibrium process [*Spiers et al.,* 2004; *Gratier et al.,* 2009] involving dissolution of material at high stressed regions (e.g. grain contacts), diffusion through a grain boundary fluid phase and precipitation on grain interfaces under low normal stress [Rutter and *Elliott,* 1976; *Raj,* 1982; *Spiers et al.,* 1990; *Shimizu,* 1995]. The importance of PSC is also recognized at high metamorphic conditions such as blueschist and amphibolite facies [*Bell and Cuff,* 1989; *Wintsch and Yi,* 2002], e.g. in the development of crenulation cleavage if stresses are not high enough for the activation of plastic deformation [Brander et al., 2011]. The most common microstructures suggesting the operation of pressure solution are stylolite, micro-fractures, mineral shadows or fringes and dissolution cleavages [Evans, 1988; Goodwin and Wenk, 1990]. In contrast with cataclasis which requires high differential stresses and act at high strain rates, pressure solution is most characteristic of slow creeping processes which take place in the upper crust at very low differential stress [Cox and Etheridge, 1989; *Gratier and Gamond,* 1990]. Pressure solution contributes significantly to the overall strain

[*Ramsay,* 1967; *Durney,* 1972; *Kerrich et al.,* 1977; *Cox and Etheridge,* 1983; *Gratier,* 1993; *denBrok,* 1998; *Spiers et al.,* 2004]: the estimations of bulk volume loss due to this process can range from 30 to 80% for slaty cleavage in low metamorphic grade rocks [*Wright and Henderson,* 1992; *Wright and Platt,* 1982; *Cox and Etheridge,* 1983, 1989; *Chester,* 1995; *Goldstein et al.,* 1995, 1998; *Kawabata et al.,* 2007].

In the light of these considerations, the "two end-members" model describing crust rheology in terms of brittle/plastic behavior needs to be reconsidered by the integration of pressure solution creep at the transition from brittle to ductile regime [*Chester,* 1988, 1995; *Scholz*, 1988; *Kirby,* 1983].

The role of pressure solution is presumably highest in subduction zones, where subducted sediments deformed along the plate interface carry along a large quantity in water [*Rutter and Elliott,* 1976]. In such setting, in order to analyze the deformation processes active near the brittle-ductile transition and the potential contribution of pressure-solution, we performed microstructural and Electron Back-Scattered diffraction (EBSD) analysis on low-grade quartz-rich metasediments from the Shimanto accretionary complex (Japan). The Hyuga Tectonic Mélange is a good example for deformation at plate interface at conditions close to the brittle/ductile transition. We describe microstructural evidences of quartz deformation principally by pressure solution and crack-seal at relatively low temperatures (~250°C) in the Hyuga Tectonic Mélange, while quartz plastic behavior is very limited. The temperature effect on the activation of quartz plasticity is then studied observing quartz microstructures from the Foliated Morotsuka, deformed at slightly higher temperatures (~340°C). Finally, using the pressure solution creep law revisited by *Gratier et al.* [2009] and the geometry of naturally deformed metasediments, we discuss the implication that pressure solution creep may have for bulk rock rheology and subduction interface strength.

1. Geological framework

1.1 General structure

The Shimanto accretionary complex, exposed on-land along the Honshu, Kyushu and Shikoku islands (**Figure 1A**), is recognized as an ancient accretionary prism [e.g. *Taira et al.* 1982*,* 1988]. The whole complex, trending parallel to the modern trench axis of the Nankai Trough, is composed of several superposed coherent sedimentary units and tectonic mélanges, younging toward the south-east and separated from the Chichibu belt by the Butsuzu Tectonic Line (BTL).

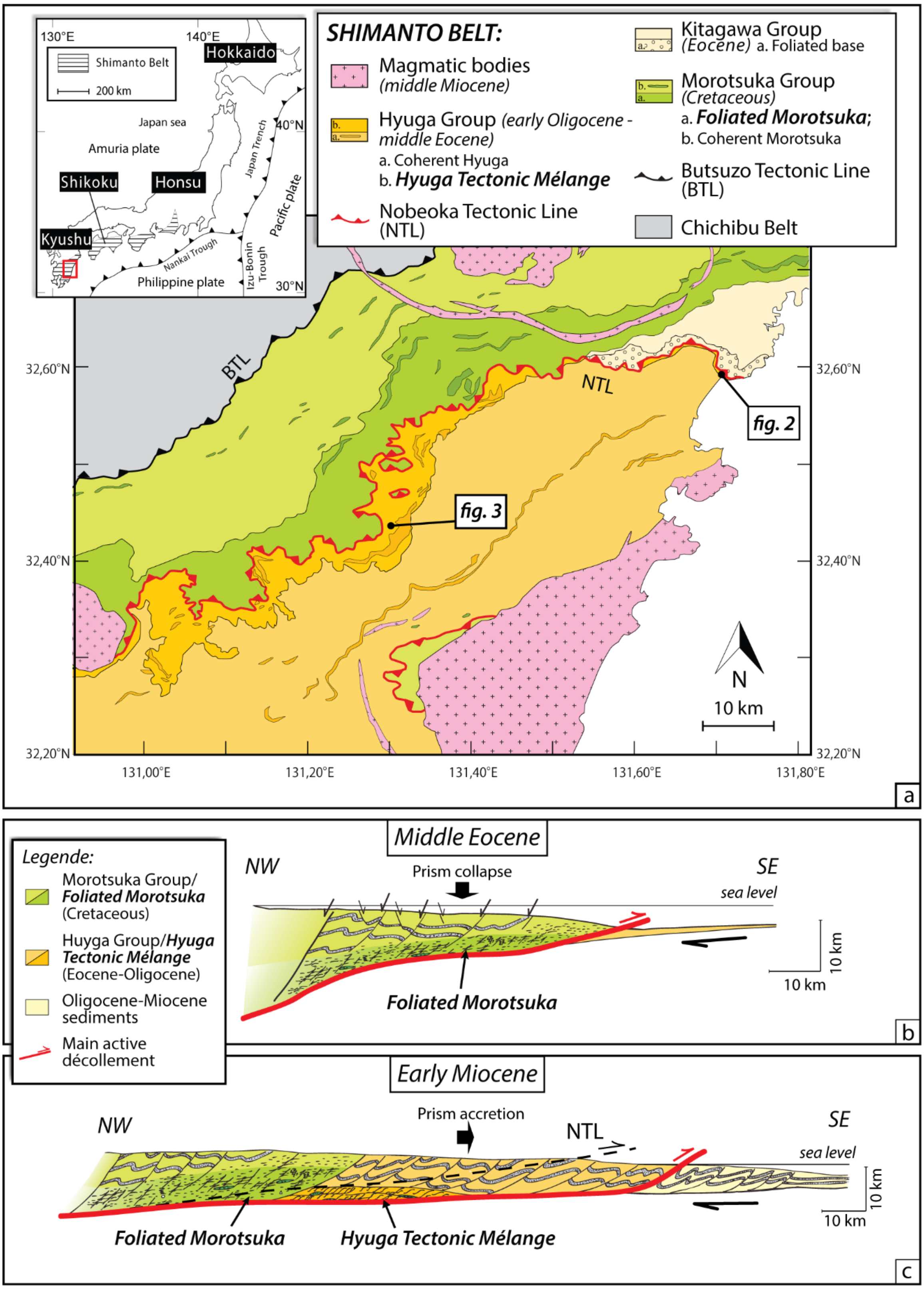

Figure 1: ***A)*** *Simplified geological map of the Shimanto accretionary complex on Kyushu Island [from Murata, 1997]. Simplified reconstructions of the Belt evolution, showing the tectonic interpretations (in B and C) of the deformation recorded in the base of Morotsuka group and Hyuga Tectonic Mélange, respectively [modified from Raimbourg et al., 2014]. B) Middle Eocene prism collapse, associated with a penetrative horizontal extension and vertical shortening in the foliated base of the Morostuka Group. C) Sometimes in Early Oligocene-Early Miocene time lapse, the Hyuga Tectonic Mélange is strongly sheared along the plate interface and underplated at the base of the prism.*

Our study focuses on the basal part of the Morotsuka Group, the Foliated Morotsuka [*Raimbourg et al.,* 2014] and the upper part of the Hyuga Group, known as Hyuga Tectonic Mélange. The two units are juxtaposed by the Nobeoka Tectonic Line (NTL), a large-scale, low-dipping thrust fault with movement toward southeast [*Murata,* 1997; *Saito et al.,* 1996].

1.2 Tectonic features

1.2.1 Hyuga Tectonic Mélange

The Hyuga Tectonic Mélange, also known as Mikado Unit [*Teraoka et al.,* 1981; *Saito et al.,* 1996], is the upper member of the Hyuga group which is exposed in the footwall of the Nobeoka Tectonic Line (**Figure 1A and 1C**).

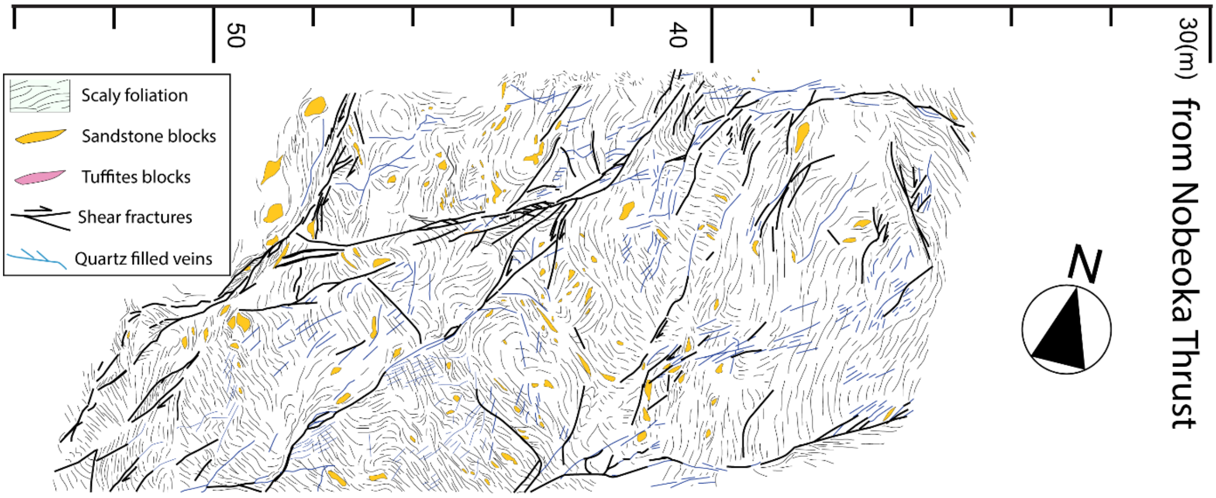

Figure 2: *Exposure of the Hyuga Tectonic Mélange along the eastern coast of Kyushu, in the vicinity of the NTL (location in* ***Fig. 1 A)***

Microfossil assemblages indicate ages from Middle Eocene to Early Oligocene [*Sakai et al.,* 1984*; Nishi,* 1988). At the outcrop scale, the Hyuga Tectonic Mélange is characterized by a typical block-in-matrix structure [e.g. *Festa et al.,* 2010a]: the coherent stratigraphic succession is disrupted and the rock is made of blocks of sandstone, siltstone breccia with minor amounts of basalt, red shales and cherts, embedded in a dark, pelitic matrix [*Saito,* 2008].

Estimation of the mineral composition by relative XRD peak intensity ratio of constituent minerals [*Fukuchi et al.,* 2014] shows that quartz constitutes from 60 to 80 % of the rocks of the unit, while phyllosilicates (mostly chlorite and white mica) form most of the rest. A peculiar feature of the mélange rocks is the abundance of domains of precipitated quartz, formed sometimes as veins cutting across sandstone boudins, but also as elongated bodies within the pelitic matrix.

The alignment of the broken and boudinaged sandstone blocks and quartz veins **(Figure 2 and 3)** defines the foliation, which dips gently to the north-northwest [*Raimbourg et al., 2014*]. A penetrative network of centimeter- to meter-long shear zones (**Figure 2 and 3**) cut across the pre-existing foliation. Shear zones carry a lineation orientated NW-SE, defined by elongated blocks and phyllosilicates, and their kinematics is systematically top-to-the-SE sense of shear.

From petrological analysis of basalts blocks, the syn-deformational metamorphic conditions are within the prehnite-pumpellyite facies [*Imai et al.,* 1971; *Toriumi and Teruya,* 1988]. Peak temperatures estimated with illite crystallinity [*Hara and Kimura,* 2008; *Mukoyoshi et al.,* 2009] and with vitrinite reflectance [*Kondo et al.,* 2005; *Mukoyoshi et al.,* 2009] range between ~250-280°C. *Raimbourg et al.* [2015] find similar temperatures by microthermometry on fluid inclusions.

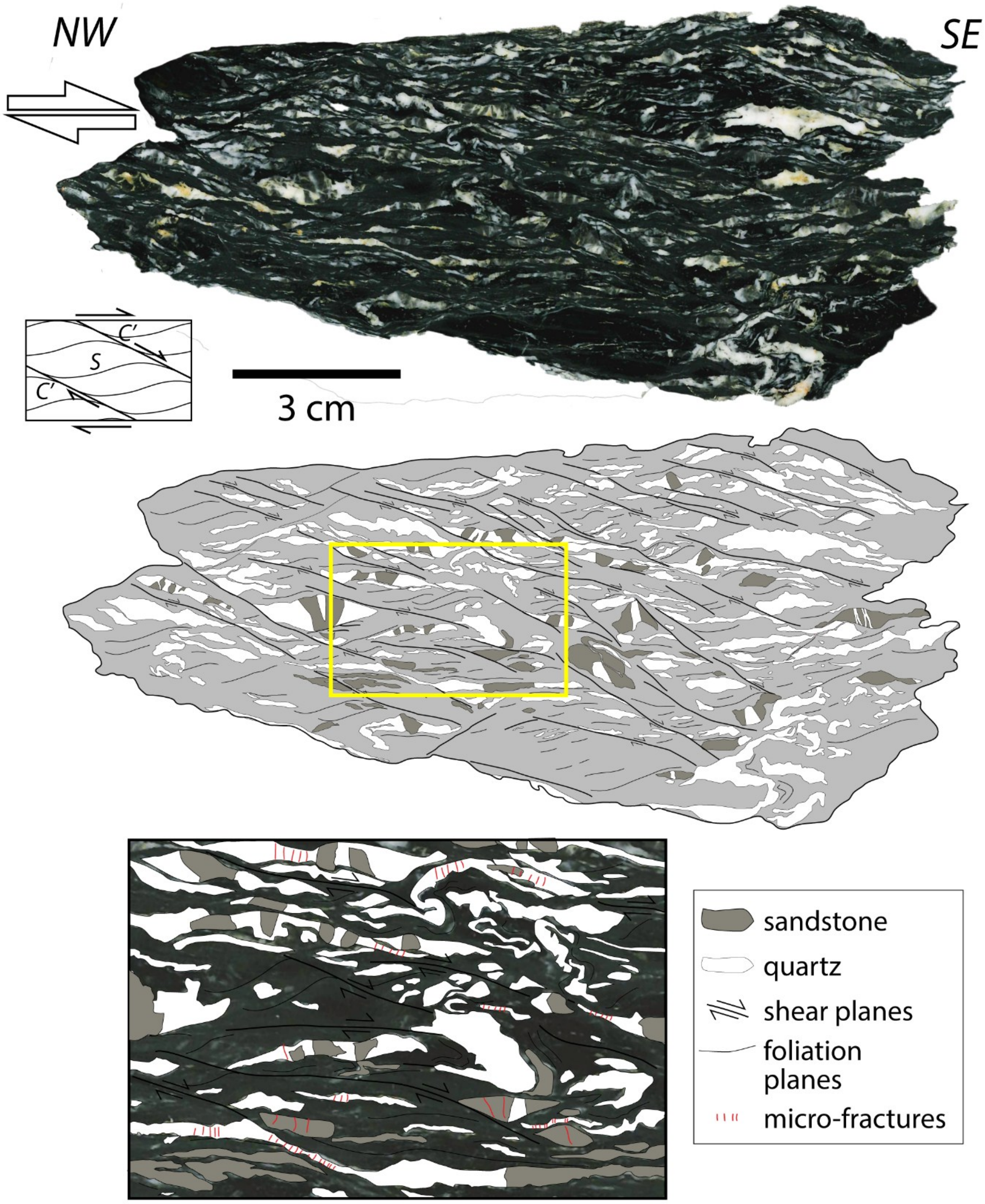

Figure 3. *Sketch of a macroscopic slice of sample of Hyuga Tectonic Mélange, with the block-in-matrix structures. Blocks are made of sandstone boudins or abundant, elongated domains of precipitated quartz. Sandstones blocks and quartz domains are both boudinaged, folded and deformed by top-to-SE shear zones. Most shear zone have a finite length and terminate on sandstone/quartz bodies.*

1.2.2 Foliated Morotsuka

The Foliated Morotsuka corresponds to the basal portion of the Morotsuka Group and form the hanging wall of the NTL along most of its length (**Figure 1A**). Ages, estimated by microfossil assemblages, indicate that this unit was deposited in the Cenomanian to Campanian/Maastrichian [*Teraoka and Okumura*, 1992].

The Foliated Morotsuka has sometimes been described as a tectonic mélange characterized by sandstone blocks and pillow basalts embedded in pelitic matrix [*Teraoka and Okumura*, 1992, Saito et al., 1996], but in most areas blocks are rare and the unit is composed simply of fine alternations of quartz-rich and phyllosilicate-rich layers defining a metamorphic foliation.

In the studied area, the metamorphic foliation gently dips to the NW. On the foliation planes, the well-developed lineation is marked by the alignment of white-mica and chlorite crystals. Deformation kinematics are principally vertical shortening associated with coaxial stretching to the NNW-SSE, with a minor contribution of top-to-the-NNW shear zones [Fabbri et al, 1990; Raimbourg et al., 2014.]. Centimeter-to-meter long quartz veins (**Figure 4**) are distributed throughout the whole unit and flattened in the foliation.

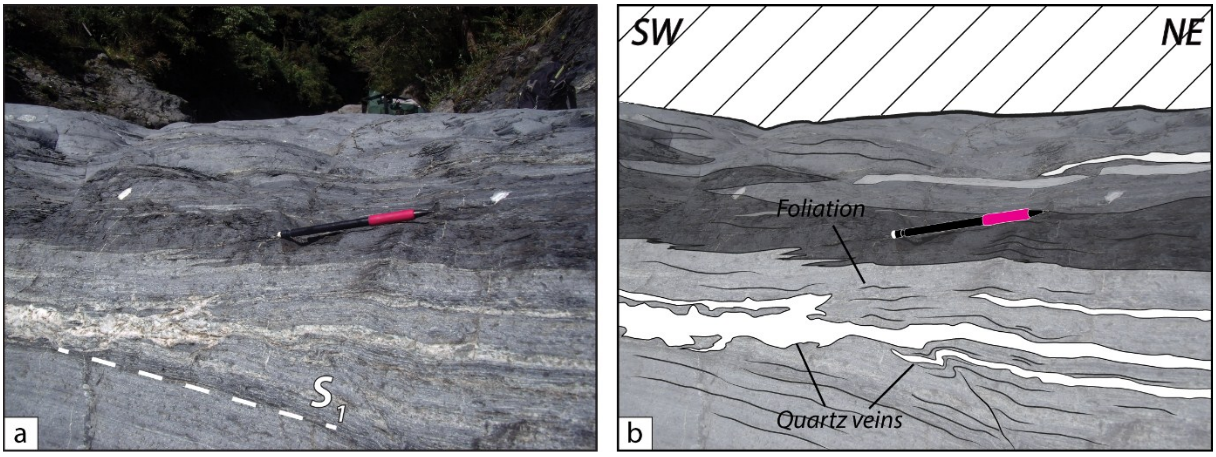

Figure 4 *: Foliated Morotsuka outcrop, showing quartz veins flattened in the foliation.*

Metamorphic conditions have been estimated to prehnite-pumpellyite to greenschist facies [*Toriumi and Teryuda*, 1988] by illite crystallinity (300 - 310°C) [*Hara and Kimura*, 2008] and vitrinite reflectance (320°C) [*Kondo et al.,* 2005].

1.3 Tectonic interpretation of the deformation

A general scheme of evolution of the Shimanto accretionary complex is developed in detail in [*Raimbourg et al., 2014*]. We recall here the principal results regarding the tectonic interpretations of the deformation recorded in the two units considered here: (1) The foliation of the base of the Morotsuka Group developed at Eocene time after it had already been accreted to the hanging wall of the plate interface. It occurred near the plate interface as a result of an event of prism collapse and horizontal extension (**Figure 1B**). (2) The deformation of the Hyuga Tectonic Mélange occurred sometimes in the time lapse Early Oligocene-Early Miocene, along the plate interface, as a result of subduction-related shearing and underplating of the unit (**Figure 1C**). This interpretation implies that both unit recorded a single stage of deformation, although at a different time and with different kinematics. **Figure 1B** represents the position of the two domains of interest before the slip on the NTL in Middle Miocene.

2 Analytical Methods

2.1 Rock samples preparation

All rock samples were cut orthogonally to the foliation (XZ-plane) to obtain polished thin sections of about 30 µm thickness for standard petrographic observations, EBSD and Raman Spectroscopy of Carbonaceous Material (RSCM) analyses. Double-polished thick sections of about 150 µm were prepared for Fourier Transform Infra-Red (FTIR) analyses.

2.2 Raman Spectroscopy of Carbonaceous Materials

RSCM is an alternative method to classical vitrinite reflectance (VR) and illite crystallinity (IC) to constraint paleo-temperatures of rocks. The RSCM method studies the evolution of Raman spectral bands of the carbonaceous material. It has been calibrated for medium to high metamorphic grade by *Beyssac et al.* [2002] and more recently for low grade metamorphic rock by *Lahfid et al.* [2010]. In this study, we applied the calibration proposed by *Lahfid et al.* [2010] in the range of 200-350°C to estimate paleo-temperatures Hyuga Tectonic Mélange and of Foliated Morotsuka.

Raman analyses were performed using a confocal Raman Renishaw InVia Reflex micro-spectrometer at BRGM, Orléans. Before each session, the micro-spectrometer was calibrated with silicon standard. The light source was a 514.5 nm argon laser focused by a Leica DM2500 microscope with a 100x magnification objective. The laser power at the sample surface was around 1 mV. After several filtering steps, the signal was finally analyzed by a CCD NIR/UV detector. Sets of 10 to 15 spectra were measured for each sample on polished thin sections. To avoid the effect of polishing on the CM structural state, we analyzed CM particles a few microns below the thin section polished surface.

2.3 Crystallographic Preferred Orientation

EBSD was employed to map the crystallographic preferred orientation (CPO) of the samples. Thin sections were previously chemically polished with a colloidal silica suspension (0.04 μm Colloidal silica suspension by Struers) and then carbon-coated to prevent charging effects. All thin sections were tilted of 70° to the electron beam to produce clear diffraction patterns. Data were collected using an EDAX PEGASUS EDS/EBSD system and OIM DC 6.4 software (manufacturer EDAX, Mahwah–USA) at the BRGM of Orléans, France. The working distance was of about 20 mm, at an accelerating voltage of 25 kV. Crystallographic Preferred Orientations were collected using a step size < 2 μm in order to sample a wide range of size of grains. Data were then processed to produce orientation charts and pole figures (PF) based on 'one-point-per-grain' analysis. This system allows assigning a similar weight to all grains separated by misorientation boundaries > 10°, independently of their size. Inverse pole figures map (IPF) are color-coded in agreement with the corresponding color key. Grain sizes estimations were derived from grain boundaries drawn manually from the superposition of image quality (IQ) and unique color grain (UCG) maps (maps obtained from EBSD analyses). In stereographic plots, X and Z directions correspond to kinematics directions, i.e. stretching direction and pole to foliation, respectively.

2.4 IR measurements

Infrared microspectroscopy is an analytical technique that allows quantifying water content in rocks. The analyses were conducted on different quartz microstructures belonging to Hyuga Tectonic Mélange and Foliated Morotsuka in order to investigate differences in water content/speciation associated to textural variation. After preparing double polished thick sections, the chosen microstructure was pre-cut by a circular micro-saw. Then the pre-cut zones were removed from the glass slides by immersion in acetone: this operation dissolves the cyanoacrylate adhesive employed to prepare sections. Each sample was put on a NaCl stage upon a stainless steel plate with a hole and then analyzed with a Nicolet Continµum FT-IR Microscope, using a 32X objective. Water amount in quartz grains was measured with a microscopic FTIR spectrometer (Nicolet-6700 FT-IR Thermo Scientific). All spectra were obtained by collecting 128 scans with a spectral range from 4000 to 1500 cm-1 and at a 4 cm-1 resolution. A background (B) was measured for the aperture area without the sample; then a sample transmission spectrum (S) was measured on the desired position of the sample. A final absorption spectrum was obtained by taking absorbance Abs (Abs= - log10 B/S) as a function of the wavenumber (cm-1). All spectra were processed with this baseline correction. The water amount in quartz was determined by the height of the absorbance peak at 3400 cm-1 (**Figure 5**) considered to be due mainly to the molecular water (H2O) in fluid inclusions contained in quartz [*Aines and Rossman,* 1984; *Kronenberg and Tullis,* 1984; *Kronenberg et al.,* 1990a]. According to the Lambert–Beer's law, A is proportional to the water concentration in a sample C (H:10^6 Si) and the sample thickness d (cm):

$$A = \varepsilon\, C\, d \qquad \text{eq.1}$$

where ε (L mol^{-1} cm^{-2}) is the molar absorption coefficient, assumed to be 0,81 [*Kats,* 1962]. Then, the molar concentrations of H:10^6Si, has been converted to weight ppm by using the relation 1 ppm H_2O to SiO_2 by weight is equal to 6.67 H:10^6Si.

The largest source of error in the water amount estimation lies in the measurement of the sample thickness d (~150 µm). This value can be obtained by microscope or by measuring the height of the peak at 1790 cm-1 making use of Lambert– Beer's Law. To allow the estimated water concentration to be compared to the results of previous studies on quartz [e.g., *Kronenberg et al.,* 1990b; *Kronenberg and Wolf,* 1990; *Post and Tullis,* 1998], we also used the calibration proposed by *Paterson et al.* [1982], based on the integral of absorption coefficient as:

$$C = 1/d \; 1/(I \text{ eff}) \int K(\nu) \, d\nu \qquad \text{eq.2}$$

where d (cm) is the thickness of the sample, K is the absorption coefficient, ν (cm) is the wavenumber and I eff (cm^{-2} per mol H/liter of quartz) is the effective integral molar absorption coefficient. Values of I eff vary according to the concentration in H and we made the calculations with a value of 27000 cm-2 corresponding to concentrations of 4000H/106 Si.

3 Results

3.1 Raman Spectroscopy of Carbonaceous Material

The estimated peak temperatures for Hyuga Tectonic Mélange and Foliated Morotsuka by RSCM are 244 ± 30°C and 342 ± 30°C and, respectively. These values are in good agreement with previously estimated peak temperatures with illite crystallinity and vitrinite reflectance [e.g. *Kondo,* 2005] techniques for the Hyuga Tectonic Mélange. For Foliated Morotsuka, ~ 40°C difference are observed between these results and the measurement proposed by *Mukoyoshi et al.* [2009] by vitrinite reflectance. Data are presented in **Table 1** and the corresponding samples locations are reported in **Figure 5**.

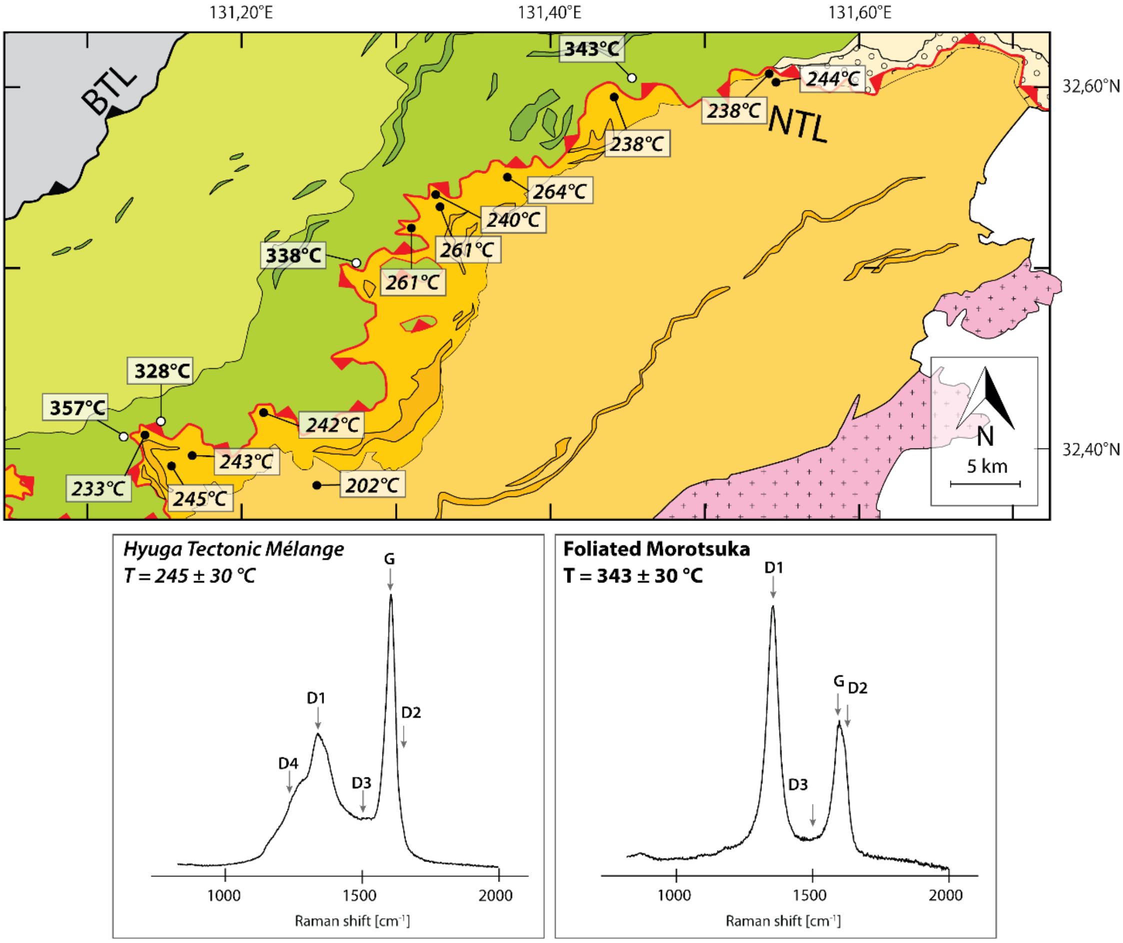

Figure 5: *Paleo-temperatures map of the studied area derived from Raman Spectroscopy of Carbonaceous Material and two examples of spectra associated to the two units. Italic titles/black dots indicate temperatures for Hyuga Tectonic Mélange while bold titles/white dots are employed for Foliated Morotsuka data. GPS coordinates for each sample are listed in Table 1.*

Sample	**Longitude**	**Latitude**	**Unit**	**Number of analyses**	**Raman parameter**	**T mean [°C]**	**SD**
HN 52	131,24250	32,41610	FM	10	6,63E-01	356	22
HN 63	131,47757	32,60295	FM	9	6,52E-01	343	8
HN 64	131,46297	32,59442	HTM	9	5,65E-01	237	5
HN 65	131,40357	32,54517	HTM	10	5,67E-01	240	6
HN 68	131,39924	32,54939	HTM	10	5,87E-01	264	22
HN 75	131,17177	32,40026	HTM	10	5,59E-01	243	10
HN 77	131,24460	32,41619	HTM	10	5,85E-01	261	27
HN 85	131,31481	32,42867	HTM	10	5,69E-01	241	11
HN 91	131,24250	32,41610	HTM	10	5,61E-01	232	8
HN 93	131,58203	32,60445	HTM	10	5,70E-01	243	16
HN 94	131,57563	32,60837	HTM	10	5,63E-01	234	12
HN 181	131,35247	32,50364	FM	13	6,48E-01	338	20
HN 285	131,23915	32,42005	FM	12	6,40E-01	328	27
HN 236	131,25534	32,40831	HTM	15	5,70E-01	243	23
HN 300	131,27903	32,40331	HTM	14	5,72E-01	245	5

Table 1. *Peak-temperatures derived from Raman Spectroscopy of Carbonaceous Material for the Hyuga Tectonic Mélange (HTM) and the Foliated Morotsuka (FM). Raman parameter is defined as ratio of the areas of the measured peaks: (D1 + D4) / (D1 + D2 + D3 + D4 + G) area ratio [Lafhid et al. 2010]. SD is standard deviation.*

3.2. Microstructural description

3.2.1 Hyuga Tectonic Mélange

At the micro-scale, foliation planes are defined by fine-grained phyllosilicates (mostly chlorite), which form wavy surfaces through the matrix, and that wrap around sandstone blocks and quartz veins (**Figure 3 and 6**). Spacing between cleavage planes varies from <10 µm to several tens of micrometers and its density increase in areas where blocks/veins are close to each other. Many quartz ribbons are found the matrix, displaying a high density of micro-veins and fluid inclusions (**Figure 6B** and **D**), the latter giving a dusty color to the quartz. Fluids inclusions tend to be arranged in a dense network of planar trails. Fluid inclusions trails and micro-veins are particularly abundant in thinned domains of the ribbons ("neck" in **Figure 6**) and they are preferentially orientated perpendicular to the major axis of ribbons, i.e. to the main stretching direction (**Figure 6B** and **D** and **Figure 7**).

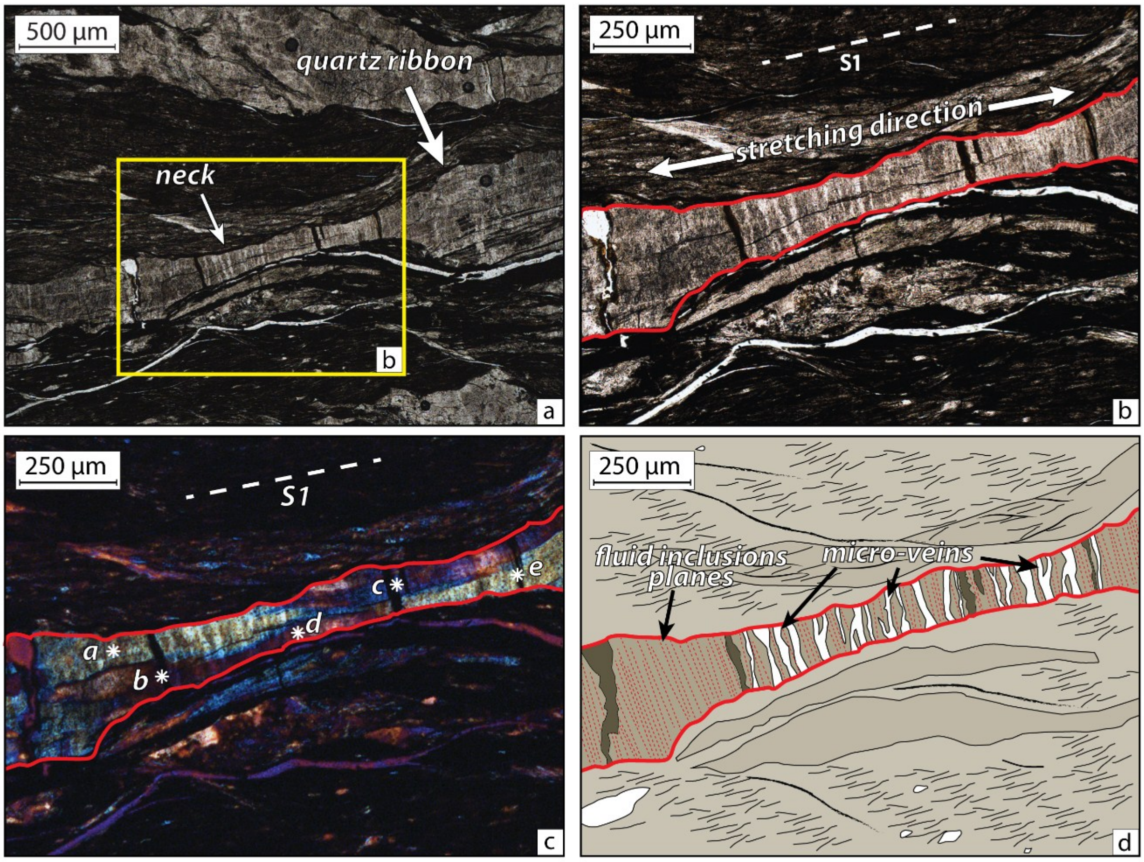

Figure 6. *A-B-C) Microphotographs of Hyuga Tectonic Mélange quartz ribbons, showing the structure of elongated necks parallel to the stretching lineation. The quartz ribbon is composed of several elongated quartz crystals, apparent through their different interference colors here indicated by the asterisk and a letter. D) Interpretation of B): the neck in the quartz ribbon is filled by multiple micro-fractures, fluid inclusions trails (red dotted lines) and veins (thick white veins), aligned perpendicularly to the main stretching direction. A-B) Optical microscope transmitted light , C) with cross nicols.*

Ribbons are composed by several elongated, superposed quartz crystals of several hundred micrometers of length (**Figure 6C)**. The superposed crystals are delimited by boundaries which can vary from slightly curved to sutured, comparable to the “saw-tooth” grain contacts described by *Fagereng et al. [2010]*. (**Figure 7C and D**). Domains were boundaries are sutured are depleted in fluid inclusions (**Figure 7B**). Undulose extinction is commonly observed along quartz ribbons as well as the presence of local small bulges.

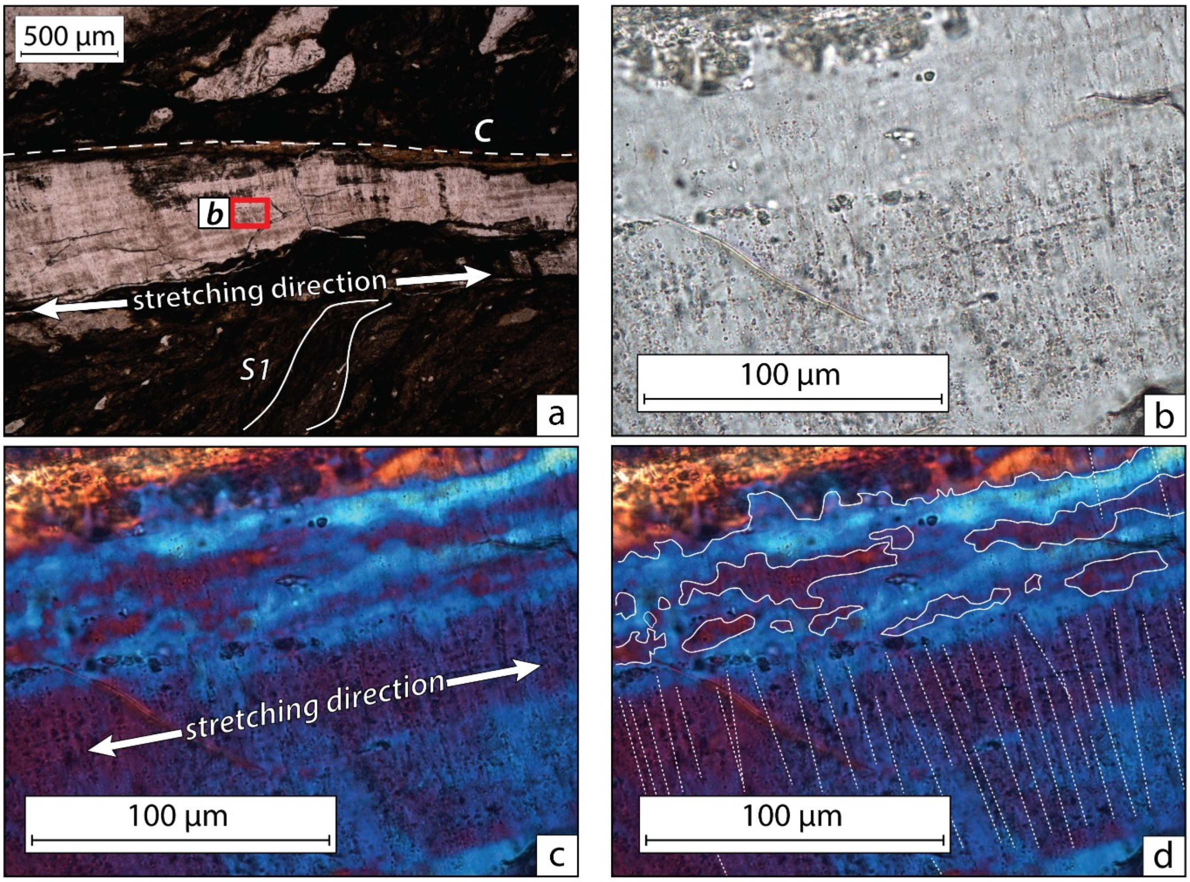

Figure 7: *Internal structure of a quartz ribbon elongated along a shear plane (C'). The distribution of fluid inclusions is very heterogeneous: the upper part of quartz (fig. 7A and B) is depleted in fluid inclusions contrarily to the lower part. In the depleted domain, sutured boundaries, called "saw-tooth" boundaries, are apparent (fig. 7C and interpretative sketch in fig. 7D). In the fluid inclusion-rich domain, most of the inclusions align along planes perpendicular to the stretching lineation. A-B) Optical microscope transmitted light, C) with cross nicols and wave plate.*

Narrow shear zones cutting across quartz ribbons are also observed (**Figure 8)**. They are characterized by strong decrease in fluid inclusion density with respect to the surrounding material (**Figure 8A and B**) associated to a large grain size reduction (**Figure 8C**). Inside these deformation bands, new bulging inside relict grains as well as sutured grain boundaries bonding small grains are observed**.**

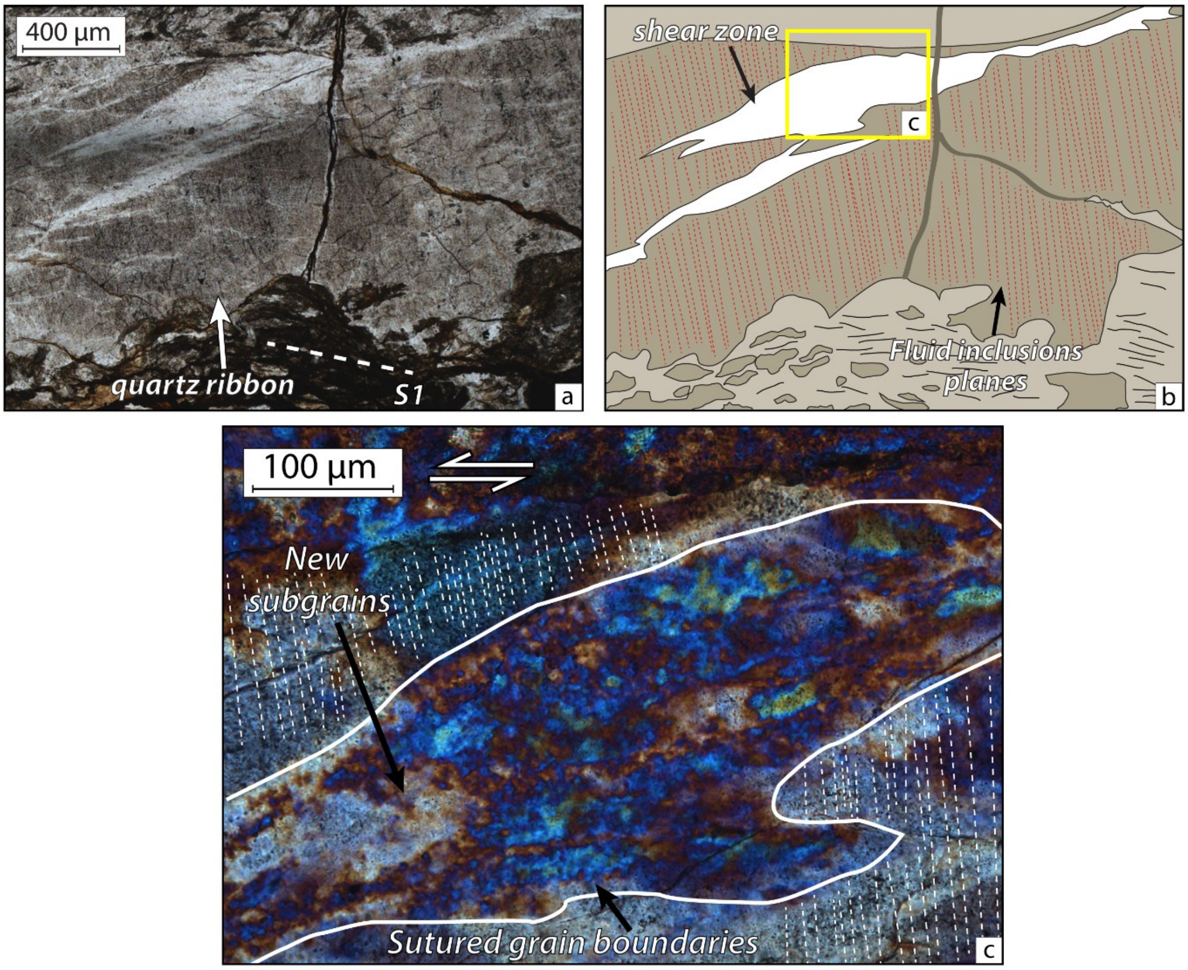

Figure 8: *A-B) Shear band cutting across a quartz ribbon. The shear band is characterized by a low density in fluid inclusions with respect to the surrounding quartz, apparent in the color contrast. Grain size reduction is observed inside the shear band. The small grains are characterized by sutured boundaries. A) Optical microscope transmitted light, B) with cross nicols and wave plate.*

3.2.2 Foliated Morotsuka

The fine-grained phyllitic matrix (**Figure 9A**) is deformed mainly by pressure solution as attested by the development of a metamorphic foliation. Pressure solution is also evidenced by the frequent strain shadows next to pyrite grains. The large number of quartz veins cutting across the matrix have flattened almost parallel to the cleavage planes (**Figure 9A**). Within the deformed veins, large relict porphyroclasts (between 250 µm and 1 mm size) display undulose extinction and elongated ‘blocky’ subgrains (**Figure 9B**). Domains of small (5 to 10 µm) recrystallized grains develop around large relict porphyroclasts elongated parallel to the stretching direction. Bulged inlets are frequently observed between crystals as well as equant recrystallized grains which decorate porphyroclasts rims (**Figure 9C**). The grain boundary at the limit between relict and recrystallized domains is strongly sutured (**Figure 9D**).

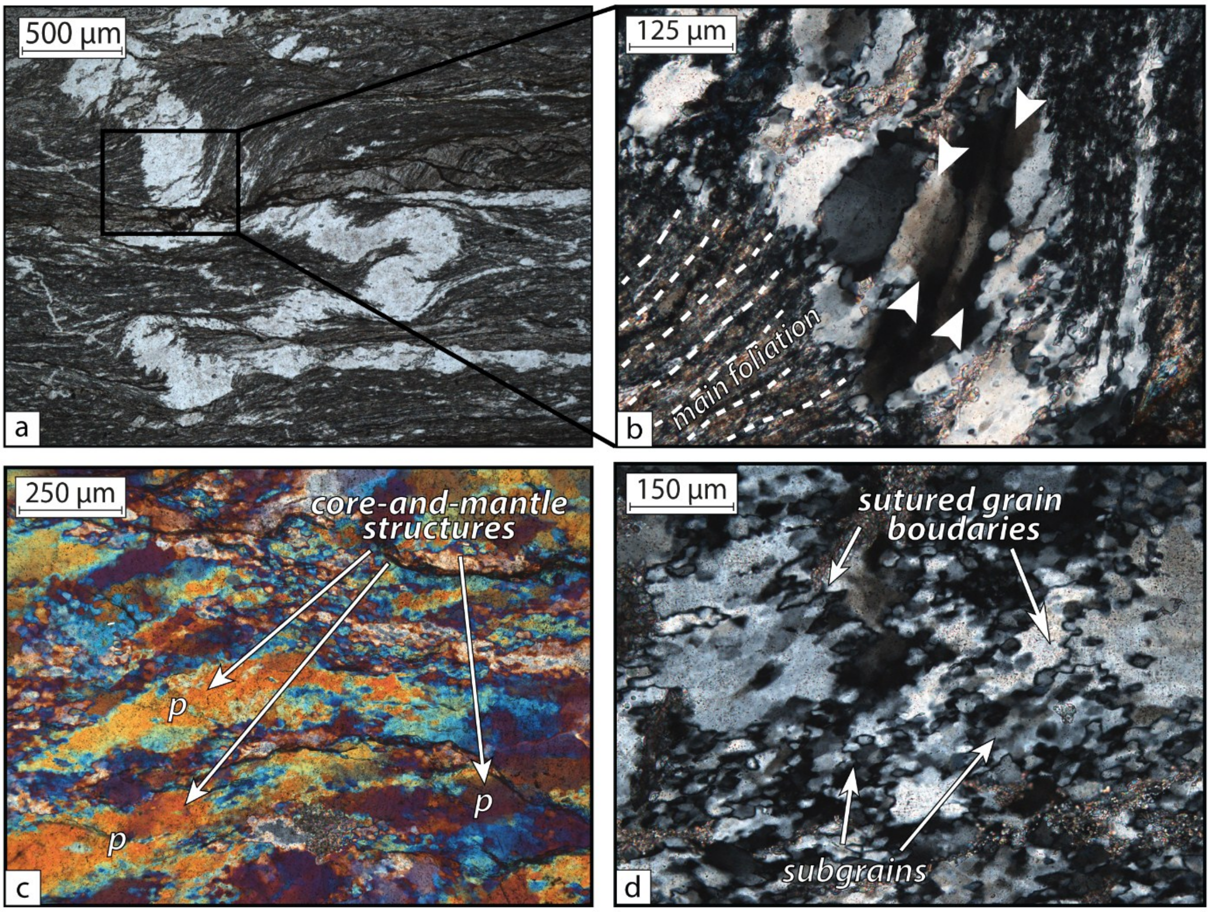

Figure 9. *Example of microstructures observed in the Foliated Morotsuka. A-B) Folded, flattened and partly sheared quartz vein. B) Elongated subgrains (indicated by white arrows) develop within the deformed quartz grains. C) Core-and-mantle structures defined by domains of small, recrystallized grains surrounding large, relict porphyroclasts ("p") elongated parallel to the foliation. D) Sutured grain boundaries between recrystallized and relict domains of quartz. A-B-D) Optical microscope transmitted light, C) with cross nicols and wave plate.*

3.3 Crystallographic Preferred Orientation

3.3.1 Hyuga Tectonic Mélange

Quartz ribbons display quite strong *c*-axes CPO with a well-defined maximum in the X-direction (stretching direction) (**Figure 10**).

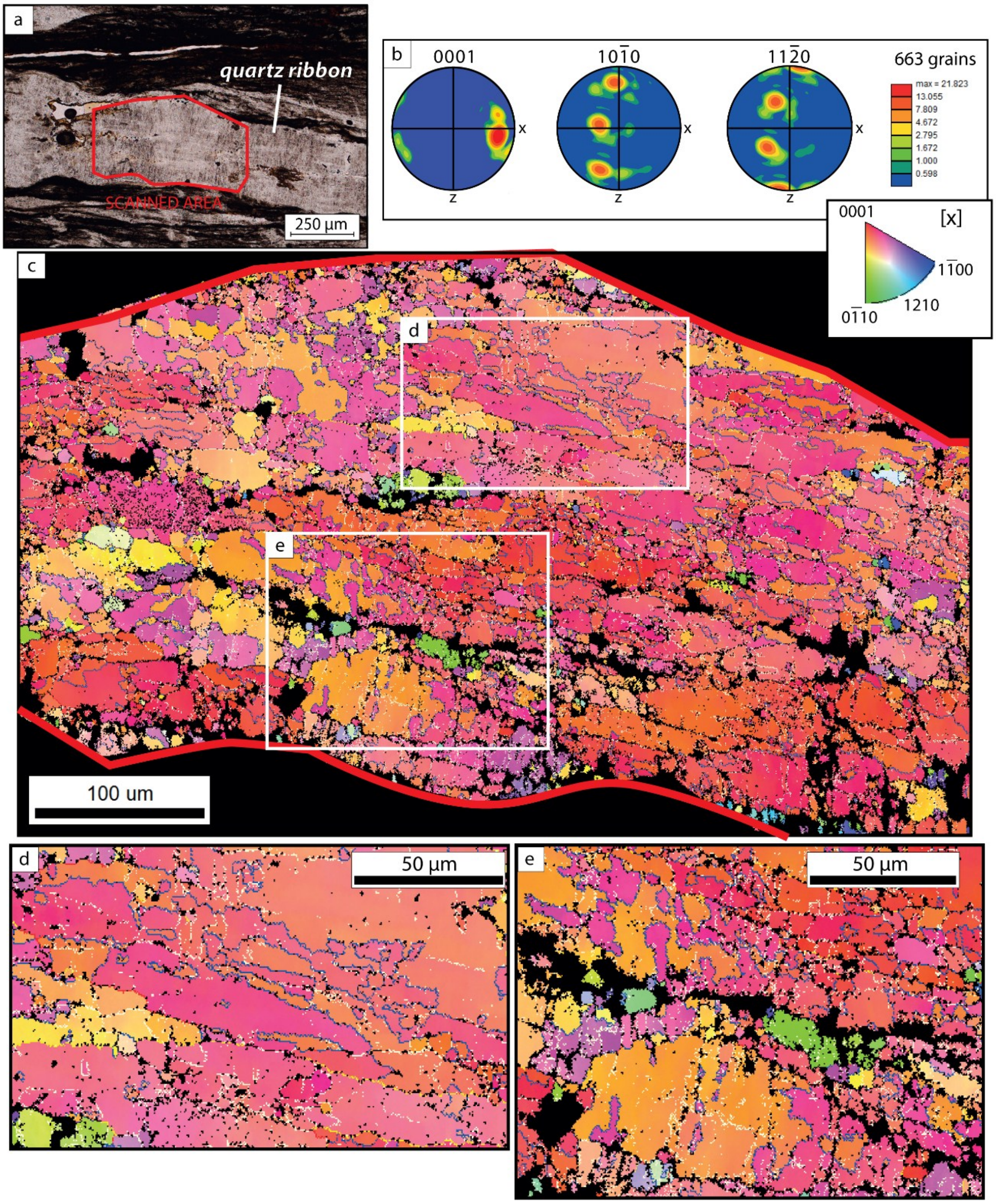

Figure 10. *Quartz crystallographic fabrics in a ribbon in the Hyuga Tectonic Mélange. A) Optical microscope image of the scanned area. B) Lower hemisphere pole figure of c <0001> and a <10-10> axes and m (11-20)-planes. c-axis distribution has a strong maximum parallel to the stretching lineation (X direction). c-d-e) EBSD map of the ribbon (with a color code associated to inverse pole figure of X direction), showing a net preferred orientation of c-axes in the X-direction. D) Quartz domains developed parallel to the main stretching direction are interpreted as the equivalent of "saw-tooth" grain boundaries observed in* ***Figure*** *7. e) In contrast, domains almost perpendicular to the stretching direction are probably the evidences of sealed microfractures. Misorientations angles lower and higher than 10° are represented with white and blue boundaries respectively.*

Inverse pole figure of the X direction show the strong preferred orientation of quartz crystals: the dominant colors are red to orange.

Crystal's boundaries have two dominant orientations: They are preferentially orientated perpendicular (**Figure 10D**) or parallel (**Figure 10E**) to the stretching direction.

In contrast to quartz ribbons, quartz CPO in shear bands accompanied by grain size reduction **(Figure 11)** display a cluster of *c*-axes nearly perpendicular to the foliation and to the shear zone boundaries **(Figure 11B).**

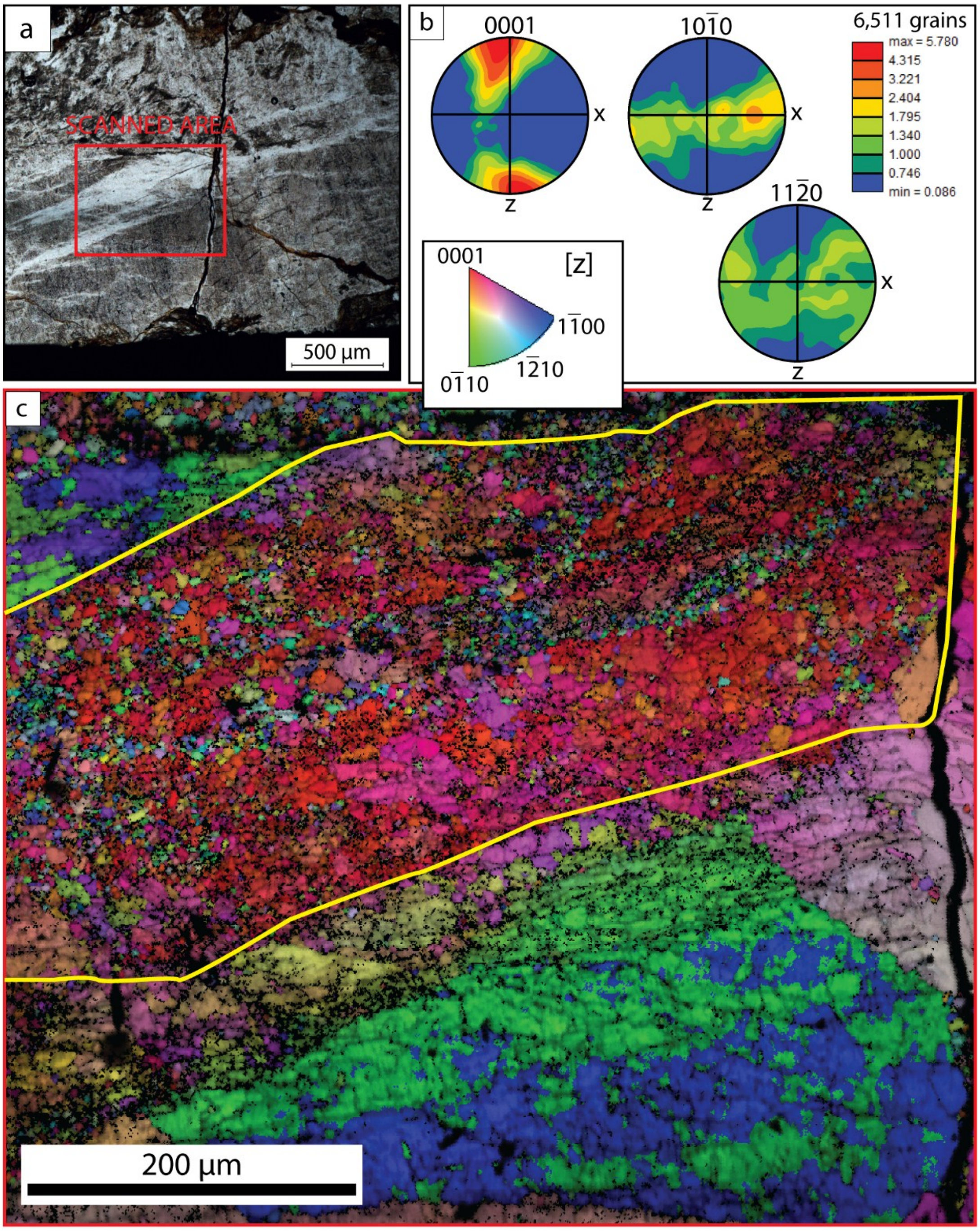

Figure 11. *Quartz crystallographic fabrics in a shear band in the Hyuga Tectonic Mélange. A) Optical microscope image of the scanned area. B) Lower hemisphere pole figure of c <0001> and a <10-10> axes and m (11-20)-planes corresponding to the area highlighted by the yellow polygon in C). Note the strong c-axis maxima in Z direction (normal to the foliation plane). C) EBSD map of the shear zone (with a color code associated to inverse pole figure of Z direction), showing the preferential orientation of c-axes close to the Z-direction.*

3.3.2 Foliated Morotsuka

In this unit, all studied samples show a weak CPO, as attested by the large range in grain color in IPF Map (**Figure 12A**). The CPO is nevertheless systematic: *c*-axes cluster are generally at a small angle to Z-axis (**Figure 12B**).

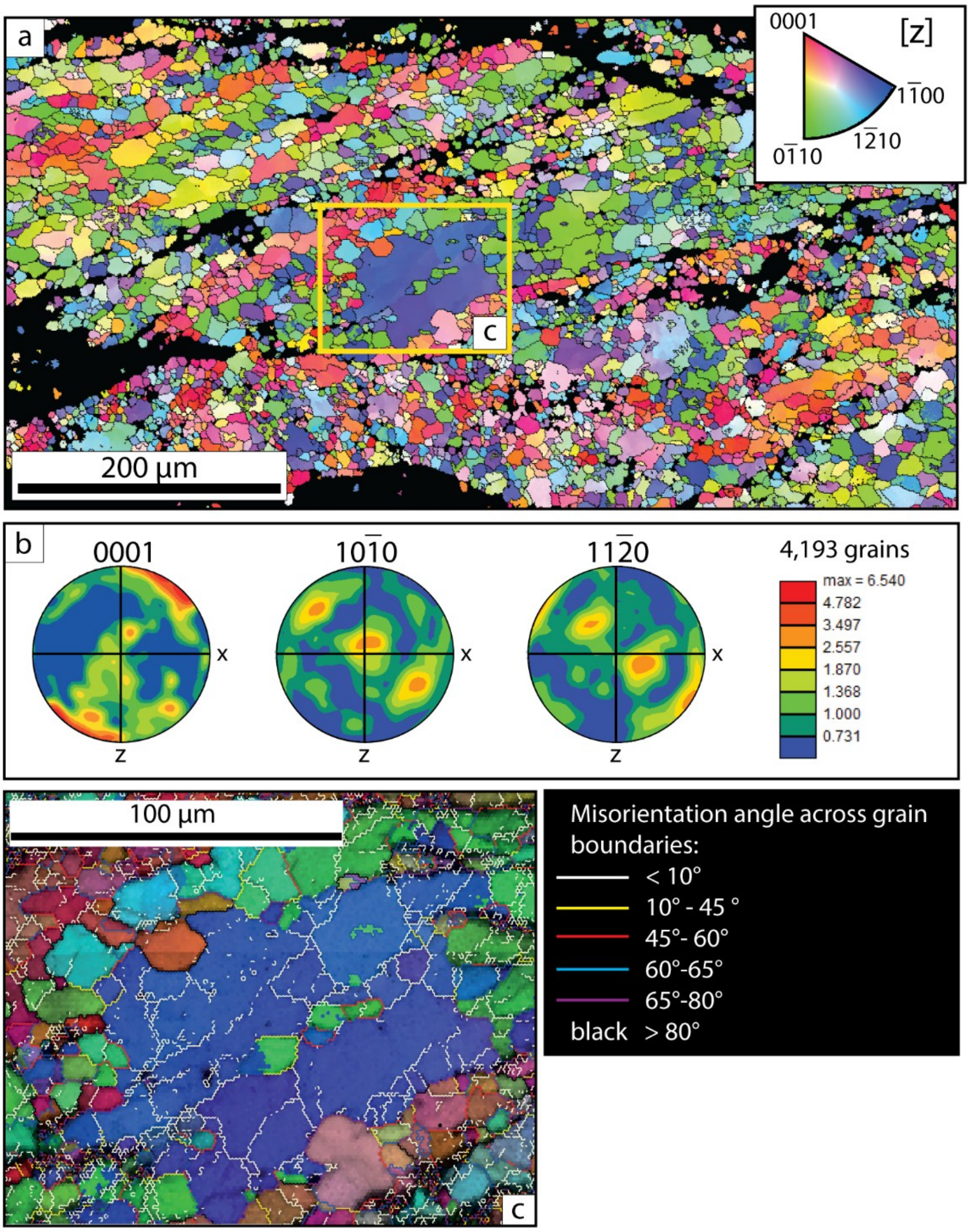

Figure 12: *Quartz crystallographic fabrics in a deformed vein in the Foliated Morotsuka. A) EBSD map of the quartz vein (with a color code associated to inverse pole figure of Z direction). B) Lower hemisphere pole figure c <0001> and a <10-10> axes and m (11-20)-planes of the whole map. C) Close-up view of the yellow rectangle in A). Grain boundaries are colored according to misorientation angle across the*

boundary. The relict bleu grain shows evidences of bulging (see brown grain in upper left part) and initial stages of internal recrystallization.

Relict crystals (**Figure 12C**) show lobate external rims as well as internal variations in crystal orientation defining subgrains of size ~ 10 µm. These domains are countered by low angle misorientation boundaries.

3.4 Intra-crystalline water content

Four different microstructures have been analyzed: the quartz ribbons and the shear bands in the Hyuga Tectonic Mélange, the relict and the recrystallized quartz grains in Morotsuka unit. All the IR spectra have a broad band around 3400 cm-1 characteristic for molecular water [*Aines and Rossman*, 1984). A typical IR spectrum of this study is shown in Figure 13, in this case a spectrum inside a quartz ribbon in the Hyuga Tectonic Mélange and for recrystallized grains in the Morotsuka unit. A broad absorption band representing O–H stretching vibration is observed around 3400 cm-1. Seven peaks, characteristic of quartz, were observed from 2000 to 1400 cm-1 (1990, 1870, 1790, 1680, 1610, 1524, 1490 cm-1) due to overtone and combination modes of Si–O vibrations (Ito and *Nakashima,* 2002].

The concentration in “liquid-like’’ water is at first order controlled by the density of fluid inclusions. In Hyuga, the larger quantities have been found for quartz ribbons, with mean values of ~20,000 H/106Si, while shear bands with recrystallized grains, poorer in fluid inclusions, show a lower amount ~13,000 H/106Si. In Foliated Morotsuka, the cores of relict grains show water amounts of ~17,500 H/106 Si, whereas surrounding recrystallized grains, poorer in fluid inclusions, have a much lower water content (~2,900 H/106 Si). Note that the values in recrystallized grains incorporate, in addition to the water within the grain interiors, the contribution of water along the grain boundary, because recrystallized grain size (see Table 2) is smaller than the FTIR window aperture (50x50 µm^2).There is therefore a clear decrease in water content resulting from recrystallization. This decrease is associated with the “annealing” of pre-existing fluid inclusions during recrystallization, possibly as a result of extensive grain boundary migration.

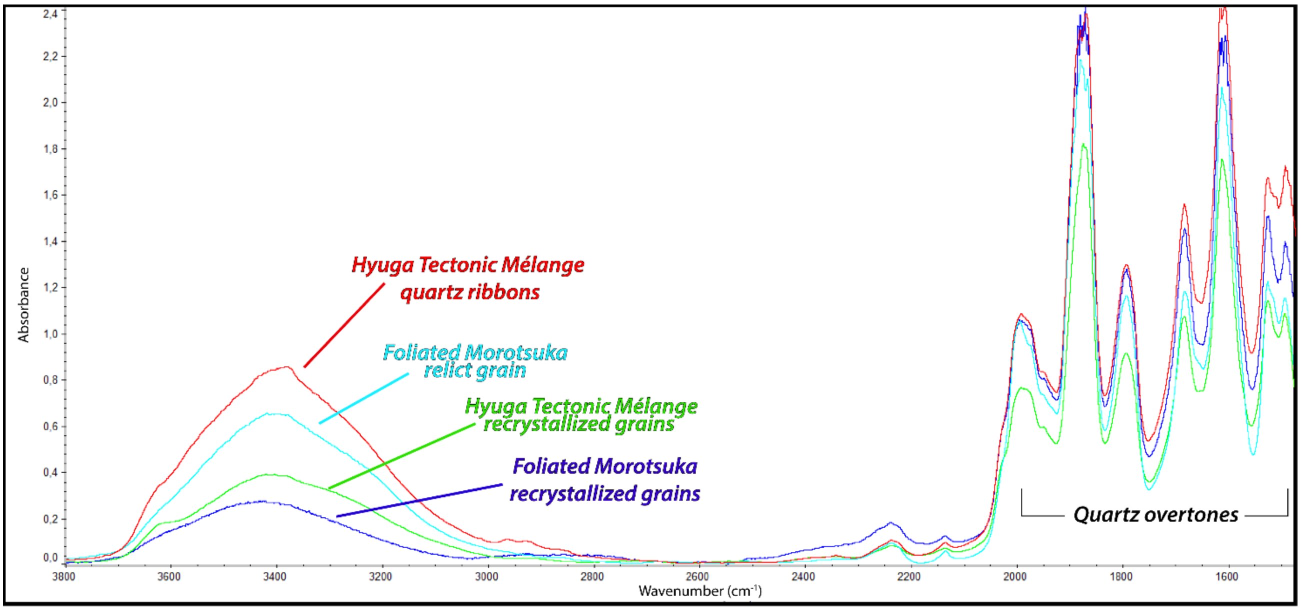

***Figure 13**. Characteristic FTIR spectra for quartz ribbons (red) and recrystallized grains in shear bands (green) in Hyuga Tectonic Mélange and relict (cyan) and recrystallized grains (blue) in quartz veins in Foliated Morotsuka. Si-O vibrations are the 7 peaks from 2000 to 1400 cm^{-1}.*

Unit	**Sample**	**Microstructure**	**N of analysis**	**Integrated Area (cm^{-1})**	**Sample thickness (cm)**	**Water content ^{A} (H/10^{6} Si)**	**Water content ^{B} (H/10^{6} Si)**
HTM	298	Ribbons	22	307	0,0126	19,790	20,431
HTM	HN77	Shear band	12	208	0,0130	12,977	13,417
FM	285A-3	Relict grains	35	271	0,0127	17,442	17,893
FM	285A-4	Recrystallized grains	84	47	0,0131	2,916	3008

***Table 2**: Molecular water content in Hyuga Tectonic Mélange (HTM) and Foliated Morotsuka (FM). A) absorption coefficient by Kats [1962]; B) absorption coefficient by Paterson [1982].*

4 Discussion

4.1 Deformation Mechanisms

4.1.1 Hyuga Tectonic Mélange

The elongated crystals constituting the quartz ribbons have a composite internal structure, made of a succession of bands perpendicular to the stretching direction (**Figures 6B**-**D** and **10E**). Some of these bands are clearly recognized as veins, while a smaller set of veins is attested by fluid inclusions planes also perpendicular to the stretching direction. The growth of the elongated crystals in the ribbons is therefore the result of repetitive cycles of fracturing and fracture-filling. The large water amount measured in quartz ribbons by FT-IR is thus directly related to crack-healing. An analogue of quartz ribbons could be the "shear or bedding veins", commonly found in low grade deformed meta-sedimentary rocks [*Cox,* 1987; *Labaume et al.,* 1991; *Cosgrove,* 1993; *Le Hebel et al.,* 2002; *Fagereng et al.,* 2010]. The strong CPO, with *c*-axes parallel to the main stretching direction, developed as only favorably oriented crystals grew by this cyclic process. Similar crystallographic fabrics are reported in literature for low metamorphic grade rocks by *Cox and Etheridge* [1983], *Hippertt* [1994], *Becker* [1995], *Stallard and Shelley* [1995]. The authors associated the *c*-axes X-maximum to crystal growth in response to pressure solution. The observed microstructures are thus comparable to slickenside fibers developed along shear planes during shear. The source of the new deposited crystalline material is inferred to be the quartz fraction dissolved along foliation surfaces from the surrounding clay matrix. The foliation planes, pervasively distributed in the whole rock, are perpendicular to tensile micro-fracturing associated to quartz ribbons. Foliation planes (dissolution sites) and ribbons (precipitation sites) can thus be associated to deformation by pressure solution.

We also observed some evidences for the activation of quartz recrystallization inside shear bands cutting across porphyroclasts, with a large grain size decrease down to ~10 μm. The associated CPO is indicative of the activation of the basal slip system in the <a> direction [*Schmid and Casey,* 1986]. Recrystallized grains are bonded by sutured grain boundaries, suggesting that recrystallization is promoted by the mobility of grain boundaries. These shear zones contains much lower fluid inclusions than the undeformed surrounding porphyroclasts (**Figure 8A-B**), thus grain boundaries motion may also be responsible for water (i.e. fluid inclusion) expulsion. Therefore, even if subsidiary with respect to pressure solution, quartz plasticity and recrystallization are also observed in the Hyuga Tectonic Mélange.

4.1.2 Foliated Morotsuka

Compared to Hyuga Tectonic Mélange, deformed quartz veins from the Foliated Morotsuka are characterized by a much larger extent of recrystallization. Inside quartz veins, equant grains of size ~10 μm (**Figures 9C**–D **and 12A)** develop ubiquitously at the expense of parent grains. These microstructures are comparable to the 'core-and-mantle' structures, proposed by *White* [1976] and *Fitz Gerald and Stünitz* [1993] and also described by *Urai et al.* [1991] for greenschist metamorphic facies. The boundary of relict grains is sutured and show locally bulging of the recrystallized domain, as well as the incipient formation of internal subgrains (**Figure 12C**), suggesting a recrystallization controlled mostly by the motion of grain boundaries (bulging) and progressive subgrain rotation. Besides, CPO analyses with a *c*-axes maximum parallel to Z (**Figure 12 B**) reflects the activation of the basal system in the <a> direction [*Schmid and Casey,* 1986], similarly to the shear zones observed in Hyuga Tectonic Mélange. Similar fabrics have also been observed in natural quartz in low-grade metamorphic rocks by *Schmid* [1982], *Hippertt* [1994], *Stipp et al.* [2002], *Trepmann and Stockhert* [2009].

In the experimental deformation framework defined by *Hirth and Tullis* [1992], the microstructures from Foliated Morotsuka can be associated to the transition from the dislocation creep "Regime 1" to "Regime 2". Following these authors, at this transitional regime, recrystallization occurs predominantly by bulging of new grains and progressive subgrain rotation. However, in natural samples, these microstructures are usually ascribed to higher metamorphic conditions [*Hirth and Tullis,* 1992]. This is thus in contrast with the estimated temperatures for the Foliated Morotsuka (**Table 2**), temperatures at which quartz plasticity is supposed to be only incipient. As demonstrated by experimental deformation of quartz aggregates, small amount of water-added to the samples [e.g. *Hirth and Tullis,* 1992; *denBrok and Spiers,* 1991; *Gleason and Tullis,* 1995] can strongly weaken the quartz and promote recrystallization. We therefore interpret the activation of quartz plasticity at low-temperature as the result of the large water concentration in the quartz.

4.2 Rheological envelopes based on natural microstructures

The comparison of deformation microstructures recorded in the Hyuga Tectonic Mélange and Foliated Morotsuka provides clues to the evolution of quartz deformation mechanisms with increasing temperature near the brittle-ductile transition. Below ~300°C, quartz plasticity is only locally activated and pressure solution creep is the dominant deformation process for quartz. Above ~300°C, quartz plasticity is fully activated and controls its rheology. The temperature of this transition is relatively low, probably as a result of the very large water content of the material considered.

Then, to build rheological envelopes from quartz deformation mechanisms requires the key assumption that quartz rheology controls the bulk flow laws. This is not intuitive, as Hyuga Tectonic Mélange contains a pervasive network of phyllosilicate-rich shear zones, which can be observed at all scales and which are presumably weaker than quartz (**Figure 2** and **3**). A closer look at the meter-scale shear zones shows that they are mostly discontinuous, i.e. they terminate in the matrix, and curved. This geometry implies that slip on the shear zones involves a large component of matrix deformation. Then, at smaller-scale (**Figure 3**), the matrix itself is heterogeneous, constituted of small shear zones and quartz-rich boudins. Just like at larger-scale, small-scale shear zones are curved and terminate along quartz-rich sandstones blocks or ribbons. The deformation of the matrix itself involves therefore the deformation of quartz domains, as illustrated by quartz ribbons necked at the termination of phyllosilicate-rich shear zones (**Figure 3**). The geometry of the structures and microstructures in Hyuga Tectonic Mélange, typical of rocks deformed along the plate interface, supports therefore the construction of rheological envelopes on the basis of quartz mechanical behavior.

4.2.1 Pressure Solution creep

Pressure solution consists of the three following processes: dissolution, mass transfer and precipitation. In this sequence, the slowest of the three mechanisms imposes its kinetics to the whole system, becoming the “rate-limiting process” that controls the total strain rate [*Gratier et al.,* 2009, *Kawabata et al.,* 2007]. Two regimes have been proposed, either controlled by the dissolution or by the diffusion of elements [*Gratier et al.,* 2009]. The boundary between the two régimes is not easily investigable, because these processes, active at very low strain rates, are difficult to reproduce in laboratory [*Gratier et al.,* 2009].

A major factor in determining the rate-limiting process is the physical state of the material. It has been shown that, in granular material containing a fluid saturated in quartz, dissolution acts as limiting process at the grain contacts, for temperature in the range of 150-600°C (e.g. compaction tests [*Schutjens,* 1991; *Dewers and Hajash,* 1995; *Niemeijer et al.,* 2002] or shearing experiments [*Tenthorey and Cox,* 2006]). In contrast, in non-granular samples, diffusion is the mass transport inhibitor [e.g., *Rutter and Mainprice,* 1979; *Gratier et al.,* 2009]. *Kawabata et al.* [2009] provided evidences for diffusion as rate-limiting process in sheared rocks from Shimanto accretionary complex by estimating the activation energy for pressure solution for shear-dominated rocks. The obtained values, in the order of 18 kJ mol^{-1}, are in agreement with experimentally derived activation energies by *Rutter and Elliot* [1976] (e.g., 15 kJ mol^{-1} K^{-1}) for diffusion-controlled process, while dissolution-limited process has much higher activation energy (e.g., ~90 kJ mol^{-1} K^{-1} by *Gratz et al.* [1990]).

On the basis of the arguments above, we assume that the relevant régime for pressure solution in the Hyuga rocks is the diffusion-limited one. We consider the creep law proposed by *Gratier et al.* [2009], tested by experiments with an indenter for the range of conditions in the upper to middle crust, expressed by the equation:

$$\dot{e} = D\,w\,C\,V_s\,(e^{\tau * 3V_s / RT} - 1) / d^3 \qquad \textbf{(eq. 3)}$$

where ė is the strain rate, *D* is the diffusion constant along the stressed interface ($\mathrm{m}^2\ \mathrm{s}^{-1}$), *w* is the theoretical thickness of the fluid film (m) along which diffusion occurs, *C* is the solubility of quartz (mol m^{-3}), *Vs* is molar volume of the solid, *R* the gas constant (8,314 m^3 Pa mol^{-1} K^{-1}), *T* is the temperature (*K*). The factor 3 in the exponential term is due to average stress across surfaces contact [*Rutter and Elliot*, 1976; *Shimizu,* 1995; *Dewers and Ortoleva,* 1990]. The distance of mass transfer, *d,* strongly depending on source-sink path [*Gratier et al.,* 2009] is very important because it controls the kinetic of diffusion creep. In compaction experiments, this value is normally the diameter of grains but, considering a non-granular material (as a foliated rock) the mean mass-transfer distance can be considered as fracture spacing [*Gratier et al.,* 2009; *Gratier et al.,* 2011] or as the distance from dissolution to precipitation sites, i.e. in our case form the matrix to the ribbons . We thus chose the mean spacing between adjacent quartz ribbons in the Hyuga Tectonic Mélange as representative 1 mm distances of 1 mm (d_1) and 500 µm ($d_{0.5}$).These distances have been used to estimate shear stress reported in **Figure 14**. Note that these values correspond to upper bounds in stress, as considering spacing between adjacent fractures as the average transport distances would have resulted in much smaller distances (see for example **Figure 6**), hence much lower stress.

4.2.2 Dislocation creep

To account for the plastic deformation of quartz, incipient at T~250°C in Hyuga Tectonic Mélange and fully activated at T~340°C in Foliated Morotsuka, we consider a classical quartz dislocation creep flow law of the form:

$$\dot{e} = A\,\tau^{n}\exp(-Q/RT) \qquad \textbf{(eq. 4)}$$

where A is the pre-exponential number ($MPa^{-n}s^{-1}$), τ is shear stress (MPa), n is the power law stress exponent, R the gas constant (8,314 J $mol^{-}1$ K^{-1}), T is the temperature (K).

Quartz flow laws are extrapolated from laboratory experiments conducted on both natural, e.g. Simpson, Black Hills and Heavitree quartzite [*Jaoul et al.,* 1984; *Koch et al.,* 1989; *Gleason and Tullis,* 1995] or synthetic quartzites [*Paterson and Luan,* 1990; *Luan and Paterson,* 1992] in which grain size and water content are well constrained. In the light of the large water content in subduction zone meta-sediments, we considered only flow laws involving hydrated quartz. The creep flow law with the formalism proposed by *Hirth et al.* [2001] is probably the most appropriate to represent the quartz from the Shimanto accretionary complex because it considers explicitly the effect of water through a fugacity term (*f* (MPa) (with the exponent *m = 1)*. However, this is a rough approximation because water quantities in experiments behind this law are two orders of magnitude lower than for quartz ribbons and parent grains in Hyuga Tectonic Mélange and Foliated Morotsuka.

4.2.3 Strain rate evaluations

A coarse strain rate estimate along subduction plate interface can be obtained considering the relative plate velocity and the width of the shear zone [e.g. *Fagereng et al.,* 2010]. The assumption that the sheared top-to-SE metasediments of Hyuga Tectonic Mélange were accreted at plate boundary interface [*Raimbourg et al.,* 2014] allowed to a direct strain rate estimation considering i) the plate convergence rate and ii) the thickness of the deformation zone. Paleo reconstructions of the migration of the Pacific plate with respect to the Eurasian plate during the Early Middle Eocene [Maruyama and Send, 1986; Saito, 2008] indicate converging rates of 7,1 cm/y and 5,8 cm/y

[*Maruyama and Send,* 1986]. The thickness of the deformation zone at plate boundary corresponds to ~ 100 m as estimated by field observations for the Hyuga Tectonic Mélange [*Raimbourg et al.,* 2014]. This value is also in the range of plate-interface faults thicknesses proposed in the compilation of *Rowe et al.* [2013], estimated as 100 to 500 m at depth of 10-12 km. As a result, estimated strain rates are of the order ~ 10^{-11} s^{-1}.

4.2.4. Strength profiles in subduction zones

We propose a strength profile (**Figure 14**) taking into account both pressure solution and dislocation creep for quartz at strain rates of 10^{-11} s^{-1}. Considering the mean transport distance of 500 µm, the effective shear stress decreases of several tens of MPa with respect to Byerlee's predictions, never exceeding 40 MPa (light grey area). Such low shear strength values are quite in agreement with shear stress magnitude at plate interface deduced from geophysical methods, e.g. from surface heat flow measurements [*Peacock,* 1996] or from temporal change in the stress field after mega-earthquake [e.g. *Hasegawa et al.,* 2012], in the range of 5-30 MPa [e.g. *Wintsch et al.,* 1995].

The *Hirth et al.* [2001] creep flow law for quartz, although it is based for part on naturally deformed samples, predicts the onset of plastic deformation in the T-range 400-450°C, while the transition is observed in Shimanto rocks around 300°C. A more relevant flow law should be "softer" and intersect pressure solution creep flow laws around 300°C (**Figure 14**).

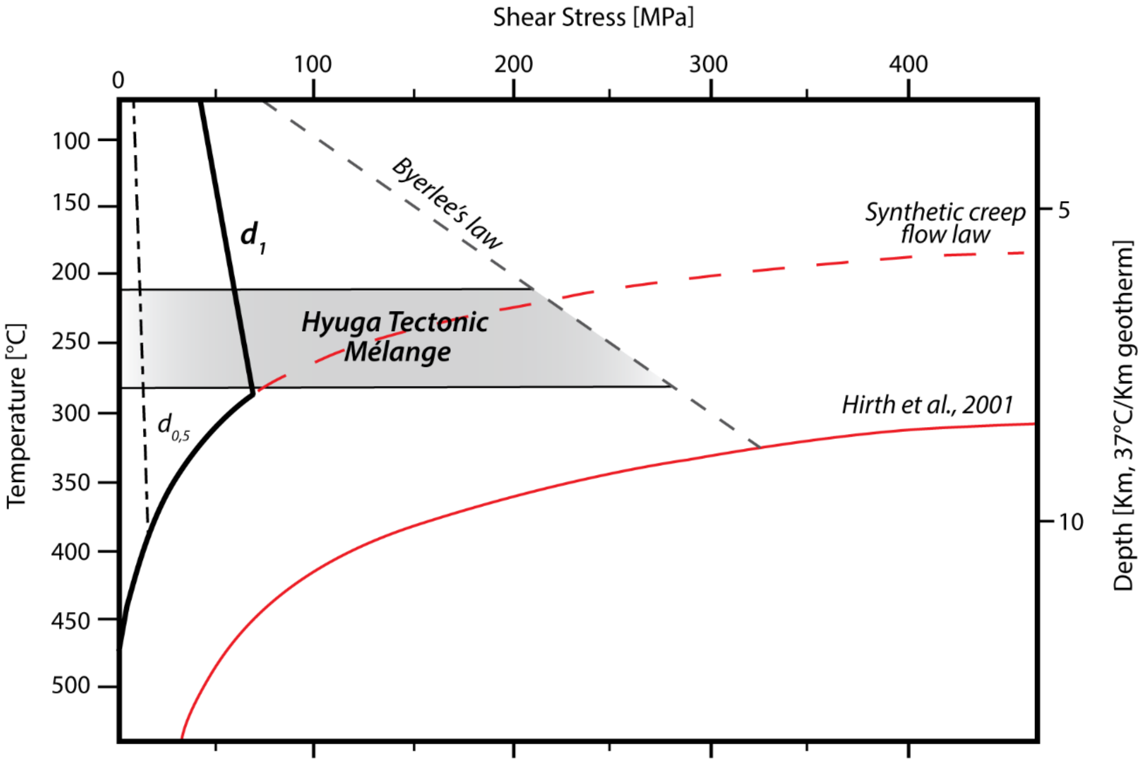

Figure 14. *Rheological envelope of a subduction zone, integrating pressure solution creep of quartz. Temperature gradient is assumed as ~37°C/km [Kondo et al., 2005]. The pressure solution curves are estimated with the two end-member distances of 1 mm (d_1 - black dotted line) and 500 µm ($d_{0,5}$ - thick black lines) (see text for more details) and at constant strain rate of ~10^{-11} s^{-1}. The estimated shear stress values are strongly lower than the classical Byerlee's law. Shear stresses predicted at plate interface are thus in good agreement with estimates derived from geophysical methods and thermal models (~ 10 to 35 MPa). The creep law of Hirth et al. [2001] (red line) is "too strong" to account for the onset plastic deformation in Hyuga samples. A softer, hypothetical creep flow law is proposed, in agreement with a temperature for the brittle-plastic transition in Shimanto metasediments around 300°C (dashed red line).*

5. Summary and conclusion

The Hyuga Tectonic Mélange, deformed along the plate interface at temperatures of 245±30°C, provides the opportunity to investigate deformation mechanisms close to the brittle-ductile transition in subduction zones. From microscopic observation and textural analysis we showed that pressure solution coupled to micro-fracturing is the dominant quartz deformation process for this temperature. As phyllosilicate-rich shear zones generally terminate on quartz domains, bulk rheology can be estimated using quartz behavior. The consideration of pressure solution creep in rheological envelopes results in strongly reducing plate interface strength. Furthermore, plastic flow laws for quartz overestimate stress, probably because subducting metasediments are extremely rich in water hence very weak.

Acknowledgements

This work has received funding from (i) the European Research Council (ERC) under the seventh Framework Program of the European Union (ERC Advanced Grant, grant agreement No 290864, RHEOLITH) and (ii) the Labex VOLTAIRE (ANR-10-LABX-100-01). Thin and thick sections were prepared by Gabriel Badin and Sylvain Janiec.

References

Aines, R.D., Rossman, G.R., 1984. Water in minerals? A peak in the infrared. J. Geophys. Res. Solid Earth 89, 4059–4071. doi:10.1029/JB089iB06p04059

Becker, A., 1995. Quartz pressure solution: influence of crystallographic orientation. J. Struct. Geol. 17, 1395–1405. doi:10.1016/0191-8141(95)00035-C

Bell, T.H., Cuff, C., 1989. Dissolution, solution transfer, diffusion versus fluid flow and volume loss during deformation/metamorphism. J. Metamorph. Geol. 7, 425–447. doi:10.1111/j.1525-1314.1989.tb00607.x

Beyssac, O., Goffé, B., Chopin, C., Rouzaud, J.N., 2002. Raman spectra of carbonaceous material in metasediments: a new geothermometer. J. Metamorph. Geol. 20, 859–871. doi:10.1046/j.1525-1314.2002.00408.x

Blanpied, M.L., Lockner, D.A., Byerlee, J.D., 1991. Fault stability inferred from granite sliding experiments at hydrothermal conditions. Geophys. Res. Lett. 18, 609–612. doi:10.1029/91GL00469

Brander, L., Svahnberg, H., Piazolo, S., 2012. Brittle-plastic deformation in initially dry rocks at fluid-present conditions: transient behaviour of feldspar at mid-crustal levels. Contrib Mineral Petrol. 163, 403–425. doi 10.1007/s00410-011-0677-5

Brok, S.W.J.D., 1998. Effect of microcracking on pressure-solution strain rate: The Gratz grain-boundary model. Geology 26, 915–918. doi:10.1130/0091-7613(1998)026<0915:EOMOPS>2.3.CO;2

Brok, S.W.J.D., Spiers, C.J., 1991. Experimental evidence for water weakening of quartzite by microcracking plus solution–precipitation creep. J. Geol. Soc. 148, 541–548. doi:10.1144/gsjgs.148.3.0541

Burov, E.B., 2011. Rheology and strength of the lithosphere. Mar. Pet. Geol. 28, 1402–1443. doi:10.1016/j.marpetgeo.2011.05.008

Chester, F.M., 1988. The brittle-ductile transition in a deformation-mechanism map for halite. Tectonophysocs 154, 1–2, 125-136. doi:10.1016/0040-1951(88)90230-2

Chester, F.M., 1995. A rheologic model for wet crust applied to strike-slip faults. J. Geophys. Res. 100, 13033. doi:10.1029/95JB00313

Cosgrove, J.W., 1993. The interplay between fluids, folds and thrusts during the deformation of a sedimentary succession. J. Struct. Geol. The Geometry of Naturally Deformed Rocks 15, 491–500. doi:10.1016/0191-8141(93)90143-X

Cox, S.F., 1987. Antitaxial crack-seal vein microstructures and their relationship to displacement paths. J. Struct. Geol. 9, 779–787. doi:10.1016/0191-8141(87)90079-4

Cox, S.F., Etheridge, M.A., 1983. Crack-seal fibre growth mechanisms and their significance in the development of oriented layer silicate microstructures. Tectonophysics, Deformation processes in tectonics 92, 147–170. doi:10.1016/0040-1951(83)90088-4

Cox, S.F., Etheridge, M.A., 1989. Coupled grain-scale dilatancy and mass transfer during deformation at high fluid pressures: examples from Mount Lyell, Tasmania. J. Struct. Geol. 11, 147–162. doi:10.1016/0191-8141(89)90040-0

Dewers, T., Ortoleva, P., 1990. A coupled reaction/transport/mechanical model for intergranular pressure solution, stylolites, and differential compaction and cementation in clean sandstones. Geochim. Cosmochim. Acta 54, 1609–1625. doi:10.1016/0016-7037(90)90395-2

Dewers, T., Hajash, A., 1995. Rate laws for water-assisted compaction and stress-induced water-rock interaction in sandstones. J. Geophys. Res. Solid Earth 100, 13093–13112. doi:10.1029/95JB00912

Durney, D.W., 1972. Solution-transfer, an Important Geological Deformation Mechanism. Nature 235, 315–317. doi:10.1038/235315a0

Evans, J.P., 1988. Deformation mechanisms in granitic rocks at shallow crustal levels. J. Struct. Geol. 10, 437–443. doi:10.1016/0191-8141(88)90031-4

Fabbri, O., Faure, M., Charvet, J., 1990. Back-thrusting in accretionary prisms: microtectonics evidences from the Cretaceous-Lower Tertiary Shimanto belt of southwest Japan. J. South. Asian Earth Sc. 4 (3), 195-201

Fagereng, Å., Remitti, F., Sibson, R.H., 2010. Shear veins observed within anisotropic fabric at high angles to the maximum compressive stress. Nat. Geosci. 3, 482–485. doi:10.1038/ngeo898

Fagereng, Å., Remitti, F., Sibson, R.H., 2011. Incrementally developed slickenfibers — Geological record of repeating low stress-drop seismic events? Tectonophysics 510, 381–386. doi:10.1016/j.tecto.2011.08.015

Festa, A., Pini, G.A., Dilek, Y., Codegone, G., 2010. Melanges and melange-forming processes; a historical overview and new concepts. Int. Geol. Rev. 52, 1040–1105. doi:10.1080/00206810903557704

Fitz Gerald, J.D., Stünitz, H., 1993. Deformation of granitoids at low metamorphic grade. I: Reactions and grain size reduction. Tectonophysics 221, 269–297. doi:10.1016/0040-1951(93)90163-E

Fukuchi, R., Fujimoto, K., Kameda, J., Hamahashi, M., Yamaguchi, A., Kimura, G., Hamada, Y., Hashimoto, Y., Kitamura, Y., Saito, S., 2014. Changes in illite crystallinity within an ancient tectonic boundary thrust caused by thermal, mechanical, and hydrothermal effects: an example from the Nobeoka Thrust, southwest Japan. Earth Planets Space 66, 1–12. doi:10.1186/1880-5981-66-116

Gleason, G.C., Tullis, J., 1995. A flow law for dislocation creep of quartz aggregates determined with the molten salt cell. Tectonophysics 247, 1–23. doi:10.1016/0040-1951(95)00011-B

Goldstein, A., Pickens, J., Klepeis, K., Linn, F., 1995. Finite strain heterogeneity and volume loss in slates of the Taconic Allochthon, Vermont, U.S.A. J. Struct. Geol. 17, 1207–1216. doi:10.1016/0191-8141(95)00022-6

Goldstein, A., Knight, J., Kimball, K., 1998. Deformed graptolites, finite strain and volume loss during cleavage formation in rocks of the taconic slate belt, New York and Vermont, U.S.A. J. Struct. Geol. 20, 1769–1782. doi:10.1016/S0191-8141(98)00083-2

Goodwin, L.B., Wenk, H.-R., 1990. Intracrystalline folding and cataclasis in biotite of the Santa Rosa mylonite zone: HVEM and TEM observations. Tectonophysics 172, 201–214. doi:10.1016/0040-1951(90)90030-C

Gratier, J.P., 1987. Pressure solution-deposition creep and associated tectonic differentiation in sedimentary rocks. Geol. Soc. Lond. Spec. Publ. 29, 25–38. doi:10.1144/GSL.SP.1987.029.01.03

Gratier, J.P., 1993. Le Fluage des roches par dissolution-cristallisation sous contrainte, dans la croute superieure. Bull. Soc. Geol. Fr. 164, 267–287

Gratier, J.P., Gamond, J.F., 1990. Transition between seismic and aseismic deformation in the upper crust. Geol. Soc. Lond. Spec. Publ. 54, 461–473. doi:10.1144/GSL.SP.1990.054.01.42

Gratier, J.P., Guiguet, R., Renard, F., Jenatton, L., Bernard, D., 2009. A pressure solution creep law for quartz from indentation experiments. J. Geophys. Res. 114. doi:10.1029/2008JB005652.

Gratier, J.P., Richard, J., Renard, F., Mittempergher, S., Doan, M.L., Di Toro, G., Hadizadeh, J., Boullier, A.M., 2011. Aseismic sliding of active faults by pressure solution creep; evidence from the San Andreas Fault Observatory at Depth. Geol. Boulder 39, 1131–1134. doi:10.1130/G32073.1

Gratz, A.J., Bird, P., Quiro, G., 1990. Dissolution of quartz in aqueous basic solution, 106-236°C: surface kinetics of ”perfect” crystallographic face. Geoc. Et Cosm. Acta. 54, 2911– 2922

Griggs, D.T., Blacic, J.D., 1965. Quartz: Anomalous Weakness of Synthetic Crystals. Science 292

Hara, H., Kimura, K., 2008. Metamorphic and cooling history of the Shimanto accretionary complex, Kyushu, Southwest Japan: Implications for the timing of out-of-sequence thrusting. Isl. Arc 17, 546–559. doi:10.1111/j.1440-1738.2008.00636.x

Hasegawa, A., Yoshida, K., Asano, Y., Okada, T., Iinuma, T., Ito, Y., 2012. Change in stress field after the 2011 great Tohoku-Oki earthquake. Earth Planet. Sci. Lett. 355-356, 231–243. doi:10.1016/j.epsl.2012.08.042

Hippertt, J.F., 1994. Microstructures and c-axis fabrics indicative of quartz dissolution in sheared quartzites and phyllonites. Tectonophysics 229, 141–163. doi:10.1016/0040-1951(94)90026-4

Hirth, G., Tullis, J., 1992. Dislocation creep regimes in quartz aggregates. J. Struct. Geol. 14, 145–159. doi:10.1016/0191-8141(92)90053-Y

Hirth, G., Teyssier, C., Dunlap, J.W., 2001. An evaluation of quartzite flow laws based on comparisons between experimentally and naturally deformed rocks. Int. J. Earth Sci. 90, 77–87. doi:10.1007/s005310000152

Hyndman, R.D., Yamano, M., Oleskevich, D.A., 1997. The seismogenic zone of subduction thrust faults. Isl. Arc 6, 244–260. doi:10.1111/j.1440-1738.1997.tb00175.x

Imai, I., Teraoka, Y., Okumura, K., 1971. Geologic structure and metamorphic zonation of the northeastern part of the Shimanto terrane in Kyushu, Japan. Chishitsugaku Zasshi J. Geol. Soc. Jpn. 77, 207–220

Ito, Y., Nakashima, S., 2002. Water distribution in low-grade siliceous metamorphic rocks by micro-FTIR and its relation to grain size: a case from the Kanto Mountain region, Japan. Chem. Geol. 189, 1–18. doi:10.1016/S0009-2541(02)00022-0

Jaoul, O., Tullis, J., Kronenberg, A., 1984. The effect of varying water contents on the creep behavior of Heavitree quartzite. J. Geophys. Res. Solid Earth 89, 4298–4312. doi:10.1029/JB089iB06p04298

Kawabata, K., Tanaka, H., Kimura, G., 2007. Mass transfer and pressure solution in deformed shale of accretionary complex: Examples from the Shimanto Belt, southwestern Japan. J. Struct. Geol. 29, 697–711. doi:10.1016/j.jsg.2006.11.009

Kawabata, K., Tanaka, H., Kitamura, Y., Ma, K.-F., 2009. Apparent activation energy and rate-limiting process estimation from natural shale deformed by pressure solution in shallow subduction zone. Earth Planet. Sci. Lett. 287, 57–63. doi:10.1016/j.epsl.2009.07.032

Kerrich, R., Beckinsale, R.D., Durham, J.J., 1977. The transition between deformation regimes dominated by intercrystalline diffusion and intracrystalline creep evaluated by oxygen isotope thermometry. Tectonophysics 38, 241–257. doi:10.1016/0040-1951(77)90213-X

Kirby, S. H., 1983. Rheology of the lithosphere. Rev. Geoph. Space Physics 21, 6, 1458-1487. doi/10.1029/RG021i006p01458

Kitamura, Y., Kimura, G., 2012. Dynamic role of tectonic mélange during interseismic process of plate boundary mega earthquakes. Tectonophysics, Chaos and Geodynamics: Melanges, Melange Forming Processes and Their Significance in the Geological Record 568–569, 39–52. doi:10.1016/j.tecto.2011.07.008

Koch, P.S., Christie, J.M., Ord, A., George, R.P., 1989. Effect of water on the rheology of experimentally deformed quartzite. J. Geophys. Res. Solid Earth 94, 13975–13996. doi:10.1029/JB094iB10p13975

Kohlstedt, D.L., Evans, B., Mackwell, S.J., 1995. Strength of the lithosphere: Constraints imposed by laboratory experiments. J. Geophys. Res. Solid Earth 100, 17587–17602. doi:10.1029/95JB01460

Kondo, H., Kimura, G., Masago, H., Ohmori-Ikehara, K., Kitamura, Y., Ikesawa, E., Sakaguchi, A., Yamaguchi, A., Okamoto, S. 'ya, 2005. Deformation and fluid flow of a major out-of-sequence thrust located at seismogenic depth in an accretionary complex: Nobeoka Thrust in the Shimanto Belt, Kyushu, Japan. Tectonics 24, TC6008. doi:10.1029/2004TC001655

Kronenberg, A.K., Tullis, J., 1984. Flow strengths of quartz aggregates: Grain size and pressure effects due to hydrolytic weakening. J. Geophys. Res. Solid Earth 89, 4281–4297. doi:10.1029/JB089iB06p04281

Kronenberg, A.K., Kirby, S.H., Pinkston, J., 1990a. Basal slip and mechanical anisotropy of biotite. J. Geophys. Res. Solid Earth 95, 19257–19278. doi:10.1029/JB095iB12p19257

Kronenberg, A.K., Segall, P., Wolf, G.H., 1990b. Hydrolytic weakening and penetrative deformation within a natural shear zone. Geophys. Monogr. 56, 21–36

Kronenberg, A.K., Wolf, G.H., 1990. Fourier transform infrared spectroscopy determinations of intragranular water content in quartz-bearing rocks: implications for hydrolytic weakening in the laboratory and within the earth. Tectonophysics 172, 255–271. doi:10.1016/0040-1951(90)90034-6

Labaume, P., Berty, C., Laurent, P., 1991. Syn-diagenetic evolution of shear structures in superficial nappes: an example from the Northern Apennines (NW Italy). J. Struct. Geol. 13, 385–398. doi:10.1016/0191-8141(91)90012-8

Lahfid, A., Beyssac, O., Deville, E., Negro, F., Chopin, C., Goffé, B., 2010. Evolution of the Raman spectrum of carbonaceous material in low-grade metasediments of the Glarus Alps (Switzerland). Terra Nova 22, 354–360. doi:10.1111/j.1365-3121.2010.00956.x

Hebel, F.L., Gapais, D., Fourcade, S., Capdevila, R., 2002. Fluid-assisted large strains in a crustal-scale décollement (Hercynian Belt of South Brittany, France). Geol. Soc. Lond. Spec. Publ. 200, 85–101. doi:10.1144/GSL.SP.2001.200.01.06

Letouzey, J., Kimura, M., 1985. Okinawa Trough genesis: Structure and evolution of a backarc basin developed in a continent, Mar. Petrol. Geol. 2, 111–130

Luan, F.C., Paterson, M.S., 1992. Preparation and deformation of synthetic aggregates of quartz. J. Geophys. Res. Solid Earth 97, 301–320. doi:10.1029/91JB01748

Maruyama, S., Send, T., 1986. Orogeny and relative plate motions: Example of the Japanese Islands. Tectonophysics, Tectonics of the Eurasian Fold Belts 127, 305–329. doi:10.1016/0040-1951(86)90067-3

Matsumura, M., Hashimoto, Y., Kimura, G., Ohmori-Ikehara, K., Enjoji, M., Ikesawa, E., 2003. Depth of oceanic crust underplating in subduction zone -inference from fluid inclusion analysis of crack-seal veins. Geology 31, 1005–1008

Mercier, J.-C.C., Anderson, D.A., Carter, N.L., 1977. Stress in the Lithosphere: Inferences from Steady State Flow of Rocks, in: Wyss, M. (Ed.), Stress in the Earth, Contributions to Current Research in Geophysics (CCRG). Birkhäuser Basel, pp. 199–226

Mukoyoshi, H., Hirono, T., Hara, H., Sekine, K., Tsuchiya, N., Sakaguchi, A., Soh, W., 2009. Style of fluid flow and deformation in and around an ancient out-of-sequence thrust: An example from the Nobeoka Tectonic Line in the Shimanto accretionary complex, Southwest Japan. Isl. Arc 18, 333–351. doi:10.1111/j.1440-1738.2009.00670.x

Murata, A., 1991. Duplex structures of the Uchinohae Formation in the Shimanto Terrane, Kyushu, Southwest Japan, J. Geol. Soc. Jpn., 97, 39–52

Murata, A., 1997. Geological map of Miyazaki prefecture, 1:200,000, Miyazaki Prefectural Government

Murata, A., 1998. Duplexes and low-angle nappe structures of the Shimanto terrane, southwest Japan (in Japanese with english abstract), Mem. Geol. Soc. Jpn., 50, 147–158

Niemeijer, A.R., Spiers, C.J., Bos, B., 2002. Compaction creep of quartz sand at 400–600°C: experimental evidence for dissolution-controlled pressure solution. Earth Planet. Sci. Lett. 195, 261–275. doi:10.1016/S0012-821X(01)00593-3

Niemeijer, A., Marone, C., Elsworth, D., 2008. Healing of simulated fault gouges aided by pressure solution: Results from rock analogue experiments. J. Geophys. Res. Solid Earth 113, B04204. doi:10.1029/2007JB005376

Niemeijer, A. R., Spiers, C. J., Peach, C. J., 2008. Frictional behaviour of simulated quartz fault gouges under hydrothermal conditions: Results from ultra-high strain rotary shear experiments. Tectonophysics 460, 288–303. doi:10.1016/j.tecto.2008.09.003

Nishi, H., 1988. Structural analysis of the Shimanto Accretionary Complex, Kyushu, Japan, based on foraminiferal biostratigraphy. Tectonics 7, 641–652. doi:10.1029/TC007i003p00641

Paterson, M.S., Hobbs, B.E., McLaren, A.C., 1972. The Plasticity of Single Crystals of Synthetic Quartz. Eos Trans. Am. Geophys. Union 53, 514–515

Paterson, M.S., Luan, F.C., 1990. Quartzite rheology under geological conditions. Geol. Soc. Lond. Spec. Publ. 54, 299–307. doi:10.1144/GSL.SP.1990.054.01.26

Peacock, S.M., 1996. Thermal and Petrologic Structure of Subduction Zones, in: Bebout, G.E., Scholl, D.W., Kirby, S.H., Platt, J.P. (Eds.), Subduction Top to Bottom. American Geophysical Union, pp. 119–133

Poirier, J.-P., 1985. Creep of Crystals – High Temperature Deformation Processes in Metals, Ceramics and Minerals. Cambridge University press, Cambridge, 260 pp

Post, A., Tullis, J., 1998. The rate of water penetration in experimentally deformed quartzite: implications for hydrolytic weakening. Tectonophysics 295, 117–137. doi:10.1016/S0040-1951(98)00145-0

Raimbourg, H., Augier, R., Famin, V., Gadenne, L., Palazzin, G., Yamaguchi, A., Kimura, G., 2014. Long-term evolution of an accretionary prism: The case study of the Shimanto Belt, Kyushu, Japan. Tectonics 33, 2013TC003412. doi:10.1002/2013TC003412

Raimbourg, H., Vacelet, M., Ramboz, C., Famin, V., Augier, R., Palazzin, G., Yamaguchi, A., Kimura, G., 2015. Fluid circulation in the depths of accretionary prisms; an example of the Shimanto Belt, Kyushu, Japan. Tectonophysics 655, 161–176. doi:10.1016/j.tecto.2015.05.023

Raj, R., 1982. Creep in polycrystalline aggregates by matter transport through a liquid phase. J. Geophys. Res. Solid Earth 87, 4731–4739. doi:10.1029/JB087iB06p04731

Ramsay, J.G., 1967. Folding and fracturing of rocks, ed. Mc-Gray Hill. New York

Ramsay, J.G., 1980. Shear zone geometry: A review. J. Struct. Geol., Shear zones in rocks 2, 83–99. doi:10.1016/0191-8141(80)90038-3

Rowe, C.D., Moore, J.C., Remitti, F., the IODP Expedition 343/343T Scientists, 2013. The thickness of subduction plate boundary faults from the seafloor into the seismogenic zone. Geology 41, 991–994. doi:10.1130/G34556.1

Rutter, E.H., Elliott, D., 1976. The Kinetics of Rock Deformation by Pressure Solution (and Discussion]. Philos. Trans. R. Soc. Lond. Math. Phys. Eng. Sci. 283, 203–219. doi:10.1098/rsta.1976.0079

Rutter, E.H., Mainprice, D.H., 1979. On the possibility of slow fault slip controlled by a diffusive mass transfer process. Gerlands Beitraege Zur Geophys. 88, 154–162

Rutter, E.H., 1986. On the nomenclature of mode of failure transitions in rocks. Tectonophysics 122, 381–387. doi:10.1016/0040-1951(86)90153-8

Saito, M., 1996. Geological Map of Japan, 1:50,000, Geol. Surv. Jpn., Shiibamura

Saito, M., 2008. Rapid evolution of the Eocene accretionary complex (Hyuga Group) of the Shimanto terrane in southeastern Kyushu, southwestern Japan. Isl. Arc 17, 242–260. doi:10.1111/j.1440-1738.2008.00615.x

Sakai, T., et al. 1984. Microfossil stratigraphy of the Paleogene system in Kyushu Shimanto Belt, in Biostratigraphy and International Correlation of the Paleogene System in Japan, edited by T. Saito et al., pp. 95–112, Yamagata Univ., Yamagata, Japan. (in Japanese with English abstract)

Schmid, S.M., 1982. Microfabric studies as indicators of deformation mechanisms and flow laws operative in mountain building. Acad. Press : London, United Kingdom, United Kingdom, pp. 95–110

Schmid, S.M., Casey, M., 1986. Complete fabric analysis of some commonly observed quartz C-axis patterns. In: Hobbs, B.E., Heard, H.C. (Eds.), Mineral and Rock Deformation: Laboratory Studies. American Geophysical Union Monograph, vol. 36, pp. 263–286

Scholz, C.H., 1988. The brittle-plastic transition and the depth of seismic faulting. Geol. Rundsch. 77, 319–328. doi:10.1007/BF01848693

Schutjens, P.M.T.M., 1991. Experimental compaction of quartz sand at low effective stress and temperature conditions. J. Geol. Soc. 148, 527–539. doi:10.1144/gsjgs.148.3.0527

Shibata, K., T. Nozawa, T., 1982. Radiometric age map, granitic rocks, scale 1/4 000 000, in Geological Atlas of Japan, edited by Geol. Surv. Jpn., pp. 66–67, Tsukuba, Japan

Shimizu, I., 1995. Kinetics of pressure solution creep in quartz: theoretical considerations. Tectonophysics, Influence of Fluids on Deformation Processes in Rocks 245, 121–134. doi:10.1016/0040-1951(94)00230-7

Spiers, C.J., Schutjens, P.M.T.M., Brzesowsky, R.H., Peach, C.J., Liezenberg, J.L., Zwart, H.J., 1990. Experimental determination of constitutive parameters governing creep of rocksalt by pressure solution. Geol. Soc. Lond. Spec. Publ. 54, 215–227. doi:10.1144/GSL.SP.1990.054.01.21

Spiers, J., De Meer, S, Niemeijr, A, R., Zhang, X., 2004. Kinetics of rock deformation by pressure solution and the role of thin aqueous films. In: Physicochemestry of Thin Film Water. Edited by S. Nakashima et al., by Universal Academy Press, Inc/Tokyo, Japan. pp 129-158

Stallard, A., Shelley, D., 1995. Quartz c-axes parallel to stretching directions in very low-grade metamorphic rocks. Tectonophysics 249, 31–40. doi:10.1016/0040-1951(95)00040-T

Stöckhert, B., Gerya, T.V., 2005. Pre-collisional high pressure metamorphism and nappe tectonics at active continental margins: a numerical simulation: High pressure metamorphism and nappe tectonics. Terra Nova 17, 102–110. doi:10.1111/j.1365-3121.2004.00589.x

Taira, A., Okada, J., McD, Whitaker, H., Smith, A, J., 1982. The Shimanto Belt of Japan: Cretaceous-lower Miocene active margin sedimentation. J.K. Leggett (ed), Trench-Forearc Geology. Geol.Soc. London, special Pubblication 10, 5-26

Taira, A., Katto, J., Tashiro, M., Okamura, M., Kodama, K., 1988. The Shimanto Belt in Shikoku, Japan; evolution of Cretaceous to Miocene accretionary prism. Mod. Geol. 12, 5–46

Tenthorey, E., Cox, S.F., 2006. Cohesive strengthening of fault zones during the interseismic period: An experimental study. J. Geophys. Res. Solid Earth 111, B09202. doi:10.1029/2005JB004122

Teraoka, Y., and K. Okumura 1992. Tectonic division and Cretaceous sandstone compositions of the Northern Belt of the Shimanto Terrane, southwest Japan. Mem. Geol. Soc. Jpn., 38, 261–270

Thompson, W.K., 1965. Infrared spectroscopic studies of aqueous systems I. Trans. Faraday Soc. 61, 1635– 1640

Toriumi, M., Teruya, J., 1988. Tectono-metamorphism of the Shimanto Belt, Mod. Geol., 12, 303–324

Trepmann, C.A., Stoeckhert, B., 2009. Microfabric of folded quartz veins in metagreywackes; dislocation creep and subgrain rotation at high stress. J. Metamorph. Geol. 27, 555–570. doi:10.1111/j.1525-1314.2009.00842.x

Tse, S.T., Rice, J.R., 1986. Crustal earthquake instability in relation to the depth variation of frictional slip properties. J. Geophys. Res. 91, 9452–9472. doi:10.1029/JB091iB09p09452

Tullis, J., Yund, R.A., 1977. Experimental deformation of dry westerly granite. J. Geophys. Res. 82, 5705–5718. doi:10.1029/JB082i036p05705

Tullis, J., Yund, R.A., 1980. Hydrolytic weakening of experimentally deformed Westerly granite and Hale albite rock. J. Struct. Geol. 2, 439–451. doi:10.1016/0191-8141(80)90005-X

Urai, J.L., Williams, P.F., van Roermund, H.L.M., 1991. Kinematics of crystal growth in syntectonic fibrous veins. J. Struct. Geol. 13, 823–836. doi:10.1016/0191-8141(91)90007-6

White, S.H., 1976. The effects of strain on the microstructures, fabrics and deformation mechanisms in quartz. Philos. Trans. R. Soc. Lond., A 283, 69–86

Wintsch, R. P., R. Christoffersen, Kronenberg A.K., 1995. Fluid-rock reaction weakening of fault zones, J. Geophys. Res., 100 (B7), 13021–13032, doi:10.1029/94JB02622

Wintsch, R.P., Yi, K., 2002. Dissolution and replacement creep: a significant deformation mechanism in mid-crustal rocks. J. Struct. Geol., Micro structural Processes: A Special Issue in Honor of the Career Contributions of R.H. Vernon 24, 1179–1193. doi:10.1016/S0191-8141(01)00100-6

Wright T.O., Platt L.B., 1982. Pressure dissolution and cleavage in the Martinsburg shale. Am. J. Sci. 282, 122–135

Wright, T.O., Henderson, J.R., 1992. Volume loss during cleavage formation in the Meguma Group, Nova Scotia, Canada. J. Struct. Geol. 14, 281–290

CHAPITRE III

Ce chapitre est proposé sous forme de publication scientifique. Nous y exposons les résultats d'une série des expérimentations menées en Presse Griggs sur deux typologies de quartz: le premier est un quartz très hydraté obtenu par extraction mécanique du Mélange tectonique de Hyuga (pour une description détaillée faire référence au Chapitre II) ; le deuxième est un quartz du Brésil peu hydraté. Les deux matériaux, préalablement concassés et tamisés à la taille de 200-250 µm ont été mélangés avec une matrice commune pour constituer différents assemblages avec I) 30% de porphyroclasts et 70% matrice, II) 70% de porphyroclasts et 30% matrice et III) 100% de matrice. Les différents assemblages ont été déformés tous à les mêmes conditions expérimentales, température 800°C, pression de confinement de 1.5 GPa et vitesse de déformation 10^{-5} s^{-1}.

Les modes de déformation ainsi que la rhéologie de ces deux différents matériaux sont décrits et discutés. Les porphyroclasts de quartz très hydraté sont très étirés et montrent des microstructures imputables à des mécanismes de déformation par fluage dislocation. Inversement, les porphyroclasts du quartz du Brésil maintiennent une forme ronde et n'exhibent pas d'évidences de recristallisation dynamique au cœur. Seulement les bordures des porphyroclasts sont recristallisées probablement à cause de l'incorporation d'eau pendant les stages initiaux de la déformation. Le mécanisme responsable de telle incorporation est probablement la microfracturation. Dans le cas de porphyroclasts du quartz du Brésil, l'utilisation de différentes proportions de porphyroclasts a ainsi permis d'évaluer l'évolution de propriétés mécaniques de la matrice.

Les analyses Infrarouge ont permis d'évaluer la quantité d'eau avant et après déformation : les porphyroclasts de quartz très hydraté ont expulsé l'eau en excès via migration de joint de grains et l'eau a migré dans la matrice. Inversement, les porphyroclasts secs de quartz de Brésil ont incorporé des petites quantités d'eau. En plus, la présence de pics secondaires superposés sur la bande principale de l'eau liquide, a permis d'identifier spéciation chimique de l'eau par rapport à la position microstructurale occupée, plutôt aux joints de grains ou aux dislocations.

CHAPTER III

Effect of water on experimentally deformed quartz aggregates

INTRODUCTION

Even if the hydrolytic weakening effect of water on quartz has been demonstrated in many laboratory studies [*Griggs and Blacic*, 1965; *Griggs,* 1967; *Kekulawala et al.,* 1978, 1981; *Kronenberg and Tullis,* 1984], a thorough understanding of this process is still lacking.

In particular, the water species responsible for weakening are not fully identified. The original works on weakening proposed that OH groups along dislocation enhanced their glide [*Griggs and Blacic,* 1965, *Griggs,* 1967]. Other models proposed that the hydrogarnet defect would be responsible for weakening [*Cordier and Dhoukan,* 1989]. Finally, the close association between nanometer-scale clusters of water and dislocation loops led *McLaren et al.* [1989] and *FitzGerald et al.* [1991] to propose that enhanced dislocation generation at 10′s of nanometer-scale fluid inclusions was at the origin of weakening.

Definition of "dry" quartz may probably be generalized as quartz containing water amounts lower than 100 H/10^6 Si [*Griggs and Blacic,* 1965; *Den Brock,* 1994; *Christie et al.,* 1964b] which deforms under the semi-brittle to brittle conditions at laboratory strain rates and temperatures.

This amount of water is usually several order of magnitude lower than what can be contained in natural quartz in the form of µm-scale fluid inclusions. Thus, in many natural cases, reservoirs of water exist in the crystal, but mechanical weakening requires the process, which is well understood, and neither fast, because of the very low solubility nor diffusive transport of water in quartz [e.g. *Kronenberg et al.,* 1986]. The value of ~100 H/10^6Si is somewhat higher than the estimated equilibrium solubility of water (<100 H/10^6 Si in the form of $(4H)_{Si}$ [*Paterson,* 1986]. Weakening of quartz consequently necessitates the penetration of water or OH-defects into the quartz crystal. Micro-fracturing [*Kronenberg et al.,* 1986, 1990] and diffusion (along subgrain boundaries or dislocation cores [*Post and Tullis,* 1998], have been proposed as mechanisms responsible for water uptake as well as grain boundary migration [G*leason and DeSisto,* 2008], because oxygen diffusion may be increased at high dislocation densities sites [*Post and Tullis,* 1998].

The question of quartz weakening is different if considering synthetic and natural material containing a relatively low and homogeneous distribution of crystal defects such as OH-groups, hydrogarnets $(4H)_{Si}$ of nm clusters of water or natural crystals containing a much larger concentration in water in the form of heterogeneously distributed fluid inclusions. In the latter case, where the medium is best described as two-phase and composed of solid crystal and fluid inclusions, the process of weakening, which involves the interactions between the inclusions and the adjacent crystal, still remains to be described. Experiments on quartz single crystal [*Cordier and*

Doukhan, 1989] and quartzite [*Kronenberg and Tullis,* 1984] stated that the intensity of mechanical weakening increases with increasing water content [*Griggs,* 1967; *Blacic and Christie,* 1984, *Cordier and Doukhan,* 1989, *Hirth and Tullis,* 1992; *Den Brok et al.* 1994]. High water content has also strong effects on recrystallization microstructure development [*Jaoul et al.,* 1984; *Tullis and Yund,* 1989; *Hirth and Tullis*, 1992].

This study is focused on the effect that water has on deformed quartz aggregates strength in the natural case of strongly hydrated quartz samples from contexts such as subduction zones where large amounts of water are available. A strongly hydrated natural milky quartz and a dry quartz were deformed at the same experimental conditions to better understand the role of water on recrystallization and the effect of recrystallization on water speciation.

1 Methods

1.1 Experimental procedure

All experiments were performed in a Griggs-apparatus at 800°C, ~1500 MPa and constant strain rate of 10^{-5} s^{-1}. These conditions were chosen in order to activate the dislocation creep regime by dislocation climbing [*Hirth and Tullis,* 1992]. We used in all experiments 45° pre-cutted Al_2O_3 pistons inserted in a pre-annealed platinum (Pt) jacket. Between these pistons, in the form of a ~1mm thick disk, we deposited a mixture of quartz containing a fixed proportion of large grains ("porphyroclasts") and matrix. The matrix is the same in all experiments and the porphyroclasts constitute the material to be tested. In all experiments, the matrix is constituted of Brazil crystal crushed in a stainless steel cup. The selected size, in the range of 6 to 20 µm, was obtained by repeated cycles of decantation in water column. Granulometric analisis reveal the presence of a low volumetric fraction (<1,6 %) of about 60 µm size clasts. These powders were then dried at 100°C for 48 hours before preparing the mixture. We performed experiments with two distinct kinds of porphyroclasts. One material was natural dry Brazil quartz. A single euhedral crystal of ~4cm long was cut trying to avoid optically visible secondary fuild inclusions planes. Porphyroclasts were obtained directly by crushing the selected part of the crystal in a stainless steel cup. Porphyroclasts with size in the range of 200-250 µm were get by sieving. The second material was milky quartz from veins in Hyuga Tectonic Mélange, a low-grade metamorphic unit from the Shimanto Belt in Japan [*Raimbourg et al., 2014*; *Palazzin et al.,* submitted). Fragments from mm-wide veins were crushed in an agathe mortery and quartz was separated from the remaining matrix by density (Sodium Polytungstate) and magnetic techniques (with Frantz® device). The material was sieved to 200-250 µm size. A final hand-picking was made to avoid any possible clay contamination. Two main experimental mixtures were composed by mixing respectively 30% and 70% porphyroclasts of Hyuga/Brazil quartz in pure Brazil quartz matrix. In addiction we deformed a sample with 100% pure Brazil matrix.

To ensure an homogenous repartition in the blend, porphyroclasts and matrix were mixed in a glass beaker with acetone in an ultrasonic bath, until complete acetone evaporation. The porphyroclats+matrix mixtures were then placed on the lower piston surface after adding distilled water with a micropipette. Water amount to be added was calculated with respect to matrix proportion, corresponding thus to 0,1 wt. % and 0,05 % wt. % in the case of 30% and 70%

porphyroclasts blend respectively. Then, the second pre-cut piston was placed and the top of the Pt jacket was mechanically welded with a Lambert welding device. This assemblage was then placed in the center of a graphite furnace and thus into the solid confining medium (sodium chloride, NaCl). A simplified example of sample assembly used in the experiments is illustrated in **Figure 1**. To get the desired temperature and pressure conditions, the pumping and heating procedures were made progressively, normally in ~9 hours. Confining pressure was initially increased to 150 MPa before heating. Then temperatures was increased by in steps of 100°C at a rate of 25°C per minute and so on the confining pressure till 1.5 GPA and 800°C. At this conditions, deformation was started by activating the axial piston at constant strain rate of 10^{-5} s^{-1}. At the end of each experiment the sample was quenched by rapidly lowering simultaneously the temperature at 200°C and the differential stress in order to minimize changes in the deformation microstructures. Some unloading cracks are nevertheless observed in some samples were quenching procedure was too rapid. Some experiments failed during the P/T conditions achievement due to pressure vessel or thermocouple crack. These unsuccessful samples were useful to get additional information during the initial steps of the experiments. For example, a sample where failure occurred after pressurization but before shearing with 30% Hyuga porphyroclasts has been taken as equivalent of hydrostatic conditions. All samples have been cut along their longitudinal part in order to provide thin and thick sections for microscopy and FTIR analysis.

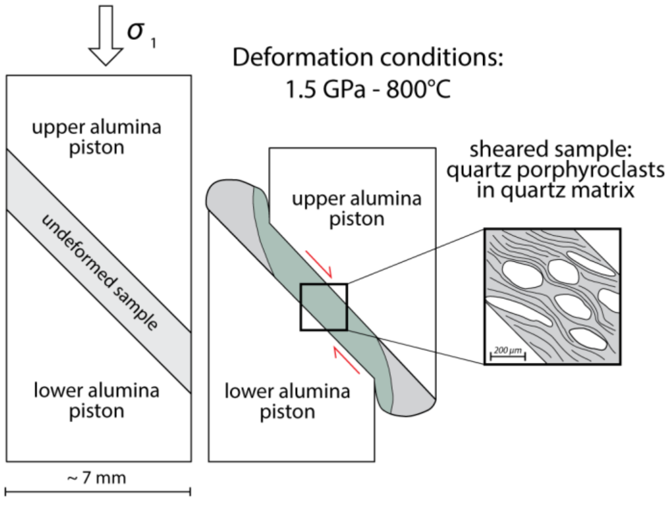

__Figure 1__. Schematic representation of the sample assembly used in this study, in the starting position [no stress applied = hot pressing) and after deformation showing the pistons final position and the state of the deformed "porphyroclats+matrix" mixture.

1.2 FTIR

To enable analysis of the starting material, we doubly polished a slice of the single Brazil quartz crystal (cut in the direction orthogonal to the [c]-axes) to the thickness of about 130-140 μm. Single porphyroclasts of Hyuga quartz were selected and fixed in orthodontic acrylic resin (Vertex Ortoplast) and double polished too. Deformed samples were cut vertically through their central axe and in the X-Z plane to produce double polished thick sections of about ∼100–200 μm thickness. The intragranular water content was determined by Fourier Transform Infrared (FTIR) spectroscopy with a Nicolet Continuum FTIR microscope attached to a microscopic FTIR spectrometer (Nicolet-6700 FT-IR Thermo Scientific) at the Institute de Science de la Terre d'Orléans (France). All the measurements were carried out at atmospheric temperature and the sample area was purged with dry air in order to avoid measurement of atmospheric water. A sodium chloride window was used to collect the background for each measurement then subtracted from all spectrum. The 50×50 μm aperture window for all the analyses allowed precise measurements inside porphyroclasts. 256 scans per spectrum were collected with 4 cm^{-1} resolution. We estimated concentration from "molecular" water integral absorption band between ~2800 and 3800 cm^{-1} using the Beer-Lambert law,

$$A = C * t * \epsilon \qquad \text{eq. 1}$$

C is concentration, t is the thickness and ϵ is the integrated molar absorption coefficient. Samples thicknesses was obtained from the height of the peak at 1790 cm^{-1} corresponding to the Si–O band, again making use of Lambert–Beer's Law [e.g., *Ito and Nakashima*, 2002]. The molar concentrations of C Si, has been converted to weight ppm by using the relation: 1 ppm H_2O to SiO_2 by weight is equal to 6.67 H:10_6 Si [e.g., *Gleason and DeSisto,* 2008]. To allow the estimated water concentration to be compared to the results of previous studies on quartz [e.g., Kronenberg et al., 1990b; Kronenberg and Wolf, 1990; Post and Tullis, 1998], we also used the calibration proposed by Paterson et al. (1982), based on the integral of absorption coefficient as:

$$C = 1/d \ 1/(I \ eff) \int K(\nu) \, d\nu \qquad \text{eq. 2}$$

where d (cm) is the thickness of the sample, K is the absorption coefficient, ν (cm) is the wavenumber and I eff (cm^{-2} per mol H/liter of quartz) is the effective integral molar absorption coefficient. Values of I eff vary according to the concentration in H and we made the calculations with a value of 27000 cm^{-2} corresponding to concentrations of 4000H/106 Si.

1.3 EBSD – CIP

Crystallographic preferred orientation (CPO) of the deformed quartz grains was measured by electron backscatter diffraction (EBSD) [*Lloyd and Freeman,* 1994] and by computer integrated polarized (CIP) microscopy [*Heilbronner and Pauli,* 1993; *Heilbronner and Tullis,* 2006]. Diffraction patterns were recorded using an EDAX PEGASUS EDS/EBSD system (manufacturer EDAX) at the BRGM of Orléans, France. Acquisitions were obtained on 70° tilted samples, at 20 kV acceleration voltage, ~30 nA beam current and 18 to 20 mm working distances. EBSD maps were acquired with 0.25 to 1 µm spacing. We used a threshold of 0.1 in the confidence index given by OIM DC 6.4 software to define correct analyses. In additions, to avoid incorrectly indexed points, we defined grains as being composed of at least 4 adjacent pixels with similar crystallographic orientation

CIP method combines polarization light microscopy with image analysis techniques to measure [c]-axis orientations of uniaxial materials. This technique allowed a good estimation of CPO for over an area of larger size than standard EBSD map. Thin section images are color-coded according to color Look-Up Table (LUT) and with respect to their [c]-axis orientation. Quartz [c]-axis preferred orientation of recrystallized grains and non-recrystallized clasts were obtained, and represented by area-weighted [c]-axis pole figures. The general sense of shear is indicated for each image. In addition, because EBSD and CIP investigations were conducted only for part of the samples, the extents of recrystallization were estimated by visual inspections of the entire sample using a light microscope.

3. Results

3.1 Characterization of the starting material

Hyuga quartz has a very milky aspect due to the abundance of very tiny fluid inclusions. These inclusions range from 5 to 10 µm in diameter [*Raimbourg et al.,* 2015], and they are heterogeneously distributed in the porphyroclasts which are very milky and look dark in this sections (**Figure 2A**). As shown by FTIR spectrum (**Figure 2A)** water amount is thus considerably variable in reponse to fluid inclusions distribution. Mean measured values (listed in **table 1)** are however in the order of ~2,000 ppm. Some residual clay crystals are rarely observed even after quartz separation from clays and they represent less then 1% of the whole sample. This quantities are thus comparable with the impurities reported for Black Hills Quarzite [e.g. *Hirth and Tullis,* 1992; *Heilbronner and Tullis,* 2006] and are presumed to have no significant influence on mechanical data.

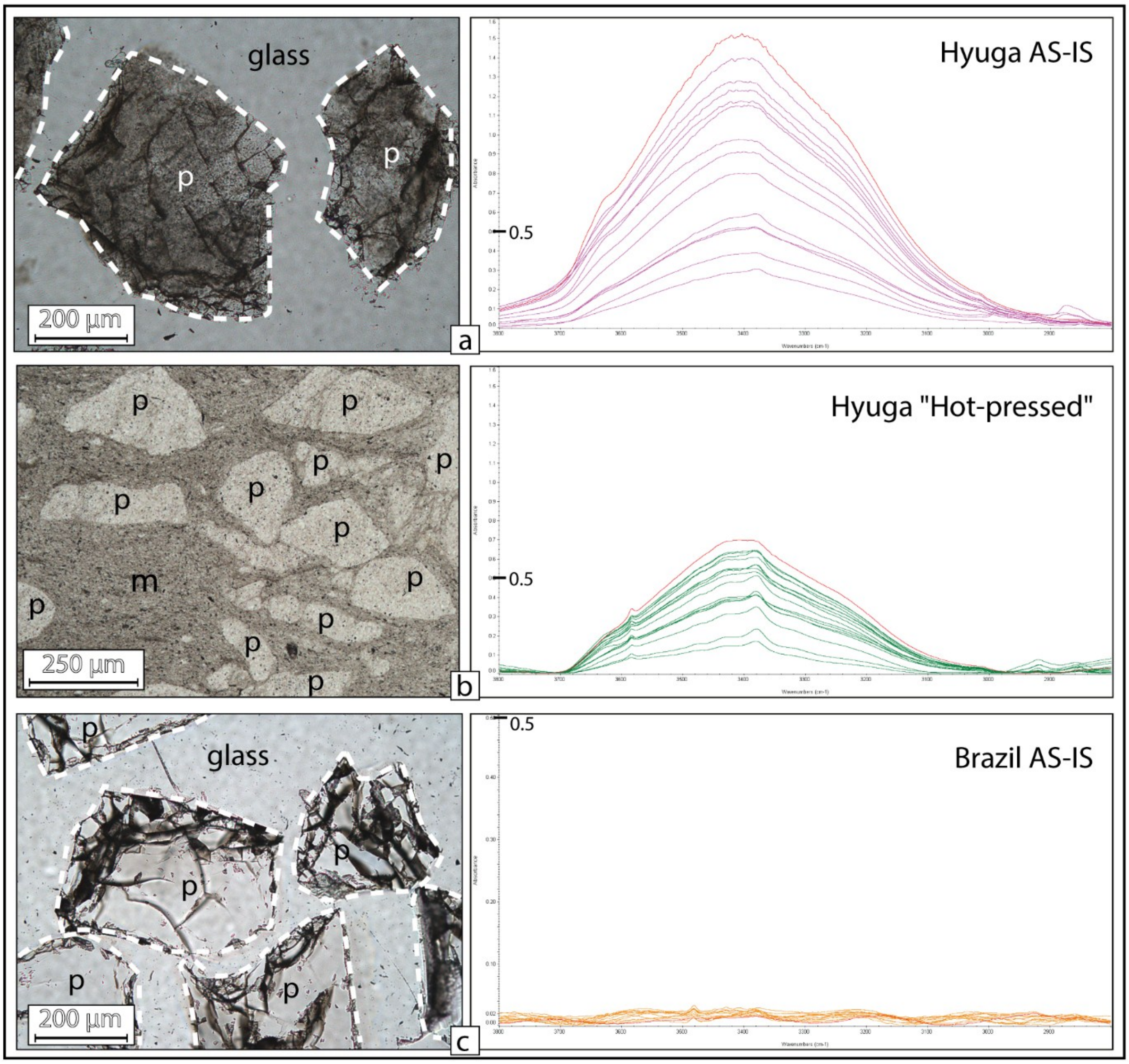

Figure 2*: Characterization of the starting material. All the spectrum are represented with a common scale. A)Light photograph of milky Hyuga porphyroclast (p) delimited by white dashed lines and associated IR spectrum. Note the abundance of tiny fluid inclusions (which confer a dark aspect to porphyroclasts) and their variable distribution inside each single grain. Inhomogeneous absorption in IR spectrum depend on the fluid inclusion density in the analyzed zone. B) Thin section of "hot-pressed" sample with 30% Hyuga porphyroclasts (p) embedded in the Brazil quartz matrix (m). Note the lower fluid inclusions abundance*

inside porphyroclasts and the general lower absorbance values. C) Brazil quartz porphyroclasts (p) are transparent (white dashed lines) and display only few large fluid inclusions. The big difference in water amount between this material and Hyuga porphyroclasts in outlined by the value of 0.5 on the absorption axis.

After pressurization, porphyroclasts show lower abundance of fluid inclusions with respect to the starting material and they appear clearer (**Figure 2B**). At these conditions, measured water amount is generally lowered to a half of initial quantity (**Figure 2B**).

Porphyroclasts of dry Brazil quartz are optycally strain free and contain some secondary fluid inclusions with size ranging from 50 to 100 μm. Mean measured water amount in Brazil quartz (about 20 ppm) confirm that this material is almost dry (**Figure 2C).**

Material	**Conditions**	**Microstructures**	**T (cm)**	**Abs**	**C (mol/L)**	**ppm**	**H/10^{6}Si**
Hyuga p.	as-is	core	0.014	343	332	2,261	15,071
Hyuga p.	Hot pressing	core	0.013	170	154	1,051	7,011
Hyuga p.	deformation	recrystallized	0.014	40	32	220	1,469
Brazil p.	as-is	core	0.014	3.9	3	16	112
Brazil p.	deformation	core	0.012	7	6	41	258
Brazil p.	"	recrystallized	0.013	26	22	150	998
Matrix in H sample	Hot pressing	-	0.013	66	51	351	2,342
Matrix in H sample	deformation	-	0.013	45	42	284	1,893
Matrix in B sample	deformation	-	0.013	15	12	84	561

Table 1. Molecular water content of Hyuga and Brazil porphyroclasts, Brazil matrix at different conditions: "as-is", "hot-pressed" and "deformed". (Th=thickness; Abs= integrated absorbance area; C= molar concentration; ppm= part per million weight; H/10^{6}Si with the Stolper [1982] and Kats [1962] calibration.

3.2 Mechanical Behavior

Mechanics curves are presented in **Figure 3** and flow stress values listed in **Table 2.** Curve shapes, as well the strength values, indicate dominant plastic deformation in all samples. All curves are characterized by a first stage (gamma =0 to ~0.5/1.3) of a rapid increase in stress up to a peak which is followed by a stage of weakening at much slower rate.

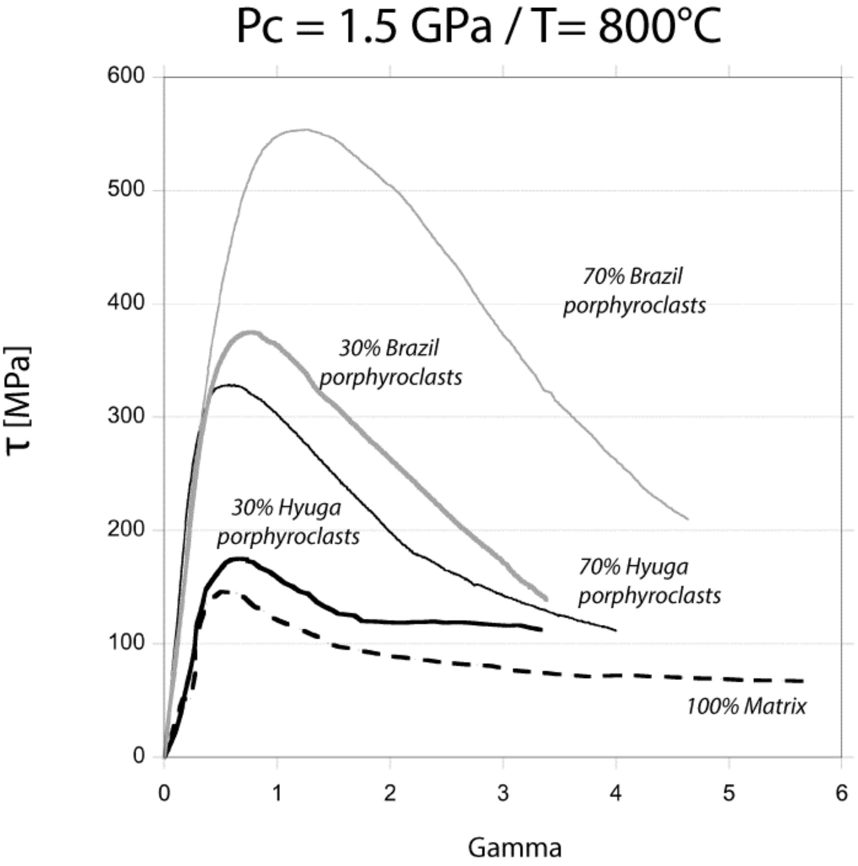

Figure 3. *Shear stress/shear strain curves for the five samples deformed in this study; for final stress values see Table 2.*

The experiment with 100% matrix shows the weaker curve, with lower peak stress reached at gamma ~0.5. This sample display mechanical steady state after weakening with flow values of about 68 MPa. Similar behavior is observed for the sample with 30% Hyuga porphyroclasts even if the peak stress is little bit higher (180 MPa) as well as the steady state flow value (110 MPa).

Samples with Brazil porphyroclasts show steeper curves during the first stage and reach higher peak stress. The sample with 70% Brazil porphyroclasts show the higher peak stress value (up to 550 MPa) at gamma 1.3 in contrast to the experiment with only 30% Brazil porphyroclasts. After the peak of stress the two curves display a very similar shape, characterized by an important weakening down to low stress values, 140 MPa for 30% porphyroclasts and 211 MPa for the experiment with 70% porphyroclasts.

The curve representing the experiment with 70% of Hyuga porphyroclasts show slope down comparable with the curves with Brazil porphyroclasts but the peak stress value is lower, 320 MPa and it is reached at lower gamma (0.56). At about gamma 2 we observe a flection of this curve which becomes gentler and starts to tend to the horizontal. Samples with 70% Hyuga p. do not reach steady state flow but from the behavior of the curve, it would be reached at higher gamma.

From **Figure 3** we also observe that most mechanic curves converge to a similar value after about gamma 3-4.

Sample	**Assembly**	**% water added**	**Peak stress [MPa]**	**ɣ gamma Peak Stress**	**Final stress [MPa]**	**ɣ gamma**	**Grain Size (matrix)**
GP426	30% Brazil p.	0.1	**370**	**0.78**	**140**	**3.38**	**2.5**
GP428	30% Hyuga p.	0.1	**180**	**0.61**	**113**	**3.33**	**1.6**
GP465	70% Brazil p.	0.45	**555**	**1.26**	**211**	**4.61**	**1.0**
GP456	70% Hyuga p.	0.45	**325**	**0.56**	**113**	**3.98**	**2.6**
GP457	100% matrix	0.15	**150**	**0.53**	**68**	**5.66**	**1.6**

Table 2. Deformation conditions (deformation time, gamma, peak stress and final stress values) and sample parameters (assembly, added H2O) of all deformation experiments. Confining pressure (Pc) = 1.5 GPa; Temperature (T) =800°C; strain rate = 10^{-5} s^{-1}.

3.3 Microstructural Observations

3.3.1 Porosity

Figure 4 is representative of porosity in the matrix at "hot-pressing" condition. Pores are observed at triple junctions **(Figure 4 e.g. white arrow)** where rarely exceed 1μ diameter, and less often along grain boundaries (**Figure 4, e.g. black arrow)**. At these conditions, porosity is estimated to be lower than 1.5 % of the total sample volume. After deformation, porosity is still observed in all samples but it is strongly reduced and not visible at grain boundaries.

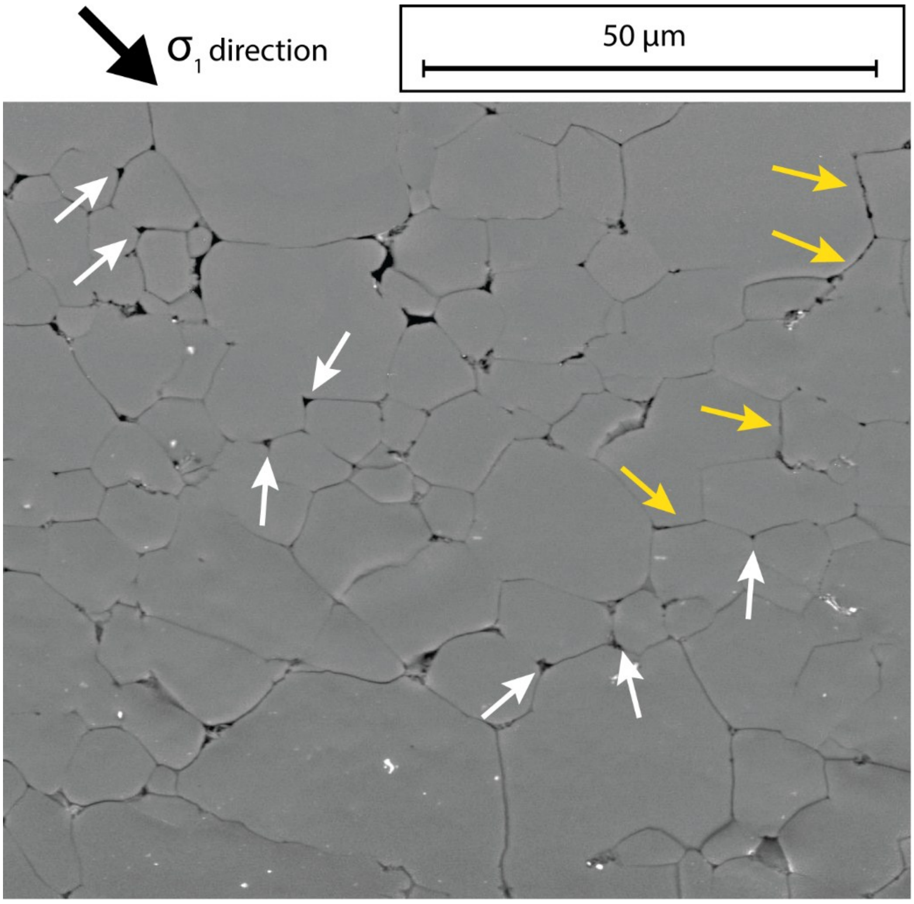

Figure 4. *SEM images of the matrix composed by Brazil quartz at "hot-pressed" condition (confining pressure 1.5 GPa; T=800°C). Porosity is observed at triple junctions between polygonal grains [white arrow) and at grain boundaries (black arrow). Grains show almost hexagonal shape and smooth-edges. White particles are carbon grains from carbon-coating in order to prevent charging effects.*

3.3.2 100% Matrix sample

Sample with pure 100% matrix (**Figure 5**) is characterized by strongly recrystallized grains. The grains at pistons margins are almost equant and preserve sutured grain boundaries while moving to the center of the samples it is not possible to recognize grain because of their very similar extinction colors. This trend defines a recrystallization gradient trough the thickness of the sample. A low angle oblique preferred orientation is defined by the extinction colors and cuts across the sample.

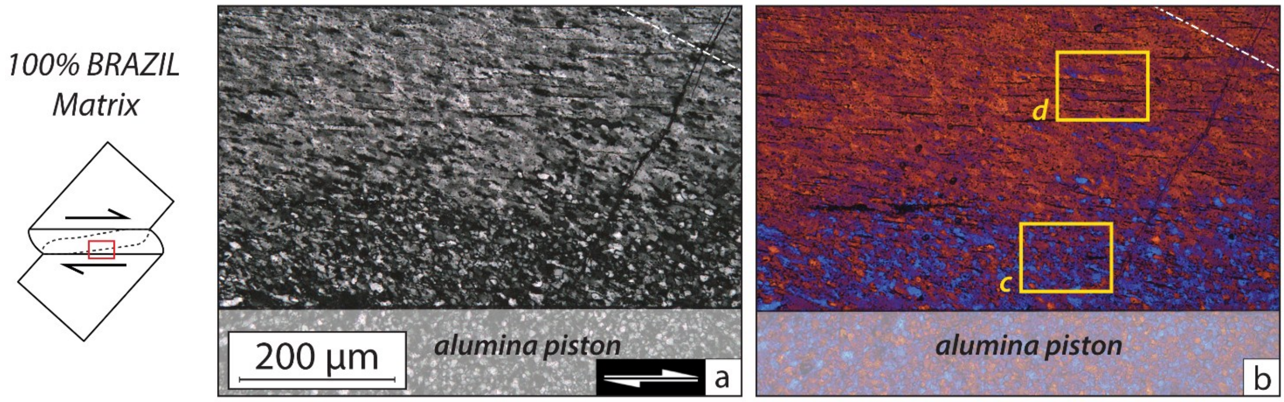

Figure 5. *Cross polarized (a) with analyzer (b) images of the sample of 100% matrix. The low angle (~25°) oblique preferred orientations indicated by the stippled white line.*

3.3.3 Experiment with porphyroclasts

3.3.3.1 Brazil porphyroclasts and their matrix

In these samples, a foliation results from the alignment of porphyroclasts at about 20-25° from the shear zone boundaries (pistons).

Porphyroclasts in the 30% assembly show a certain variability in shape: they are more stretched with sharp limit when they are close to the shear zone boundaries while in the central part they are more rounded with smooth-edges (**Figure 6A**.**).** In the sample with 70% porphyroclasts, it is recurrent to observe tails of strongly stretched quartz (**Figure 6C** and **D**) which decorate round porphyroclasts (i.e., σ-type with tendency to δ-type porphyroclasts [*Hanmer,* 1984b; *Passchier and Simpson,* 1986; *Hooper and Hatcher*, 1988]. Tails display the same extinction color as the parent core (**Figure 6F**) and a net color change with the surrounding matrix. In both experiments the effects of recrystallization on porphyroclasts are limited: we clearly distinguish relict cores and recrystallized rims (**Figure 6F**, white arrows**)**. Especially in the 70% porphyroclasts sample, these sutured rims characterized by small recrystallized grains, confer a gradual transition of the cores with the surrounding matrix. In the cores, strain is accommodated by deformation lamellae which are often associated with sweeping extinction in bands of ~40 µm large (**Figure 6F** and **6f** and **Figure 8a** and **b**). Porphyroclasts boundaries are sutured and display some evidences of bulging (**Figure 8a** and **b**). Strain shadows develop beside cores in the direction perpendicular to σ1: at these sites small equant grains develop (**Figure 6F,** dashed boxes and **Figure 7a** and **b**). Matrix is characterized by sutured grain boundaries and show homogenous extinction colors. Some local variations are observed where the matrix is squeezed between two porphyroclasts (especially in the sample with 70% porphyroclasts) (**Figure 6F**). At very high magnifications, tiny (<10 µm) fluid inclusions are observed at porphyroclasts rims, parallel to the foliation.

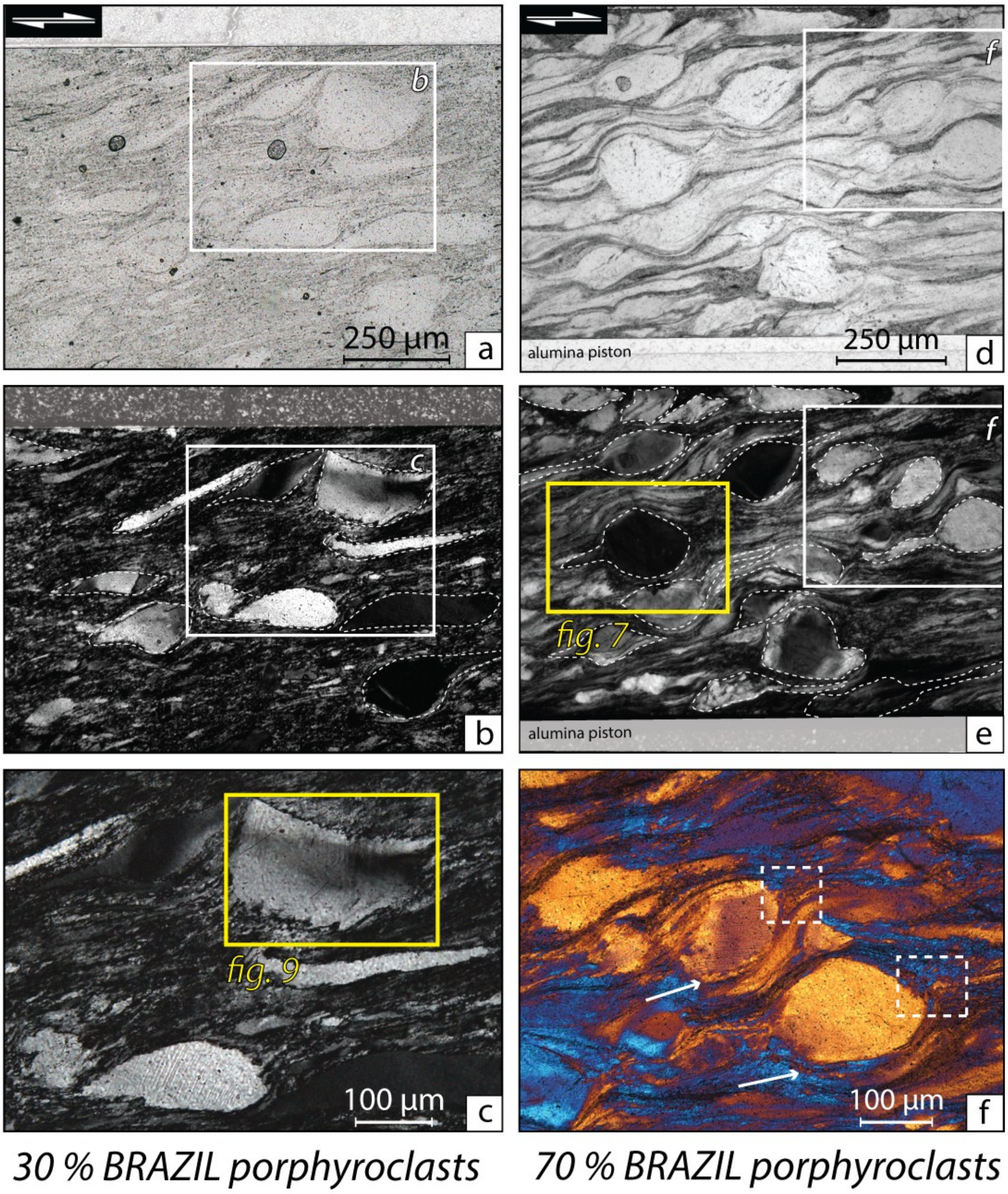

Figure 6. *Natural light (a-d), cross-polarized (b-c-e) and cross-polarized with analyzer (f) images of the samples GP426 (left) and GP465 (right) with Brazil porphyroclasts. Dextral shear sense is common for all the images. Right and left column for 30% and 70% porphyroclasts respectively. a) Porphyroclasts are quite variable in shape, from stretched (mostly in the upper part of the picture) to round, in the central portion of the sample. A foliation develops at about 25° from the shear zone boundary (pistons limit). b) Brazil porphyroclasts core (excluding recrystallized rims) are outlined by dashed lines. They may display homogeneous internal polarized colors (lower right corner) or sweeping extinction. c) Close up on some Brazil porphyroclasts. Deformation lamellae and sweeping extinction are observed. d) Porphyroclasts display almost round smooth-edges shape, only at the piston contact they are flattened. The low matrix percentage appears dark gray colored. e) Porphyroclasts core (dashed lines) display stretched tails which can wrap around other porphyroclasts. Sweeping extinction and deformation lamellae are commonly observed. f) Close up on some Brazil porphyroclasts, which display homogeneous internal extinction colors*

sometime associated to undulose extinction and deformation lamellae. Their outer rims, as well as pressure shadows (dashed boxes) are composed of finer recrystallized grain with different extinction colors. Matrix squeezed in between porphyroclasts display yellow extinction color in contrast with the other portions which are almost red and blue.

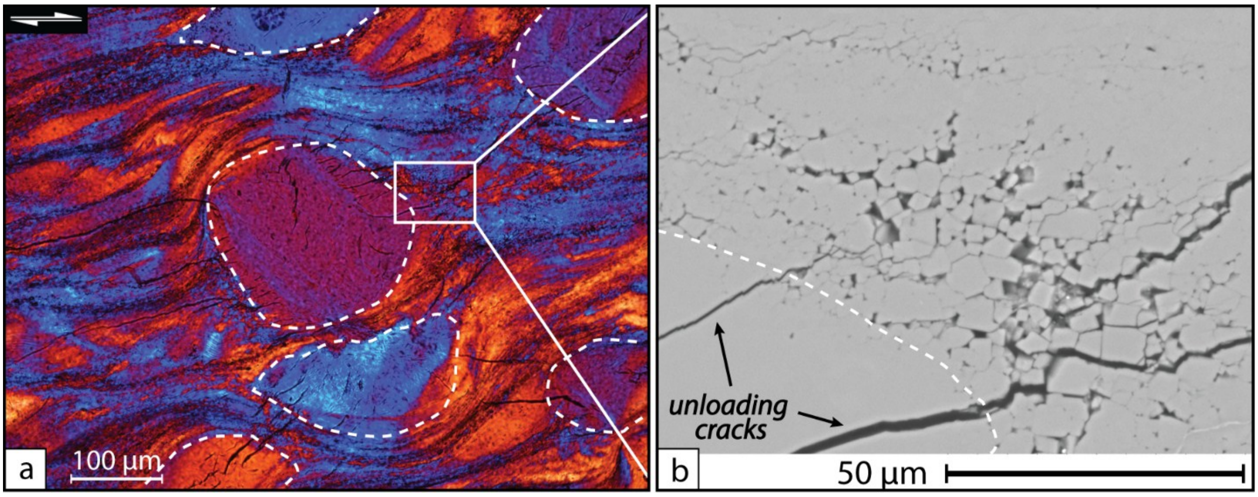

***Figure** 7. a) Cross-polarized (with analyzer) image of deformed Brazil porphyroclasts and their matrix. Pressure shadows are observed on the right (white rectangle) and left sides of the central porphyroclast. Unloading cracks overprint the ductile microstructures. b) Equant rectangular grains develop in cavities at pressure shadows Voids are observed.*

3.3.3.2 Hyuga porphyroclasts and their matrix

At natural light microscope, porphyroclasts (**Figure 8A and D**) defines the foliation planes at about 11-13° from the pistons margins. They are discernable from the surrounding matrix as regions with a lower fluid inclusion density. Porphyroclasts display a strong shape preferred orientation (SPO), an important aspect ratio (10:1) and smooth-edges boundaries. At polarized light we can observe extensive recrystallization, which almost completely prevents to distinguish between porphyroclasts and matrix (**Figure 8B** and **8E**). Porphyroclasts are constituted of strongly elongated domains which can display quite homogenous extinction colors or they display internally recrystallized fine-grains characterized by sutured grain boundaries (**Figure 8C** and **F**). These stretched domains are bonded by sutured grain boundaries and internally present small subgrains which are distinguishable one form another by their different extinction colors (**Figure 8C** and **F figure 9C** and **d**). Comparing the recrystallization microstructures of the assembly with 30% and 70% Hyuga porphyroclasts, in the former, porphyroclasts appear more recrystallized. Contrasting with this general high recrystallization rate, some domains are preserved deformation lamellae (e.g. **Figure 10A** and **B**). In these samples, matrix is strongly recrystallized and display serrated grain boundaries and almost homogenous extinction colors.

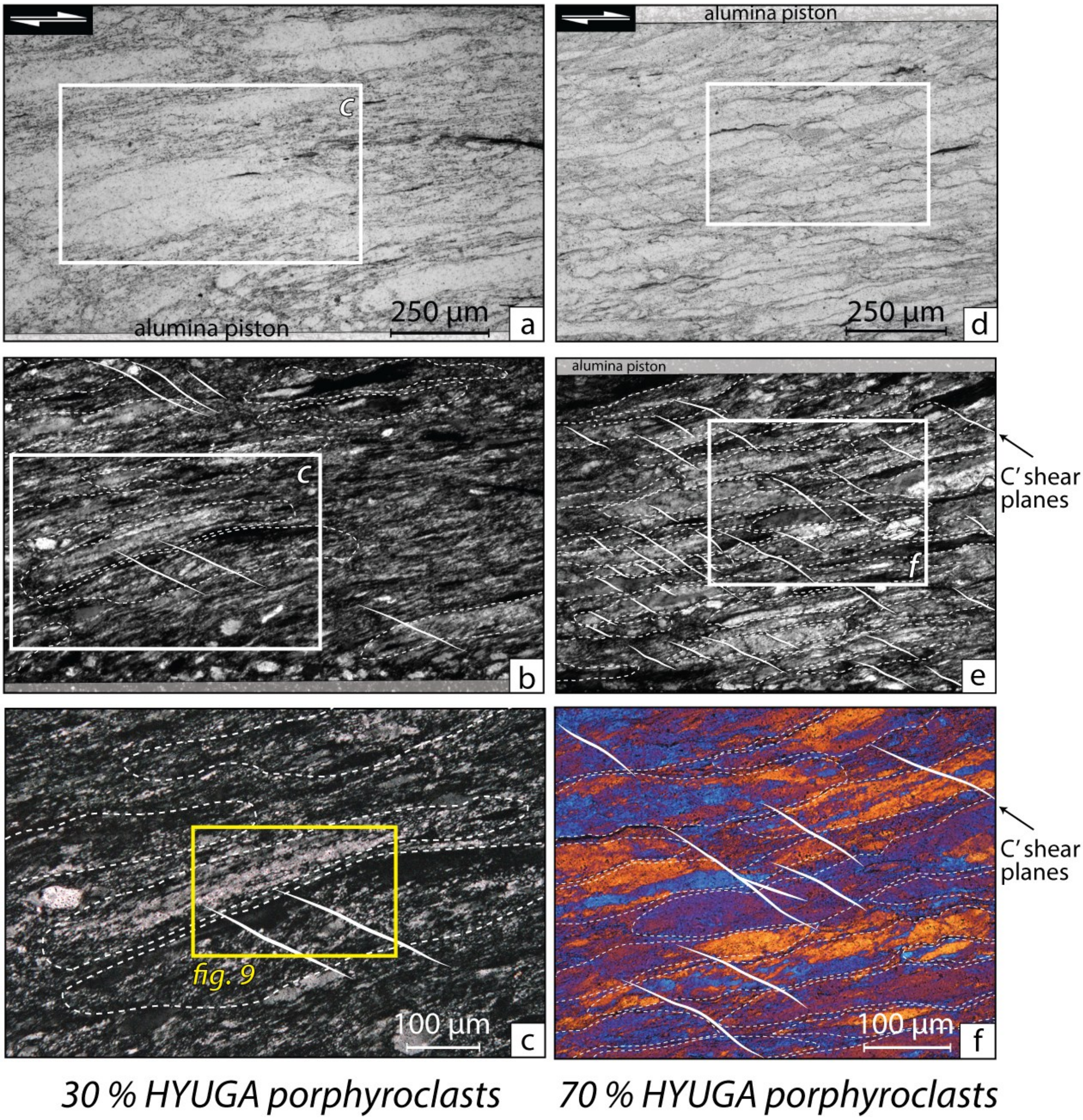

Figure 8. *Natural light (a-d), cross-polarized (b-c-e) and cross-polarized with analyzer (f) images of samples GP428 (left) and GP456 (right) with Hyuga porphyroclasts. Dextral shear sense is common for all the images. Right and left column for 30% and 70% porphyroclasts respectively. a) All porphyroclasts are strongly flattened and stretched. Note the presence of larger clasts in the matrix with respect to a) and dark impurities on the middle-right of the picture (clays). b) Hyuga porphyroclasts boundaries are highlighted by dotted lines, otherwise it will not possible to recognize them. Note the presence of few discrete C' shear planes, developed coherently with the imposed dextral shear sense. c) Close up on some recrystallized porphyroclasts. d) Porphyroclasts are strongly flattened (aspect ratio ~10:1) and cut by several shear planes developed at 25-30° from the shear zone boundaries (piston limit). Note the presence of a thin dark clay pockets in the central part of the picture. Foliation is defined by the alignment of porphyroclasts and*

develops at ~20° from the shear zone boundaries. e) Strongly recrystallized domains are disposed parallel to the general stretching direction are observed. Porphyroclast and matrix are cut across by abundant shear planes. f) Close up on some highly recrystallized Hyuga porphyroclasts evidenced by dashed contours. Some not recrystallized domain whit an elongated shape preferred orientation is observed. Note sutured boundaries describing recrystallized domains.

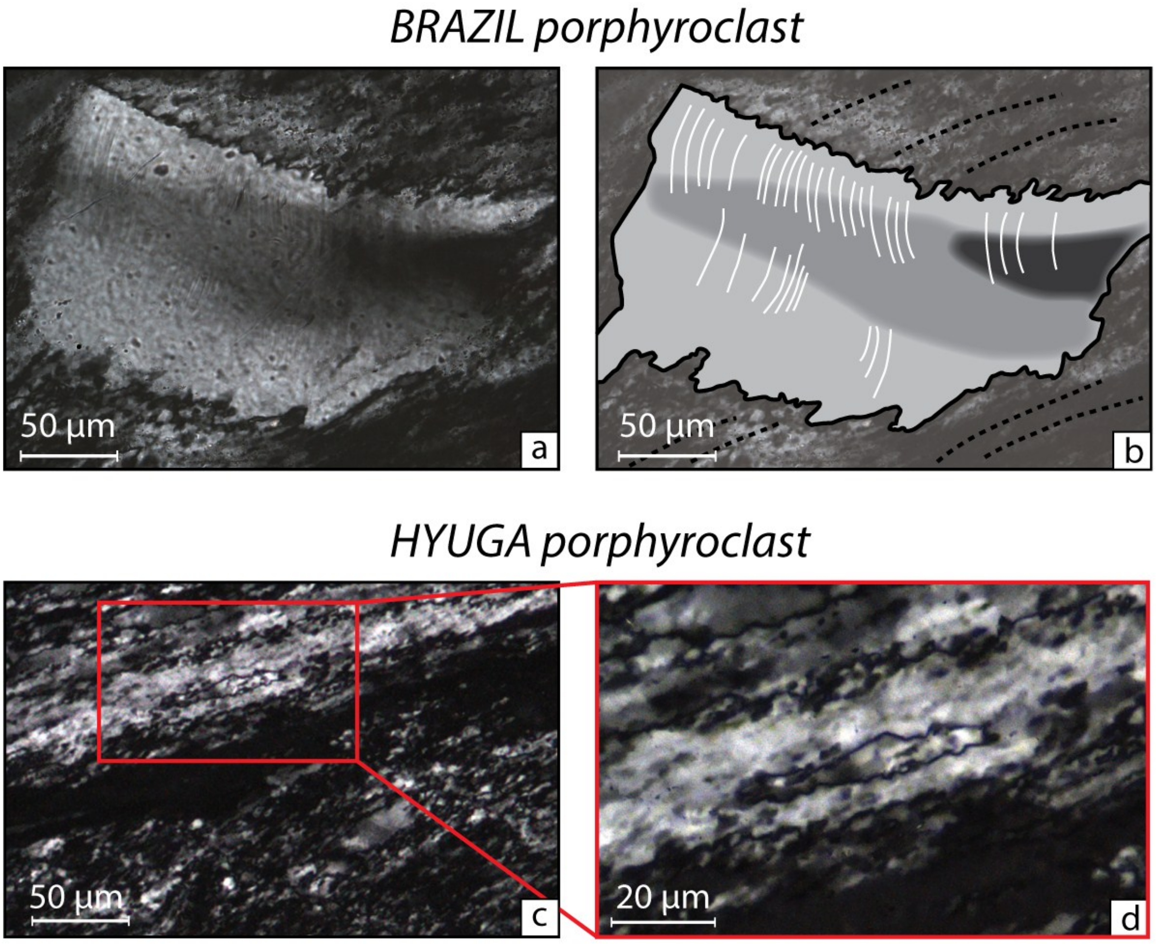

***Figure 9**. Close up of the deformed Brazil and Hyuga quartz porphyroclasts in **Figure 6** and **8**. a) Note the sutured porphyroclast boundaries, the sweeping extinction and the deformation lamellae. b) Interpretation of microstructural features observed in a): foliation (dashed black lines); sutured porphyroclast boundaries (black lines); deformation lamellae (white lines). For simplicity, pressure shadows are not drawn in details. c) Sutured grain boundaries delimit elongated domains which are characterized by almost homogenous extinction colors. d) At higher magnification, the first-look homogeneous extinction colors domains reveal heterogeneous extinction colors which indicate small recrystallized subgrains.*

3.3.4 Shear Bands

In both experiments with Hyuga porphyroclasts and pure matrix, C' shear bands develop oblique to the shear zone boundaries, in a synthetic orientation with the imposed shear sense (**Figure 8B** and E). The angle between these planes and the shear zone boundary vary statistically between 25-35°. In this context, the stretched porphyroclasts defines the S-plane in a SC' foliation. Plane polarized light images show that trails of small fluid inclusions are present at these sites (**Figure 10A**) which are also characterized by different extinction colors at crossed polarized with analyzer with respect to the surrounding material (**Figure 10B**). SEM micrographs (**Figure 10**) were helpful to better describe these deformation zones as sites of high porosity in which grains of about 2-5 µm diameter are observed. These grains have straight boundaries, round edges and equant shape and the transition with the surrounding material is marked by a general decrease of porosity (**Figure 10C**). The C' shear bands are most ubiquitous in the sample with 70% porphyroclasts of Hyuga porphyroclasts where they cut across the matrix and the stretched porphyroclasts inside which they are generally deflected to slightly higher values. A mean angular values of 27° has been estimated between C' planes and porphyroclasts major axis.

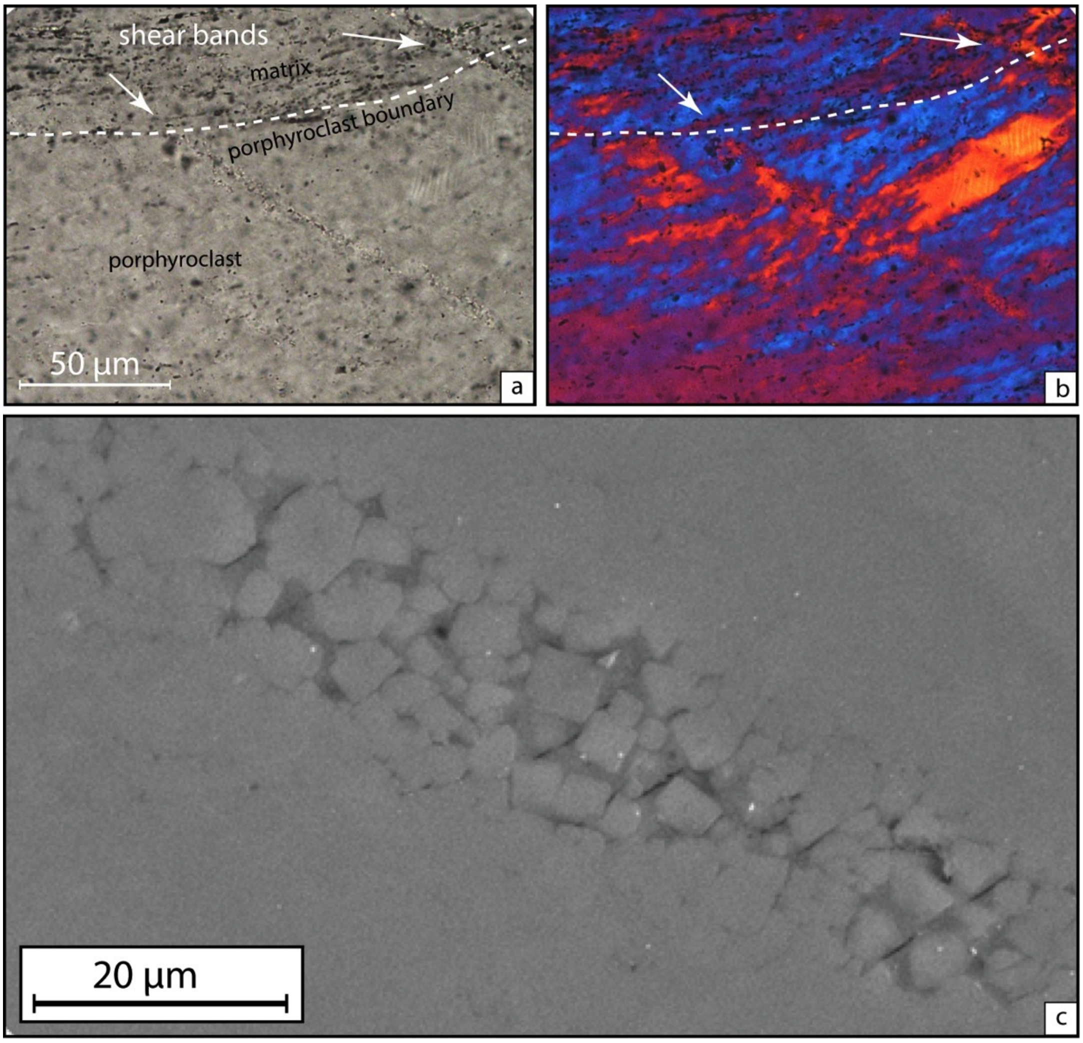

Figure 10. *Close up on shear bands in sample GP456 (70% Hyuga porphyroclasts). a) Shear bands cut across the matrix and a porphyroclast. Note the abundance of tiny fluid inclusions along the shear planes (natural light image). b) Shear bands have different extinction color (yellow) with respect to the surrounding material. Note that even if the porphyroclast is generally highly recrystallized, a portion still present deformation lamellae (large yellow grain). Crossed polarized (with analyzer) image. c) SEM image of the shear band inside the porphyroclast. Grains are almost equant with regular shape and smooth-edges. Most of them are smaller than 5 µm in size. Note the high porosity in the shear band contrasting with the low porosity in the surrounding material at which only few triple junction pores are observed.*

3.4 Water content/Distribution

In order to quantify the water amount and explore water distribution within the samples, we carried out FTIR analysis both on matrix and on porphyroclasts for each experimental set-up.

3.4.1 Matrix

As we described in the “Experimental Setup”, the matrix is crushed Brazil quartz. It has been hydrated by adding distilled water, proportionally to the weight of the matrix employed for each experiments. **Figure 10** shows matrix spectra for “hot-pressed” and deformed condition with both Hyuga and Brazil porphyroclasts. Water amount decrease is registered by IR spectrum in samples with Hyuga porphyroclasts from hot pressing to deformation. The matrix surrounding Brazil porphyroclasts show quite flat absorption bands. Water estimations indicate however relatively higher quantities with respect to the initial one in Brazil porphyroclasts (**Table 1**).

These spectra do not show significant modifications in shape but in peak distribution: the peaks at 3382 cm^{-1} is still observed but the peak at 3585 cm^{-1} becomes smaller after deformation. The peak at 3595 cm^{-1} seems to be stable. The most prominent absorption band in this material is at 3595 cm^{-1} whereas the peak at 3360 cm^{-1} and the shoulder at 3382 cm^{-1} are smaller.

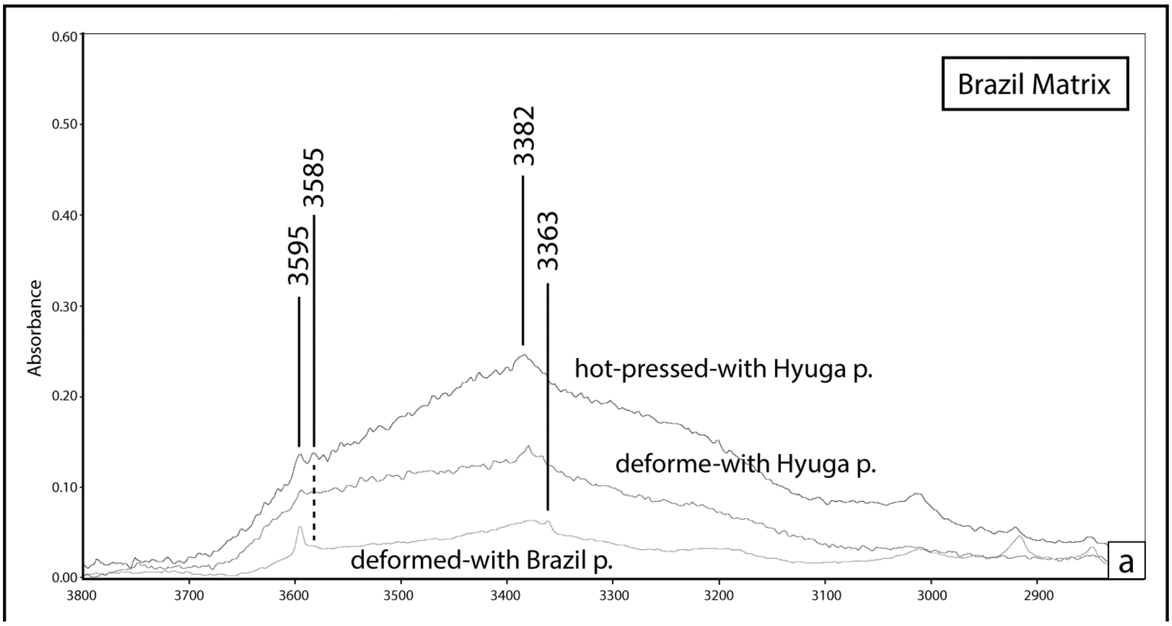

Figure 11. FTIR spectrum in the Brazil matrix. The higher absorption values are registered in the "hot-pressed" sample (with Hyuga porphyroclasts). Note the presence of the sharp absorption band at 3595 cm-^{1} which is detected since "hot-pressed" conditions. The band at 3585 cm^{-1} disappear after deformation.

3.4.2 Porphyroclasts

Brazil and Hyuga porphyroclasts show several differences in spectrum shapes and secondary bands. Hyuga quartz displays a broad absorption band in the region between 3000 and 3800 cm^{-1} (**Figure 12A**) centered on 3430 cm^{-1} and generally considered to be related to molecular water (H_2O) such as water in fluid inclusions. This major band is characterized by the presence of several secondary bands, related to structurally bound OH. **Figure 12A-B** represents absorption spectrum of the "hot-pressed" sample always with Hyuga porphyroclasts. The broad band of molecular water shows a general decrease and the secondary absorption bands are modified. A new absorption band is detected at 3585 cm^{-1} while the one at 3382 cm^{-1} becomes stronger. The flat absorption spectrum for Brazil quartz (**Figure 12C**) display only one secondary absorption band at 3485 cm^{-1}, similarly to Hyuga porphyroclasts.

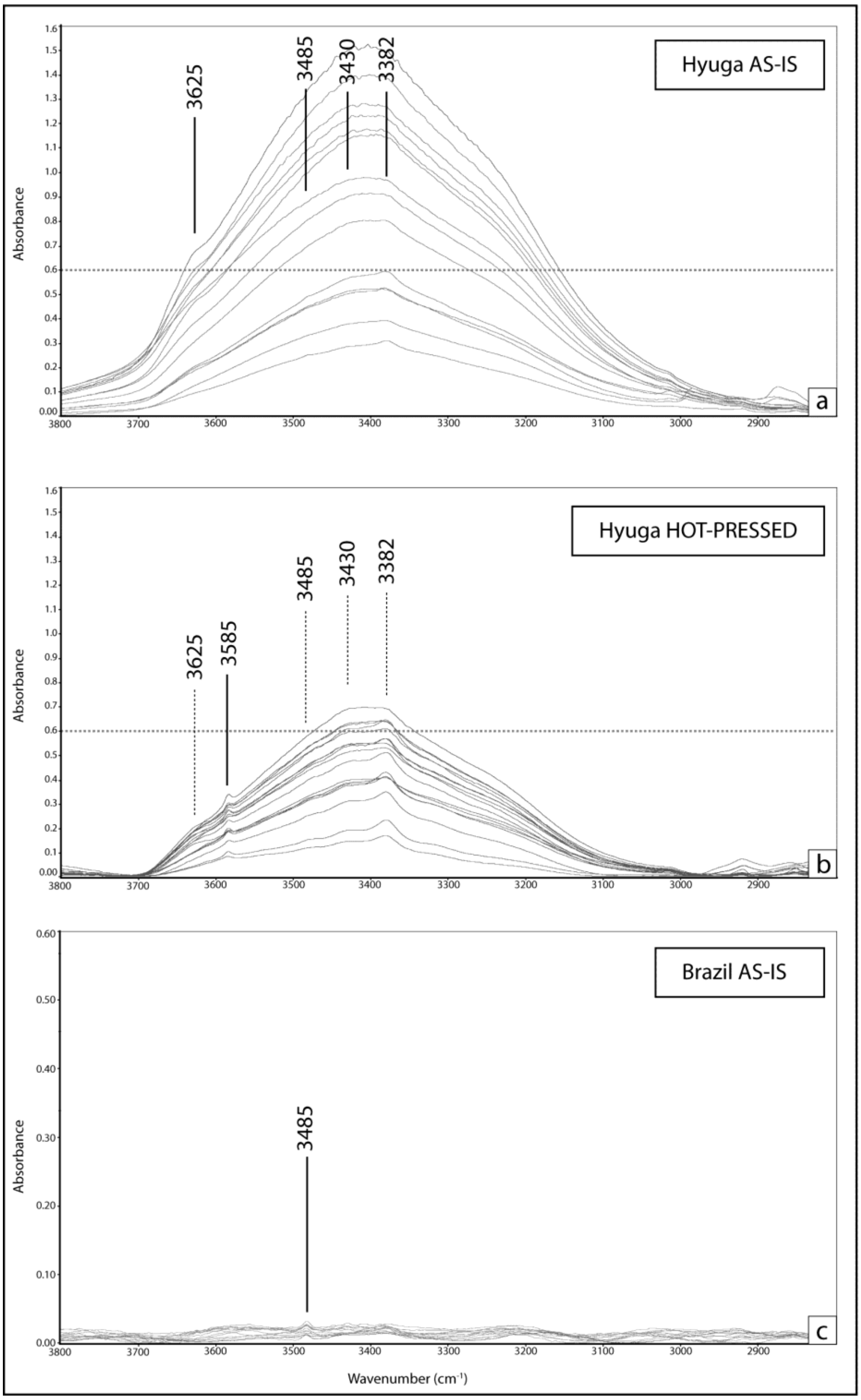

Figure 12*. FTRI spectrum and relative absorption bands of the two starting materials. In a) and b) are represented spectrum of Hyuga quartz respectively at "as-is" and "hot-pressed" conditions. At "hot-pressed" conditions, we observe the same secondary absorption bands and the new one at 3585 cm^{-1}. c) Spectrum of Brazil "as-is" quartz which are characterized by only a prominent absorption band at 3485 cm^{-1}. Note that even if the Hyuga quartz shows a great variability in water distribution, the water amount notably larger than in Brazil quartz. The absorbance value of 0.6 is highlighted to allow a direct comparison with Brazil quartz spectrum.* After deformation significant changes are observed in spectrum. Hyuga

porphyroclasts show a strong water amount decreases (of about a factor 10, see **Table 1**). The broad band associated to molecular water is here flattened (**Figure 13**.). Previously registered discrete absorption bands at 3625, 3485, 3430, 3382 cm^{-1} disappear together with the appearance of a new band at 3595 cm^{-1}. The bands at 3585 and 3382 cm^{-1} are not affected by deformation.

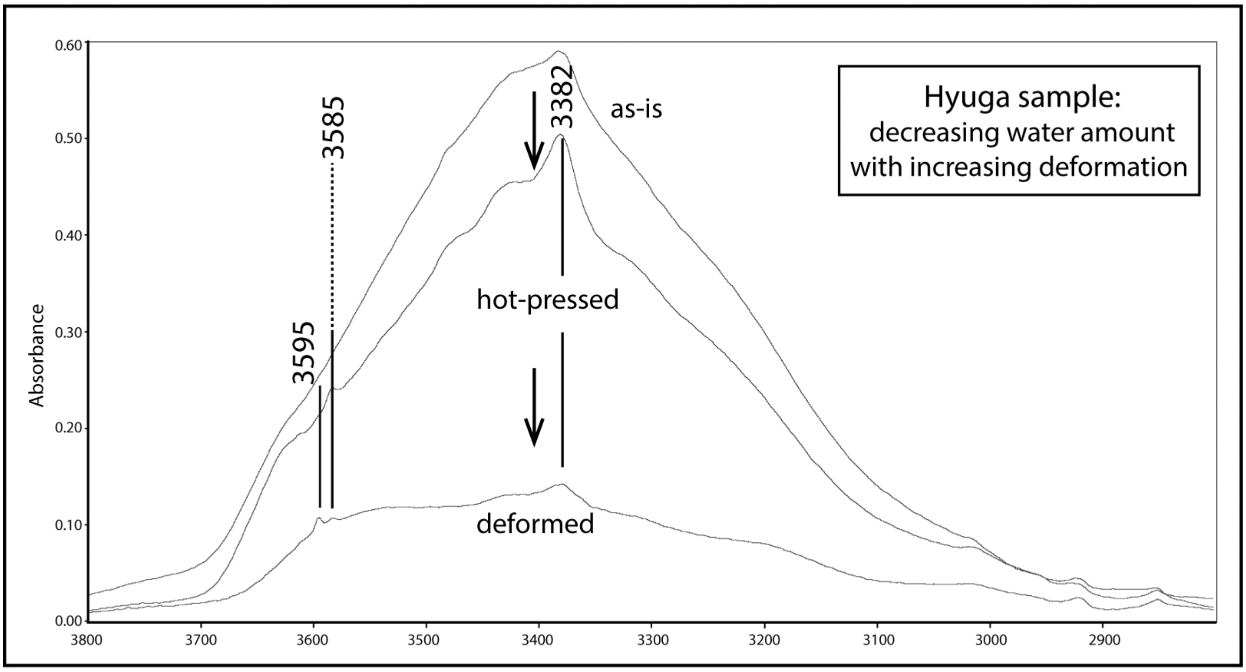

Figure 13. Effect of deformation on FTRI spectrum. All the spectrum are represented with a common scale. a) Evolution of water quantity and absorption bands in Hyuga porphyroclasts. Note the important sharpening in secondary bands from the "as-is" to the hot pressed material. Most of secondary bands disappear with increasing deformation conditions while a new band is detected at 3595 cm^{-1}.

In **Figure 14** two typical spectra for Hyuga porphyroclasts and the surrounding matrix after deformation are represented. The spectra are flat and show similar water amounts (see **Table 1**).

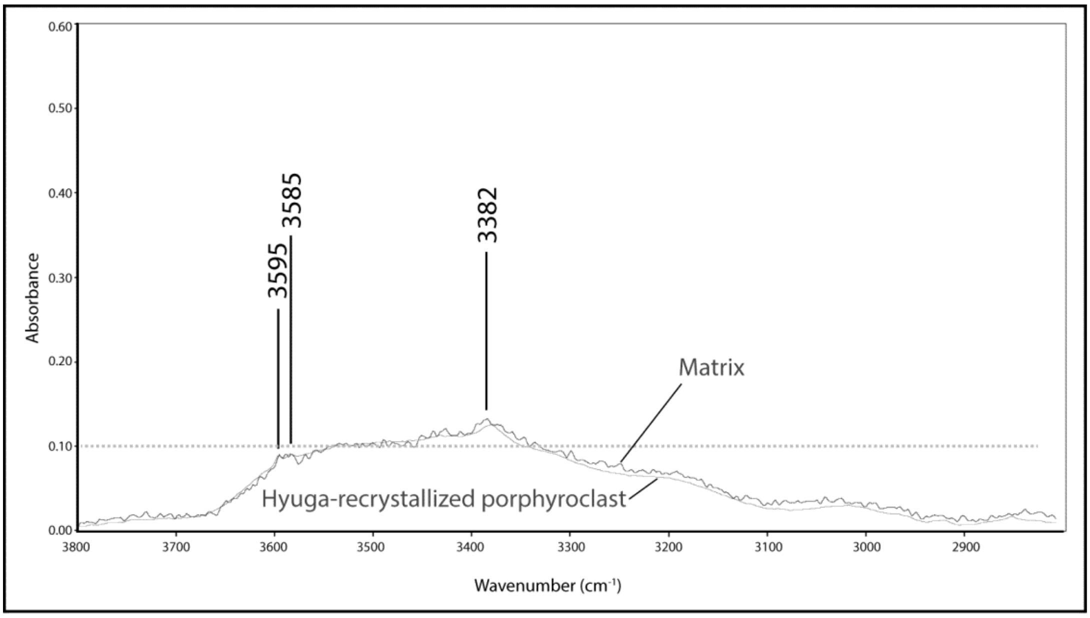

Figure 14. Comparison between water amount in recrystallized Hyuga porphyroclasts and the surrounding matrix. The two FTIR spectrum show the same shape and the same secondary absorption bands.

Brazil material displays different water amount with respect to the analyzed microstructures. An example is showed in **Figure 15** where an undeformed core (**Figure 15A)** displays lower water amount than recrystallized zones (**Figure 15B).** Furthermore in **Figure 15C** new secondary absorption bands are observed are 3585 cm^{-1} in undeformed cores and at 3595 and 3363 cm^{-1} for recrystallized grains.

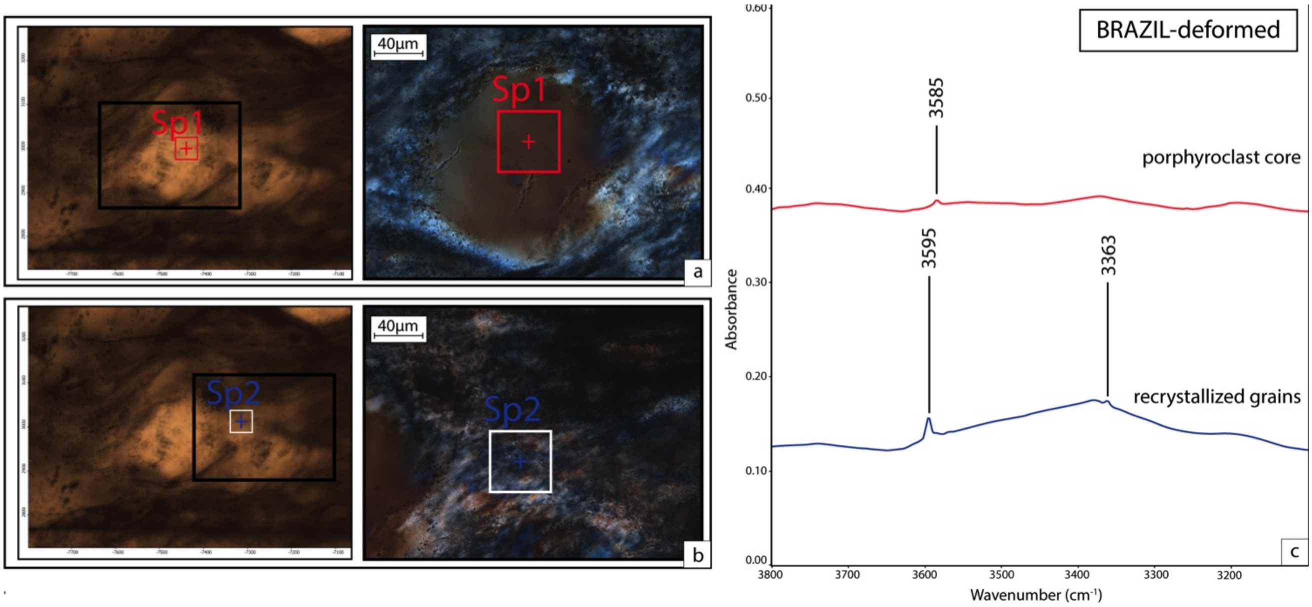

Figure 15*. Natural light and cross-polarized images of a Brazil quartz porphyroclast and correlated FTRI spectrum. A) Close-up on a porphyroclast core. Note the absence of macroscopically deformation features. The red rectangle corresponds to the FTIR analyze window and to Sp1 (red spectra) in* ***Figure 15C****. B) Close-up on porphyroclast recrystallized tail. Recrystallized grains are about 4 µm large. The withe rectangle corresponds to the FTIR analyze window and to Sp2 (blue spectra) in* ***Figure 15C. C****) FTIR spectrum (offset-scale) of the microstructures in A) and B). Note the dissimilar shapes corresponding to differences in water amounts and the different secondary bands (see discussion for details).*

3.5 Crystallographic orientation analysis

Crystallographic preferred orientation analysis were carried on porphyroclasts and matrix; trying to characterize in detail significant differences between the two employed materials.

3.5.1 100% Matrix

This sample show a strong CPO of c-axis which are oriented parallel to the Z-axis reference direction. More intense recrystallization is achieved in the central part of the samples where uniform IPF colors are displayed (**Figure 16**).

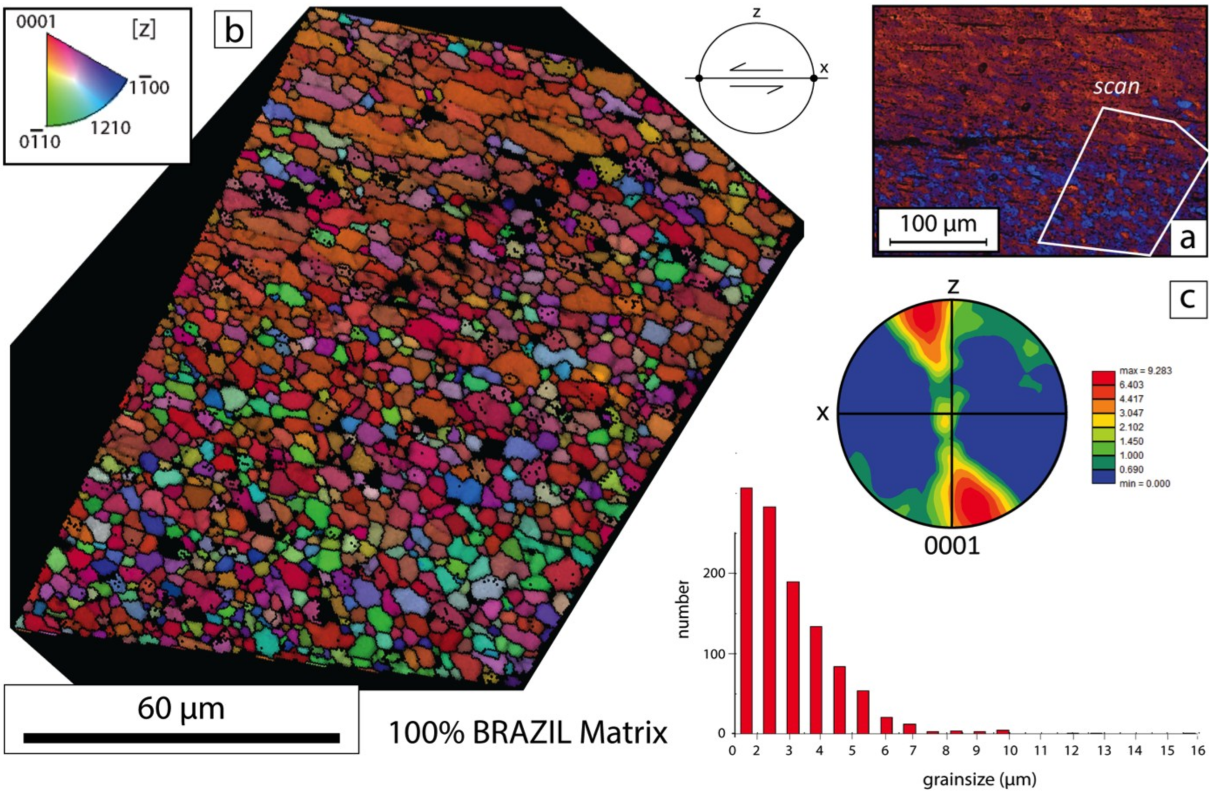

Figure 16. *Sample GP457 with 100% Brazil matrix deformed at gamma 5.5 (see* ***Table 2****). Left shear sense. a) Natural light (cross-polarized) image of the EBSD analysis. b) Invers Pole figure and Confidential Index (IPF + CI) map. Orientation colors according to the inverse pole figure given in the upper left corner of the image. c) CPO texture associated to the orientation map.*

3.5.2 Brazil porphyroclasts and matrix CPO

Figure 17 shows EBSD map, pole figures and misorientation profiles for a porphyroclast in the sample with 30% Brazil porphyroclasts. The variation in IPF map color inside the stretched porphyroclast (**Figure 17B**) is indicative of internal lattice distortion and probably embryonic development of new subgrains as confirmed by the presence of low misorientation angles (**Figure 17D**). The misorientation angular values at 60° correspond to Dauphiné twin boundaries. Porphyroclasts/matrix contact is clear-cut and outlined by high angle misorientation (**Figure 17E,** profile a) and outlined by local sutured boundaries (**Figure 17D**, white arrows). Porphyroclast c-axis is oriented in the X-Z plane and at ~45° to the Z and X axes (**Figure 17C**).

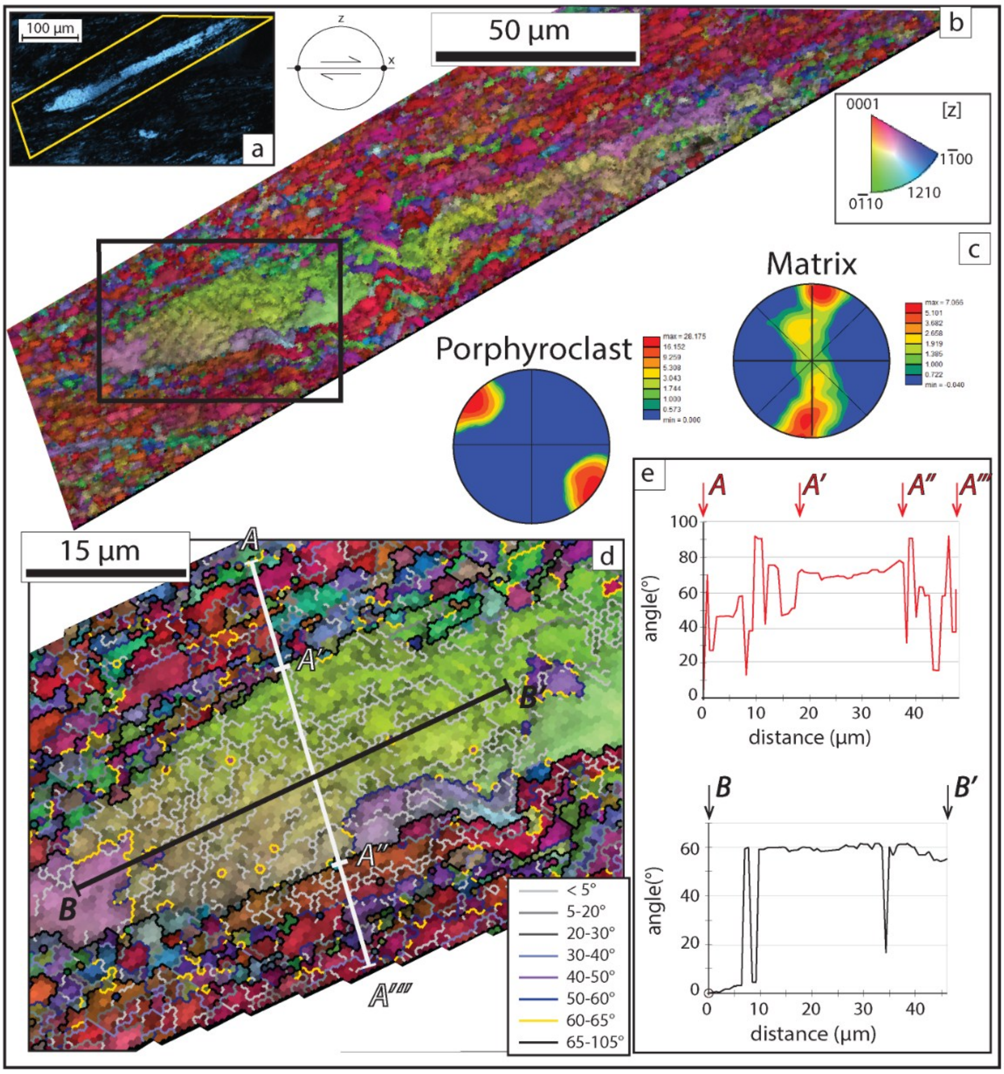

Figure 17. *Sample GP426 with 30% Brazil porphyroclasts deformed at gamma 3.38 (see* ***Table 2****). Dextral shear sense. a) Natural light (cross-polarized) image of the EBSD analysis. b) Invers Pole figure and Confidential Index (IPF + CI) map of the porphyroclasts and the matrix. Note that the upper left part of the porphyroclast shows important IPF color variations which are not observed in the natural light image. Orientation colors according to the inverse pole figure given in the upper right corner of the image. The select rectangle corresponds to* ***Figure 16d****. c) CPO textures for the recrystallized matrix and the stretched porphyroclast. d) Close-up of the IPF + CI map showing superimposed grain boundary misorientations. Misorientation angles are taken between nearest neighbor pixels. Note the abundance of domains of*

dominant low misorientation boundaries (light gray, <5°) zones within the porphyroclasts of dominant higher misorientation (dark gray-violet, 5-50°) inside matrix grains. e) Misorientation angles profiles (not at scale) across (AA') and within (BB') the porphyroclats+matrix. Note the net angular discrepancy between them while porphyroclasts show very little internal variations (except for twin boundaries at 60°).

Detailed analysis on blocky quartz grains at pressure shadows (**Figure 18A)** show that these display random orientations (**Figure 18B and C)**.

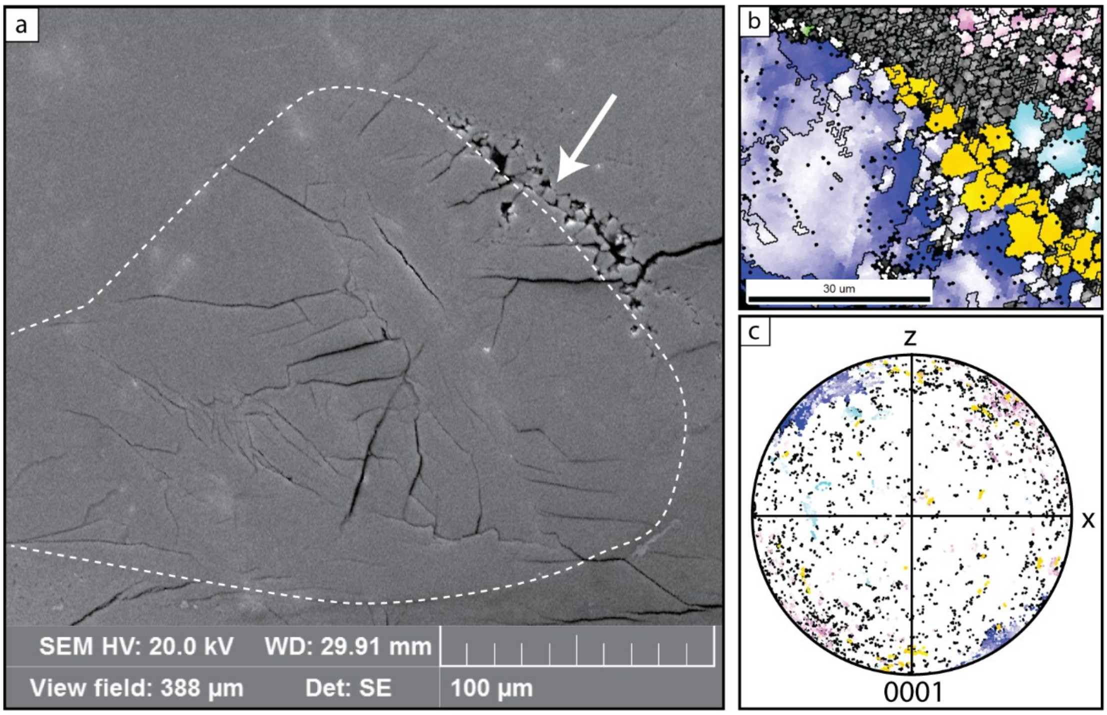

Figure 18. *Details of Brazil deformed porphyroclast. a) SEM micrograph of a porphyroclast (white dashed line) and its pressure shadow (white arrow) are highlighted. B) IQ [Image quality) from EBSD analysis with highlighted grains: blue is porphyroclast; yellow are grains at pressure shadow; light blue are grains at the transition between pressure shadow and the matrix; pink is matrix. c) Discrete pole figure (equal area) of the highlighted grains in b). The porphyroclast and the matrix show a well-defined CPO orientation. Contrarily, grains at pressure shadow and at the transition with the matrix do not display a clear CPO.*

3.5.3 Hyuga porphyroclasts and their matrix

EBSD orientation map for Hyuga material is presented in **Figure 19.** Recognizing porphyroclast limits from the surrounding matrix could be done only by comparing natural light microscope images with color coded maps. We define a relict grain (i.e. a remnant part of original porphyroclast) as a crystallographic domain of size >5 µm showing internal homogenous extinction colors and with contrasted c-axis orientations with respect to the surrounding recrystallized material. In **Figure 19D,** CPO of recrystallized porphyroclasts and matrix show analogous orientation, close to Z-axis direction while relict grains have orientations with some clusters comparable to what observed for Brazil porphyroclasts (compare **Figure 17C and Figure 19D**). Recrystallized grains in the porphyroclast are bounded by sutured grain boundaries characterized by high angles misorientations (profiles AA' and BB' in **Figure 19C** and **E**).

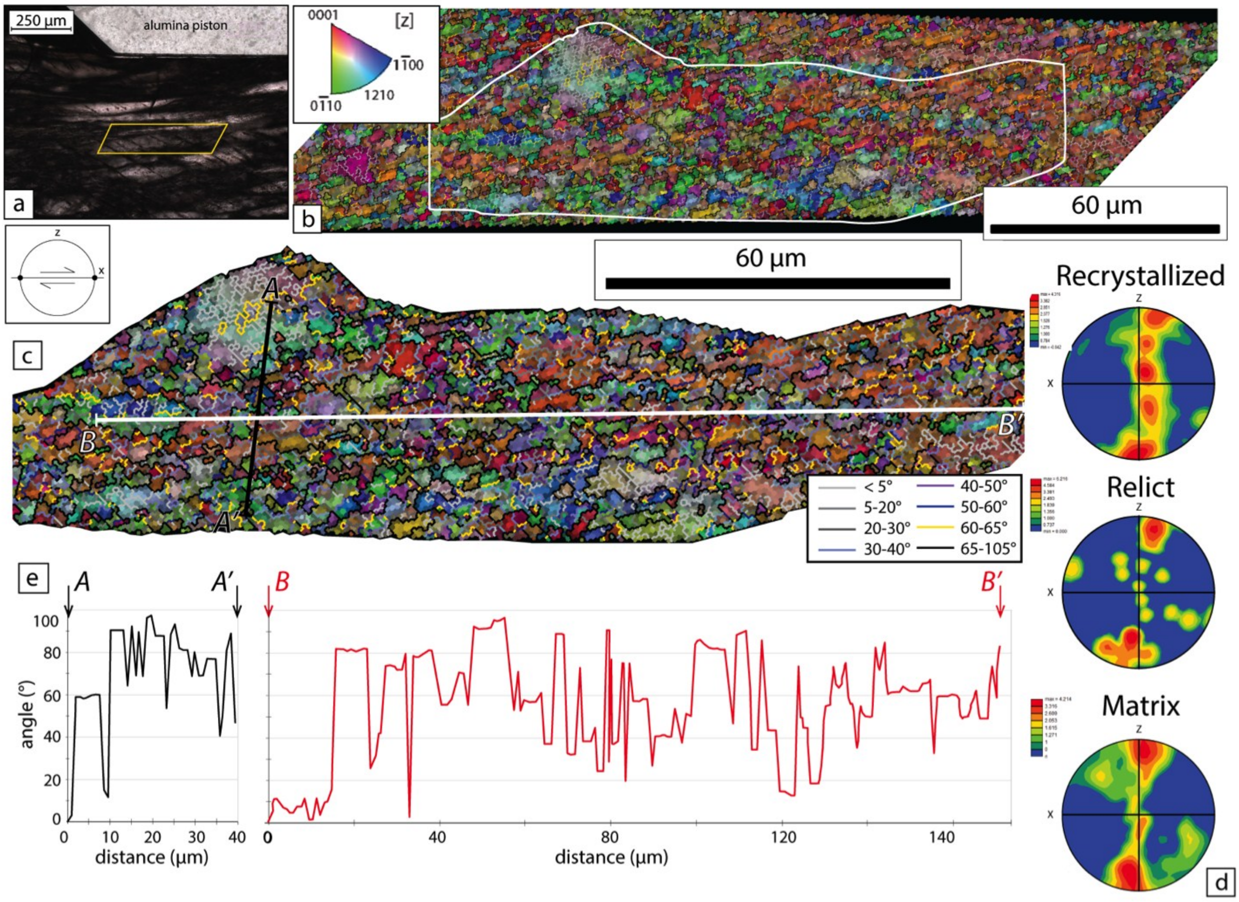

Figure 19. *Sample GP456 with 70% Hyuga porphyroclasts deformed at gamma 3.98 (see* ***Table 2****). Dextral shear sense. A) Natural light (cross-polarized) image of the EBSD area analysis. B) Inverse Pole figure and*

Confidential Index (IPF + CI) map of the porphyroclasts and the matrix. Orientation colors according to the inverse pole figure given in the upper right corner of the image. Note the presence of some large stretched zones characterized by slight differences in IPF colors corresponding to relict grains. The select zone corresponds to a porphyroclasts (close up in ***Figure 19A****). C) Cropped porphyroclast from the IPF + CI map with superposed grain boundary misorientations. Most of large domains are characterized by dominant low misorientation boundaries (light gray, <5°) and bonded by dominant higher misorientation (black > 65°) inside matrix grains. Remnant recrystallized grains show a large variability in internal misorientation angles. Misorientation angles are taken between nearest neighbor pixels. D) CPO textures for recrystallized grains, relict grains and recrystallized matrix. E) Misorientation angles profiles (not at scale) perpendicular (AA') and parallel (BB') to porphyroclasts stretching direction. Note the high angular variability in the two directions. Relict grains are generally 5-10 µm large and characterized by low misorientation angles.*

CIP analysis (**Figure 20**) of this sample reveals that quartz crystals inside shear bands have different optical orientation from the surrounding material.

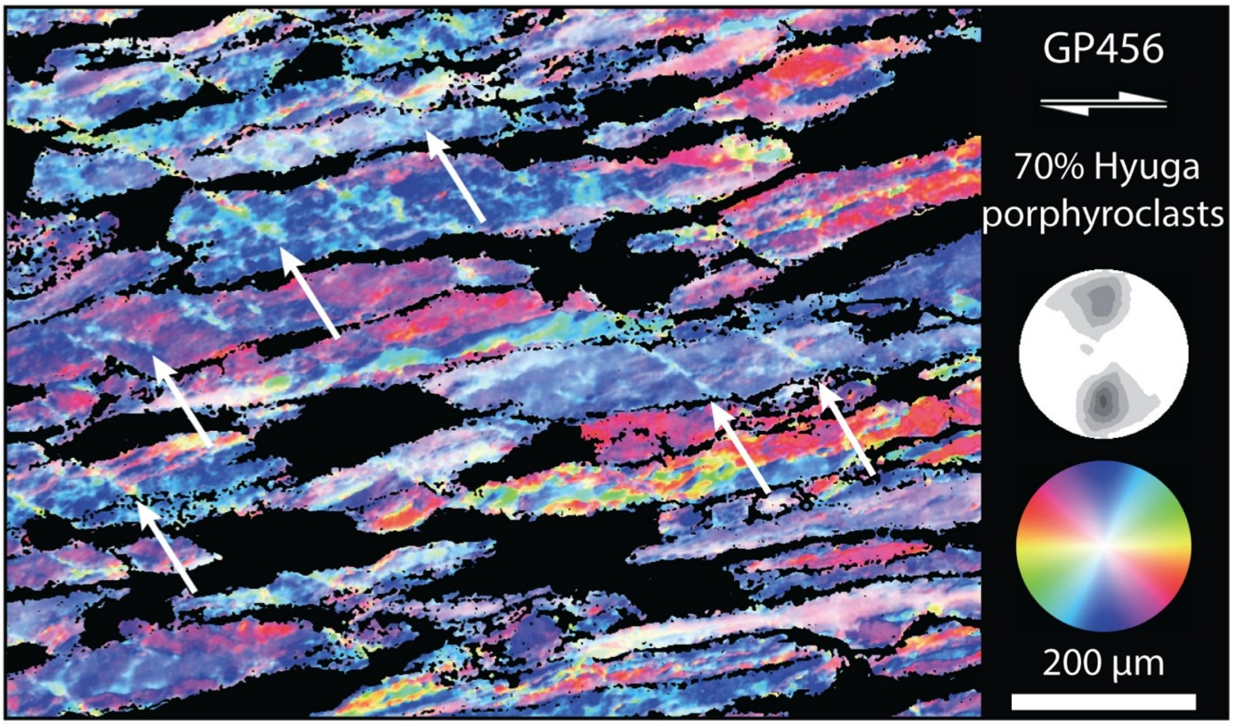

Figure 20. *CIP analysis on 70% Hyuga porphyroclasts assembly. Note shear bands dissimilar CPOs respect to surrounding porphyroclasts (white arrows).*

4 Discussion

4.1 Strength/ Mechanical Behavior

From mechanical curves, it is striking that the matrix is easy to deform than a composite assembly. This indicates that matrix alone has a low effective viscosity than when mixed with porphyroclasts, independently of their nature. This seems to indicate that water-added was enough to enhance dynamic recrystallization, otherwise it would be very strong.

Even if Hyuga quartz is extremely rich in water and thus it is supposed to be weaker than pure quartz matrix, this is not the observed trend. This aspect points out that water within Hyuga quartz is probably not immediately efficient to enhance recrystallization. The higher peak stress values may indicate that grain boundary migration play an important role in deformation and weakening happens only after the activation of this mechanism. The strain weakening behavior observed for these samples is typical for the dislocation creep regime 2 by *Hirth and Tullis* [1992] also in accord with the observed recrystallization microstructures.

Steady state is reached by the pure matrix sample and the 30% Hyuga porphyroclasts. The sample with 70% Hyuga p. nearly reaches this condition showing an inflection of the curve but only at high gamma values **Figure 3.**. This aspect probably indicates that the geometry of the assembly strongly controls the initial bulk strength of the assembly, even if the porphyroclasts are extremely reach in water. The fact that samples with dry Brazil porphyroclasts never reach steady state suggests that they behave as rigid bodies. Especially for the sample with 70% Brazil p., the high peak strength can be due to their stiffness: they act as rigid objects which try to deform in a low viscous matrix. In reason of their dry nature recrystallization is not enhanced as for Hyuga porphyroclasts. An antithetic rotation is expected for the non-recrystallized clasts in dislocation glide from a Taylor-Bishop-Hill-model and would explain the clast CPO [e.g. *Lister et al.,* 1978] oriented antithetically with respect to CPO of matrix (**Figure 17**) and to the imposed shear sense (dextral). This behavior is observed in natural clast examples [e.g. *Kilian et al.*, 2011].

We can thus assume that Brazil porphyroclasts do not deform and the surrounding matrix accommodates strain and recalculate strain rates for the samples without the whole porphyroclasts but only taking in account 5% of their size which corresponds to the recrystallized rims. These new strain rates are in the order of $2.9*10^{-5}$ s^{-1} and $1.3*10^{-5}$ s^{-1} considering 35 and the 75 % of matrix. Recalculated strain rates in the matrix are thus higher than the bulk strain rates imposed during the experiments (10^{-5} s^{-1}). Applying the empirical quartz flow law by *Hirth et al.* [2001], and the *Paterson & Luan* [1990] flow laws, we estimated the corresponding flow stress of the "new" matrix. These flow laws yield higher values of flow stress when considering the mechanically imposed strain rate (10^{-5} s^{-1}) and the same trend is observed for the new rates with the *Paterson & Luan* [1990] flow law. Contrarily, the *Hirth et al.* [2001] flow law predicts lower flow stress with respect to our results. A possible explication for this is strength/strain rate dependence may be the contribution of a grain-size sensitive process (GSS).

4.2. Paleopiezometer

Estimation of average recrystallized matrix grain size in all samples and the corresponding theoretical stress are represented with the quartz paleopiezometer [*Stipp and Tullis,* 2003] in **Figure 21** (see values reported in **Table 2**). Our results are lower than the theoretical values the predicted by the curve. This deviation can be explained by the contribution of grain-size sensitive process (GSS) which participate to lower grain size.

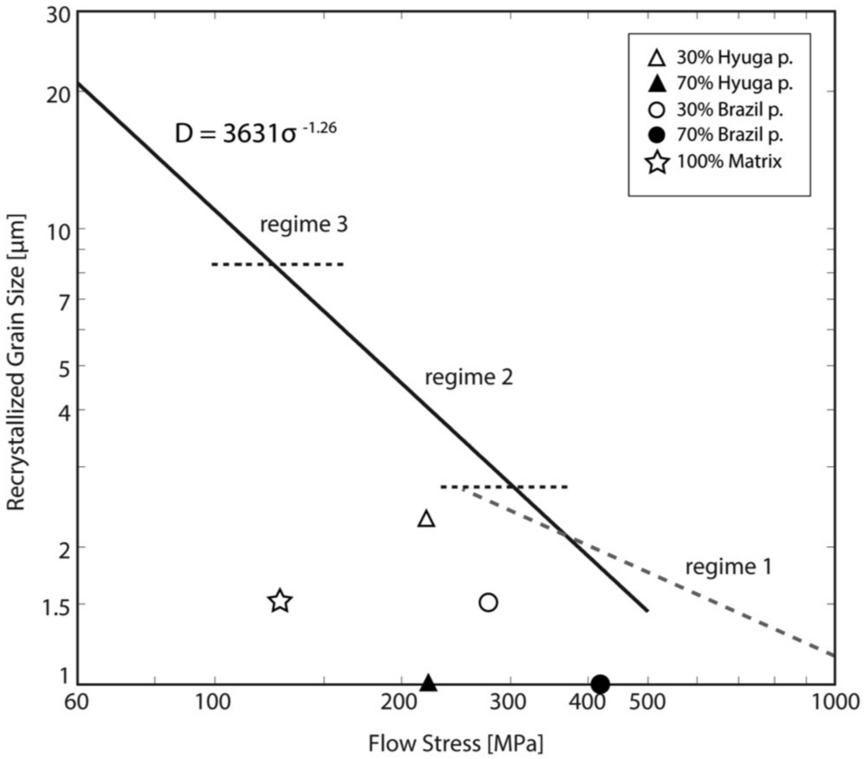

Figure 21. *Estimated grain sizes are plotted with the corresponding shear stress values on the diagram of recrystallized grain size paleopiezometer of quartz from Stipp and Tullis [2003]. The two curves represent the relationships estimated by the paleopiezometer for the Regime 1 (dashed grey line) and Regime 2 and 3 (black line) by Hirth and Tullis [1992].*

4.3 Effect of water on recrystallization

Our samples are deformed by crystal-plastic processes. The experimental paper by *Hirth and Tullis* [1992], commonly take as reference to describe quartz microstructures, is here used to get a direct comparison between our experimental results and what is expected at the applied deformation conditions. Even if both Brazil and Hyuga porphyroclasts deform at the same P and T, the intensity of recrystallization is totally different in the two materials. Dry Brazil porphyroclasts show undulose extinction and abundant deformation lamellae as typical features for the dislocation glide regime characterized by high stress deformation without much recrystallization. These elements may be indicative for submicroscopic fractures, kinks and dislocation tangles [*Hirth and Tullis,* 1992] and can be compared to microstructures observed in the dislocation creep regime 1 of *Hirth* *and Tullis* [1992]. Only at their rims the presence of small recrystallized grains suggests the onset of subgrain rotation recrystallization. Matrix CPO suggests the activation of slip on the basal <a> system [Schmidt and Casey, 1986; Law, 1990]. Deformed milky Hyuga quartz show very different microstructures. The shape of highly stretched Hyuga porphyroclasts can be compared with natural quartz aggregates deformed at mid-greenschist conditions [*Law,* 1984] or with experimentally deformed Black Hill Quarzite (BHQ) described in Regime 2 by *Hirth and Tullis,* 1992] or by *Hirth et al.* [2001]. Furthermore, these flattened grains display inner recrystallized domains indicative of transition to Regime 3. Similar microstructures, and corresponding activated slip systems, are reported also for BHQ [*Heilbronner and Tullis,* 2006] deformed at higher temperatures and higher strain rates. According to the microstructural observations and CPO, recrystallization acted by bulging and subgrain rotation. The development of common CPO for recrystallized porphyroclasts and matrix, indicates that deformation is homogenously accommodated within the whole system by the activation of the basal <a>, the rhombohedral <a> slip systems. The activation of the prismatic <a> slip system (cluster in the center of the plot) is also observed both in the porphyroclasts and in the matrix. Even if all samples were deformed in dislocation creep regime 1 at the transition with regime 2 [*Hirth and Tullis,* 1992], the resulting microstructures reflect the onset of much important recrystallization processes probably connected to the abundance of liquid-like water during deformation. Our observations further support the effect of water on enhancing microstructural development proposed by *Jaoul et al.* [1984], *Tullis and Yund* [1989] and *Hirth and Tullis* [1992].

4.4 Evolution of water

4.4.1 Water speciation

Our samples show a large set of discrete secondary absorption bands distributed between 3660 and 3300 cm^{-1} (**Figure 2** and **Figure 12**; **Table 3**). Most of these absorption bands are observed in the “as-is” Brazil/Hyuga. They have already been described in natural clear quartz and in amethyst [*Kronenberg,* 1994] or in “as-is” quartzite [e.g. Black Hill Quarzite, *Stipp et al.,* 2006]. They are generally interpreted as H-defects associated with aluminum point defects (e.g. the peak at 3382 cm^{-1}) [*Kats,* 1962*; Kronenberg et al,* 1994] or alkali (e.g. the peak at 3485 cm^{-1}) defects substituting for Si [e.g., *Kats,* 1962). The band at 3430 cm^{-1}, observed in natural quartz and citrine [*Chakraborty* *and Lehmann,* 1976] has been interpreted as alumina/alkali–H defects in the crystal lattice [*Bambauer,* 1961; *Kats,* 1962;] whereas the band at 3625 cm^{-1} has been assigned to surface Si-OH groups [*Yamagishi et al.,* 1997].

Material	Conditions	3363	3382	3430	3485	3585	3595	3625
Hyuga porphyroclasts	as is		x	x	x			x
-	Hot-pressed		x	x	x	x		x
-	Deformed		**x**			**x**	**x**	
Brazil porphyroclasts	as-is				x			
-	Deformed	**x**				**x**	**x**	
Brazil matrix in Hyuga assembly	Hot-pressed		x				x	
-	Deformed		**x**				**x**	
Brazil matrix in Brazil assembly	Deformed	**x**					**x**	

Table 3. Absorption bands and associated materials with respect to experimental deformation conditions.

At hot-pressing conditions and after deformation, only the 3382 cm^{-1} band is observed in Hyuga sample, otherwise new peaks at 3595 and 3585 cm^{-1} are detected. These latter are observed also in deformed Brazil porphyroclasts spectrum in addition to the band 3363 cm^{-1}.

The sharp absorption band at 3595 cm^{-1} is not detected in all samples but it is related only to particular contests. For example, in Hyuga porphyroclast, it is not observed at hot-press conditions, while the small but well defined peak appears after deformation (**Figure 13**). This is also observed in analysis on Brazil porphyroclasts but exclusively in recrystallized zones (**Figure 15**). Furthermore, it is useful to observe that also the FTIR spectrum of the matrix display this peak. It is important to point out that the mean water content in recrystallized porphyroclasts is strongly lowered with respect to the initial water amount (from ~2,000 ppm to ~200 ppm, see **Table 1)**. This is a striking signal of water expulsion from crystals due to recrystallization. Furthermore we have to consider that both matrix and recrystallized Hyuga porphyroclasts have grain size in the order of few microns (**Table 1**) contrary to not recrystallized/relict Brazil porphyroclasts where this peak is not detected (**Figure 15**). Thus water amount estimation we include also water stored at grain boundaries. The evidence that the band 3595 cm^{-1} is observed when grain boundaries are analyzed, yield to the hypothesis that it is the expression of a particular OH-species bonded at these structures. Grain boundaries are instable transition sites at which diffusion is orders of magnitude faster than volume diffusion inside larger grains [*Nakashima et al.,* 1995]. This is because grain boundaries may contain kinks or macro-steps interfaces [*Urai et al.,* 1986] where O-Si-O bond may be incomplete. During grain boundary migration, molecular water on the form of fluid inclusions, may be trapped at the migrating grain boundary surface [*Schmatz and Urai,* 2010] which is in constant disequilibrium, and there it can be stored and partially bonded. A possible mechanism of fluid migration is the motion of dislocations which incorporated OH-related species (maybe clusters) and release it at grain boundaries. This band was also observed by *Gleason and DeSisto* [2008] in recrystallized mylonitic quartz where grain boundaries where probably included in their measurement. The band 3595 cm^{-1} has been detected in different kinds of natural clear quartz and natural/synthetic amethyst [e.g. *Kats,* 1962; *Aines and Rossman,* 1984; *Rovetta,* 1989; *Kronenberg,* 1994], as well in natural deformed granites [*Niimi et al.,* 1999] with the general interpretation of H^{+} charge compensating for Al^{3+} substituting for Si^{4}. EMPA analysis [*Raimbourg et al.,* 2015] showed variable Al^{3+} percentage in Hyuga quartz which may find an accord with the interpretation of Niimi et al. [1999] but to confirm this point the same analysis on Brazil quartz are required.

The water related to the peak 3595 cm^{-1} is thus different from the one detected at 3625 cm^{-1} and classically assigned to surface Si-OH groups [*Yamagishi et al,* 1997].

The absorption band at 3585 cm^{-1}, observed in Hyuga hot-pressed sample, is present in both matrix and Hyuga and Brazil porphyroclasts after deformation (**Figure 11** and **12**). Despite to the fact that this band has been observed in several different materials as amethyst [*Kronenberg,* 1994, *Chakraborty and Lehmann,* 1976a), metamorphic cherts [*Ito and Nakashima,* 2002], chalcedony [*Frondel*, 1982; *Graetsch,* 1985,1987], flint [*Graetsch,* 1987], agate [*Yamagishi et al.,* 1997] and synthetic quartz [*Wood,* 1960, *Kats,* 1962, *Aines and Rossman*, 1984, *Cordier and Doukhan,* 1989; *Chakraborty and Lehmann,* 1976a; *Paterson,* 1986; *Rovetta,* 1989], its interpretation is still cloudy. One possible interpretation is the presence of H^{+} defects associated to monovalent charge substitution (e.g. Na^{+1} or Li^{+1}) [*Kats,* 1962] or structurally bonded OH-defects in quartz basal plane [*Chakraborty and Lehmann*, 1976a, b; *Pankrath,* 1991]. More recently, *Stalder and Konzett* [2012] observed a direct relationship between the increases of this band with increasing pressure (1.5 GPa) in their experiments to conclude that the band 3585 cm^{-1} corresponds to hydrogarnet defects in crystal lattice. Stünitz et al. in prep, (personal communication) find that the appearing of this band is strictly related to deformed parts of their natural single quartz crystal after deformation experiments in a Griggs apparatus. They suggest that the band 3585 cm^{-1} may record OH-defects dislocations. The systematic association between this band and deformation microstructure is also apparent in our samples. In fact this band appears in Hyuga milky quartz samples after both hot-pressing and deformation (**Figure 12A** and **13**) while in Brazil quartz it is observed only in not recrystallized porphyroclasts cores (**Figure 15**). From these observations, we think that the band 3585 cm^{-1} may record structurally bond OH-group in dislocations during plastic deformation. We propose that a new structurally OH-groups are bonded on dislocations in response to dislocation motion. A hypothesis to explain why this absorption band is not detected in the recrystallized matrix may be that OH-defects, and the dislocations bearing them, are erased along with recrystallization. OH-defects are then transferred along grain boundaries during their motion. New recrystallized grains in the matrix are thought to have low dislocation density and as consequence, low OH-defects.

Finally, the sharp absorption band at 3382 cm^{-1} and at 3363 cm^{-1} seem to be related to the nature of the starting material. The former is systematically observed in Hyuga milky quartz before and after deformation. It has been detected in gneiss [*Gleason and DeSisto*, 2008] and in cherts [*Ito and Nakashima*, 2002]. Several authors [*Kronenberg,* 1994; *Suzuki and Nakashima*, 1999; *Gleason and DeSisto*, 2008] are in accord to assign it to OH groups bonded with Al^{+3} substituting for Si. This interpretation seems also relevant in our case, where Hyuga quartz contains a large aluminum content [*Raimbourg et al.,* 2015]. Whatever, these peaks may also be related to OH-groups associated to larger defects as dislocations or grain boundaries, so that the assignment to Al^{+3} is not totally justified.

To resume, we infer that three different “kinds” of water are observed after deformation. The first one is water incorporated in porphyroclasts on the form of fluid inclusions, represented by the broad absorption band between 3800 and 3000 cm^{-1} and related to molecular water. The second type of water is stored in grain boundaries as a result of recrystallization processes and grain boundary migration. It is represented by the band at 3595 cm^{-1} corresponding to structurally bonded OH-defects at these sites. The third type of water is characterized by the band at 3585 cm^{-1} and probably due to OH-defects on dislocations. The OH-defects have been probably incorporated through well oriented nanometer scale micro-fractures which have been erased during deformation.

4.4.2 Mechanisms of water incorporation and expulsion

As observed in IR spectrum the dry Brazil and the hydrated Hyuga quartz show two opposite trends regarding water concentration in the crystal during deformation.

Dry Brazil porphyroclasts show very moderate water incorporation (**Table 1, Figure 11c**) after deformation. This allow to speculate about possible ways to incorporate water into quartz. Two main mechanisms are generally proposed to explain water absorption, these are micro-fracturing and water diffusion. Micro-fracturing is considered to be the most efficient natural process which can operate in several geological contests, from low [*Palazzin et al.,* submitted] to high metamorphic conditions [*Kronenberg,* 1994]. Also at laboratory scale, micro-fracturing seems to play the key role for water incorporation [*Kronenberg et al.,* 1986, *Gerretsen et al.,* 1989] because water diffusion through the crystal is not rapid enough to enable significant incorporation at the experimental scale [*Kronenberg*, 1986]. *Rovetta et al.* [1989] proposed that at high controlled H_2 fugacity (e.g. hematite-magnetite buffered), the mechanism of OH uptake is 2-3 order magnitudes more efficient than at unbuffered conditions. Without any evidences of micro-cracks, they proposed that hydrogen diffusion and its reaction with lattice oxygen may be the best way to produce new hydroxyl defects into quartz (hydrogarnet). However micro cracks are very difficult to detect when they are healed and it is well known that fluid inclusions decrepitate during increasing of pressure and temperature [*Tarantola et al.,* 2010].

During our experiments, we do not buffered the system, so the fast hydrogen diffusion is probably not the process responsible for water uptake. Furthermore, the H solubility in quartz has been estimated to be very low ($<100\ H/10^6Si$, i.e. <15 ppm) thus to render difficult to believe that hydrogen may be responsible for the large water quantities detected in our samples. The mean water quantity of ~40 ppm (corresponding to $258\ H/10^6\ Si$) within Brazil porphyroclast are however considerably higher than their initial H_2O content and much higher than the equilibrium solubility of water in quartz ($<100\ H/10^6\ Si$) [*Paterson,* 1986]. Our FTIR measurements are made on fluid-inclusions free-zones in porphyroclasts and if fluid inclusions are existing, they are not visible at high microscopic magnification. No micro-fractures are observed in porphyroclasts cores but we cannot exclude that they were present during the initial stages of deformation. Deformation lamellae and undulatory extinction (**Figure 6B, Figure 7E** and **Figure 9A** and **B**) are otherwise typically observed. The presence of dislocation lamellae and the low misorientation angles observed in the EBSD map (**Figure 17B**) are indicative of dislocation glide and may create favorable conditions at which water can be stored on the form of OH-defects. The signature of these OH-related defects may correspond to the sharp absorption band at 3585 cm^{-1}.

Contrarily, in milky Hyuga quartz, water is progressively expulsed from the crystals, already during the "hot-pressed" and again during deformation conditions (**Figure 12B**). In the "hot-pressed" sample water content is lower than in the "as-is" samples but no recrystallization features are observed (**Figure 2C)**. At these conditions, fluid inclusions cannot be carried outside the grains via grain boundary migration and liquid-like water has to be expulsed via another mechanisms, most likely micro-fracturing [*Tarantola et al.,* 2010] Contrarily, during deformation, the mechanism responsible for intragranular water expulsion is dynamic recrystallization by grain boundary migration The important modifications that grain boundary mobility may have on volume and distribution of fluid inclusions [*Olgaard and FitzGerald,* 1993; *Schmatz et al.,* 2011] is strongly supported by the evidences that, after recrystallization, the abundance of fluid inclusions is strongly lowered in recrystallized porphyroclasts (in agreement with the broad absorption band height decrease). Water expulsion is interpreted as the migration of fluid inclusions from porphyroclast cores to newly-formed grain boundaries. The weakening behavior registered by mechanical curves after the peak stress (**Figure 3**) corresponds probably to the inset of grain boundary migration. Before water is not available because still trapped inside porphyroclasts. We can infer that water-added in the matrix plays only a secondary role in weakening: the major role of lubricant able to enhance dynamic recrystallization is attributable to intragranular water. A direct consequence of this large water contribution is the filling of the existent porosity and C' shear bands.

4.4.3 Water budget

H_2O amounts in matrix and in Hyuga porphyroclasts in the deformed sample (**Figure 14** and **Table 1**) converge to very similar values. This point seems to indicate that for the estimated average grain size of ~2.5 μm, only a certain water volume can be kept at grain boundaries, this amount is in between 220-260 ppm. The corresponding grain boundary thickness is probably in the range of 0.5 nm [*Ito and Nakashima*, 2002]. Although 1–10 nm is generally accepted value for grain boundary thickness [*Farver and Yund*, 1991], similar width are proposed by *Hiraga et al.* [1999] in natural mylonite. Moreover, we estimate that much large water amounts should be present in the sample because the initial water content inside porphyroclasts was ~1 order magnitude larger than after deformation. This yield to infer that the "exceeding" water has be released (not bonded/stored) and consequently has been driven in C' shear zones. The mutual water amount of ~220-280 ppm (which is comprehensive of water within recrystallized grains and at grain boundaries) shown in **Figure 14**, may corresponds to the saturation capacity which can be stored at grain boundaries under these conditions. This "saturation" value is not reached in samples with dry Brazil porphyroclasts where initial water amount (**Figure 2D** and **Figure 12C)** was initially low.

4.5. C' shear bands development

C' shear zones are observed in experiments where hydrated Hyuga porphyroclasts were employed. Other deformational studies on quartz aggregates describe an isotropic reorganization of water in planes oriented parallel to or in C' planes at about 25° from the shear zone boundaries [e.g. *Den Brock et al.,* 1994, *Schmocker et al.,* 2003]. A possible scenario of the formation of these microstructures is proposed making the assumption that the system was closed with respect to water throughout sample preparation (including welding) and deformation. At the beginning of each experiment, water added to the matrix is homogeneously distributed in the sample, partly filling pores at triple junctions as well as some grain boundaries. During pressurization, porosity is reduced by compaction and frictional grain boundary sliding. In the case of Hyuga porphyroclasts, fluid inclusions probably start to decrepitate in smaller ones and water is are added to the matrix. With the onset of deformation, two main processes take place. Porosity tends to decrease in response to shearing and thinning of the sample. At the same time, the onset of dynamic recrystallization causes grain boundary migration and liberation of fluid inclusions in the system. This causes local fluid overpressure in the matrix with local development of dilatant pores. As only a certain water quantity can be stored at grain boundaries, this water surplus migrates in preferential pathways corresponding to C' shear bands, favorably oriented with respect to major stress axis. In these free-fluid "reservoirs" small quartz grains with equant shape are found (**Figure 10**). These grains may be indicative of the activation of a fluid assisted process, like pressure solution. An interesting analogy can be made with samples with Brazil porphyroclasts: water amount in the system is not higher enough to lead the formation of C' shear bands but the exceeding water is stored at pressure shadows (**Figure 9**). The blocky grains at these sites develop random CPO (**Figure 18B and C**). As pointed out previously, FTIR estimation of bulk water amount in our samples are really lower than water amount supposed to be inside the system. Shear bands thus represent a kind of “reservoir” of excess of fluids but they are not responsible for any mechanical weakening because they are not interconnected.

5. Conclusion

In this experimental study we present five shear deformation experiments performed at T=800°C, gamma rate=10^{-5} s^{-1} and Pc=1.5 GPa, on quartz aggregates of different nature, in order to evaluate the effect of water on rheological properties and recrystallization, and the evolution in water speciation and distribution in the crystal along with strain.

From these results we propose several conclusions:

- the intragranular water on the form of fluid inclusions in hydrated Hyuga quartz is responsible for the activation of recrystallization by subgrain rotation and grain boundary migration.
- the changes in the physicochemical states of water in response to recrystallization are expressed by the secondary absorption bands at 3585 cm^{-1} and 3595 cm^{-1}.
- water is incorporated in undeformed Brazil cores probably by micro-fractures and the stored at dislocations tips.
- the weakening behavior of dry Brazil quartz is not reached with our experimental conditions but we demonstrate that water can be incorporated within grains, probably by micro cracking.
- grain-size sensitive processes probably participate to dislocation creep.
- exceeding water which is not consumed by recrystallization is stored in C’ shear planes or at pressure shadows.

Acknoledgment

This work has received funding from (i) the European Research Council (ERC) under the seventh Framework Program of the European Union (ERC Advanced Grant, grant agreement No 290864, RHEOLITH) and (ii) the Labex VOLTAIRE (ANR-10-LABX-100-01). Great thanks to S. Janiec and G. Badin for thin and thick sections preparation, I. Di Carlo and J. Precigout for help in EBSD analysis, R. Heilbronner, S. Marti and B. Richter for their grateful help in CIP and mechanical data processing.

References

Aines, R.D., Rossman, G.R., 1984. Water in minerals? A peak in the infrared. J. Geophys. Res. Solid Earth 89, 4059–4071. doi:10.1029/JB089iB06p04059.

Bambauer, H.U., Brunner, G.O., Laves, F., 1961. Beobachtungen über Lamellenbau an Bergkristallen. Z. Für Krist. 116, 173.

Blacic, J. D., Christie, J. M., 1984. Plasticity and hydrolytic weakening of quartz single crystals, J. Geophys. Res. Solid Earth, 89(B6), 4223–4239.

Chakraborty, D., Lehmann, G., 1976a. On the structures and orientations of hydrogen defects in natural and synthetic quartz crystals. Phys. Status Solidi A 34, 467–474. doi:10.1002/pssa.2210340206.

Chakraborty, D., Lehmann, G., 1976b. Distribution of OH in synthetic and natural quartz crystals. J. Solid State Chem. 17, 305–311. doi:10.1016/0022-4596(76)90136-5.

Christie, J. M., Griggs D. T., Carter N. L., 1964b. Experimental evidence of basal slip in quartz. J. Geol., 734–756.

Cordier, P., Doukhan, J.-C., 1989. Water solubility in quartz and its influence on ductility. Eur. J. Mineral., 221–238.

den Brok, B., Meinecke, J., Röller, K., 1994. Fourier transform IR-determination of intragranular water content in quartzites experimentally deformed with and without added water in the ductile deformation field. J. Geophys. Res. Solid Earth 99, 19821–19828. doi:10.1029/94JB01473.

Farver, J.R., Yund, R.A., 1991. Oxygen fugacity in quartz: dependence on temperature and water fugacity. Chem. Geol. 90, 55–70.

Frondel, C., 1982. Structural hydroxyl in chalcedony (type B quartz), Am. Mineral 67, 1248–1257.

FitzGerald, J.D.F., Boland, J.N., McLaren, A.C., Ord, A., Hobbs, B.E., 1991. Microstructures in water-weakened single crystals of quartz. J. Geophys. Res. Solid Earth 96, 2139–2155. doi:10.1029/90JB02190.

Gerretsen, J., Paterson, M. S., McLaren, A. C., 1989. The uptake and solubility of water in quartz at elevated pressure and temperature, Phys. Chem. Miner., 16(4), 334–342.

Gleason, G.C., DeSisto, S., 2008. A natural example of crystal-plastic deformation enhancing the incorporation of water into quartz. Tectonophysics 446, 16–30. doi:10.1016/j.tecto.2007.09.006.

Graetsch, H., Flörke, O.W., Miehe, G., 1985. The nature of water in chalcedony and opal-C from brazilian agate geodes. Phys. Chem. Miner. 12, 300–306. doi:10.1007/BF00310343.

Graetsch, H., Flörke, O.W., Miehe, G., 1987. Structural defects in microcrystalline silica. Phys. Chem. Miner. 14, 249–257. doi:10.1007/BF00307990.

Griggs, D.T., Blacic, J.D., 1965. Quartz: Anomalous Weakness of Synthetic Crystals. Science 292.

Griggs, D., 1967. Hydrolytic Weakening of Quartz and Other Silicates. Geophys. J. R. Astron. Soc. 14, 19–31. doi:10.1111/j.1365-246X.1967.tb06218.x.

Hanmer, S., 1984b. The potential use of planar and elliptical structures as indicators of strain regime and kinematics of tectonic flow. Geol Surv Can Pap 84:133–142.

Heilbronner, R. P., Pauli, C., 1993. Integrated spatial and orientation analysis of quartz c-axes by computer-aided microscopy, J. Struct. Geol., 15, 369–382.

Heilbronner, R., Tullis, J., 2006. Evolution of c axis pole figures and grain size during dynamic recrystallization: Results from experimentally sheared quartzite. J. Geophys. Res. Solid Earth 111, B10202. doi:10.1029/2005JB004194.

Hiraga, T., Nagase, T., Akizuki, M., 1999. The structure of grain boundaries in granite-origin ultramylonite studied by high-resolution electron microscopy. Phys. Chem. Miner. 26, 617–623.

Hirth, G., Tullis, J., 1992. Dislocation creep regimes in quartz aggregates. J. Struct. Geol. 14, 145–159. doi:10.1016/0191-8141(92)90053-Y.

Hirth, G., Teyssier, C., Dunlap, J.W., 2001. An evaluation of quartzite flow laws based on comparisons between experimentally and naturally deformed rocks. Int. J. Earth Sci. 90, 77–87. doi:10.1007/s005310000152.

Hooper, R.J., Hatcher, R.D., 1988. Mylonites from the Towaliga fault zone, central Georgia: products of heterogeneous non-coaxial deformation. Tectonophysics 152:1–17.

Ito, Y., Nakashima, S., 2002. Water distribution in low-grade siliceous metamorphic rocks by micro-FTIR and its relation to grain size: a case from the Kanto Mountain region, Japan. Chem. Geol. 189, 1–18. doi:10.1016/S0009-2541(02)00022-0.

Jaoul, O., Tullis, J., Kronenberg, A., 1984. The effect of varying water contents on the creep behavior of Heavitree quartzite. J. Geophys. Res. Solid Earth 89, 4298–4312. doi:10.1029/JB089iB06p04298

Kats, A. (1961), Hydrogen in alpha-quartz, TU Delft, Delft University of Technology.

Kekulawala, K. R. S. S., Paterson, M. S., Boland, J. N., 1978. Hydrolytic weakening in quartz, Tectonophysics, 46, T1 – T6.

Kekulawala, K. R. S. S., Paterson, M. S., Boland, J. N., 1981. An experimental study of the role of water in quartz deformation, Mech. Behav. crustal rocks Handin Vol., 49–60.

Kilian, R., Heilbronner, R., Stünitz, H., 2011. Quartz grain size reduction in a granitoid rock and the transition from dislocation to diffusion creep. J. Struct. Geol. 33, 1265–1284. doi:10.1016/j.jsg.2011.05.004.

Kronenberg, A.K., Tullis, J., 1984. Flow strengths of quartz aggregates: Grain size and pressure effects due to hydrolytic weakening. J. Geophys. Res. Solid Earth 89, 4281–4297. doi:10.1029/JB089iB06p04281.

Kronenberg, A. K., Kirby, S. H., Aines, R. D., and Rossman, G. R., 1986. Solubility and diffusional uptake of hydrogen in quartz at high water pressures: implications for hydrolytic weakening, J. Geophys. Res. Solid Earth, 91(B12), 12723–12741.

Kronenberg, A.K., Segall, P., Wolf, G.H., 1990. Hydrolytic weakening and penetrative deformation within a natural shear zone. Geophys. Monogr. 56, 21–36.

Kronenberg, A.K., 1994. Hydrogen speciation and chemical weakening of quartz. Rev. Mineral. Geochem. 29, 123–176.

Law, R.D., Knipe, R.J., Dayan, H., 1984. Strain path partitioning within thrust sheets: microstructural and petrofabric evidence from the Moine Thrust zone at Loch Eriboll, northwest Scotland. J. Struct. Geol. 6, 477–497. doi:10.1016/0191-8141(84)90060-9.

Law, R.D., 1990. Crystallographic fabrics: a selective review of their applications to research in structural geology. Geol. Soc. Lond. Spec. Publ. 54, 335–352. doi:10.1144/GSL.SP.1990.054.01.30.

Lister, G., Paterson, M., Hobbs, B., 1978. Simulation of fabric development in plastic deformation and its application to quartzite e Model. Tectonophysics 45 (2e3), 107e158.

Lloyd, G.E., Freeman, B., 1994. Dynamic recrystallization of quartz under greenschist conditions. J. Struct. Geol. 16, 867–881. doi:10.1016/0191-8141(94)90151-1.

McLaren, A. C., Gerald, J. D., Gerretsen, J., 1989. Dislocation nucleation and multiplication in synthetic quartz: relevance to water weakening, Phys. Chem. Miner., 16(5), 465–482.

Nakashima, S., H. Matayoshi, T. Yuko, K. Michibayashi, T. Masuda, N. Kuroki, H. Yamagishi, Y. Ito, Nakamura, A., 1995. Infrared microspectroscopy analysis of water distribution in deformed and metamorphosed rocks, Tectonophysics, 245(3), 263–276.

Niimi, N., Aikawa, A., Shinoda, K., 1999. The infrared absorption band at 3596 cm-1 of the recrystallized quartz from Mt. Takamiyama, southwest Japan. Mineralogial Magazine 63, 693–701.

Olgaard, D.L., Fitz Gerald, J.D., 1993. Evolution of pore microstructures during healing of grain boundaries in synthetic calcite rocks. Contrib. Mineral. Petrol. 115, 138–154.

Palazzin, G., Raimbourg, H., Famin, V., Jolivet, L., Kusaba, Y., Yamaguchi, A., 2016. Deformation processes at the down-dip limit of the seismogenic zone: the example of Shimanto accretionary complex. Tectonophysics. Pankrath, R., 1991. Polarized IR spectra of synthetic smoky quartz. Phys. Chem. Miner. 17. doi:10.1007/BF00202238.

Passchier, C.W., Simpson, C., 1986. Porphyroclast systems as kinematic indicators. J Struct Geol 8:831–844.

Paterson, M. S., 1986. The thermodynamics of water in quartz, Phys. Chem. Miner., 13(4), 245–255.

Paterson, M.S., Luan, F.C., 1990. Quartzite rheology under geological conditions. Geol. Soc. Lond. Spec. Publ. 54, 299–307. doi:10.1144/GSL.SP.1990.054.01.26.

Post, A., Tullis, J., 1998. The rate of water penetration in experimentally deformed quartzite: implications for hydrolytic weakening. Tectonophysics 295, 117–137. doi:10.1016/S0040-1951(98)00145-0.

Raimbourg, H., Augier, R., Famin, V., Gadenne, L., Palazzin, G., Yamaguchi, A., Kimura, G., 2014. Long-term evolution of an accretionary prism: The case study of the Shimanto Belt, Kyushu, Japan. Tectonics 33, 2013TC003412. doi:10.1002/2013TC003412.

Raimbourg, H., Vacelet, M., Ramboz, C., Famin, V., Augier, R., Palazzin, G., Yamaguchi, A., Kimura, G., 2015. Fluid circulation in the depths of accretionary prisms: an example of the Shimanto Belt, Kyushu, Japan. Tectonophysics. doi:10.1016/j.tecto.2015.05.023.

Rovetta, M.R., 1989. Experimental and spectroscopic constraints on the solubility of hydroxyl in quartz. Phys. Earth Planet. Inter. 55, 326–334. doi:10.1016/0031-9201(89)90080-0.

Schmatz, J., Urai, J.L., 2010. The interaction of fluid inclusions and migrating grain boundaries in a rock analogue: deformation and annealing of polycrystalline camphor-ethanol mixtures. J. Metamorph. Geol. 28, 1–18. doi:10.1111/j.1525-1314.2009.00849.x.

Schmatz, J., Schenk, O., Urai, J.L., 2011. The interaction of migrating grain boundaries with fluid inclusions in rock analogues: the effect of wetting angle and fluid inclusion velocity. Contrib. Mineral. Petrol. 162, 193–208. doi:10.1007/s00410-010-0590-3.

Schmid, S.M., Casey, M., 1986. Complete fabric analysis of some commonly observed quartz C-axis patterns. In: Hobbs, B.E., Heard, H.C. (Eds.), Mineral and Rock Deformation: Laboratory Studies. American Geophysical Union Monograph, vol. 36, pp. 263–286.

Schmocker, M., Bystricky, M., Kunze, K., Burlini, L., Stünitz, H., Burg, J.-P., 2003. Granular flow and Riedel band formation in water-rich quartz aggregates experimentally deformed in torsion. J. Geophys. Res. Solid Earth 108, 2242. doi:10.1029/2002JB001958

Stalder, R., Konzett, J., 2012. OH defects in quartz in the system quartz–albite–water and granite–water between 5 and 25 kbar. Phys. Chem. Miner. 39, 817–827. doi:10.1007/s00269-012-0537-5.

Stipp, M., Tullis, J., 2003. The recrystallized grain size piezometer for quartz. Geophys. Res. Lett. 30, 2088. doi:10.1029/2003GL018444.

Stipp, M., Tullis, J., Behrens, H., 2006. Effect of water on the dislocation creep microstructure and flow stress of quartz and implications for the recrystallized grain size piezometer. J. Geophys. Res. Solid Earth 111, B04201. doi:10.1029/2005JB003852;

Stolper, E., 1982. The speciation of water in silicate melts. Geochim. Cosmochim. Acta 46, 2609–2620. doi:10.1016/0016-7037(82)90381-7.

Stünitz, H., Thust, A., Heilbronner, R., in prep. Water redistribution in experimentally deformed natural quartz single crystals – implications for H_2O-weakening processes

Suzuki, S., Nakashima, S., 1999. In-situ IR measurements of OH species in quartz at high temperatures. Phys. Chem. Miner. 26, 217–225. doi:10.1007/s002690050180.

Tarantola, A., Diamond, L.W., Stünitz, H., 2010. Modification of fluid inclusions in quartz by deviatoric stress I: experimentally induced changes in inclusion shapes and microstructures. Contrib. Mineral. Petrol. 160, 825–843. doi:10.1007/s00410-010-0509-z.

Tullis, J., Yund, R.A., 1989. Hydrolytic weakening of quartz aggregates: The effects of water and pressure on recovery. Geophys. Res. Lett. 16, 1343–1346. doi:10.1029/GL016i011p01343.

Urai, J.L., Means, W.D., Lister, G.S., 1986. Dynamic recrystallization of minerals, in: Hobbs, B.E., Heard, H.C. (Eds.), Geophysical Monograph Series. American Geophysical Union, Washington, D. C., pp. 161–199.

Yamagishi, H., Nakashima, S., Ito, Y., 1997. High temperature infrared spectra of hydrous microcrystalline quartz. Phys. Chem. Miner. 24, 66–74. doi:10.1007/s002690050018.

CHAPTER IV

Discussion

General discussion: the role of quartz at the brittle ductile transition

1. Quartz plasticity at low temperature

The Hyuga Tectonic Mélange and the Foliated Morotsuka are two metasedimentary units deformed at conditions close to the brittle-ductile transition. These two units show several microstructures indicative of the activation of quartz low-temperature plasticity. An example are the presence of undulose extinction as well as the sutured grain boundaries associated to new recrystallized subgrains.

Evidences for dislocation creep in low metamorphic grade rocks are usually observed at about 350°C [e.g. *Scholz,* 1998] or ~300°C in the case of mylonites deformed at geologically very low shear strain rates (10^{-14} s^{-1}) [e.g. *Stockert,* 1999]. The temperatures recorded by the Hyuga Tectonic Mélange are significantly lower, of the order of 250+/-30°C (**Ref. Chapter II**), pointing to possibility of the activation of quartz plasticity at very low temperatures in subduction zones.

From experimental works on quartz [e.g. *Hirth and Tullis,* 1992] we know that mineral plasticity can be enhanced at very high stress, very low strain rate or the presence of water. The shear stress estimation at modern plate boundaries, evaluated with several methods [e.g. *Peacock*, 1996; *Hasegawa et al.,* 2012] indicate that slip occurs under very low values (~10-35 MPa) of shear stresses. We thus exclude that high shear stress could be responsible for dislocation creep inception in Hyuga Tectonic Mélange and Foliated Morotsuka. Very low strain rates are similarly unlikely near the plate interface (our estimates in Hyuga Tectonic Mélange are in the range of ~10^{-11} s^{-1}, see **Chapter 2 Section 4.2**) [e.g. *Maruyama and Send,* 1986].

The most likely explanation for the observed low temperature quartz plasticity in the Hyuga and Foliated Morotsuka is the abundance of molecular water. Water, in the form of fluid inclusions, is observed in a large spectrum of quartz-rich rocks, including quarzites and granites. The compilation by *Kronenberg and Wolf* [1990], to which we added our measurements and values from *Ito and Nakashima* [2002], provides information about water contents in quarzitic rocks.

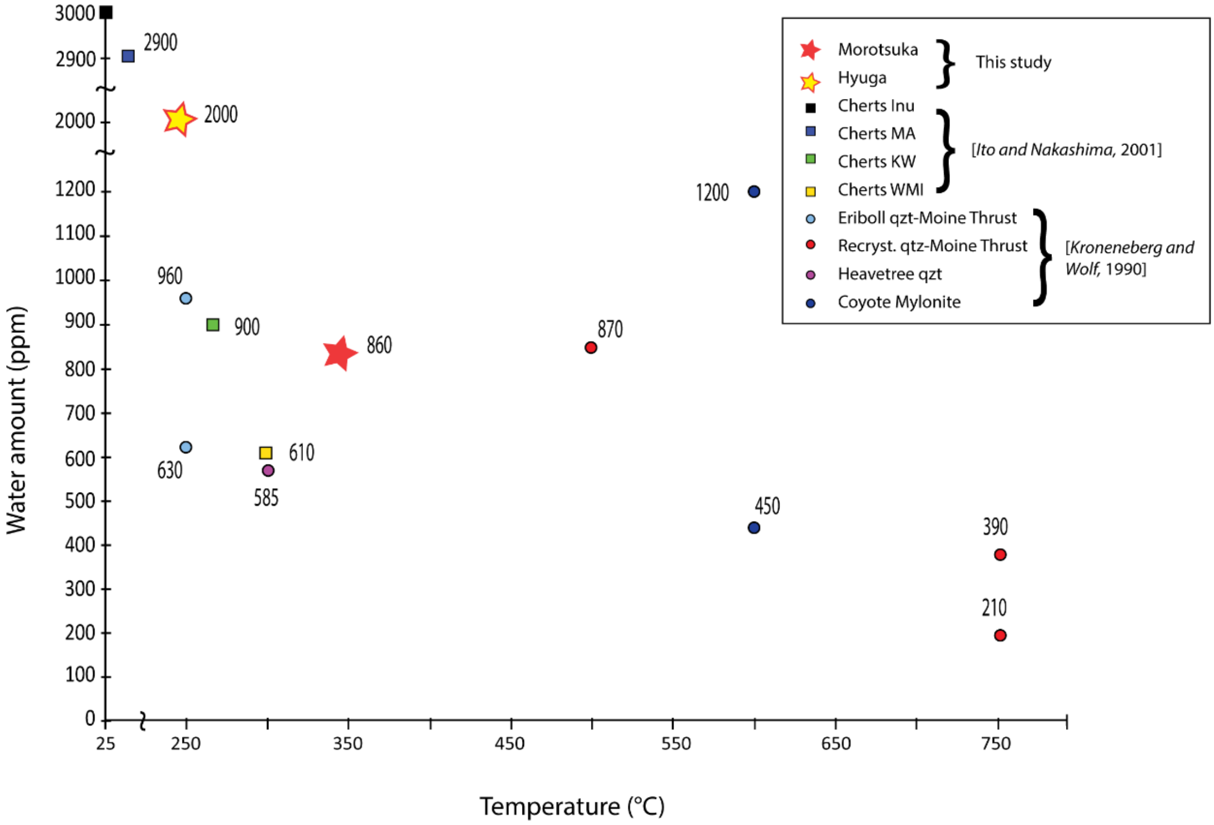

***Figure 1**. Water distribution and corresponding deformation temperatures in natural samples of various origin: hydrothermal quartz (this study), cherts [Ito and Nakashima, 2001], quartzite and granites [Kronenberg and Wolf 1990]. Note the gaps in x- and y-scales.*

A general decrease of water amount is also observed with respect to increasing metamorphic grade [e.g. *Nakashima*, 1995]. We also observe that the lowest values of water at high temperatures are higher than 220 ppm (**figure 1**). The way by which molecular water may have effect on strength is not entirely understood but some models [e.g. *McLaren et al.,* 1983; *Gerretsen et al.,* 1987] invoke the role of fluid inclusions in promoting nucleation of dislocation and the consequent activation of dislocation motion to reduce shear strength.

Water-rich rocks at plate-boundaries interface are probably a good natural example to illustrate that low wt. % of water may have a direct effect on quartz strength as it has been observed in quartz deformational experiments [*Hirth and Tullis*, 1992]. From our microstructural observations on deformed quartz in the two low-grade metasedimentary units, it appears that the large amount of water, on the form of fluid inclusions, may be responsible for the activation of plasticity.

Other examples of quartz low-grade plasticity in plate-boundary rocks have been reported in literature as, for example, in the tectonic mélanges of the Kodiak Formation [e.g. *Meneghini et al.,* 2009; *Fisher and Brantley,* 2014]. These rocks, very rich in quartz veins, are good examples of the large fluids circulation at plate interface (see *Fisher and Brantley* [1992; 2014] for detailed description), but almost no information about water quantities the quartz have been provided.

To better constrain the physical processes acting at plate interface and thus provide information about plate-boundary strength at depth of the brittle-ductile transition, additional information about quartz microstructures and estimations of water amount of several tectonic mélanges are probably needed.

2. Pressure solution and seismic manifestation: slow slip events

Pore-fluid pressure has been invoked as a mechanism to explain the apparent low shear stresses along plate interfaces [*Davis et al.,* 1983; *Rice,* 1992]. In fact, pore-fluid pressure can counteract normal stress and exerts a direct control on the mechanical response of sediments [*e.g. Davis et al.,* 1983; *Hubbert and Rubey,* 1959a, b]. Slow-slip events and tremors observed in the last decade in worldwide seismogenic zones [*Schwartz and Robowsky,* 2007] have thus been associated to the presence of excessive pore pressure [*e.g. Ito and Obara,* 2006b*; Liu and Rice,* 2007*; Fagereng and Ellis*, 2009] at depth corresponding to the brittle-ductile transition. A possible way to interpret these slow slip event resides in the observation of microstructures developed at such conditions.

Quartz slicken-fibers along shear planes in Hyuga Tectonic Mélange grew as a result of successive micro-fracturing events as attested by the presence of micro-veins and fluid inclusion trails. The interpretation of micro-cracking is bivalent: several authors propose that crack-seal veinlets may be the result of i) micro-seismic behavior by rapid slip, or ii) nearly continuous aseismic fault creep by continuous opening [*Gaviglio,*1986*; Davison,*1995*; Lee and Wiltschko,* 1999]. An intermediate solution is proposed by *Gratier et al.* [1993] who observed that along the same fault, aseismic vs seismic behavior is expressed by coated slicken-fibers in different manners. Euhedral fractured fibers may be the result of imposed high rates at which pressure solution creep is not efficient to ensure slip. In this case, strength rises and cataclasis is produced. After the seismic energy release, the rate of deformation is as slow as needed for pressure solution creep and continuous mineral fibers can develop.

Quartz ribbons in Hyuga tectonic mélange are composed by single superposed crystals which grew by several stages of continuous micro-cracking followed by immediate healing by quartz deposition. Quartz ribbons are therefore slicken-fibers which developed by little increments along shear planes. It is thus reasonable to associate the time needed to fill fractures to the time scales required to slip along the shear plane. Based on the calculation proposed by *Fisher and Brantley* [1992, 2014] we estimated the critical time required to seal the described shear veins. These predictions are based on the assumption that silica diffusion is the dominant transport mechanism for temperature and pressure conditions corresponding to that of Hyuga Tectonic Mélange as evidenced by experimental results [*Gratier et al.,* 2009].

$$t = 2\,x\,10^{-16}\,\frac{\emptyset^3}{k^2}\frac{D^2}{\Delta P^2} \qquad \textbf{(eq. 1)}$$

The critical time is expressed by the constant $2\,x\,10^{-16}$ [*Fisher and Brantley*, 1992; 2014]. Porosity $\emptyset$ has been chosen of 1% as best representative for porosity of underthrusted sediments close to the décollement surface [e.g. *Screaton et al.,* 2002]. *k* is the permeability of the matrix (10^{-21} m^{-2}) in agreement with permeability estimated for underthrusted sediments [*e.g. Skarbek and Saffer,* 2009; *Gamage and Screaton,* 2006]. ΔP is the pressure drop along the flow path (Pa) and is estimated as the viscous flow of a fluid around a rigid spherical inclusion [e.g. *Lamb,* 1932] and corresponds to about 5 times the value of shear strength at plate interface [*Fisher and Brantley*, 1992]. Finally D is the crack spacing (m) which in our case corresponds to the mean distance between shear planes: these values, reported in **Chapter 2 section 4.2**, varies between 1 mm and 500 µm. The critical time needed to fill shear planes with the characteristic quartz ribbons at shear strengths of plate interface somehow coincides better with Non Volcanic Tremors durations (**Figure 2**) rather than with earthquakes duration.

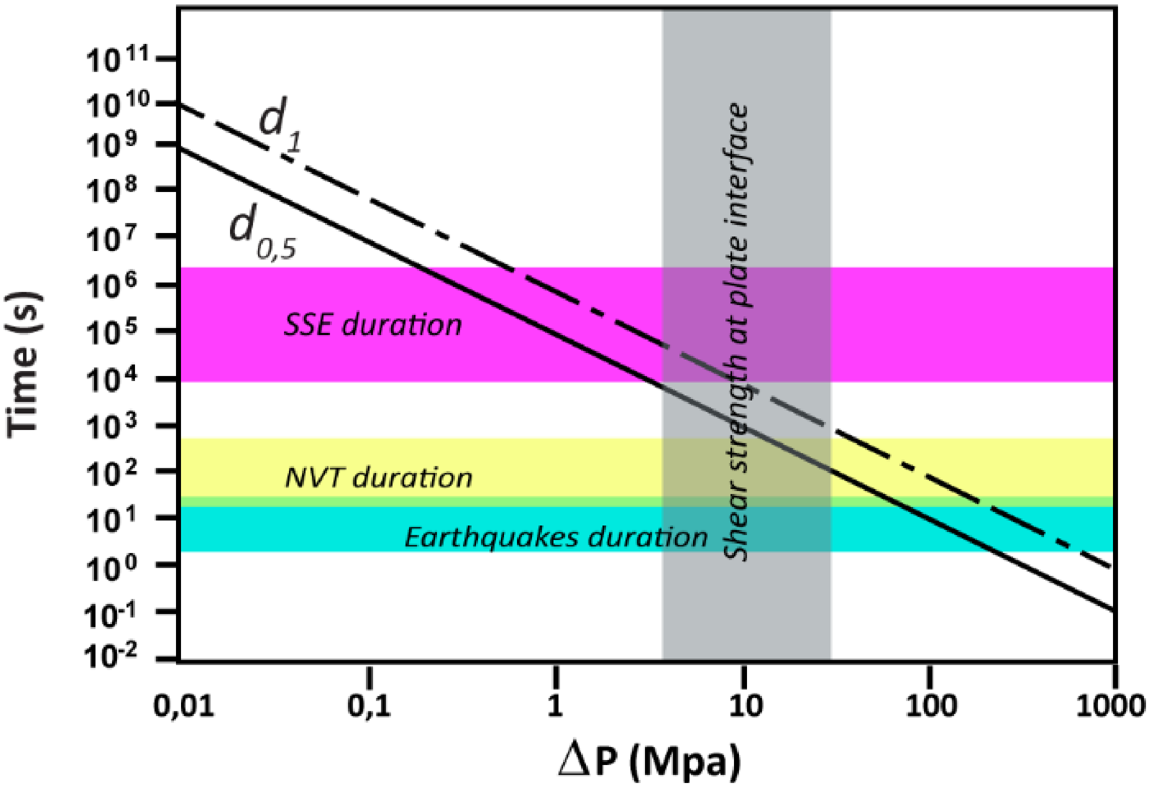

Figure 2. *Estimation of the critical time needed to fill shear veins along shear planes in the Hyuga tectonic mélange in function of* ΔP*. Two critical distance D are presented, 500 µm and 1 mm as upper and lower bonds. Porosity of phyllosilicate is assumed to 3%. SSE, NVT and Earthquakes durations are from Schwartz and Robowsky [2007] and Marone and Richardson [2015]. Modified by Fisher and Brantley [2014].*

3. Quartz plasticity and water transport at low temperatures

3.1 Effect of water on plasticity

3.1.1. Microstructures – Influence of recrystallization on strength

The activation of ductility of quartzite and quartz-rich rocks deformed at greenschist or higher metamorphic facies is attested by their deformation microstructures and crystallographic fabrics. These aspects combined with the experimental observations that dry quartz deforms in a semi-brittle way even at elevated pressure and temperatures at experimental conditions [*Griggs and Blacic,* 1965] seems to outline that water may facilitate deformation.

In the past, most of experimental works on quartz have been done using either dry quartz with about 100 ppm water [*Cordier et al.,* 1991], synthetic wet quartz with about 1000 ppm [e.g. *Muto et al.,* 2011], or natural quartz aggregates (quarzites) with different amount of liquid water-added [e.g. *Stipp et al.* 2006]. The large difference between our experiments and previous ones is the nature of the wet quartz. In our case it derives from the metasedimentary unit of the Hyuga Tectonic Mélange (see **Chapter 2**). The water content in this material is even larger than in other hydrated synthetic crystals described in literature [e.g. Aines and Rossman, 1984].

The chosen experimental conditions (temperature 800°C, confining pressure 1.5 GPa and strain rates 10^{-5} s^{-1}) allowed a direct comparison of our experiments with the microstructural classification established by the experimental work of *Hirth and Tullis,* [1992] (**Figure 3).**

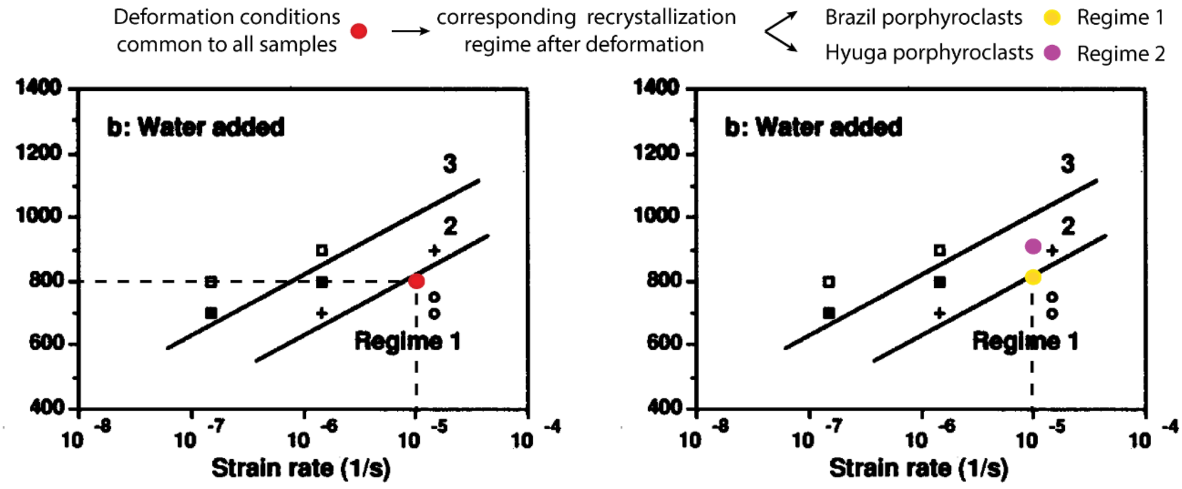

***Figure 3**. Recrystallization regimes derived by experiments on quartz (water-added conditions) by Hirth and Tullis, [1992]. Red point represents deformation conditions applied to our samples, both Brazil and Hyuga. After experiments, microstructures representative for Hyuga are similar to those described for the recrystallization Regime 2 (pink point) while microstructures observed in Brazil porphyroclasts are well described in the Regime 1. Modified from Hirth and Tullis [1992].*

Microstructures developed in Hyuga porphyroclasts are primarily due to the operation of different mechanisms of dynamic recrystallization. The formation of new grains by bulging and grain boundary rotation recrystallization can be compared with the recrystallization Regime 2 described by these authors. Contrarily, deformation features found in Brazil porphyroclasts, as dislocation lamellae and undulose extinction, can be associated to the Regime 1, as expected (**Figure 3)**.

The strong contrast offered by these two materials in developing microstructures (**Figure 4**) may be explained by the role of water in enhancing recrystallization: *Hirth and Tullis* [1992] outlined that at the same deformation conditions, the addition of few 0.1 wt. % water is equivalent, in terms of strength and microstructures, to increase the temperature of about ~100°C.

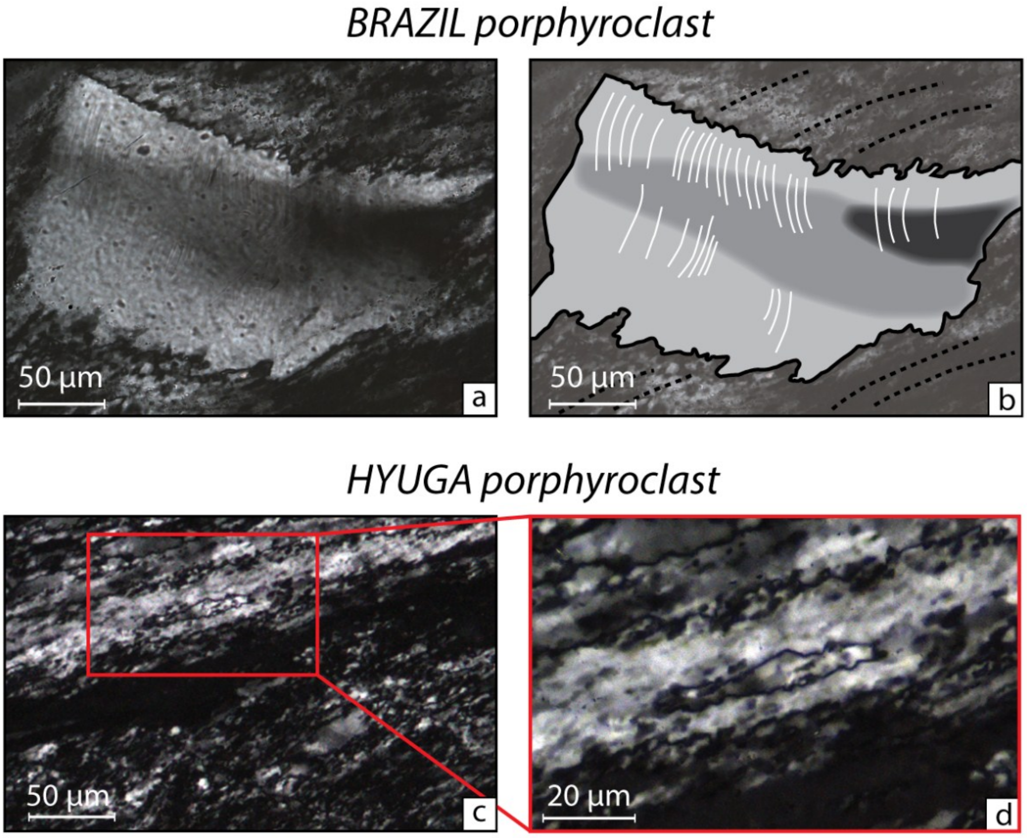

Figure 4. *A) Close up of the deformed Brazil quartz porphyroclast. Note the sutured porphyroclast boundaries, the sweeping extinction and the deformation lamellae. B) Interpretation of microstructural features observed in a): foliation (dashed black lines); sutured porphyroclast boundaries (black lines); deformation lamellae (white lines). For simplicity, pressure shadows are not drawn in details. C) Close up of a Hyuga porphyroclasts. Sutured grain boundaries delimit elongated domains which are characterized by almost homogenous extinction colors. D) At higher magnification, also the first-look homogeneous extinction colors domains, are characterized by small recrystallized subgrains distinguishable by the high variability in grey.*

Besides microstructures, the differences between the two materials are also expressed by a different mechanical behavior.

For example at the same gamma (~4), the shear stress of 70 % Hyuga sample is about 100 MPa lower than the 70 % Brazil one (**Figure**).

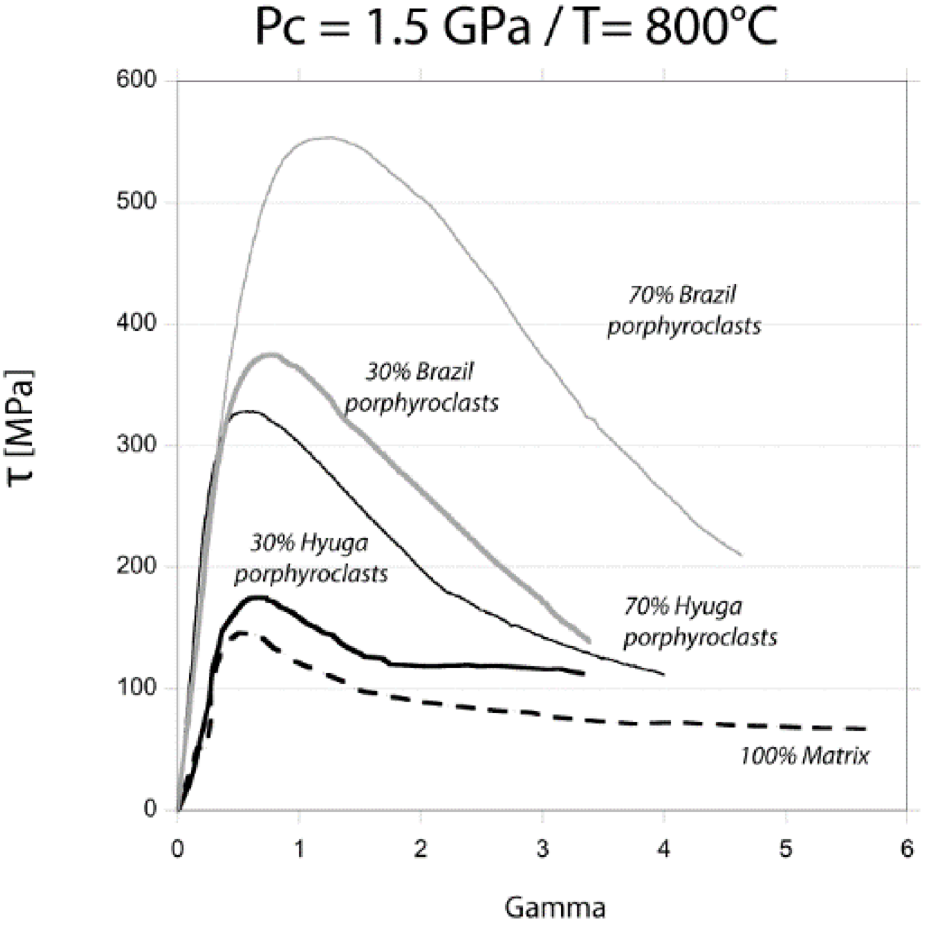

Figure 5. *Mechanical curves of our experimental work. All experiments consist of a constant matrix, to which a variable proportion of quartz porphyroclasts (either Brazil quartz or Hyuga quartz) is added, indicated in %.*

The strength dependence on pressure demonstrated in quartz deformation experiments has been associated to water fugacity [e.g. *Kronenberg and Tullis*, 1984]. Water fugacity has been recognized as potentially affecting both strain rate and stress [e.g. *Evans and Kohlstedt,* 1995] and to control the dislocation climb [*e.g. Post et al.,* 1996] but the extrapolation of realistic values for natural systems is actually very difficult due mainly to the complex composition of pore fluids [*Stockhert et al.,* 1999] and the uncertainty on the amplitude of fluid overpressure [*e.g. Saffer and Tobin,* 2011]. In order to verify if these flow laws adequately model our experiments (**Figure 6**) we chose two of the most commonly employed flow laws in lithosphere numerical modeling [e.g.

Burov et al., 2011], the one calibrated by *Hirth et al.,* [2011] which considers water fugacity and the *Paterson and Luan* [1990].

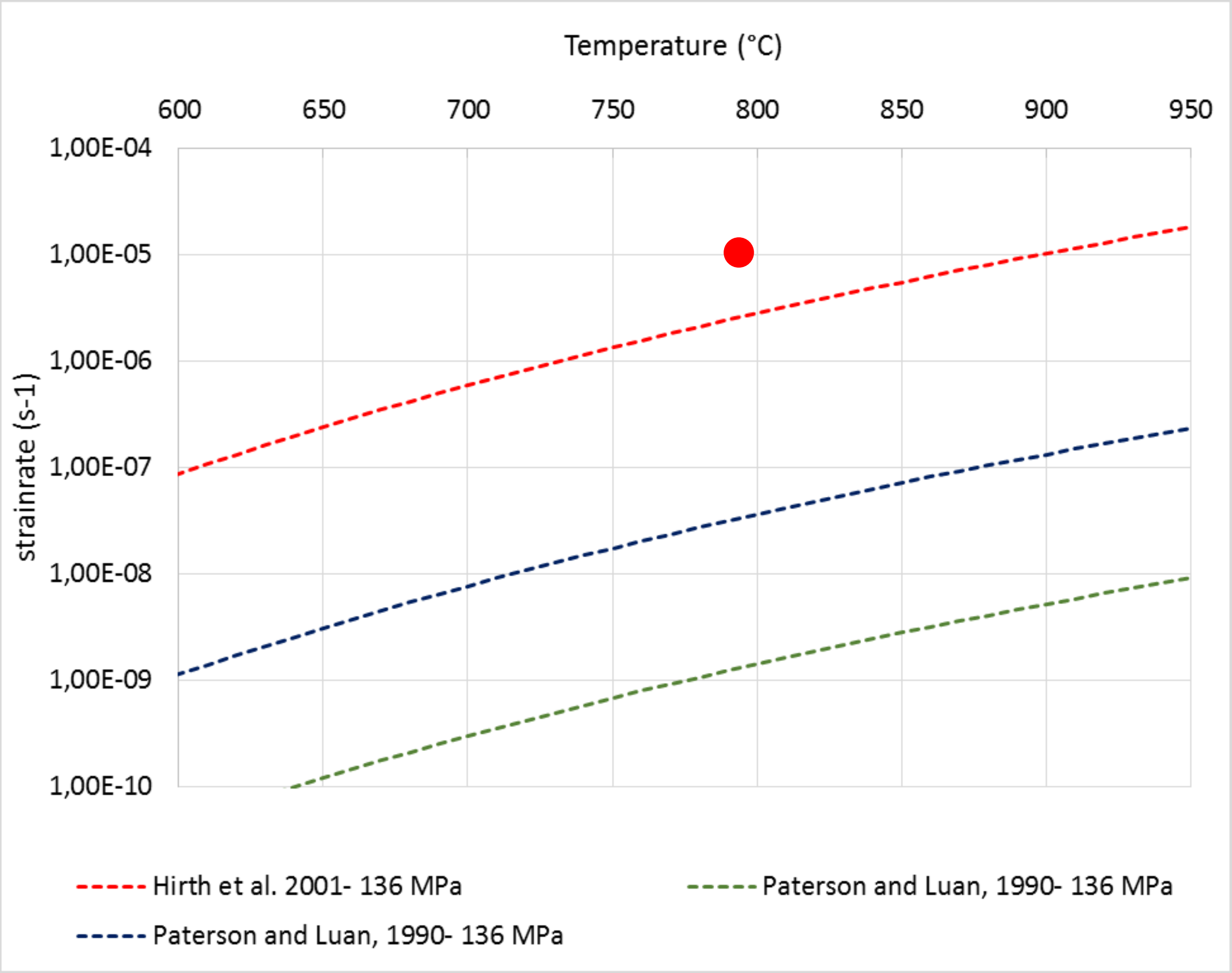

Figure 6*. Strain rates estimated with the Hirth et al., [2011] and the Paterson and Luan [1990] (silica gel and silicic acid) flow laws considering the mechanical flow stress of ~140 MPa (τ=68 MPa) obtained deforming the sample with 100% matrix. Red point corresponds to our experimental conditions.*

For experiments with the pure matrix deformed at strain rates = 10^{-5} s^{-1}, both flow laws overestimate the strength of the quartz assemblage. Furthermore, experiments on assemblages containing a fraction of Brazil porphyroclasts provide insights into the stress-strain rate dependence. From the very large increase in stress that they trigger (**Figure 6**) and from their absence of recrystallization microstructures (**Figure 4**), one can consider that the Brazil porphyroclasts in experiments GP426 and GP465 behave like rigid bodies in the deforming matrix. Consequently, they cause the surrounding matrix to accommodate strain. We assume that bulk strain rate is equivalent to the sum of matrix and porphyroclasts strain rates with respect to their volume proportion as illustrated in the equation:

$$\dot{\varepsilon}_{bulk} = \dot{\varepsilon}_m \emptyset_m + \dot{\varepsilon}_p \emptyset_p \qquad \textbf{(eq. 2)}$$

where $\emptyset_m$ and $\emptyset_p$ indicate the volume proportion of matrix and porphyroclasts and $\dot{\varepsilon}_m$ and $\dot{\varepsilon}_p$ the strain rate partitioned in the matrix and porphyroclasts. We consider $\emptyset_m$=35% and 75% matrix respectively, slightly above initial matrix proportion, to account for the fact that a small proportion of the porphyroclasts (their rims), is recrystallized and deforms along with the matrix. Matrix strain rates values calculated according to this scheme are $1{,}33 \cdot 10^{-5}$ s^{-1} and $2{,}9 \cdot 10^{-5}$ s^{-1} respectively (**Table 1**).

Matrix percentage		H-2001 (MPa)			P&L-1990-Sg (MPa)			P&L 1990-Sa (MPa)		
	$\dot{e}$ (s^{-1})	A	Q	n	A	Q	n	A	Q	n
		-11,2	135	4	-7,18	135	3	-9,4	135	4
35% matrix	2,9E-05	243			1169			718		
75% matrix	1,3E-05	201			907			593		
100% matrix	1 E-05	187			824			552		

Table 1*. Flow stresses estimated with the Hirth et al. [2011](H-2001) and the Paterson and Luan [1990] for silica gel (P&L-1990-Sg) and silicic acid (P&L 1990-Sa) flow laws considering strain rates for 35% - 75% and 100% matrix. The flow law has the form* $\dot{e} = \sigma^n A \exp(-QR/T)$. *$\sigma$ the differential stress (MPa); n is the stress exponent; A is the pre-exponential factor* ($MPa^{-n}s^{-1}$)*; Q the activation energy* (kJ mol^{-1})*, R is the gas constant, T the absolute temperature (K).*
In the Hirth et al. [2011] fugacity (MPa) is added to the flow law: $\dot{e} = \sigma^{n} A f^{m} \exp(-QR/T)$*; the exponent m is 1. Fugacity at 800°C and 1.5 GPa confining pressure has been calculated using an online JavaScript code (http://www.geo.umn.edu/people/researchers/withe012/ fugacity.htm) that solves the analytical equation for fugacity given in Sterner and Pitzer [1994].*

Recalculated strain rates in the matrix are thus higher than the bulk strain rates imposed during the experiments (10^{-5} s^{-1}) (**Figure 7**).

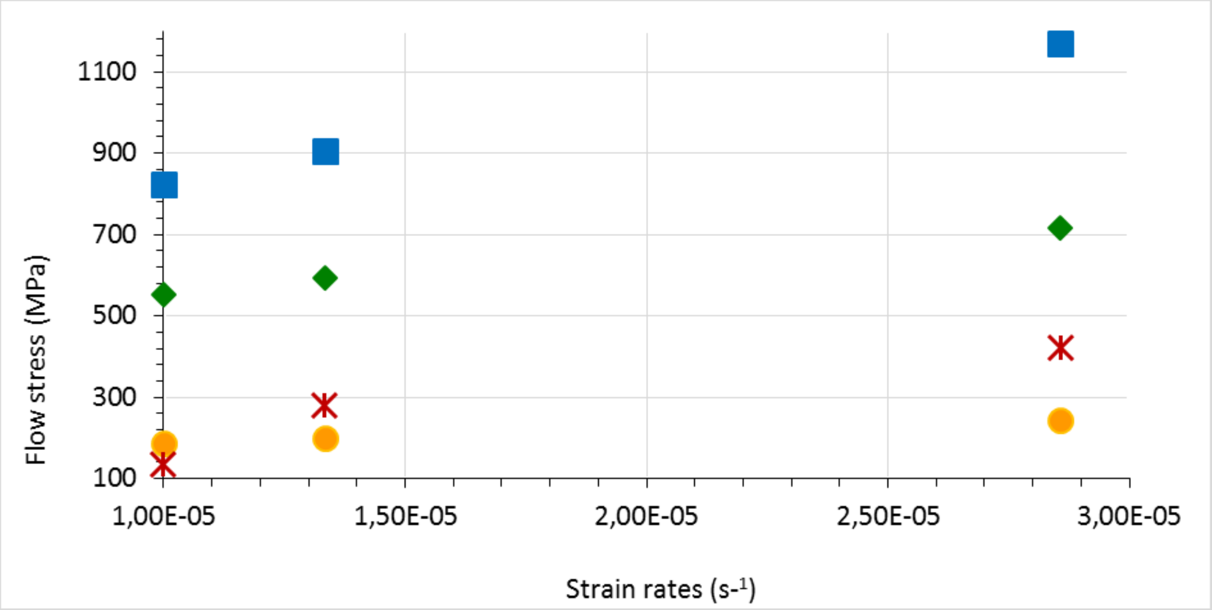

***Figure** 7. Flow stress/Strain rate plot for recalculated strain rates of 1.3*10^{-5} s^{-1} and 2.9*10^{-5} s^{-1} considering an assembly composed of 70% and 30% pure matrix. The Hirth et al. [2001] (yellow dots) flow law shows the lower strength values probably because of the effect of water fugacity. Paterson and Luan [1990] flow laws for silica gel (green rhombs) and silicic acid (bleu squares) overestimate experimental results (red stars).*

At higher strain rates, *Paterson and Luan* [1990] flow laws still largely overestimate the strength of the quartz matrix, while *Hirth et al.* [2001] yields lower values of stress. A possible explication for this is strength/strain rate dependence, represented by the stress exponent (**Figure 8**): in the experiments, the stress exponent is close to 1, while all flow law used have a much larger exponent, in particular *Hirth et al.* [2011] flow law with n=4. The small stress exponent in our experiments reflects the contribution of a grain-size sensitive process (GSS).

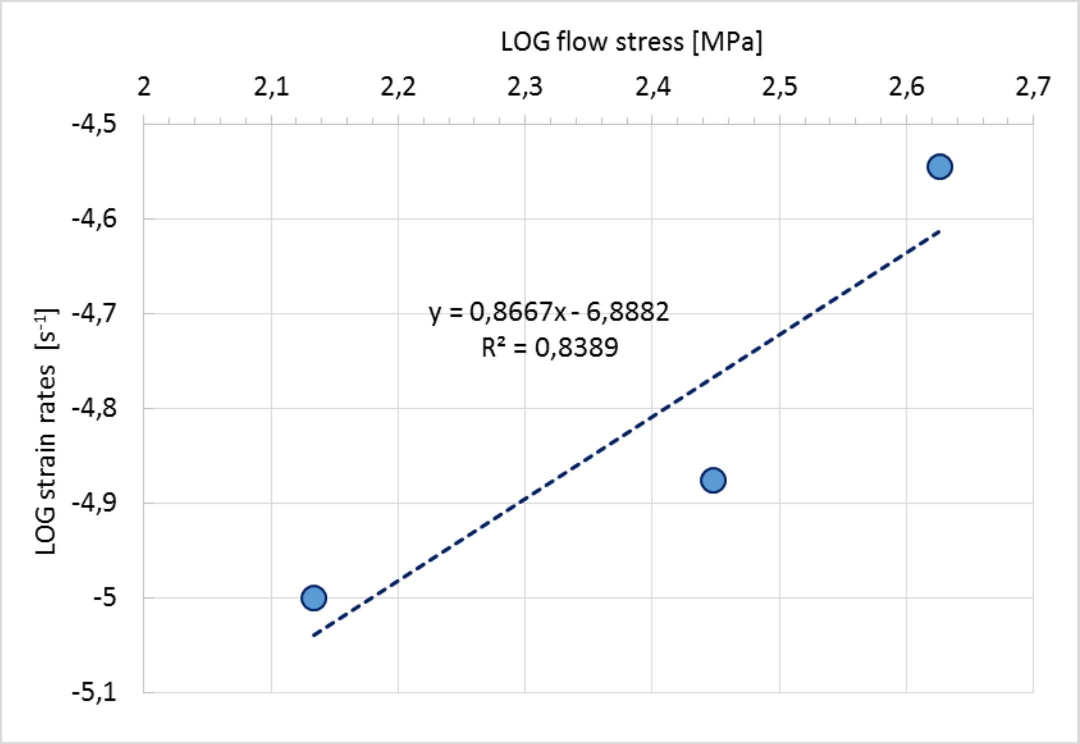

Figure 8. *Log stress-log strain rate plot for 35-75-100% matrix proportions.*

The consequence of this contribution of GSS process is that there a dependency between stress and matrix grain size. This dependency probably explains the strain-weakening observed in experiments with Hyuga quartz (**Figure 5**). The Hyuga porphyroclasts contain in their initial state enough water to be intrinsically weak and they even lose water during deformation, so water content cannot account for the weakening observed. In contrast, porphyroclasts largely recrystallize, so the average grain-size decreases. This has no effect in dislocation creep regime, but if GSS processes are active, this recrystallization results in weakening. Therefore, both the low stress exponent and the macroscopic behavior are in agreement with a significant contribution of GSS processes during experimental deformation.

3.2 Effect of plastic deformation on water distribution

3.2.1 Water transport

The hydrolytic weakening observed in quartz during experiments [e.g. *Griggs and Blacic,* 1965, 1967] is not fully understood at the microscopic scale, notably because multiple species of water are present in the crystal and may play a role. We will discuss the principal mechanisms of water incorporation in quartz proposed in literature with the aim of describing the behavior observed in the dry and wet porphyroclasts.

Following the model proposed by *Griggs and Blacic* [1965, 1967] *Kronenberg et al.* [1986] demonstrated that volume diffusion of hydrogen does not result in weakening. Despite the fast hydrogen diffusion coefficient (~10^{-11} m²s^{-1}), the hydrogen equilibrium solubility in the form of $(4H)_{Si}$ defects in quartz (< 100 ppm H/10^6Si) is one limiting factor [*Paterson,* 1986, 1989]. In contrast with hydrogen, in their experiment of quartz annealing in doped $H_2{}^{18}O$, *Kronenberg et al.* [1986] observed no oxygen diffusion, nor did they observe in the annealed crystal the broad IR band associated with mechanical weakening (between 2800 and 4000 cm^{-1}). These evidences show that water penetration is necessary to weakening, though it is not clear from these experiments how it can percolate through the crystal.

Post and Tullis [1998] propose H_2O volume diffusion in quartz to explain the increase in molecular water amount detected by FTIR using the oxygen diffusion proposed by *Farver and Yund* [1992] and *Giletti and Yund* [1984].

The relationship between the distance d (m) that oxygen can diffuse in and the time t (s) is expressed by $d = 2*(t*D)^{1/2}$ where D is the diffusion coefficient (m²s^{-1}). Estimation of hydrothermal oxygen diffusion corrected with water fugacity factor at confining pressure of 1500 MPa [*Kronenberg et al.,* 1986] at 800°C, are in the order of 10^{-16} m² s^{-1} [*Farver and Yund*, 1992]. The distance estimated with this diffusion coefficient would allow to water percolation over a distance of 26 µm considering the experimental duration of about ~80. If these estimation are true a wider portion of porphyroclasts rims should be recrystallized contrasting with the observed thickness of about 10 µm.

It is probably more realistic that micro fractures affected the external rims of Brazil porphyroclasts providing the penetration of small water bubbles at their rims. This water improved their recrystallization. Brazil porphyroclasts cores are however affected by a small water increase after deformation and their IR spectra are characterized by the secondary absorption band at 3585 cm^{-1}.

According to *Kekulawala et al.* [1981] who observe this peak but only after pressurization, this band is never detected at "as-is" conditions (P=1 atm and T=25°C). At the light of these consideration we interpret the gentle increase of water at porphyroclasts cores as incorporated by firstly by micro cracking in the external rims and then diffused along dislocations which have nucleated at crack tips [C*ordier et al.,* 1989].

Contrarily to Brazil porphyroclasts, Hyuga quartz grains (with initial H_2O up to 2000 ppm) lost almost 50% of their water during pressuring and reach stable values of ~220 ppm after deformation. The remarkable water decreases during the hot-pressing (from ~2000 ppm to 1000 ppm) may be explained in terms of fluid inclusions decrepitation [*Tarantola et al.,* 2010]. In deformed samples, dynamic recrystallization microstructures are ubiquitously developed within porphyroclast thus may have erased pre-existing microstructural features, thus eventually micro-fractures. The principal recrystallization mechanism observed in Hyuga porphyroclast is grain boundary migration. This mechanism has been proposed as capable to remove a significant volume of fluid from grains [*Drury and Urai*, 1990] by interacting with fluid inclusions. Furthermore experimental models with rock-analogue systems show that the migration of grain boundaries is responsible for morphology and volume change of fluid inclusions [*Urai*, 1983; *Olgaard and Fitz Gerald*, 1993*; Schmatz and Urai,* 2010]. The incorporation of fluid inclusions at grain boundaries depends on the wetting properties of the grain boundary [*Schenk and Urai*, 2005], on fluids composition and fluid inclusions size [*Schmatz and Urai,* 2010], thus that fluid inclusions can migrate at grain boundaries or being redistributed in the crystals. Grain boundary migration, commonly observed in metamorphic rocks [e.g., *Wilkins and Barkas,* 1978] has been demonstrated to occur at a higher rates in presence of water [*Tullis and Yund,* 1985; *Urai et al.,* 1986; *Schenk et al.,* 2006]. Grain boundary migration is thus considered to be responsible for the expulsion of molecular water in excess of the intragranular water in Hyuga quartz.

To summarize, two different mechanisms related to water incorporation are observed in our samples. The dry Brazil quartz show water increase which is interpreted as due to micro cracking followed by oxygen diffusion. The wet Hyuga quartz show molecular water expulsion due to grain boundary migration.

3.2.2 Water redistribution

FTIR estimations of water quantities in our samples, before and after deformation, are reported in **Figure 9** with a compilation of other water quantities measured in several experimental studies [*denBrok and Spiers,* 1991; *Post and Tullis,* 1998; *Stipp et al.,* 2006; *Muto et al.,* 2011; *Thust, 2012*]. We observe that in several experiments, after deformation, molecular water amounts is lowered and tends to values between 200-400 ppm. In this compilation are considered water amounts both in polycrystalline materials and single quartz crystals and the reported measurements may include water at grain boundaries [e.g. *Stipp et al.,* 2006], leading to overestimate water quantities in the cores of the grains. In our study, the initial water quantities (at P=1atm and T=25°C) are referred exclusively to the cores of grains while, after deformation, this is true only for Brazil porphyroclasts. This is due to the fact that Brazil porphyroclasts are almost not recrystallized and thus no grain boundaries are observed within them, in contrast to Hyuga porphyroclasts. The average value found in Hyuga porphyroclasts is ~220 ppm and incorporate grain boundaries to some extent as the recrystallized grain size is ~3 µm inside the porphyroclasts and the FT-IR analysis window size is 50 µm. Water amount measured in deformed 70% Hyuga porphyroclasts and their matrix are quite comparable: the similar amount of ~220-280 ppm (which is inclusive of water within recrystallized grains and at grain boundaries) may correspond to a saturation quantity which can be stored at grain boundaries under these conditions.

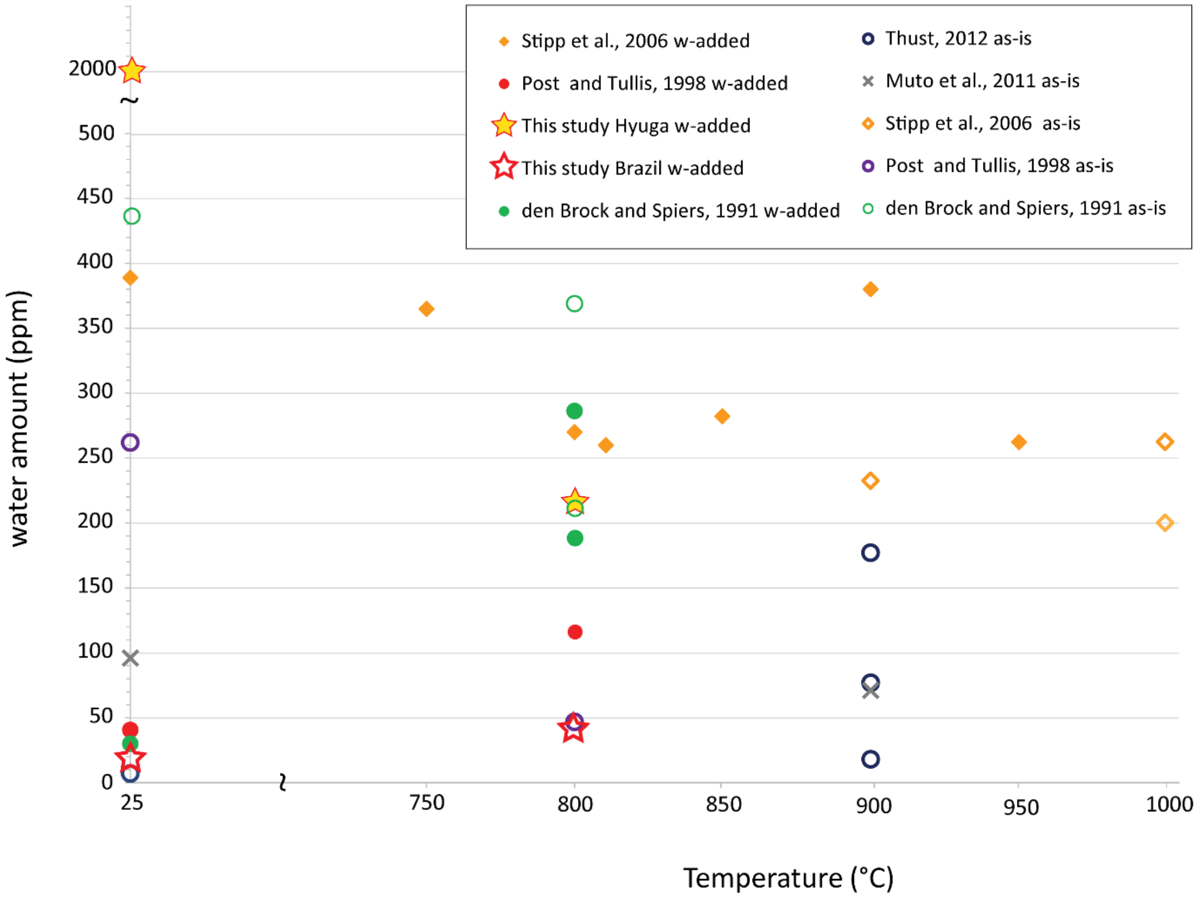

Figure 9*. Compilation of water amounts in experimentally deformed quartz. Initial water quantities are reported for 25°C. The final quantities are plotted with the corresponding deformation temperature and they cluster between 200 and 400 ppm weight.*

Our experiments with wet Hyuga quartz show that large amount of molecular water initially present in the form of fluid inclusions is ejected and added to the matrix.

Considering the experiment with 70% Hyuga porphyroclasts, the final water budget indicates that water a large quantity of water is no more inside the system. In fact in this experiment the matrix was hydrated by about 450 ppm water. During the run of the experiment, the 70 % porphyroclasts (containing about 2200 ppm) have lost 90% of their intragranular water which has been added to the matrix. But the final water amount measured in the matrix are well lower than the initial 450 ppm (**Figure 10**).

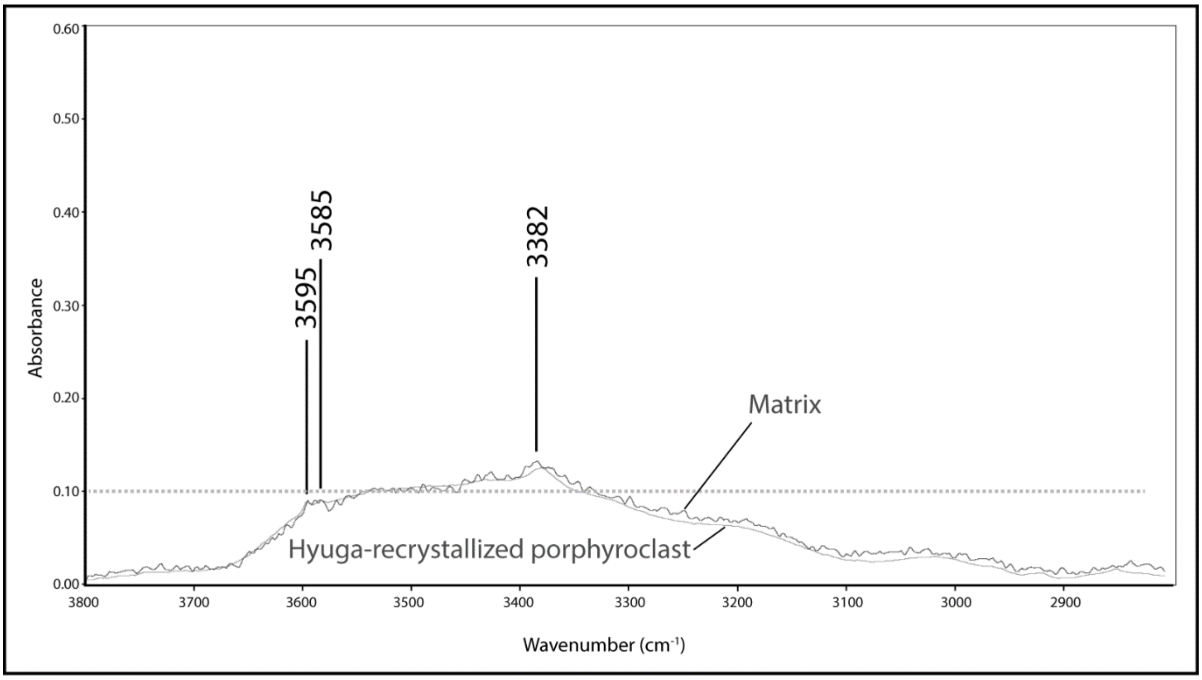

Figure 10. *Comparison between water amount in recrystallized Hyuga porphyroclasts and the surrounding matrix. The two FTIR spectrum show the same shape and the same secondary absorption bands.*

We believe that the observed C' shear bands acted as "reservoir" where the large amount of water released during recrystallization has been stored. The euhedral crystal shape of the quartz crystals in these shear bands suggests that these crystals grew within a free water phase. Shear bands seem to not affect the bulk shear strength probably because they are not interconnected. Shear bands are not observed in samples with dry Brazil porphyroclast, in agreement with their much lower water content. The presence of a free fluid phase is observed only in experiments where the initial water content exceeds some "equilibrium" value.

References

Aines, R.D., Rossman, G.R., 1984. Water in minerals? A peak in the infrared. J. Geophys. Res. Solid Earth 89, 4059–4071. doi:10.1029/JB089iB06p04059.

Brok, S.W.J.D., Spiers, C.J., 1991. Experimental evidence for water weakening of quartzite by microcracking plus solution–precipitation creep. J. Geol. Soc. 148, 541–548. doi:10.1144/gsjgs.148.3.0541.

Burov, E.B., 2011. Rheology and strength of the lithosphere. Mar. Pet. Geol. 28, 1402–1443. doi:10.1016/j.marpetgeo.2011.05.008.

Cordier, P., Doukhan, J.-C., 1989. Water solubility in quartz and its influence on ductility, Eur. J. Mineral., 221–238.

Cordier, P., Doukhan, J.-C., 1991. Water speciation in quartz; a near infrared study, Am. Mineral., 76(3-4), 361–369.

Davison, I., 1995. Fault slip evolution determined from crack-seal veins in pull-aparts and their implications for general slip models. J. Struct. Geol. 17, 1025–1034. doi:10.1016/0191-8141(94)00131-I.

Evans, B., Kohlstedt, D.L., 1995. Rheology of Rocks, in: Ahrens, T.J. (Ed.), Rock Physics & Phase Relations. American Geophysical Union, pp. 148–165.

Fagereng, A., Ellis, S., 2009. On factors controlling the depth of interseismic coupling on the Hikurangi subduction interface, New Zealand. Earth Planet. Sci. Lett. 278, 120–130. doi:10.1016/j.epsl.2008.11.033.

Farver, J.R., Yund, R.A., 1992. Oxygen diffusion in a fine-grained quartz aggregate with wetted and nonwetted microstructures. J. Geophys. Res. Solid Earth 97, 14017–14029. doi:10.1029/92JB01206.

Fisher, D., Brantley, S., 1992. Models of quartz vein and overgrowth formation: fluid flow in an ancient accretionary wedge. J. Geophys. Res. 97, Solid Earth 20043–20063.

Gamage, K., Screaton, E., 2006. Characterization of excess pore pressures at the toe of the Nankai accretionary complex, Ocean Drilling Program sites 1173, 1174, and 808: Results of one-dimensional modeling, J. Geophys. Res., 111, B04103, doi: 10.1029/2004JB003572.

Gerretsen, J., Paterson, M. S., McLaren, A. C., 1989. The uptake and solubility of water in quartz at elevated pressure and temperature, Phys. Chem. Miner., 16(4), 334–342.

Gaviglio, P., 1986. Crack-seal mechanism in a limestone: A factor of deformation in strike-slip faulting. Tectonophysics 131, 247–255. doi:10.1016/0040-1951(86)90177-0.

Giletti, B.J., Yund, R.A., 1984. Oxygen diffusion in quartz. J. Geophys. Res. Solid Earth 1978–2012 89, 4039–4046. doi:10.1029/JB089iB06p04039.

Gratier, J.-P., 1993. Experimental pressure solution of Halite by an indenter technique. Geophys. Res. Lett. 20, 1647–1650. doi:10.1029/93GL01398.

Griggs, D.T., Blacic, J.D., 1965. Quartz: Anomalous Weakness of Synthetic Crystals. Science 292.

Griggs, D., 1967. Hydrolytic Weakening of Quartz and Other Silicates. Geophys. J. R. Astron. Soc. 14, 19–31. doi:10.1111/j.1365-246X.1967.tb06218.x.

Hasegawa, A., Yoshida, K., Asano, Y., Okada, T., Iinuma, T., Ito, Y., 2012. Change in stress field after the 2011 great Tohoku-Oki earthquake. Earth Planet. Sci. Lett. 355-356, 231–243. doi:10.1016/j.epsl.2012.08.042.

Hirth, G., Tullis, J., 1992. Dislocation creep regimes in quartz aggregates. J. Struct. Geol. 14, 145–159. doi:10.1016/0191-8141(92)90053-Y.

Hirth, G., Teyssier, C., Dunlap, J.W., 2001. An evaluation of quartzite flow laws based on comparisons between experimentally and naturally deformed rocks. Int. J. Earth Sci. 90, 77–87. doi:10.1007/s005310000152.

Hubbert, M.K., Rubey, W.W., 1959. Role of Fluid Pressure in Mechanics of Overthrust Faulting I. Mechanics of Fluid-Filled Porous Solids and Its Application to Overthrust Faulting. Geol. Soc. Am. Bull. 70, 115–166. doi:10.1130/0016- 606(1959)70.

Ito, Y., Nakashima, S., 2002. Water distribution in low-grade siliceous metamorphic rocks by micro-FTIR and its relation to grain size: a case from the Kanto Mountain region, Japan. Chem. Geol. 189, 1–18. doi:10.1016/S0009-2541(02)00022-0.

Kronenberg, A.K., Tullis, J., 1984. Flow strengths of quartz aggregates: Grain size and pressure effects due to hydrolytic weakening. J. Geophys. Res. Solid Earth 89, 4281–4297. doi:10.1029/JB089iB06p04281.

Kronenberg, A. K., Kirby, S. H., Aines, R. D., Rossman, G. R., 1986. Solubility and diffusional uptake of hydrogen in quartz at high water pressures: implications for hydrolytic weakening. J. Geophys. Res. Solid Earth, 91(B12), 12723–12741.

Kronenberg, A.K., Segall, P., Wolf, G.H., 1990. Hydrolytic weakening and penetrative deformation within a natural shear zone. Geophys. Monogr. 56, 21–36.

Kronenberg, A.K., Wolf, G.H., 1990. Fourier transform infrared spectroscopy determinations of intragranular water content in quartz-bearing rocks: implications for hydrolytic weakening in the laboratory and within the earth. Tectonophysics 172, 255–271. doi:10.1016/0040-1951(90)90034-6.

Lamb, H., Hydrodynamics, Cambridge University Press, New York, 1932.

Lee, Y.-J., Wiltschko, D.V., 1999. Fault controlled sequential vein dilation; competition between slip and precipitation rates in the Austin Chalk, Texas. J. Struct. Geol. 22, 1247–1260.

Liu, Y., Rice, J.R., 2007. Spontaneous and triggered aseismic deformation transients in a subduction fault model. J. Geophys. Res. 112, B09404.

McLaren, A.C., Cook, R.F., Hyde, S.T., Tobin, R.C., 1983. The mechanisms of the formation and growth of water bubbles and associated dislocation loops in synthetic quartz. Phys. Chem. Miner. 9, 79–94. doi:10.1007/BF00308151.

Meneghini, F., Marroni, M., Moore, J.C., Pandolfi, L., Rowe, C.D., 2009. The processes of underthrusting and underplating in the geologic record: structural diversity between the Franciscan Complex (California), the Kodiak Complex (Alaska) and the Internal Ligurian Units (Italy). Geol. J. 44, 126–152. doi:10.1002/gj.1144.

Muto, J., Hirth, G., Heilbronner, R., Tullis, J., 2011. Plastic anisotropy and fabric evolution in sheared and recrystallized quartz single crystals. J. Geophys. Res. Solid Earth 116, B02206. doi:10.1029/2010JB007891.

Nakashima, S., Matayoshi, H., Yuko, T., Michibayashi, K., Masuda, T., Kuroki, N., Yamagishi, H., Ito, Y., Nakamura, A., 1995. Infrared microspectroscopy analysis of water distribution in deformed and metamorphosed rocks. Tectonophysics, Influence of Fluids on Deformation Processes in Rocks 245, 263–276. doi:10.1016/0040-1951(94)00239-6.

Olgaard, D.L., Fitz Gerald, J.D., 1993. Evolution of pore microstructures during healing of grain boundaries in synthetic calcite rocks. Contrib. Mineral. Petrol. 115, 138–154.

Paterson, M. S., 1986. The thermodynamics of water in quartz, Phys. Chem. Miner., 13(4), 245–255.

Paterson, M. S., 1989. The interaction of water with quartz and its influence in dislocation flow: an overview, Rheol. Solids Earth, 107–142.

Paterson, M.S., Luan, F.C., 1990. Quartzite rheology under geological conditions. Geol. Soc. Lond. Spec. Publ. 54, 299–307. doi:10.1144/GSL.SP.1990.054.01.26.

Peacock, S.M., 1996. Thermal and Petrologic Structure of Subduction Zones, in: Bebout, G.E., Scholl, D.W., Kirby, S.H., Platt, J.P. (Eds.), Subduction Top to Bottom. American Geophysical Union, pp. 119–133.

Post, A., Tullis, J., 1998. The rate of water penetration in experimentally deformed quartzite: implications for hydrolytic weakening. Tectonophysics 295, 117–137. doi:10.1016/S0040-1951(98)00145-0.

Rice, J.R., 1992. Fault stress states, pore pressure distributions, and the weakness of the San Andreas Fault. Acad. Press : San Diego, CA, United States, United States, pp. 475–503.

Rubey, W.W., Hubbert, M.K., 1959. Role of Fluid Pressure in Mechanics of Overthrust Faulting Ii. Overthrust Belt in Geosynclinal Area of Western Wyoming in Light of Fluid-Pressure Hypothesis. Geol. Soc. Am. Bull. 70, 167–206. doi:10.1130/0016-7606(1959)70[167:ROFPIM]2.0.CO;2.

Schenk, O., Urai, J.L., 2005. The migration of fluid-filled grain boundaries in recrystallizing synthetic bischofite: first results of in-situ high-pressure, high-temperature deformation experiments in transmitted light. J. Metamorph. Geol. 23, 695–709. doi:10.1111/j.1525-1314.2005.00604.x.

Schenk, O., Urai, J.L., Piazolo, S., 2006. Structure of grain boundaries in wet, synthetic polycrystalline, statically recrystallizing halite - evidence from cryo-SEM observations. Geofluids 6, 93–104. doi:10.1111/j.1468-8123.2006.00134.x.

Schmatz, J., Urai, J.L., 2010. The interaction of fluid inclusions and migrating grain boundaries in a rock analogue: deformation and annealing of polycrystalline camphor-ethanol mixtures. J. Metamorph. Geol. 28, 1–18. doi:10.1111/j.1525-1314.2009.00849.x.

Scholz, C.H., 1998. Earthquakes and friction laws. Nature 391, 37–42. doi:10.1038/34097.

Screaton, E., Saffer, D., Henry, P., Hunze, S., 2002. Porosity loss within the underthrust sediments of the Nankai accretionary complex: Implications for overpressures. Geology 30, 19–22. doi:10.1130/0091-7613(2002)030<0019:PLWTUS>2.0.CO;2.

Skarbek, R.M., Saffer, D.M., 2009. Pore pressure development beneath the décollement at the Nankai subduction zone: Implications for plate boundary fault strength and sediment dewatering, J. Geophys. Res., 114, B07401, doi:10.1029/2008JB006205.

Sterner, S.M., Pitzer, K.S., 1994. An equation of state for carbon dioxide valid from zero to extreme pressures. Contrib. Mineral. Petrol. 117, 362–374. doi:10.1007/BF00307271.

Stipp, M., Tullis, J., Behrens, H., 2006. Effect of water on the dislocation creep microstructure and flow stress of quartz and implications for the recrystallized grain size piezometer. J. Geophys. Res. Solid Earth 111, B04201. doi:10.1029/2005JB003852.

Stockhert, B., Wachmann, M., Kuster, M., Bimmermann, S., 1999. Low effective viscosity during high pressure metamorphism due to dissolution precipitation creep: the record of HP-LT metamorphic carbonates and siliciclastic rocks from Crete. Tectonophysics 303, 299–319. doi:10.1016/S0040-1951(98)00262-5.

Tarantola, A., Diamond, L.W., Stünitz, H., 2010. Modification of fluid inclusions in quartz by deviatoric stress I: experimentally induced changes in inclusion shapes and microstructures. Contrib. Mineral. Petrol. 160, 825–843. doi:10.1007/s00410-010-0509-z.

Thust, A., 2014. Experimentelle Verformung von natürlichen Quarzeinkristallen: Einfluss der Wasserneuverteilung auf die Deformation und mikrostrukturelle Untersuchungen., PhD Thesis, University of Basel, Faculty of Science. doi: 10.5451/unibas-006258281.

Tullis, J., Yund, R. A., 1985. Hydrolytic weakening of quartz aggregates: requirement for rapid water penetration Eos Trans. AGU, 66, 1084.

Urai, J.L., Means, W.D., Lister, G.S., 1986. Dynamic recrystallization of minerals, in: Hobbs, B.E., Heard, H.C. (Eds.), Geophysical Monograph Series. American Geophysical Union, Washington, D. C., pp. 161–199.

Urai, J.L., n.d. Water assisted dynamic recrystallization and weakening in polycrystalline bischofite [WWW Document]. URL https://www-sciencedirect-com.budistant.univ-orleans.fr/science/article/pii/0040195183902470 (accessed 1.31.16).

Wilkins, R.W.T., Barkas, J.P., 1978. Fluid inclusions, deformation and recrystallization in granite tectonites. Contrib. Mineral. Petrol. 65, 293–299. doi:10.1007/BF00375515.

CONCLUSION

This dissertation provides additional knowledge about the mechanical behavior of quartz under ductile deformation conditions. In particular, this work highlights the role played by pressure solution at the transition to plasticity. Furthermore, our experimental study described quantitatively the weakening associated with the presence of water and the micro-processes behind such weakening.

In chapter II we focused our interest on quartz microstructures developed at conditions close to the brittle-ductile transition. The CPO and the internal structures unraveled by optical microscopy of the strongly elongated quartz ribbons observed in the Hyuga tectonic mélange have been interpreted as the result of intense pressure solution creep, microcracking and immediate healing. Under these low-T conditions, pressure solution is the microscopic process accommodating macroscopic ductile deformation. Using the available flow laws, the activation of pressure solution is shown to result in a large strength decrease of the plate interface (< than 30 MPa).
Estimations of the rates necessary to produce these microstructures are of about 10^4 seconds at strength corresponding to plate interface. These values may partly fit with the duration reported for non-volcanic tremors.

In chapter III we deformed experimentally two different kinds of quartz, either strongly hydrated or dry, with the aim of understanding the influence of water in quartz deformation and the effect of deformation in water speciation. To do that we studied the behavior of porphyroclasts of the hydrated quartz from the Hyuga Tectonic Mélange and dry Brazilian quartz deformed in a common matrix.
From our experimental work it is clear that intragranular molecular water has a large mechanical effect: in presence of abundant water, strength is decreased by several factors with respect to dry quartz. The weakening is correlated with enhanced dynamic recrystallization: wet Hyuga porphyroclasts are strongly recrystallized at the end of the experiments while Brazil porphyroclasts are almost undeformed.

The stress exponent close to one of the deforming matrix and the pronounced mechanical weakening of water-rich porphyroclasts of a large initial grain size may indicate the contribution of grain-size sensitive process to deformation.

The main mechanisms which allow the transfer of molecular water from Hyuga porphyroclasts to the surrounding matrix is probably grain boundary migration recrystallization. Contrarily, micro-fracturing is the best candidate which can justify the presence of external recrystallized rims in Brazil porphyroclasts and the small increase of water in porphyroclasts cores. We observed also the changes in the physicochemical states of water in response to recrystallization which are expressed by the apparition of secondary absorption bands at 3585 cm^{-1} and 3595 cm^{-1} which we associate to OH-groups at dislocation tips and to water bonded at grain boundaries, respectively. Finally, water in excess of the storage capacity of grain boundaries leads to the formation of C' shear bands in sample with Hyuga porphyroclasts or at pressure shadows in sample with Brazil porphyroclasts, in the form of molecular water.

These experimental results stress out the major role played by small amounts of water to modify the mechanical properties of quartz aggregates. Furthermore, the various reservoirs/species of water (OH defect, molecular water in nm-scale aggregates, and water along grain boundaries, "free" bulk water in inclusions or in microfractures) and the transfer between them is complex and only partially elucidated by our study. Further work based on experiments and natural work is indeed necessary to describe these water-related processes and their consequences on mechanical strength.

ANNEXE I

Water estimation in experiments

Table I

Experiment GP 426 - 30% BRAZIL porphyroclasts

Porphyroclast and matrix

Porphyroclasts		Position	Thickness (cm)	Integrated Absorption (cm^{-2})	H/10 6 Si	weight ppm	Paterson molar proportion
grain 9	#1	core	1,46E-02	5,15E+00	432,60	64,89	294,56
	#2	core	1,47E-02	1,46E+01	1221,17	183,17	831,52
grain 10	#1	wing-recryst	1,43E-02	3,25E+01	2805,95	420,87	1910,63
	#2	wing-recryst	1,38E-02	3,92E+01	3491,11	523,64	2377,17
	#3	core	1,49E-02	1,44E+01	1193,01	178,94	812,35
grain 11	#1	recryst	1,47E-02	1,32E+01	1107,09	166,05	753,84
grain 13	#1	core	1,44E-02	5,96E+00	511,09	76,66	348,01
grain 14	#1	core	1,51E-02	1,22E+01	995,15	149,27	677,62
	#2	recrystallizzed	1,36E-02	5,33E+01	4820,24	723,00	3282,21
grain 15	#1	core	1,31E-02	5,15E+00	485,45	72,81	330,56
grain 16	#1	core	1,12E-02	3,95E+00	434,34	65,15	295,75
	#2	wing-recryst	1,13E-02	9,18E+00	996,12	149,41	678,28
	#3	wing-recryst	1,16E-02	2,18E+01	2318,55	347,77	1578,76
grain 17	#1	core	9,22E-03	2,78E+00	371,36	55,70	252,87
	#2	wing-recryst	9,74E-03	2,35E+01	2967,64	445,12	2020,73
grain 18	#1	core	1,09E-02	2,89E+00	327,46	49,12	222,97
	#2	wing-recryst	1,07E-02	1,48E+01	1698,59	254,78	1156,61
grain 10	#1	core	1,06E-02	2,10E+01	2444,15	366,60	1664,28
grain 12	#2	wing-recryst	1,26E-02	1,71E+01	1663,20	249,47	1132,51
grain 20	#1	core	1,25E-02	1,82E+01	1791,66	268,74	1219,98
grain 21	#2	core	8,29E-03	1,08E+01	1603,25	240,48	1091,69
grain 23	#2	recrystallizzed	7,87E-03	5,99E+00	938,00	140,69	638,70
grain 24	#1	grain boundaries	9,75E-03	5,68E+00	717,51	107,62	488,57
grain 25	#1	core	1,11E-02	4,66E+00	516,83	77,52	351,92

Matrix	#1		1,41E-02	1,77E+01	1543,37	231,49	19,27
	#2		1,35E-02	2,93E+01	2669,38	400,39	33,33
	#3		1,42E-02	1,26E+01	1091,62	163,74	13,63
	#4		1,36E-02	1,43E+01	1294,51	194,17	16,16
	#5		1,12E-02	1,08E+01	1185,13	177,76	14,80

	#6		1,08E-02	9,53E+00	1083,20	162,47	13,52
	#7		1,09E-02	9,35E+00	1055,04	158,25	13,17
	#8		1,40E-02	1,48E+01	1295,39	194,30	16,17
	#9		1,36E-02	1,54E+01	1386,59	207,98	17,31
	#10		1,44E-02	1,31E+01	1116,19	167,42	13,94
	#11		1,29E-02	1,40E+01	1335,52	200,32	16,67
	#12		1,33E-02	1,67E+01	1542,81	231,41	19,26

Table II

Experiment GP 456 - 70% HYUGA porphyroclasts

PORPHYROCLASTS and MATRIX

PORPHYRO		**Position**	**Thickness (cm)**	**Integrated area (cm^{-2})**	**H/10 6 Si**	**weight ppm**	Paterson molar proportion
grain 10	#1	Core	1,50E-02	3,47E+01	2855,56	428,31	1944,42
	#2	Core	1,50E-02	4,06E+01	33,38	5,01	**2273,06**
grain 11	#1	Shear Band	1,48E-02	3,46E+01	28,78	4,32	1959,51
grain 12	#1	Core	1,49E-02	3,81E+01	31,49	4,72	**2144,46**
grain 13	#1	Core, strongly stretched	1,47E-02	4,26E+01	35,62	5,34	2425,54
	#2	Core, strongly stretched	1,46E-02	5,65E+01	47,66	7,15	3245,00
grain 14	#1	Core	1,44E-02	3,38E+01	28,97	4,34	1972,48
grain 15	#1	Core	1,18E-02	2,88E+01	30,01	4,50	2043,72
grain 16	#1	Core	1,24E-02	2,91E+01	29,00	4,35	**1974,37**
grain 18	#1	Core	1,43E-02	4,14E+01	35,70	5,35	**2430,63**
grain 19	#1	Core	1,34E-02	4,69E+01	43,26	6,49	2945,35
grain 20	#1	Core	1,35E-02	4,66E+01	42,40	6,36	2886,99
grain 21	#1	Core	1,51E-02	4,31E+01	35,17	5,27	2394,49
Matrix	#1		1,33E-02	5,42E+01	5006,15	750,92	3408,799
	#2		1,33E-02	4,31E+01	40,02	6,00	2724,984
	#3		1,40E-02	4,07E+01	35,78	5,37	2436,452
	#4		1,36E-02	6,32E+01	57,04	8,56	3884,043
	#5		1,44E-02	5,76E+01	49,09	7,36	3342,606
	#6		1,23E-02	2,41E+01	24,21	3,63	1648,610
	#7		1,19E-02	1,96E+01	20,30	3,04	1382,113
	#8		1,19E-02	4,81E+01	49,66	7,45	3381,572
	#9		1,31E-02	5,28E+01	49,56	7,43	3374,602

Table III

Experiment GP 457 - 100% BRAZIL matrix

MATRIX

Matrix	Thickness (cm)	Integrated Absorption (cm^{-2})	H/10 6 Si	weight ppm	Paterson molar proportion
#1	1,21E-02	1,45E+01	1471,78	220,76	1002,17
MAP1 perpendicularly to the pistons					
#2	1,19E-02	1,74E+01	1802,57	270,37	1227,41
#3	1,19E-02	9,80E+00	1010,71	151,60	688,22
#4	1,16E-02	1,14E+01	1207,43	181,10	822,16
#5	1,20E-02	1,30E+01	1340,57	201,08	912,83
#6	1,22E-02	1,38E+01	1395,83	209,36	950,45
#7	1,20E-02	1,45E+01	1489,31	223,39	1014,10
#8	1,20E-02	1,45E+01	1484,76	222,70	1011,01
#9	1,22E-02	1,62E+01	1635,25	245,28	1113,48
#10	1,21E-02	1,38E+01	1403,11	210,46	955,41
#11	1,22E-02	1,27E+01	1284,49	192,66	874,64
#12	1,22E-02	1,23E+01	1239,27	185,88	843,85
#13	1,21E-02	1,34E+01	1363,74	204,55	928,60
#14	1,20E-02	1,34E+01	1377,50	206,61	937,97
#15	1,20E-02	1,56E+01	1594,31	239,13	1085,60
#16	1,17E-02	1,18E+01	1235,25	185,28	841,11
MAP 2 perpendicularly to the pistons					
#2	1,14E-02	1,02E+01	1096,49	164,47	746,63
#3	1,20E-02	9,21E+00	947,24	142,08	644,99
#4	1,18E-02	8,26E+00	861,29	129,19	586,47
#5	1,19E-02	7,25E+00	752,34	112,85	512,28
#6	1,20E-02	6,80E+00	698,93	104,83	475,92
#7	1,18E-02	8,18E+00	853,15	127,97	580,93
#8	1,18E-02	8,87E+00	926,66	138,99	630,98
#9	1,20E-02	8,57E+00	878,51	131,77	598,20
#10	1,23E-02	1,03E+01	1025,50	153,82	698,29
#11	1,19E-02	1,11E+01	1142,57	171,38	778,00
#12	1,23E-02	1,21E+01	1206,91	181,03	821,81
#13	1,23E-02	9,59E+00	958,04	143,70	652,35
#14	1,23E-02	1,02E+01	1014,00	152,09	690,46
#15	1,22E-02	8,04E+00	810,04	121,50	551,57
MAP 3 perpendicularly to the pistons					
#1	1,13E-02	1,04E+01	1134,13	170,11	772,25
#2	1,14E-02	1,30E+01	1405,22	210,77	956,84

#3	1,16E-02	9,56E+00	1016,01	152,39	691,83
#4	1,14E-02	1,18E+01	1278,35	191,74	870,45
#5	1,15E-02	1,02E+01	1092,09	163,80	743,63
#6	1,15E-02	1,02E+01	1088,93	163,33	741,48
#7	1,15E-02	8,96E+00	956,68	143,50	651,43
#8	1,15E-02	9,71E+00	1041,31	156,19	709,05
#9	1,18E-02	7,10E+00	740,62	111,09	504,30
#10	1,17E-02	7,96E+00	834,87	125,22	568,48
#11	1,18E-02	8,36E+00	874,75	131,21	595,63
#12	1,19E-02	1,17E+01	1215,56	182,32	827,70
#13	1,17E-02	1,18E+01	1241,34	186,19	845,25
#14	1,17E-02	1,31E+01	1381,52	207,22	940,71
#15	1,22E-02	1,20E+01	1209,28	181,38	823,42
#16	1,21E-02	1,14E+01	1157,29	173,59	788,03
#17	1,22E-02	9,93E+00	1004,88	150,72	684,25
#18	1,18E-02	1,38E+01	1435,44	215,31	977,43
MAP 4 perpendicularly to the pistons					
#2	1,15E-02	1,58E+01	1697,72	254,65	1156,02
#3	1,14E-02	1,08E+01	1172,46	175,86	798,35
#4	1,18E-02	9,15E+00	950,85	142,62	647,45
#5	1,17E-02	9,94E+00	1046,25	156,93	712,42
#6	1,17E-02	1,02E+01	1070,69	160,59	729,05
#7	1,17E-02	9,69E+00	1020,25	153,03	694,71
#8	1,15E-02	9,31E+00	994,48	149,17	677,17
#9	1,15E-02	9,57E+00	1025,30	153,79	698,15
#10	1,11E-02	1,92E+01	2122,98	318,43	1445,58
#11	1,18E-02	8,53E+00	893,82	134,07	608,62
#12	1,12E-02	1,11E+01	1229,42	184,40	837,14
#13	1,19E-02	9,43E+00	978,55	146,77	666,32
#14	1,18E-02	9,90E+00	1035,45	155,31	705,06
#15	1,16E-02	1,13E+01	1195,69	179,34	814,17
MAP 5 – Parallel to the piston, close to the piston					
#1	1,20E-02	1,09E+01	1120,55	168,07	763,01
#2	1,21E-02	1,52E+01	1546,18	231,91	1052,83
#3	1,19E-02	1,26E+01	1305,25	195,78	888,77
#4	1,17E-02	1,45E+01	1528,77	229,30	1040,97
#5	1,19E-02	1,40E+01	1455,99	218,39	991,41
#6	1,20E-02	1,19E+01	1223,00	183,44	832,77
#7	1,17E-02	1,10E+01	1160,43	174,06	790,17
#8	1,19E-02	9,29E+00	961,46	144,21	654,68
#9	1,17E-02	1,06E+01	1118,62	167,78	761,69
#10	1,20E-02	1,02E+01	1051,16	157,67	715,76
#11	1,17E-02	1,07E+01	1125,69	168,84	766,51

#12	1,17E-02	7,98E+00	842,45	126,36	573,64
#13	1,19E-02	8,57E+00	885,27	132,78	602,80
#14	1,18E-02	7,61E+00	791,56	118,73	538,99
#15	1,18E-02	8,82E+00	920,92	138,13	627,07
#16	1,16E-02	9,98E+00	1060,86	159,12	722,37
#17	1,19E-02	9,04E+00	938,16	140,72	638,82
MAP 6 Parallel to the piston, central portion of the sample					
#1	1,21E-02	9,78E+00	998,12	149,71	679,64
#2	1,22E-02	7,76E+00	784,97	117,74	534,50
#3	1,22E-02	1,16E+01	1171,30	175,69	797,56
#4	1,18E-02	1,82E+01	1900,61	285,08	1294,17
#5	1,23E-02	7,13E+00	715,35	107,30	487,10
#6	1,22E-02	7,09E+00	712,60	106,88	485,22
#7	1,21E-02	7,31E+00	745,99	111,89	507,96
#8	1,22E-02	8,23E+00	829,17	124,37	564,60
#9	1,18E-02	1,91E+01	1983,99	297,58	1350,94
#10	1,20E-02	1,85E+01	1889,90	283,47	1286,88
#11	1,21E-02	1,09E+01	1110,20	166,52	755,96
#12	1,21E-02	9,37E+00	951,93	142,78	648,19

Table III

GP464 – 30% Hyuga porphyroclasts

Hydrostatic

Porphyroclasts		Thickness (cm)	Integrated Absorption (cm^{-2})	c (mol H/LSiO2)	weight proportion ppm	Paterson molar proportion H/106 Si
Grain 1	#1	6,34E-03	193,04	37473,83	5620,79	25516,77
	#2	6,33E-03	235,34	45817,57	6872,29	31198,21
Grain 2	#1	6,80E-03	268,41	48594,86	7288,86	33089,33
	#2	6,86E-03	215,00	38612,33	5791,56	26292,00
Grain 3	#1	6,89E-03	224,00	40014,67	6001,90	27246,89
	#2	6,80E-03	247,00	44717,98	6707,36	30449,47
Grain 4	#1	6,78E-03	217,00	39392,82	5908,63	26823,46
	#2	7,04E-03	206,00	36032,56	5404,61	24535,38
	#3	6,75E-03	243,00	44352,44	6652,53	30200,57
Grain 5	#1	6,64E-03	135,00	25048,65	3757,11	17056,19
	#2	6,51E-03	139,00	26299,38	3944,71	17907,84
Grain 6	#1	6,55E-03	126,00	23706,17	3555,75	16142,06
	#2	6,33E-03	154,00	29982,01	4497,08	20415,42
Grain 7	#1	6,69E-03	242,00	44532,96	6679,61	30323,49
Grain 8	#1	6,69E-03	146,00	26867,00	4029,85	18294,34
Grain 9	#1	6,69E-03	69,00	12697,42	1904,52	8645,96

Matrix						
	#1	6,34E-03	44,00	8541,53	1281,17	5816,12
	#2	6,34E-03	59,00	11453,42	1717,93	7798,89
	#3	6,34E-03	42,00	8153,28	1222,93	5551,75
	#4	6,34E-03	34,00	6600,27	989,99	4494,27
	#5	6,34E-03	41,00	7959,15	1193,81	5419,57
	#6	6,34E-03	59,00	11453,42	1717,93	7798,89
	#7	6,34E-03	154,00	29895,36	4484,08	20356,42
	#8	6,34E-03	78,00	15141,80	2271,16	10310,39
	#9	6,34E-03	74,00	14365,30	2154,69	9781,66
	#10	6,34E-03	54,00	10482,79	1572,34	7137,96

ANNEXE II
Experiments

GP 426 – 30% Brazil porphyroclasts

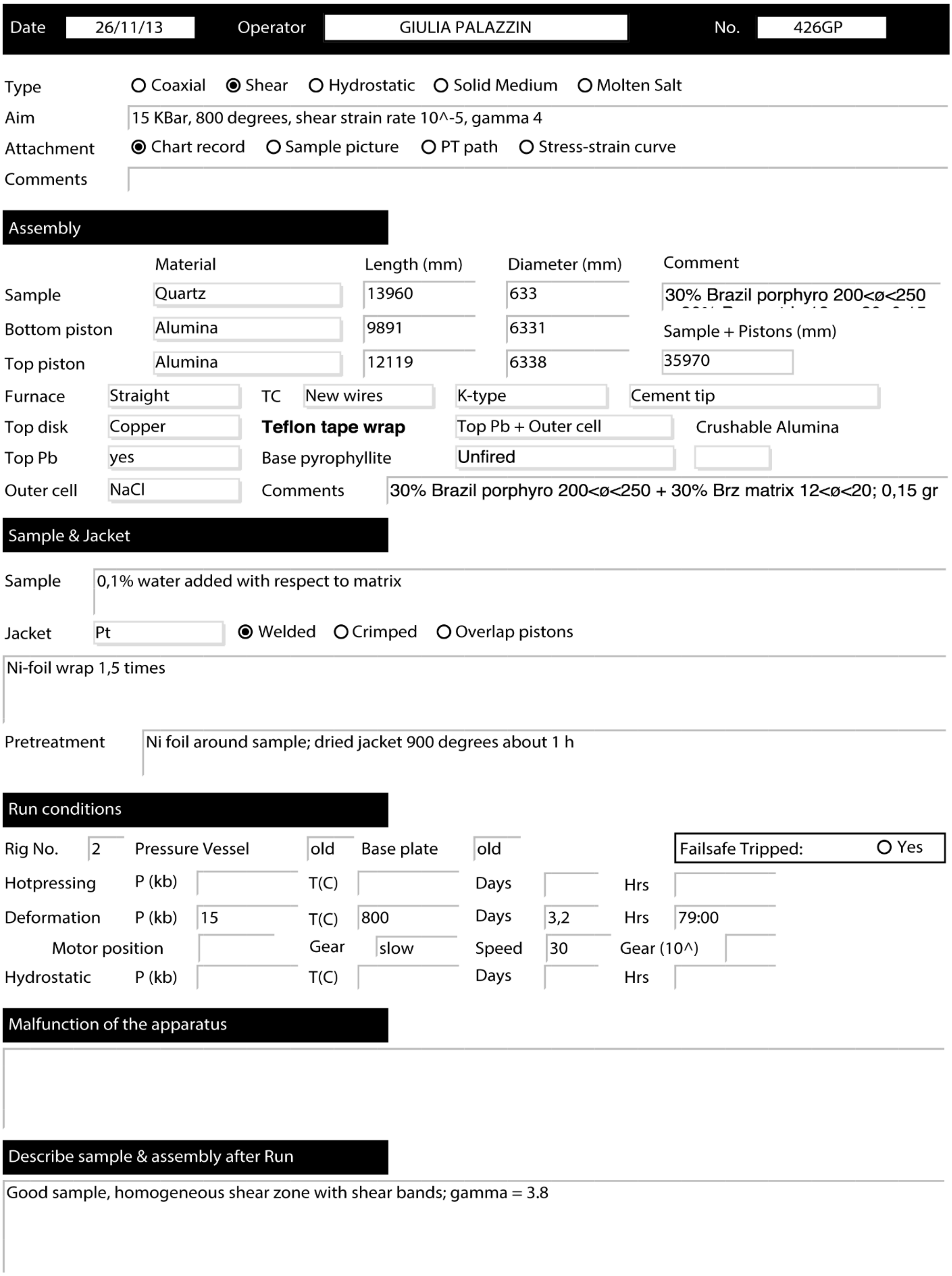

Date 26/11/13 Operator GIULIA PALAZZIN No. 426GP

Type ○ Coaxial ● Shear ○ Hydrostatic ○ Solid Medium ○ Molten Salt

Aim 15 KBar, 800 degrees, shear strain rate 10^-5, gamma 4

Attachment ● Chart record ○ Sample picture ○ PT path ○ Stress-strain curve

Comments

Assembly

	Material	Length (mm)	Diameter (mm)	Comment
Sample	Quartz	13960	633	30% Brazil porphyro 200<ø<250
Bottom piston	Alumina	9891	6331	Sample + Pistons (mm)
Top piston	Alumina	12119	6338	35970

Furnace	Straight	TC	New wires	K-type	Cement tip
Top disk	Copper	**Teflon tape wrap**	Top Pb + Outer cell	Crushable Alumina	
Top Pb	yes	Base pyrophyllite	Unfired		
Outer cell	NaCl	Comments	30% Brazil porphyro 200<ø<250 + 30% Brz matrix 12<ø<20; 0,15 gr		

Sample & Jacket

Sample 0,1% water added with respect to matrix

Jacket Pt ● Welded ○ Crimped ○ Overlap pistons

Ni-foil wrap 1,5 times

Pretreatment Ni foil around sample; dried jacket 900 degrees about 1 h

Run conditions

Rig No. 2 Pressure Vessel old Base plate old Failsafe Tripped: ○ Yes

Hotpressing	P (kb)		T(C)		Days		Hrs	
Deformation	P (kb)	15	T(C)	800	Days	3,2	Hrs	79:00
Motor position			Gear	slow	Speed	30	Gear (10^)	
Hydrostatic	P (kb)		T(C)		Days		Hrs	

Malfunction of the apparatus

Describe sample & assembly after Run

Good sample, homogeneous shear zone with shear bands; gamma = 3.8

Other remarks

Output values & PT path

Zero Start Values		Scale (mv/V FS)	Pump	
P (mv/V)	5.995	Pressure	5V	FS
F (mv/V)	2.117	Force	2V	FS
Dx (mv/V)	2.265	Displacement	0,5V	FS

Furnace Power		Pressure	Force	Temperature	
A (old:psi)	V	mV	mV	**°C**	%op
032	0,313	0,362	0,056	30	3.9
062	0,701	0,667	0,081	100	6.4
086	0,999	0,779	0,290	200	9.0
113	1,221	1,656	0,689	300	11.2
140	1,387	2,805	1,155	400	13.2
157	1,489	3,924	1,536	500	14.7
179	1,606	5,225	1,917	600	16.4
189	1,721	5,797	2,139	700	17.9
215	1,817	5,926	2,137	800	19.3

GP 428 – 30% Hyuga porphyroclasts

Date 29/11/13 **Operator** *GIULIA* **No.** **428GP**

Type ○ Coaxial ● Shear ○ Hydrostatic ○ Solid Medium ○ Molten Salt

Aim 15 Kbar, 800 degrees, deformation qtz, shear strain rate 10^-5 (mm/s)

Attachment ● Chart record ○ Sample picture ○ PT path ○ Stress-strain curve

Comments

Assembly

	Material	Length (mm)	Diameter (mm)	Comment
Sample	Quartz	1.246	633	70% BRZ QTZ matrix 12<ø<20 +
Bottom piston	Alumina	6.509	6326	**Sample + Pistons (mm)**
Top piston	Alumina	14.415	6335	22.17

Furnace	Straight	**TC**	New wires	K-type	Cement tip
Top disk	Copper	**Teflon tape wrap**	Top Pb + Outer cell	**Crushable Alumina**	
Top Pb	yes	**Base pyrophyllite**	Unfired	No	
Outer cell	NaCl	**Comments**			

Sample & Jacket

Sample

Jacket Pt ● Welded ○ Crimped ○ Overlap pistons

Pretreatment Ni foil around sample; dried jacket 900 degrees about 1 h

Run conditions

Rig No. 2 **Pressure Vessel** old **Base plate** old

Failsafe Tripped: ○ Yes

Hotpressing	**P (kb)**		**T(C)**		**Days**		**Hrs**	
Deformation	**P (kb)**	15	**T(C)**	800	**Days**	3,2	**Hrs**	80:00
Motor position		right	**Gear**	slow	**Speed**	30	**Gear (10^)**	
Hydrostatic	**P (kb)**		**T(C)**		**Days**		**Hrs**	

Malfunction of the apparatus

Missing pc registration

Describe sample & assembly after Run

Shear pistons twisted, one side is thicken than the other one , TC in good position.
Shear bands developed

Other remarks

Output values & PT path

Zero Start Values		**Scale (mv/V FS)**	Pump	
P (mv/V)		**Pressure**	5	FS
F (mv/V)		**Force**	2	FS
Dx (mv/V)		**Displacement**	0.5	FS

Furnace Power		**Pressure**	**Force**	**Temperature**	
A (old:psi)	**V**	**mV**	**mV**	**°C**	**%op**
038	0.370		0.052	30	3.9
063	0.689	0.561	0.084	100	6.3
097	0.967	0.738	0.290	200	8.8
129	1.179	1.337	0.546	300	11.0
149	1.334	2.324	0.980	400	12.9
171	1.474	3.368	1.257	500	14.7
193	1.580	4.686	1.707	600	16.3
209	1.693	5.588	1.916	700	17.8
225	1.776	5.962	2.024	800	19.2

GP456 – 70% Hyuga porphyroclasts

Date 28/3/14 **Operator** *Giulia Palazzin* **No.** **456GP**

Type ○ Coaxial ● Shear ○ Hydrostatic ○ Solid Medium ○ Molten Salt

Aim deforme 70% Hyuga porphyroclasts in a dry matrix; strain rate 10^-5

Attachment ● Chart record ○ Sample picture ○ PT path ○ Stress-strain curve

Comments

Assembly

	Material	Length (mm)	Diameter (mm)	Comment
Sample	Quartz	18.41	6.33	70% hyuga porphyro grain size
Bottom piston	Alumina	6.329	6.33	**Sample + Pistons (mm)**
Top piston	Alumina	12.575	6.33	37.314

Furnace	Straight	**TC**	New wires	K-type	Cement tip & elbow
Top disk	Copper	**Teflon tape wrap**	Top Pb + Outer cell	**Crushable Alumina**	
Top Pb	yes	**Base pyrophyllite**	Unfired	Yes	
Outer cell	NaCl	**Comments**	0.15 gr tot, 0.4 microlitres water added with respect to matrix		

Sample & Jacket

Sample 70% hyuga porphyro grain size 200-250 microns
30% brasil qtz matrix grain size 10 to 6 microns-OLD MATRIX

Jacket Pt ● Welded ○ Crimped ○ Overlap pistons

Pretreatment Annealed jacket for about 1 hour at 900 C; nickel foil wrapped around pistons and sample

Run conditions

Rig No.	2	**Pressure Vessel**	2	**Base plate**	2	Failsafe Tripped:	○ Yes
Hotpressing	**P (kb)**		**T(C)**		**Days**		**Hrs**
Deformation	**P (kb)**	15	**T(C)** 800		**Days** 5		**Hrs** 100:00
Motor position	right		**Gear** slow		**Speed** 30		**Gear (10^)**
Hydrostatic	**P (kb)**		**T(C)**		**Days**		**Hrs**

Malfunction of the apparatus

Describe sample & assembly after Run

TC half mm far from SZ; sample ok, possible SZ that cross cut the whole sample

Other remarks

Output values & PT path

Zero Start Values		Scale (mv/V FS)	Pump	
P (mv/V)	0.003	**Pressure**	5	FS
F (mv/V)	0.006	**Force**	2	FS
Dx (mv/V)	1.650	**Displacement**	0.5	FS

Furnace Power		Pressure	Force	Temperature	
A (old:psi)	**V**	**mV**	**mV**	**°C**	**%op**
0.027	0.312	0.630	0.046	30	3.9
0.054	0.680	0.823	0.157	100	6.1
0.091	0.972	1.608	0.732	200	8.8
0.109	1.172	2.399	1.016	300	11.0
0.132	1.316	3.061	1.261	400	12.6
0.152	1.425	3.905	1.569	500	14.1
0.172	1.511	4.532	1.787	600	15.5
0.178	1.604	5.191	2.016	700	16.6
0.193	1.628	5.936	2.255	800	18.0

GP465 – 70% Brazil porphyroclasts

Date	19/4/14	**Operator**	*Giulia*	**No.**	**465GP**

Type ○ Coaxial ● Shear ○ Hydrostatic ○ Solid Medium ○ Molten Salt

Aim deforme 70% brazil porphyroclasts in 30% brazil matrix

Attachment ● Chart record ○ Sample picture ○ PT path ○ Stress-strain curve

Comments

Assembly

	Material	Length (mm)	Diameter (mm)	Comment
Sample	Quartz	18.875	6.33	porphyroclasts g.s. 200to250
Bottom piston	Alumina	6.635	6.33	**Sample + Pistons (mm)**
Top piston	Alumina	16.144	6.35	41.654

Furnace	Straight	**TC**	New wires	K-type	Cement tip & elbow
Top disk	Copper	**Teflon tape wrap**	Top Pb + Outer cell	**Crushable Alumina**	
Top Pb	NaCl insert	**Base pyrophyllite**	Unfired	Yes	
Outer cell	NaCl	**Comments**	New matrix, grain size 6-10 microns		

Sample & Jacket

Sample 0.15 gr total, 0.4 mL water added with respect to matrix

Jacket Pt ● Welded ○ Crimped ○ Overlap pistons

Pretreatment Annealed at 900 C for about 1 hour

Run conditions

Rig No. 1 **Pressure Vessel** H **Base plate** H Failsafe Tripped: ○ Yes

Hotpressing	**P (kb)**		**T(C)**		**Days**		**Hrs**	
Deformation	**P (kb)**	15	**T(C)**	800	**Days**	4	**Hrs**	87:00
Motor position		right	**Gear**	slow	**Speed**	30	**Gear (10^)**	
Hydrostatic	**P (kb)**		**T(C)**		**Days**		**Hrs**	

Malfunction of the apparatus

Lead leak; inner packing ring well grinded, not enough the outer one

Describe sample & assembly after Run

Furnace cracked, filled by salt, TC intact.
Asymmetric SZ because pistons twisted on an orizontal axe
TC in good position

Other remarks

Output values & PT path

Zero Start Values		Scale (mv/V FS)	Pump	
P (mv/V)	0.004	**Pressure**	2	FS
F (mv/V)	0.017	**Force**	2	FS
Dx (mv/V)	2.800	**Displacement**	0.5	FS

Furnace Power		**Pressure**	**Force**	**Temperature**	
A (old:psi)	**V**	**mV**	**mV**	**°C**	**%op**
0.38	0.331	0.380	0.173	30	4.8
0.67	0.694	0.399	0.200	100	7.3
0.94	1.008	0.786	0.902	200	10.2
0.113	1.222	1.207	1.270	300	12.7
0.129	1.385	1.556	1.562	400	14.8
0.150	1.504	1.940	1.881	500	16.4
0.166	1.575	2.255	2.192	600	18.0
0.185	1.712	2.661	2.632	700	20.4
0.201	1.799	3.001	2.891	800	22.5

GP462 – 100% Brazil matrix

Date 13/4/14 **Operator** *Giulia* **No.** 462GP

Type ○ Coaxial ● Shear ○ Hydrostatic ○ Solid Medium ○ Molten Salt

Aim Deforme pure qtz mmatrix, 800 C , 15 Kbar, strain rate 10^-5

Attachment ● Chart record ○ Sample picture ○ PT path ○ Stress-strain curve

Comments

Assembly

	Material	Length (mm)	Diameter (mm)	Comment
Sample	Quartz	18.46	6.33	pure matrix
Bottom piston	Alumina	6.665	6.33	**Sample + Pistons (mm)**
Top piston	Alumina	15.88	6.33	41.005

Furnace	Straight	**TC**	New wires	K-type	Cement tip & elbow
Top disk	Copper	**Teflon tape wrap**	Top Pb + Outer cell	**Crushable Alumina**	
Top Pb	yes	**Base pyrophyllite**	Unfired	Yes	
Outer cell	NaCl	**Comments**	0.15 gr pure NEW matrix		

Sample & Jacket

Sample Brazil matrix + 0.1 microL water added

Jacket Pt ● Welded ○ Crimped ○ Overlap pistons

Pretreatment Jacket annealed 1 hour at 900 C

Run conditions

Rig No. 1 **Pressure Vessel** new **Base plate** 1 Failsafe Tripped: ○ Yes

Hotpressing	**P (kb)**		**T(C)**		**Days**		**Hrs**	
Deformation	**P (kb)**	15	**T(C)**	800	**Days**	5	**Hrs**	100:00
Motor position		right	**Gear**	slow	**Speed**	30	**Gear (10^)**	
Hydrostatic	**P (kb)**		**T(C)**		**Days**		**Hrs**	

Malfunction of the apparatus

Describe sample & assembly after Run

Very good sample, pistons parallel, TC in good position,; no led leak.

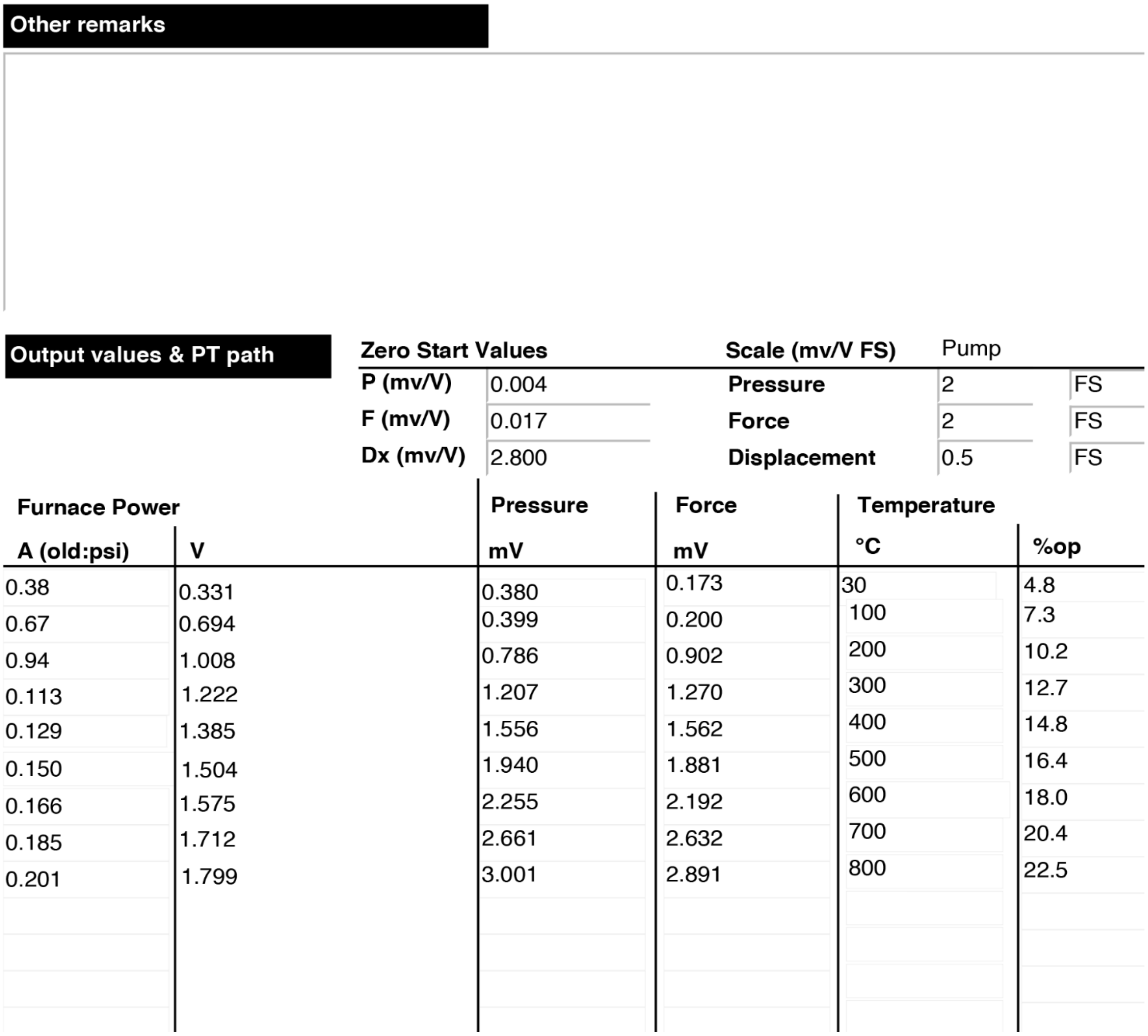

Other remarks

Output values & PT path

Zero Start Values		**Scale (mv/V FS)**	Pump	
P (mv/V)	0.004	**Pressure**	2	FS
F (mv/V)	0.017	**Force**	2	FS
Dx (mv/V)	2.800	**Displacement**	0.5	FS

Furnace Power		**Pressure**	**Force**	**Temperature**	
A (old:psi)	**V**	**mV**	**mV**	**°C**	**%op**
0.38	0.331	0.380	0.173	30	4.8
0.67	0.694	0.399	0.200	100	7.3
0.94	1.008	0.786	0.902	200	10.2
0.113	1.222	1.207	1.270	300	12.7
0.129	1.385	1.556	1.562	400	14.8
0.150	1.504	1.940	1.881	500	16.4
0.166	1.575	2.255	2.192	600	18.0
0.185	1.712	2.661	2.632	700	20.4
0.201	1.799	3.001	2.891	800	22.5

GP464 – 30% Hyuga porphyroclasts Hydrostatic

Date 18/4/14 **Operator** *Giulia* **No.** **464GP**

Type ○ Coaxial ● Shear ○ Hydrostatic ○ Solid Medium ○ Molten Salt

Aim Deforme 30% Hyuga porphyroclasts with NEW matrix

Attachment ● Chart record ○ Sample picture ○ PT path ○ Stress-strain curve

Comments

Assembly

	Material	**Length (mm)**	**Diameter (mm)**	**Comment**
Sample	Quartz	17.89	6.33	30% Hyuga porphyro
Bottom piston	Alumina	8.243	6.33	**Sample + Pistons (mm)**
Top piston	Alumina	16.912	6.33	43.045

Furnace	Straight	**TC**	New wires	K-type	Cement tip & elbow
Top disk	Copper	**Teflon tape wrap**	Top Pb + Outer cell	**Crushable Alumina**	
Top Pb	yes	**Base pyrophyllite**	Unfired	Yes	
Outer cell	NaCl	**Comments**	new matrix		

Sample & Jacket

Sample

Jacket Pt ● Welded ○ Crimped ○ Overlap pistons

Pretreatment Annealed at 900 C for about 1 hour

Run conditions

Rig No. 1 **Pressure Vessel** new **Base plate** 1 Failsafe Tripped: ○ Yes

Hotpressing	**P (kb)**		**T(C)**		**Days**		**Hrs**	
Deformation	**P (kb)**		**T(C)**		**Days**		**Hrs**	
Motor position		right	**Gear**	slow	**Speed**	30	**Gear (10^)**	
Hydrostatic	**P (kb)**		**T(C)**		**Days**		**Hrs**	

Malfunction of the apparatus

After 30 mins after running, PV cracks, Pc drops from 15Kbar to 7Kbar. Rapid decompression.
No problems with TC, T stable during P drop.

Describe sample & assembly after Run

Sample in good condition, pistons parallel

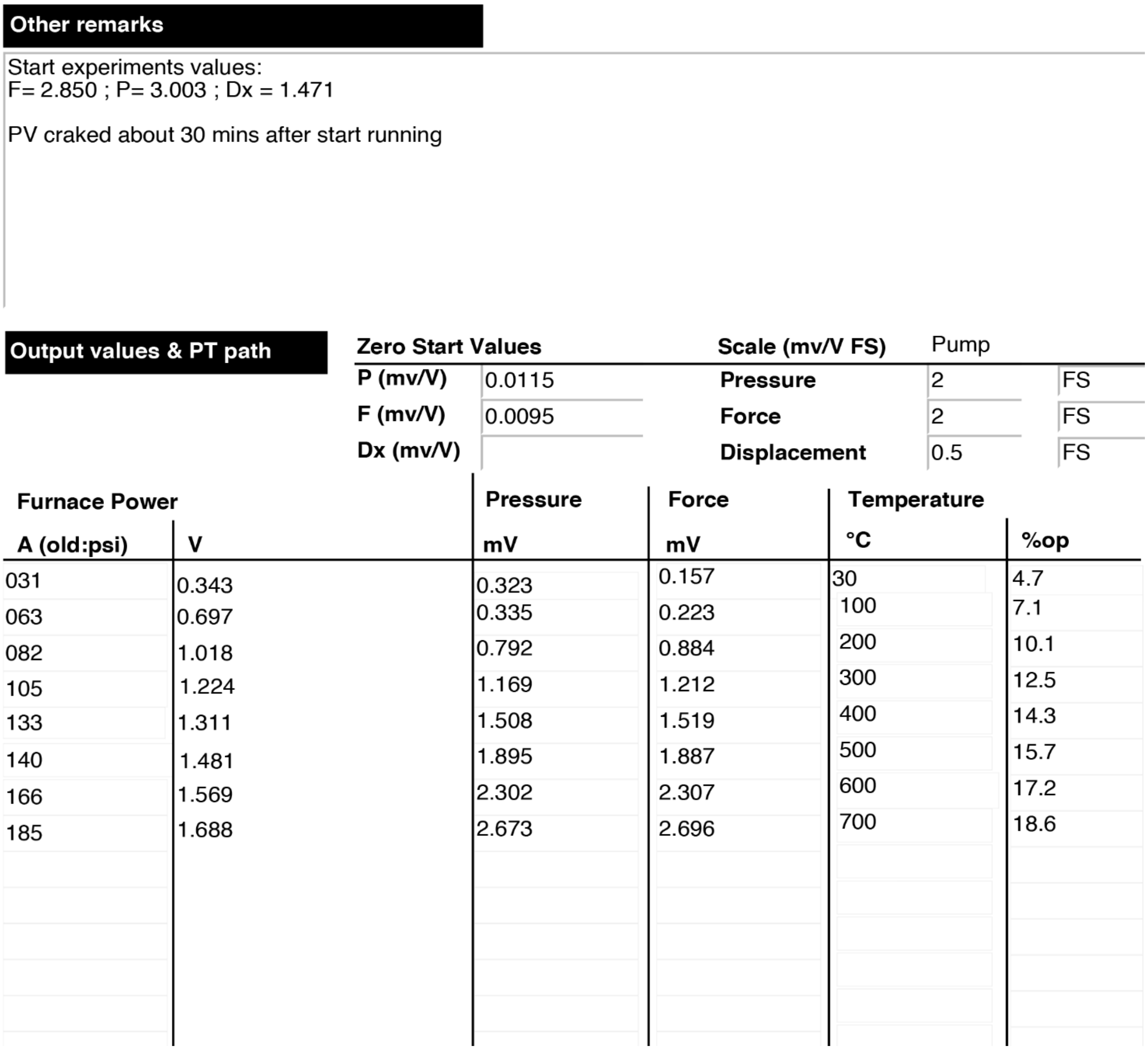

Other remarks

Start experiments values:
F= 2.850 ; P= 3.003 ; Dx = 1.471

PV craked about 30 mins after start running

Output values & PT path

Zero Start Values		**Scale (mv/V FS)**	Pump	
P (mv/V)	0.0115	**Pressure**	2	FS
F (mv/V)	0.0095	**Force**	2	FS
Dx (mv/V)		**Displacement**	0.5	FS

Furnace Power		**Pressure**	**Force**	**Temperature**	
A (old:psi)	**V**	**mV**	**mV**	**°C**	**%op**
031	0.343	0.323	0.157	30	4.7
063	0.697	0.335	0.223	100	7.1
082	1.018	0.792	0.884	200	10.1
105	1.224	1.169	1.212	300	12.5
133	1.311	1.508	1.519	400	14.3
140	1.481	1.895	1.887	500	15.7
166	1.569	2.302	2.307	600	17.2
185	1.688	2.673	2.696	700	18.6

Giulia PALAZZIN

Transition fragile-ductile en zone de subduction: le rôle du quartz

La transition d'un comportement séismique/instable à un comportement aséismique/stable est observée dans la partie en aval des zones sismogéniques (12-15 km de profondeur). Cette transition est supposée être contrôlée par l'activation de la plasticité de basse température du quartz à ~350°C. À cause de la grande profondeur à laquelle cette transition a lieu, le seul moyen pour étudier les processus physiques qui agissent en ces contestés, est l'étude des anciens prismes d'accrétion exhumés actuellement dans des chaines de montagnes. Le mélange tectonique de Hyuga et l'unité de Morotsuka appartiennent au prisme fossile de Shimanto et sont des unités metasédimentaires déformées à des températures peu inférieures ou égales à la limite fragile/ductile (~250 et ~340°C respectivement). Les résultats des observations de microstructures en microscopie optique et en microscopie électronique à balayage (diffraction des électrons rétrodiffusés) confirment que 1) la pression dissolution et une intense microfracturation sont les mécanismes de déformation principaux du quartz dans le mélange de Hyuga et localement l'activation de la plasticité du quartz est aussi observée; 2) dans l'unité de Morotsuka la recristallisation dynamique du quartz est pleinement active. Ces considérations indiquent que la température n'est pas le seul paramètre qui control l'activation de la plasticité du quartz, et laisse supposer la participation de l'effet adoucissant de l'eau. Avec le but de mieux comprendre le rôle de l'eau sur la rhéologie quartz, des expériences en Presse Griggs ont été menées, le matériel du départ étant de porphyroclasts de quartz (immergés dans une matrice sec) à la fois très riches en eau (provenant du mélange tectonique de Hyuga) et secs (quartz du Brésil). Ces expériences montrent l'effet très adoucissant de l'eau, qui à parité de conditions de déformation, favorise la migration de joint des grains dans le quartz de Hyuga tandis que le quartz du Brésil reste indéformé à exceptions de ses bordures extérieures. L'eau « en excès » est expulsée dans la matrice pour le quartz de Hyuga et stockée dans des bandes de cisaillement C'; l'eau incorporée par le quartz de Brésil n'est pas suffisantes pour favoriser la recristallisation dynamique.

Mots clés : quartz, prisme d'accrétion, transition fragile-ductile, eau, pression dissolution, déformation plastique, fluage dislocation, adoucissement

Brittle-ductile transition in subduction zones : the role of quartz

The trasition from instable seismic to stable aseismic behaviour is observed in at the lower limit of the seismogenic zones in subduction zones (12-15 km). This transition is supposed to be controlled by the onset of quartz low grade plasticity at about 350°C. Due to inaccessibility of these geodynamic contests, the only way to study the physical processes acting at these depth are exhumed accretionary prisms exposed in mountain chains. The Hyuga tectonic mélange and the Foliated Morotsuka are metasedimentary units constituting the Shimanto accretionary prism (Japan). They were deformed at temperatures of ~250°C and ~340°C respectively, so slightly lower or equal to the temperature transition. Results by optical microscopy and EBSD reveal that 1) quartz deformation mechanisms active in Hyuga Tectonic Mélange are pressure solution and microfracturation accompanied by local quartz low grade plasticity; 2) dynamic recrystallization is totally active in quartz of the Foliated Morotsuka. These considerations allow to consider the role of water in triggering quartz plasticity especially in such water-rich contest as subduction zones. With the aim to better understand the role played by water on quartz rheology, we deformed high hydrated (from Hyuga unit) and dry (classic Brazil) quartz porphyroclasts within a quartz matrix, with the Griggs apparatus. These experiments show the weakening water effect on quartz strength. At the same deformation conditions, the high hydrated Hyuga quartz show recrystallization by grain boundary migration while the dry Brazil porphyroclasts are mostly undeformed, at exception of the outer recrystallized rims. The exceeding water expulsed from Hyuga quartz is stored in C' shear bands in the matrix; water absorbed by dry Brazil porphyroclasts is not enough to promote dynamic recrystallization.

Keywords : quartz, accretionary prism, brittle-ductile transition, water, pressure solution, recrystallization, dislocation creep, hydrolitic weakening

Institut des Sciences de la Terre d'Orléans
CNRS/INSU, ISTO, UMR 7327
1A, rue de la Férollerie - 45071 Orléans Cedex 2